Computational Simulation of Chloride-Induced Corrosion Damage in Prestressed Concrete Bridge Girders

Mojtaba Aliasghar-Mamaghani

Dissertation submitted to the faculty of the Virginia Polytechnic Institute and State University in partial fulfillment of the requirements for the degree of

Doctor of Philosophy
In
Civil Engineering

Ioannis Koutromanos, Chair
Carin Roberts-Wollmann
Matthew Hebdon
Eric Jacques
Ioannis A. Kougioumtzoglou

May 10, 2023
Blacksburg, VA

Keywords:
Corrosion, Chloride ion, Chemical diffusion, Moisture transport, Heat transfer, Solar radiation, Heat conduction, Advective transport, Finite element, Nonlinear analysis, Prestressed girder, Bridge girder, Flexural capacity, Shear capacity, Oxidation-reduction reaction, Beam model, Truss model, Electrochemical reaction, Mechanical damage, Concrete cracking, Redox reaction, Chemo model, Thermo-hydro-chemo-mechanical model

Computational Simulation of Chloride-Induced Corrosion Damage in Prestressed Concrete Bridge Girders

Mojtaba Aliasghar-Mamaghani

ABSTRACT

Prestressed concrete is a popular construction material for highway bridges. A variety of girder span values, cross-sectional shapes, and prestressing strand layouts has been used in bridges across the United States. A major concern for such bridges is the possibility of corrosion damage in the prestressing strands or reinforcing bars, which is commonly caused by the use of deicing salts on the deck or saltwater spray in coastal regions. The present study aims at establishing analytical tools for the accurate simulation of chloride ingress, corrosion and mechanical damage (cracking) in the concrete, and for the evaluation of the impact of corrosion on the flexural and shear strength of bridge girders.

First, an efficient and accurate analytical scheme is formulated to enable the calculation of the load-carrying capacity of corrosion-damaged girders. The analyses rely on two types of models, namely, beam models and nonlinear truss models. The latter are deemed necessary to obtain reliable estimates of the shear capacity, as beam models are not well-tailored for capturing shear failures. A procedure to account for the reduction in area and deformability of corroded strands, based on visually observed corrosion damage, is proposed and implemented. The models are calibrated and validated with the results of experimental tests on prestressed girders which exhibited varying levels of corrosion damage. Further analyses allow the comparison of the capacity of corrosion-damaged girders to that of their undamaged counterparts. The accuracy of a simplified procedure, using equations in the AASHTO code to determine the flexural and shear capacity of the damaged girders, is also determined.

Subsequently, a computation scheme was proposed to describe the intrusion of chloride ions in prestressed bridge girder sections. The approach accounts for multiple, coupled processes, i.e., heat transfer, moisture transport, and chloride advective and diffusive transport. The constitutive models for moisture and chloride transport rely on previous pertinent work, with several necessary enhancements. The modeling scheme is calibrated with data from previous experimental tests on concrete cylindrical and prismatic specimens. The calibrated models are then validated using data from chloride titration tests conducted on girders removed from two bridges in Virginia after 34 and 49 years of service. The results indicate that the proposed framework can accurately reproduce the experimentally measured chloride content. The modeling approach also allows the evaluation of the accuracy of simplified, design-oriented tools for estimating the evolution of chloride content with time.

The multi-physics simulation scheme is further refined to account for the corrosion-induced mechanical damage (cracking), by incorporating a phenomenological description of the electrochemical reaction kinetics, generation of expansive corrosion products, and subsequent development of tensile stresses and cracking in the surrounding concrete. The impact of cracking on the chloride and moisture transport mechanisms is also taken into account.

The last part of this dissertation pursues the quantification of the uncertainty governing the chloride ingress in bridge girders, through the use of a stochastic collocation approach. The focus is on understanding how the inherent uncertainty in the value of input parameters (e.g., material transport parameters, ambient conditions etc.) is propagated, leading to uncertainty in the evolution of chloride content and the expected corrosion initiation time for a given bridge.

Computational Simulation of Chloride-Induced Corrosion Damage in Prestressed Concrete Bridge Girders

Mojtaba Aliasghar-Mamaghani

(GENERAL AUDIENCE ABSTRACT)

Prestressed concrete is widely utilized in the construction of highway bridges in the United States. A significant concern arises regarding potential corrosion damage in the prestressing strands or reinforcing bars, which is commonly attributed to the application of deicing salts on the deck or exposure to saltwater spray in coastal regions. This study aims to develop analytical tools that can accurately simulate the intrusion of corrosive agents (namely chloride ions), and subsequent damage (cracking) in concrete. Furthermore, the research seeks to assess the impact of corrosion on the bearing capacity of bridge girders.

Two different classes of analytical approaches are pursued. The first class employs purely mechanical (stress/deformation) models for capturing the strength, deformability and failure modes of girders with visual corrosion damage. These models rely on two approaches to capture the flexural and shear capacity of specimens, namely, beam-based models and truss-based models. The impact of corrosion is established through appropriate modification of the model parameters, based on the extent of visually observed corrosion damage. The analytical approaches are validated through a series of experimental tests previously conducted on corrosion-damaged girders.

The second class of analytical approaches employs multi-physics models, to describe the mechanisms leading to corrosion-induced damage. The models account for heat transfer, moisture transport, and chloride transport in prestressed beam sections. Model parameters are calibrated with experimental tests in literature. The computational scheme is used to

quantitatively describe the chloride ingress on bridge girders decommissioned from two different bridges in Virginia, after 34 and 49 years of service. The analysis results are found capable of capturing the actual chloride content at various depths from the exposure surface, as determined by chloride titration tests. The temporal evolution of chloride on the surface of prestressing strands indicates that corrosion has been taking place over a period of time for the two bridges.

The multi-physics simulation approach is further enhanced to account for the corrosion-induced mechanical damage (cracking), by explicitly incorporating a description of the reaction kinetics, generation of expansive corrosion products and subsequent development of cracking in the surrounding concrete.

The last part of this dissertation pursues the quantification of the uncertainty in the expected service life of prestressed concrete bridge structures. Given the inherent uncertainty to key values of model parameters, a parametric study is employed to investigate the propagation of uncertainty to the time history of chloride content at particular locations of the section and the probability of corrosion initiation at specific age values.

تقدیم به:

مادر زیبایم، شمسی،

پدر استوارم، مهدی،

و خواهر و برادر مهربانم، لیلی و مرتضی.

To:

my beautiful mother, Shamsi,
my strong father, Mehdi,
and my kind siblings, Lili and Morteza.

Acknowledgement

I would like to express my heartfelt appreciation and deep gratitude to my esteemed advisor, Professor Koutromanos, for his invaluable guidance and mentorship throughout my doctoral journey. I would also like to express my sincere appreciation to my committee members, Professor Wollmann, Professor Hebdon, Professor Jacques, and Professor Kougioumtzoglou, for their invaluable feedback and insightful contributions throughout the course of this study.

I am deeply grateful for the unwavering support extended by my parents and the steadfast dedication of my siblings throughout this demanding journey. Without their continuous encouragement, attaining this milestone would have been an insurmountable challenge. The adage "*In unity, we achieve greatness*" resonates deeply, as their collective support has played an indispensable role in my accomplishment. Their unwavering belief in my abilities and steadfast assistance have been pivotal in accomplishing this achievement.

I would like to express my sincere appreciation to the Virginia Department of Transportation for funding this research project (Grant No. 114590). Their support has been invaluable in enabling the successful completion of this endeavor.

I am grateful to ARC (Advanced Research Computing) for their invaluable support in facilitating the analysis on the supercomputer. Their exceptional resources have played a crucial role in my research. Additionally, I would like to express my sincere appreciation to Virginia Tech for awarding me a fellowship during the last semester of my doctoral study.

I am sincerely grateful for the unwavering support of my friends and colleagues throughout this project, specifically Dr. Mohammad-Sadegh Khalafi. I would like to express

my deep appreciation to my friends Ali Alfailakawi and Abdullah Al Rufaydah for their generous provision of the experimental data for the bridge girders.

Table of Contents

List of Figures

List of Tables

Chapter 1
Introduction

This Chapter provides an introduction to the problem at hand. The impact of corrosion-induced damage on the safety and maintenance of prestressed concrete bridge infrastructure is discussed. Subsequently, an overview of the salient physical mechanisms controlling the initiation and evolution of corrosion is provided. The inherently uncertain character of the phenomenon is also established. The Chapter is concluded with the objectives and the outline of the present dissertation.

1.1 Overview

Concrete is the most widely used construction material for bridges, buildings, and dams. The material combines many advantages, perhaps the major one being the flexibility in structural form. It is, however, well-known that the tensile strength of concrete is much lower than its compressive strength. For this reason, it becomes necessary to properly detail regions where tensile stresses are expected to develop during the service life of a structure. This detailing most commonly involves steel reinforcing bars or prestressing strands. Prestressing is deemed essential for concrete bridges that exceed a certain span length. In fact, it is noteworthy that prestressed concrete has been used more than 50% of the bridges constructed in the United States. This widespread utilization underscores its significance of ensuring the structural integrity and performance of longer-span bridges. An important concern for prestressed concrete bridges is the possibility of corrosion in the prestressing steel of the girders, which

may severely undermine the lifespan and even the safety of such structures. As shown in **Figure 1.1**, excessive corrosion of the steel ultimately leads to significant damage (cracking) in bridges.

Figure 1.1. Chloride-induced corrosion damage in prestressed bridge girders [reproduced from (Alfailakawi et al., 2020)].

Unless corrosion damage is detected and repaired in a timely manner, it can lead to failure and even collapse of structures, potentially entailing deaths, injuries and significant economic losses due to traffic disruption. A recent example of corrosion-induced bridge failure is the 2005 partial collapse of the Lake View Drive Bridge, shown in **Figure 1.2**.

Figure 1.2. Partial collapse of Lake View Drive Bridge due to corrosion [reproduced from (Harries, 2009)].

The economic impact of corrosion is hard to overstate. In 2002, the Federal Highway Administration in collaboration with the NACE (National Association of Corrosion Engineers) International (FHWA-RD-01-156) estimated the annual direct costs for maintenance of bridges in poor condition at $8.3 billion. On the other hand, the indirect costs of corrosion were estimated at more than ten times that of the direct corrosion costs. The annual direct cost is increasing on a yearly basis, and in 2020 FHWA reported (FHWA-HRT-21-001) a direct corrosion cost of $13.6 billion. In 2019, more than 47,000 of the 616,087 bridges in the United States were found structurally deficient by the American Road and Transportation Builders Association (2019 Bridge Report). However, the pace of bridge repair reached a low point in 2019, potentially endangering lives by allowing deterioration to progress. The United States Government Accountability Office found one-third of bridges in the United States susceptible to corrosion and found bridges in need of $125 billion in repair.

The load-carrying capacity of bridge structures in coastal regions or those exposed to deicing salts is affected by the extent of chloride-induced corrosion damage developed in the prestressing strands. Given that strands in prestressed bridge girders are subjected to significant stress, the existence and assessment of corrosion in these structures are of prime importance.

Flexural failure of the corroded prestressed bridge girders can occur by the crushing of the top concrete or rupturing of the prestressing strands at the bottom face, as shown in **Figure 1.3**. Depending on the extent of the damage, corrosion reduces the flexural capacity and ductility of specimens.

Figure 1.3. Flexural failure of prestressed concrete bridge girder [test conducted by Alfailakawi et al. (2020)].

The ultimate shear strength of a girder may also be affected by the extent of chloride-induced corrosion damage.

1.2 Description of Physical Mechanisms Leading to Corrosion

Corrosion in bridge girders is primarily attributed to the ingress of chloride ions and their transport (through the concrete porous structure) to the locations of reinforcing and prestressing steel. During the early ages of setting, concrete is characterized by high alkalinity. This leads to the formation of a thin oxide film around the steel bars and prestressing strands. The protective film puts the reinforcing steel in a passive condition, i.e. it inhibits the iron's natural tendency for oxidation, offering protection against corrosion.

As shown in **Figure 1.4**, the presence of chloride ions on the surface of reinforcing steel materials significantly damages the protective film. Given the porous network of concrete bridges, chemical species such as chloride ions intrude in concrete structures in harsh environments, leading to the destruction of protective film on the surrounding area of

reinforcing steel bars, corrosion incidence, and subsequently progression in the rate of corrosion.

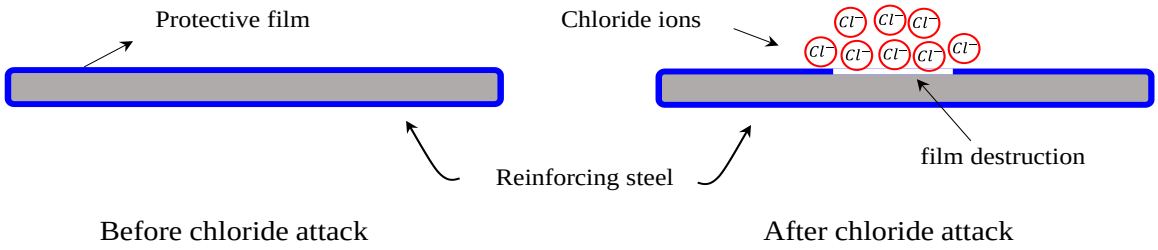

Figure 1.4. Destruction of protective film on the surface of steel wire, caused by chloride attack.

Corrosion of the prestressing strands embedded in concrete structures is associated with electrochemical reactions wherein iron in steel is converted to corrosion products. The volume of the corrosion products is greater than that of the original steel material by a factor between 2.0 and 6.4 (Youping and Richard, 1998), as shown in **Figure 1.5**. The precise corrosion products that are produced depend on various parameters, some of which are the pH of the pore solution, moisture content, and oxygen supply.

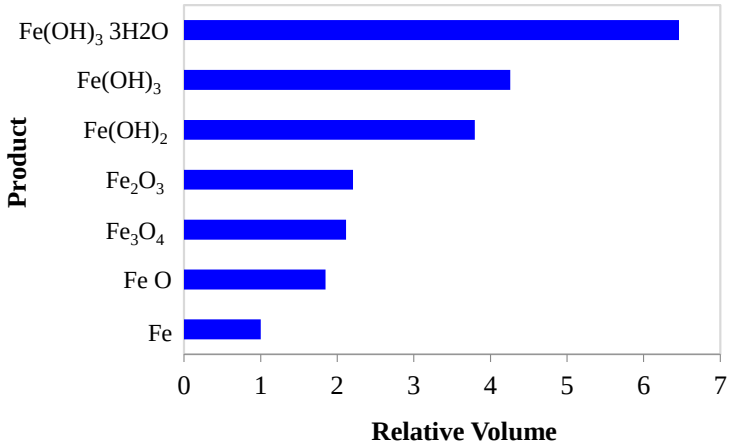

Figure 1.5. Relative volumes of corrosive products with respect to iron [reproduced from Youping and Richard (1998)].

The volumetric expansion of the corrosion products is restrained by the surrounding concrete. This in turn induces a swelling pressure on the concrete. Given that concrete has a low tensile strength, the volume expansion of corrosion products leads to the development of damage in concrete, causing initiation and progression of cracking, as shown in **Figure 1.6**.

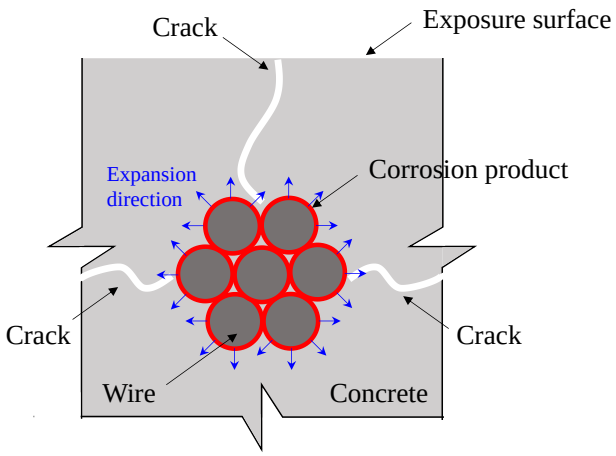

Figure 1.6. Cracking in concrete due to volumetric expansion of corrosive products.

The formation of cracks, creates new pathways that allow corrosive agents to penetrate the concrete network. In that regard, the fundamental properties of concrete, such as the chloride diffusion coefficient and moisture diffusion coefficient, undergo a significant increase, greatly exacerbating the progression of corrosion and corrosion-induced cracking. Ultimately, some of the cracks become connected, leading to the formation of wide cracks. In the late stages of the phenomenon, concrete in specific regions, i.e., near the cross-sectional corner spalls off, as denoted in **Figure 1.7**.

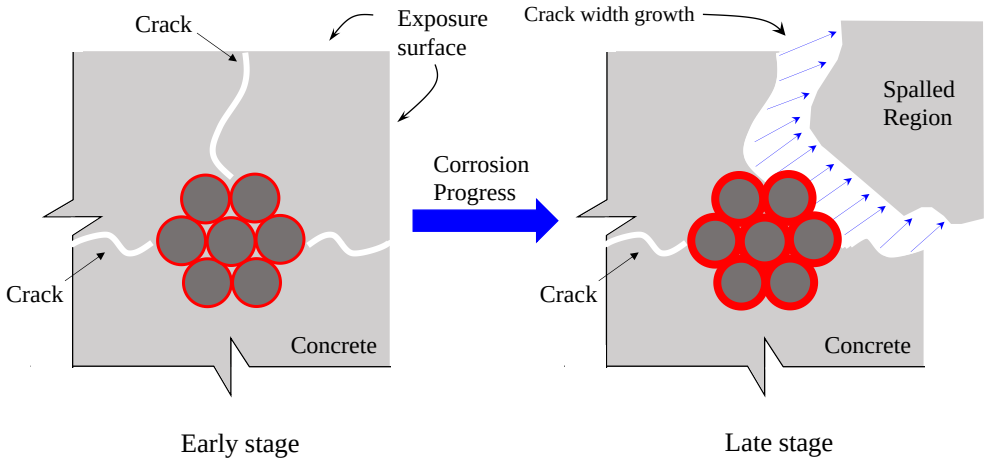

Figure 1.7. Corrosion-induced spalling of the concrete near the cross-sectional corner region.

The detrimental effects of corrosion extend beyond the mere loss of mass in prestressing strands and the resulting concrete cracking. Corrosion also significantly impacts the mechanical strength of the strands. Depending on the extent of corrosion damage, it can lead to a reduction in the elastic modulus of the strands to varying degrees, as well as affect the ultimate strain. **Figure 1.8** illustrates the influence of corrosion damage on the mechanical strength of strands. The majority of specimens exhibited a decrease in ultimate strain, with a few specimens demonstrating both phenomena simultaneously.

The other detrimental effect of corrosion pertains to bond strength decay, where it reduces the bond resistance between reinforcing steel and concrete material due to the volumetric expansion of corrosion products.

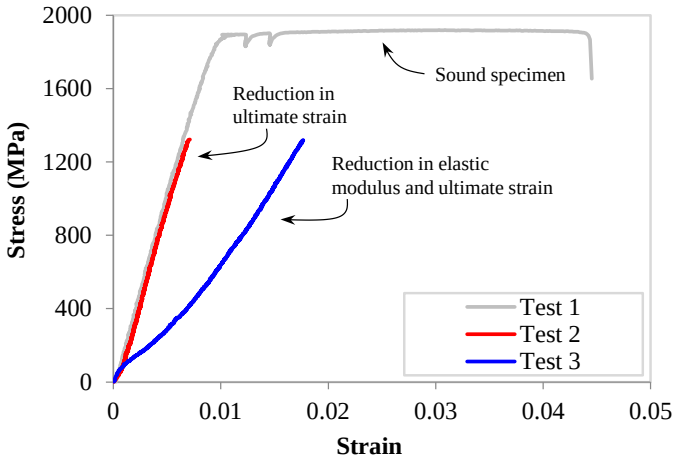

Figure 1.8. Uniaxial tensile test results for seven-wire strands with different degrees of corrosion damage.

The determination of corrosion incidence is a vital parameter in the analysis, maintenance, and if necessary, repair of prestressed bridge girders. As mentioned earlier, during the early stages of a concrete structure's life, a protective oxide film is formed on the surrounding area of prestressing strands, safeguarding it from corrosion damage. Corrosion initiation is believed to occur when the protective film on the surface of the strand is compromised or destroyed. The extent of the chloride on the surface of the prestressing strand can be indicative of the corrosion incidence and the content of chloride corresponding to this phenomenon is termed critical chloride C_{crit}. As the extent of chloride on the surface of strands exceeds C_{crit}, the rate of corrosion significantly increases. An increase in corrosion rate further intensifies the extent of damage in prestressing strands and causes corrosion to progress.

The analysis of the moment of chloride intrusion in concrete bridges enables a better understanding of the current condition of the bridge structures, which might be hidden for a period from the naked eye. The analysis is also crucial for maintenance and repair purposes.

Corrosion is associated with an electrochemical oxidation-reduction process in which iron is converted to corrosion products and significantly reduces the mechanical resistance of

the steel. Throughout this process, electrons are transferred from one chemical species to another. Oxidation occurs at the anode when electrons are given up from atoms, for instance, anodic oxidation reaction in corrosion is given by:

$$Fe(s) \rightarrow Fe^{2+}(aq) + 2e^{-} \tag{1.1}$$

where iron is oxidized into ferrous ion Fe^{2+} and dissolved into pore water; solid and aqueous states are denoted by (*s*) and (*aq*), respectively. Reduction takes place at the cathode when electrons are adsorbed and become a part of atoms, for instance, cathodic reduction reaction in the corrosion process is expressed by:

$$O_2(g) + 2H_2O(l) + 4e^{-} \rightarrow 4OH^{-}(aq) \tag{1.2}$$

where oxygen is reduced to hydroxyl ions; gaseous and liquid phases are denoted by *g* and *l*. Upon the formation of ferrous and hydroxyl ions, corrosion reactions take place, and corrosion products are produced.

$$Fe^{2+}(aq) + OH^{-}(aq) \rightarrow Fe(OH)_2(s) \tag{1.3}$$

Ferrous hydroxide $Fe(OH)_2$ further reacts with other chemical species to produce other corrosion products (Ji et al., 2013), for instance:

$$2Fe(OH)_2 + \frac{1}{2}O_2 + H_2O \rightarrow 2Fe(OH)_3 \tag{1.4}$$

or,

$$4Fe(OH)_2 + O_2 \rightarrow 2Fe_2O_3 \cdot H_2O + 2H_2O \tag{1.5}$$

or,

$$6Fe(OH)_2 + O_2 \rightarrow 2Fe_3O_4 \cdot H_2O + 2H_2O \tag{1.6}$$

where Fe_2O_3 and Fe_3O_4 are known as hematite and magnetite, respectively. The schematic procedure of the corrosion reaction process is shown in **Figure 1.9**. As stated earlier, electrons

are liberated from the anodic site (iron), moving toward the cathode (oxygen molecules). This electron movement corresponds to an electric current from the anode to the cathode (opposed to the conventional current direction). Incoming electrons react with oxygen in the vicinity of reinforcing steel and produce hydroxyl ions. The availability of ferrous ions and hydroxide ions facilitates the formation of corrosion products. In particular, under specific circumstances different forms of corrosion product might be produced (see **Figure 1.5**), for instance, ferrous hydroxide $Fe(OH)_2$, ferric hydroxide $Fe(OH)_3$, etc.

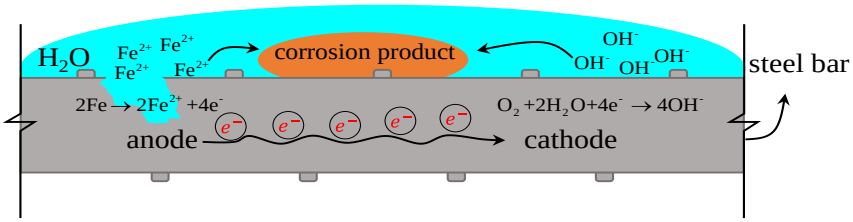

Figure 1.9. Schematic illustrating the electrochemical oxidation-reduction reaction, resulting in the formation of corrosion products.

Two mechanisms are responsible for the corrosion of reinforcing steel in concrete structures. The first is micro-cell corrosion where anodic and cathodic half-cell reactions occur in practically the same metal region on a microscopic scale (Hansson et al., 2006) [see **Figure 1.9**]. Macro-cell corrosion is the second corrosion mechanism and occurs when anodic and cathodic half-cell reactions take place on macroscopically distant locations, for instance when an active steel bar is connected to a passive bar (Hansson et al., 2006), as shown in **Figure 1.10**. Macro-cell corrosion is shown to be less common than micro-cell corrosion. The latter is believed to cause uniform corrosion, while the former was found to cause pitting corrosion (Hansson et al., 2006). Corrosion of reinforcing steel in macro-cell type is proportional to the

cathodic and anodic area of half-cells. It has been shown that the rate of macro-cell corrosion significantly diminishes over time, as the passivity in the reinforcing steel disappears by uniform or micro-cell type of corrosion (Zhang et al., 2020). Macro-cell corrosion was found to be predominant in specific environments, i.e., structures under external charges, such as underground structures subjected to stray current, or a difference in the natural electrode potential, such as cluster structures connected to underground water in coastal regions with different chloride concentrations (Wang et al., 2021).

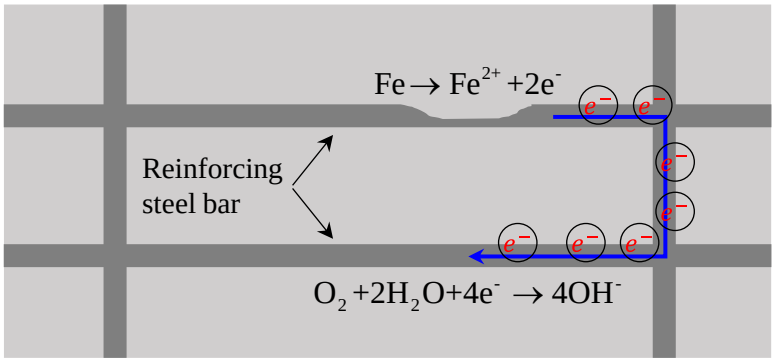

Figure 1.10. Schematic of macro-cell corrosion mechanism, reproduced from Hansson et al. (2006). The anodic and cathodic reactions take place in steel bars that are apart from each other.

The first step toward the understanding of corrosion damage is the calculation of the corrosion rate, which can be found from the kinetics of the electrochemical reaction. Considering the half-cell reactions described in equations (1.1) and (1.2), after the occurrence of corrosion, a short circuit is formed in the electrochemical cells where electrons flow from the anode to the cathode. This effect causes a non-equilibrium state in the system leading to potential disparities in standard electrode potentials. The displacement of electrode potential from standard electrode potential is called polarization and the magnitude of this displacement is termed overvoltage (Callister et al., 2021).

There are two primary polarization mechanisms in electrochemical reactions. The first, called activation polarization, occurs when the rate of the overall reaction is primarily governed by a single step in the sequence, specifically the step with the slowest rate (Callister et al., 2021). The overvoltage in activation polarization is described by:

$$\eta_a = \pm\beta \log \frac{i}{i_0} \tag{1.7}$$

where β is model parameter, i_0 is the exchange current density, and i is the current density. Activation polarization for the hydrogen atom is shown in **Figure 1.11**, with two different branches showing oxidation and reduction reactions. As shown, oxidation occurs at the anode with a positive overvoltage rate and reduction occurs at the cathode with a negative overvoltage rate. A potential must be taken with respect to a reference value (which-by definition-corresponds to zero value of potential). The referential electrode cell, corresponding to zero potential, is typically taken to be the Hydrogen molecule. The displacement of the electrode from the standard state (a difference from zero volts in the vertical axis) is overvoltage which might be positive or negative depending on the half-cell reaction types.

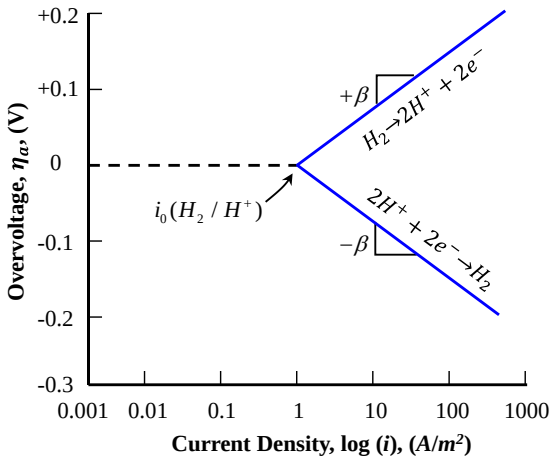

Figure 1.11. Activation polarization overvoltage for the hydrogen atom (reproduced from Callister et al. (2021)].

Concentration polarization is the second polarization mechanism, governed by the diffusion process (Callister et al., 2021). Considering reaction half-cells shown in **Figure 1.11** it is always assumed that there is an adequate amount of hydrogen ions that feed electrochemical reactions between two half-cells. However, in cases where hydrogen concentrations are low or high, hydrogen ions might not replenish half-cell reactions at a sufficient rate to keep up the electrochemical reaction and a depletion zone might be formed in the immediate vicinity of electrode cells. Therefore, concentrations of hydrogen ions govern the rate of reaction leading to the occurrence of concentration polarization. The overvoltage in cathodic polarization is established in the following form:

$$\eta_c = \frac{2.3RT}{nF} \log\left(1 - \frac{i}{i_l}\right) \tag{1.8}$$

where T is the absolute temperature, F is the Faraday's constant, i_l is the limiting diffusion current density, and n is the number of electrons in the ionization of a metal atom. The scheme of concentration polarization along with activation polarization is shown in **Figure 1.12**.

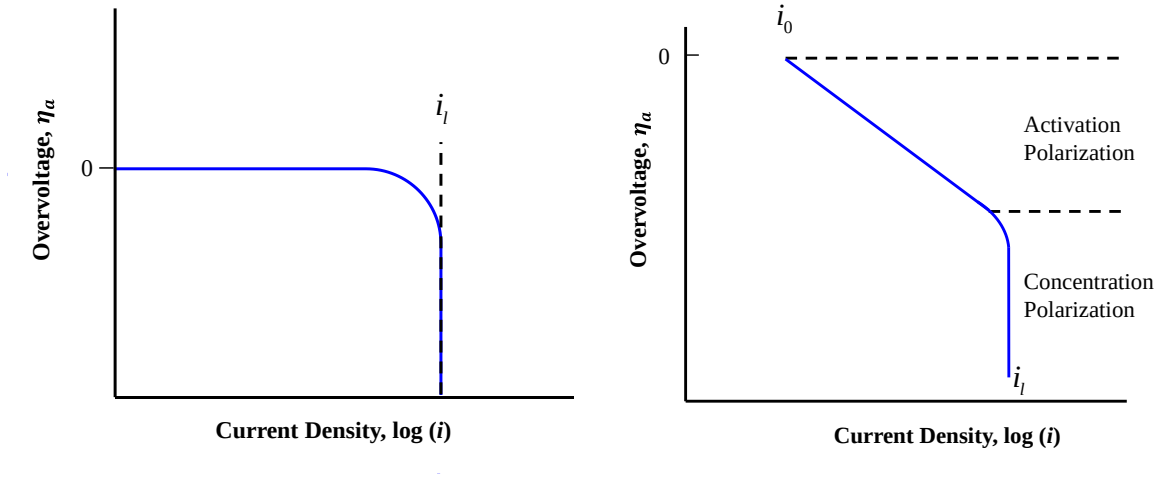

(a) Concentration polarization curve

(b) Activation-concentration polarization curve

Figure 1.12. Schematic illustration of polarization mechanisms [reproduced from Callister et al. (2021)].

The rate of corrosion reaction can be reasonably estimated via polarization curves of two half-cells, which account for both activation and concentration polarization. Activation polarization curves for an electrochemical cell containing zinc and hydrogen half-cells are shown in **Figure 1.13**a. Conservation of electric charge stipulates that all electrons liberated from the anodic half-cell are to be consumed by the cathodic half-cell. This implies that the current density, i_{corr}, must be the same for the two half-cells. As such, the only possible point that meets this criterion is the intersection point of polarization curves. The projection of the intersection point on the vertical and horizontal axes gives the corrosion potential, E_{corr}, and corrosion current density, i_{corr}, respectively.

The electrochemical reaction kinetic of activation-concentration polarization curves for two different metals is shown in **Figure 1.13**b. Throughout this process, the zinc atom, Zn, is oxidized and the hydrogen ion, H^+, is reduced.

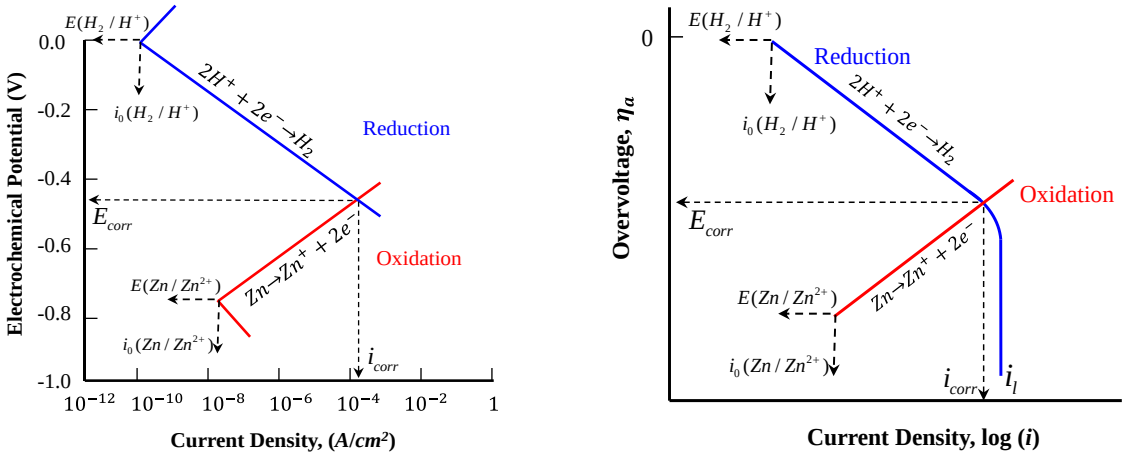

(a) Schematic for activation polarization mechanism

(b) Schematic for activation-concentration polarization mechanism

Figure 1.13. Electrochemical reaction kinetic of an acid solution and zinc atom reproduced from Callister et al. (2021).

As stated earlier, due to the highly alkaline nature of concrete in the early stages of the concrete setting, a thin protective film forms on the surface area of reinforcing and prestressing steel, which makes it passive against corrosion. This phenomenon is termed passivity, which reduces the rate of corrosion by several orders of magnitude. The polarization curve for passive steel has an S-shaped behavior shown in **Figure 1.14**a (Callister et al., 2021). The specific curve is a coalescence of three distinct regions, namely active, passive and transpassive. The active region describes the behavior of steel in normal conditions with a linear oxidation (or reduction) behavior. As the electrode potential increases, the current density in the passive region significantly reduces and becomes independent of the potential. As electrode potential increases further, steel enters the transpassive zone where an increase in the electrode potential leads to an increase in the current density.

The impact of passivity on the electrochemical reaction rate can be described on the basis of polarization curves, as shown in **Figure 1.14**b. Given the polarization curve of the

reduction reaction in two solutions, labeled A and B, corrosion current density which corresponds to the projection of intersection points in the horizontal axis is very low in the former [$i_c(i)$]. Given that current density is shown on a logarithmic scale, the passivation might reduce the corrosion rate by several orders of magnitude (Callister et al., 2021).

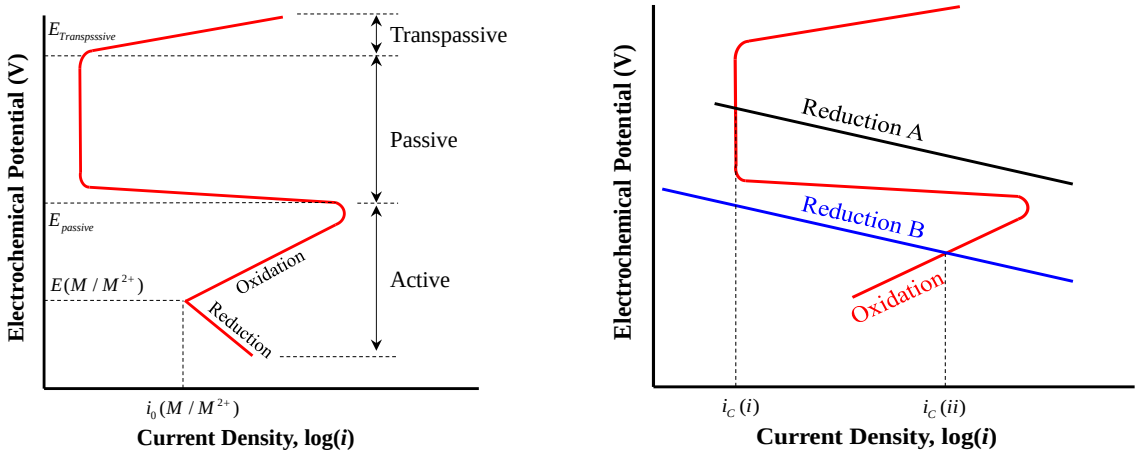

(a) Schematic illustration of polarization curve for steel showing active, passive, and transpassive zones

(b) Active and passive corrosion behaviors for steel in different solution

Figure 1.14. Polarization curve and corrosion behavior for passive steel, reproduced from Callister et al. (2021).

1.3 The Need for Uncertainty Quantification

The physical mechanisms described in the previous section are controlled by a number of parameters, and each parameter is characterized by aleatory (inherent) uncertainty. For instance, the ambient (climatic) conditions in the vicinity of a bridge affect the moisture transport mechanism, which in turn is instrumental for chloride ingress in the concrete. Furthermore, the amount of chloride inflow in the surface of a bridge is highly uncertain, and a wide range of values for this quantity has been proposed/reported in the literature. Even if a

concrete bridge is subjected to highly controlled environmental conditions, the porous structure in the concrete is itself highly variable, which in turn implies an inherent uncertainty on various constitutive parameters (e.g., moisture and/or chloride diffusivity) which significantly affect the chloride ingress and corrosion. In light of the above, it should come as no surprise that the extent of observed chloride-induced corrosion damage can significantly vary for different girders in a bridge, and even at different locations of the same girder. An example bridge span demonstrating such variability is provided in **Figure 1.15**, which presents girders which were decommissioned from the Lesner bridge in Virginia after 49 years of service. As **Figure 1.15** shows, the girders had exhibited corrosion damage in localized regions, marked with circles in the figure, which had been repaired (patched).

Figure 1.15. Chloride-induced corrosion damage in Lesner Bridge, Virginia [reproduced from (Alfailakawi et al., 2020)].

1.4 Objectives

The overarching goal of this dissertation is to enhance the understanding of the process leading to chloride-induced corrosion damage in prestressed concrete bridge girders. The work can be subdivided into four parts, each with its own objectives.

The objective of the first part is to investigate the bearing capacity of corrosion-damaged prestressed concrete bridge girders. A nonlinear finite element approach is established to accurately evaluate the shear and flexural capacity of girders exhibiting visual corrosion damage.

The second part of the present study is aimed to develop a nonlinear finite element approach for assessing the temporal evolution of the sectional distribution of chloride in girders. Additionally, this approach aims to qualitatively evaluate the service life performance of these girders. A coupled finite element analysis scheme, accounting for moisture, heat, and chloride transport is formulated, calibrated and validated.

The primary focus of the third part of this dissertation is to present a nonlinear finite element approach that effectively captures corrosion-induced damage in prestressed concrete bridge girders. To this end, the analysis scheme of the second part is further enhanced with the capability to account for the kinetics of the electrochemical oxidation-reduction equation, the formation of expansive products, the occurrence of cracking and the impact of this cracking on the chloride ingress.

The fourth and final part of this dissertation focuses on quantifying the uncertainty associated with the expected service life of corrosion-affected prestressed concrete bridge structures. This is accomplished by establishing a mathematical description of the (aleatory) uncertainty associated with various parameters of the problem at hand, and then determining the propagation of this uncertainty to the expected service life.

1.5 Dissertation Outline

Chapter 2 provides a review of literature on strength assessment of corrosion-damaged girders and analytical modeling of chloride ingress in concrete and corrosion-induced cracking.

Chapter 3 proposes a computational approach for obtaining the flexural and shear resistance of prestressed concrete bridge girders with visually observed chloride-induced corrosion damage. Two types of simplified models, which rely on uniaxial material laws, are used, namely, beam models with a fiber section and nonlinear truss models.

Chapter 4 establishes a phenomenological approach to describe the intrusion of corrosion-inducing chloride ions in concrete bridge girders. Various physical processes affecting the ingress of chloride, i.e., coupled heat, moisture, and chloride transport, are taken into account. The scheme is calibrated and validated with experimental data on cylindrical and prismatic specimens and are applies to real-life bridge girders.

Chapter 5 investigates the impact of corrosion-inducing chloride ions in the spatial distribution of corrosion damage. A computational scheme is proposed to describe various significant processes affecting chloride-induced corrosion damage in sound and cracked concrete. The scheme includes phenomenological laws to account for the kinetics of the corrosion electrochemical process, the formation of expansive corrosion products and the ensuing formation of cracking in the surrounding concrete. The impact of cracking on the temporal evolution of chloride content in key locations of the bridge section is also investigated.

Chapter 6 deals with the uncertainty quantification of chloride-induced corrosion damage in concrete bridges. The analysis relies on the stochastic collocation approach.

Chapter 7 presents the main conclusions of this research and provides recommendations for future research building on the findings of the present study.

Chapter 2
Literature Review

This chapter provides a review of the literature pertaining to the topic of the present study. The review is subdivided into several thematic classes, i.e. i) experimental and analytical evaluation of load-carrying capacity in corrosion-damaged prestressed girders, ii) mathematical modeling and computational simulation of chloride ingress, corrosion and corrosion-induced cracking in concrete, and iii) quantification of uncertainty governing the evolution of chloride content and corrosion in bridge girders.

2.1 Load-Carrying Capacity of Corroded Bridge Girders

Prestressed concrete bridges are one the most popular constructional systems that provide a safe crossing feature for transportation connectivity of the roadway network. They are available in a variety of cross-sectional geometry, spans, and prestressing strand layouts across the United States. The eventuality of chloride-induced corrosion damage is a major concern for concrete bridges (Weyers et al., 1994), which is usually caused by saltwater spray in coastal zones, or the use of deicing salts on the top of the specimen (i.e., deck).

The load-carrying capacities of prestressed concrete bridge girders with chloride-induced corrosion damage have been investigated in a number of experimental studies.

Shenoy and Frantz (1991) focused on the structural performance of two prestressed girders recovered from a bridge after 27 years of service, which was subjected to extensive use of deicing salts. The experiment was meant to investigate the impact of chloride-induced

corrosion damage on the flexural resistance of girders through a four-point bending configuration. While minor corrosion was present in the girders, it was found to have a minimal effect on deformability and flexural strength of girder specimens.

Tabatabai and Dickson (1993) performed a series of experimental tests to evaluate the flexural resistance, serviceability, and material properties of a post-tensioned bridge girder. The girder was removed from a 34-year-old bridge subjected to severe winter cycles and extensive use of deicing salts. Though some of the wires had evidence of corrosion, and corrosion had been manifested in the anchorage system at end regions, similar to the study by Shenoy and Frantz (1991), the flexural resistance of the girder was not affected by the extent of corrosion damage. Given the limited experimental tests performed to that date, they recommended additional experimental tests on the structural performance of bridge girders with a variety of corrosion damage.

Harries (2009) performed a set of experimental tests to investigate the extent of corrosion and flexural performance of two prestressed concrete bridge girders. The specimens were subjected to saltwater spray and were removed from a partially collapsed bridge after 42 years of service. Based on visual inspections and four-point bending tests, it was found that the flexural resistance and deformability of specimens were heavily affected by chloride-induced corrosion damage. The results of the forensic analysis performed after flexural tests also confirmed significant damage in prestressing strands, which was originally underestimated by visual inspections. In that respect, the extent of corrosion had been manifested in different layers of prestressing strands along the soffit of the girders.

Pape and Melchers (2011) focused on the impact of chloride-induced corrosion damage caused by saltwater spray on the structural performance of three girders removed from a 45-

year-old bridge. The girders had significant signs of corrosion damage from cracking to the spalling of the concrete. The flexural strength of specimens was investigated by a four-point bending configuration. According to the results, corrosion had a major impact, with cross-sectional area loss in excess of 75% for several strands. It also affected the bearing strength of the specimens resulting in a flexural capacity degradation of up to 50% and a pronounced loss in deformability. Further investigation has also revealed advanced signs of corrosion, such as wire pitting, formation of corrosion products in different colors (Green, Blue, and Brown rusts), and anaerobic corrosion products which are indicative of bacteria activity. Similar conclusions were also reached in another study by Pape and Melchers (2013) on the impact of corrosion damage on the bearing capacity of bridge girders.

A study by Murray et al. (2019) focused on the load-carrying capacity of two girders recovered from a bridge subjected to deicing salts after 45 years of service. The girder specimens had a variety of chloride-induced corrosion damage from minor to moderate at the end regions, which is a major concern for resistance against shear forces for urbane bridge inventory. The bearing capacity of specimens was evaluated through a three-point-loading configuration with various shear-span-to-depth ratios from 2.0 to 3.83. It was found that corrosion had caused some bond-slip damage in the end regions of the girders leading to shear failure of some specimens. However, the damage pattern was not found to affect the shear resistance of girders.

Alfailakawi et al. (2020) performed several experimental tests to investigate the impact of chloride-induced corrosion damage on the flexural resistance of prestressed concrete bridge girders. Multiple bridge girders with a variety of cross-sectional shapes and geometry were removed from different bridges in Virginia after 34 and 49 years of service and were tested

under a four-point bending scheme. Some bridge girders were exposed to extensive use of deicing salts, while others were subjected to the use of saltwater spray. According to the results of non-destructive tests, and destructive flexural tests, corrosion was found to cause a significant cross-sectional loss in the area of prestressing strands and reduced the flexural resistance of some girder specimens.

A study by Al Rufaydah (2021) focused on the influence of chloride-induced corrosion damage on the shear resistance of bridge girders. Two prestressed concrete bridge girders were removed from bridges in the state of Virginia after 34 and 49 years of service. The girder specimens were subjected to saltwater spray, or use of deicing salts. The resistance of the girders was evaluated through a three-point-loading scheme with different shear-span-to-depth ratios. According to the results, corrosion played a minor role in the shear strength of the girder specimen, while affecting the mode of failure most. In particular, the extent of the corrosion in prestressing strands at the bottom face of the girder, between the support and pointed load, impacts the deformability of strands and girder specimens, changing the mode of failure from shear to flexure. The cornerstone of this transition was manifested in the load-carrying capacity of the specimens, where the strength of the girder failed in shear-flexure was smaller than that failed in shear.

Some researchers adopted an analytical approach for the evaluation of the load-displacement response of girder specimens, that uses the moment-area principle to calculate deflections (Shenoy and Frantz, 1991; Tabatabai and Dickson, 1993).

The beam model is a widely used approach in the literature that has been shown to provide an accurate and numerically efficient solution to the nonlinear response and ultimate flexural resistance of beams. In particular, Dall'Asta and Dezi (1998) have introduced a new

scheme for the structural analysis of prestressed composite beams to overcome some restrictions for the slip of tendons at the saddle points, as well as construction stages. The scheme involves nonlinear constitutive laws for the material properties and a linear definition of kinematics. According to the results, the approach was found capable of capturing the structural response of prestressed beams with external tendons.

A study by Ariyawardena and Ghali (2002) focused on the structural analysis of prestressed beams with external or internal tendons. The analysis scheme has been supplemented with multiple features, such as nonlinear material properties, tension stiffening, and friction and loss of tendons at the deviator block. Based on the results, the approach was found capable of capturing the structural response of externally and internally prestressed beams which was verified with the experimental tests.

A study by Dall'Asta et al. (2007) developed a simplified approach for capturing the flexural response of prestressed concrete beams with external tendons. The scheme was focused on the slip of the tendons in the deviator blocks, which governed the global displacement of structure, supplemented by a nonlinear analysis approach for beam-tendon structure. The analysis scheme gave a good estimate of the flexural response of prestressed concrete beams with external tendons, validated with experimental tests. The results of a parametric study showed that the scheme was generally affected by the length of the beam and quantity of reinforcing steel material, as opposed to other parameters, e.g., span-to-depth ratio and cross-sectional geometry, which was in agreement with previous studies (Harajli et al., 2002; Ng, 2003; Roberts-Wollmann et al., 2005).

The underlying assumption behind the beam theory asserts that plane sections of a beam remain plane and also remain perpendicular to the reference axis of the beam (Koutromanos,

2018). This assumption is shown to be violated in discontinuity regions (Naaman, 1982; Nawy, 1996). According to Saint-Venant's principle, the distribution of stresses originating from axial or flexural loads is linear at a specific distance away from the discontinuity region.

According to the beam theory and Saint-Venant's principle, beams are divided into two regions, namely B-region, where beam theory is true, and D-region, where beam theory is violated. Discontinuity region exists in the vicinity of supports, concentrated loads, or regions with an abrupt change in the structural geometry.

A commonly employed approach toward the analysis of shear strength of prestressed bridge girder with discontinuity regions is strut-and-tie modeling (Pei et al., 2008; Martin et al., 2011; Ross et al., 2011), which uses the truss analogy method. Compression members in the strut-and-tie modeling approach are termed struts, while tension members are ties, joined at nodes. A node (also termed joint or connection) is the intersection of at least three members for equilibrium concern and is assumed as a hinge connection without transferring bending moments (Naaman, 1982; Nawy, 1996; Dolan and Hamilton, 2019). While the strut-and-tie model is supposed to capture the shear strength of prestressed beam members with a good rate of accuracy in the discontinuity region, a wide range of accuracy in the analysis results have been reported in the literature.

A study by Martin et al. (2011) focused on the shear strength of a prestressed concrete bridge girder after 40 years of service. The resistance of the girder was evaluated by a variety of approaches, including the strut-and-tie modeling method. According to the results, the shear capacity of the girder specimen was underestimated by more than a factor of 2.0.

Ross et al. (2011) investigated the shear capacity of four 30-year-old prestressed concrete bridge girders. The specimens were experimentally tested under a three-point-loading

configuration with various span-to-depth ratios. Similar to the conclusion drawn by Martin et al. (2011), the strut-and-tie model gave a conservative estimate of the shear strength of girder specimens, where it underestimated the capacity by a maximum factor of 2.36.

Pei et al. (2008) focused on the shear strength of a prestressed bridge girder and concluded that the shear resistance of bridge girders is conservatively estimated by the strut-and-tie model, which was in line with previous research (Martin et al., 2011; Ross et al., 2011). On the other hand, some researchers have found the strut-and-tie model to give a reasonable estimate of shear strength (Osborn et al., 2012; Higgs et al., 2015; Al Rufaydah, 2021).

The availability of design-oriented, simplified equations for estimating shear resistance of prestressed bridge girders is also a point of consideration herein. AASHTO LRFD Specification (AASHTO, 2020) has presented various approaches, some of which have backgrounds in Modified Compression Field Theory (MCFT) (Vecchio and Collins, 1986), while the American Concrete Institute (ACI, 2019) has introduced another method called, *Vci* - *Vcw*.

Several studies have investigated the modeling of corroded strands for analysis or design calculations. Two different approaches have been proposed in the literature. The first is to assign an appropriately modified constitutive law to the corroded strands/wires to account for the reduction in, e.g., deformability (Zhang et al., 2019; Jeon et al., 2020; Franceschini et al., 2022).

A study by Zhang et al. (2019) focused on the variability of steel cross-section loss caused by corrosion. They performed accelerated corrosion tests on several seven-wire prestressing strands and proposed a stochastic constitutive law for corroded strands. According

to the results, the model was found capable of capturing the stress-strain relation of corroded seven-wire strands, verified with experimental tests.

Jeon et al. (2020) studied the impact of corrosion on the mechanical properties of seven-wire strands. Several strands were extracted from two naturally corroded post-tensioned bridge girders and some empirical relationships were proposed to describe the impact of corrosion on the ultimate stress and strain of strands. This model was meant to entail an increased accuracy compared to earlier formulations, which had considered a single pit configuration (Val and Melchers, 1997; Stewart, 2009; Lu et al., 2016). The section loss of corroded wires was calculated in accordance with pit morphology, whether it is hemispheric, concave, or planar, as shown in **Figure 2.1**. Subsequently, four prestressed concrete beams were manufactured and artificially corroded to investigate the accuracy of the proposed laws. According to the results, the proposed relation could satisfactorily estimate the ultimate stress developed in the corroded strands, validated with experimental tests on the flexural resistance of artificially corroded beams.

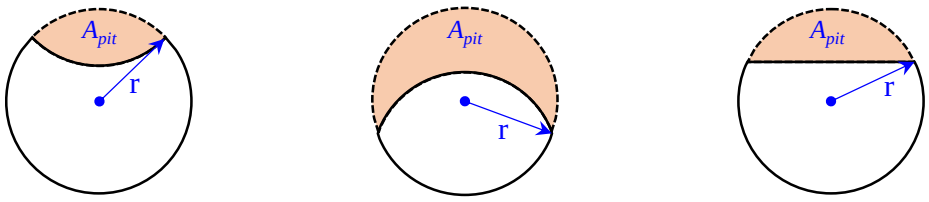

(a) hemispherical pit (b) concave pit (c) planar pit

Figure 2.1. Definition of pit configuration for various pit morphology [reproduced from Jeon et al. (2020)]. The section loss of corroded wires was found from pit morphology (Jeon et al., 2020), with the area of the pit shown in different color.

Along the same lines, a study by Franceschini et al. (2022) focused on the development of a constitutive law for corroded seven-wire strands. The calculation for section loss of

corroded wires relies on three types of pit morphology [originally introduced by Jeon et al. (2020), see **Figure 2.1**], which governs the stress-strain relationship. The proposed law assigned 8.1%, 10.7%, and 5.4% as critical section loss limits for the most corroded wires in hemispheric, concave, or planar pit configurations. The model was shown to give a good estimate of the stress-strain curve, verified with several mechanical tests on corroded strands extracted from prestressed concrete beams.

The second approach is more oriented towards design-based calculations and involves a reduction in the area of damaged strands without any modification in the assumed strength or deformability of materials (Naito et al., 2010a; Naito et al., 2010b; Alfailakawi et al., 2020).

A comprehensive study by Naito et al. (2010a) focused on the forensic analysis of chloride-induced corrosion damage in several prestressed bridge girders. The study relied on several evaluation techniques, including destructive and non-destructive tests. The former entailed experimental tests on bearing capacity, while the latter focused on half-cell potential mapping, visual inspection of chloride-induced cracks, and material testing. The overarching goal of the research was to introduce a qualitative scheme for a reliable estimate of corrosion damage in prestressed girders based on visually observed damage. The proposed scheme focused on visual inspection and considered a 5% reduction in the area of all prestressing strands embedded in the girder, a 25% reduction in the area of prestressing strands adjacent to cracks, i.e., within a distance of 3 in., and a 100% reduction in the area of exposed strands, as schematically shown in **Figure 2.2**. According to the results, longitudinal cracks gave a good estimate of the corrosion condition of non-visible prestressing strands, in contrast with the half-cell testing results. According to several tests, the proposed scheme gave a reliable estimate of corrosion extent and subsequently bearing capacity of girders.

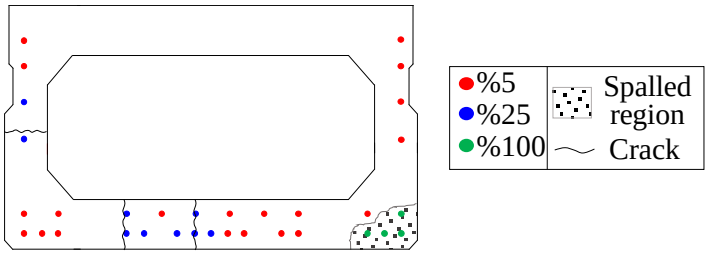

Figure 2.2. Schematic illustration of rating recommendation by Naito et al. (2010a) [redrawn from Naito et al. (2010a)].

A follow-up study by Naito et al. (2010b) delved into the chloride-induced corrosion damage by focusing on the chloride concentration test results to correlate the extent of corrosion-inducing chloride ion to the surface cracking and subsequently, reduction in the area of prestressing strands. The primary goal of the research was to provide qualitative rating guidelines and recommendations on the extent of chloride-induced corrosion damage on the surface of prestressing strands and their correlations to visually observed damage. The surface condition of strands was judged on the bases of various experimental tests, namely, mechanical tests, petrographic examinations, air void analyses, carbonation and chloride concentration tests, and visual inspections. The authors have concluded that the existence of hairline cracks could be indicative of corrosion, as shown in **Figure 2.3**. They also provided rating guidelines for the extent of corrosion on the surface of strands, classified under nine different categories from immediate failure to excellent condition. Given the presumption that enough oxygen and moisture were present on the surface of prestressing strands, they have identified the content of critical chloride that destructs the protective film on the surface of strands, which was 0.032% of the concrete mass.

	External Surface Condition	Strand Cond. (In-situ)	Strand Cond. (Removed)	Wire Condition	Average Condition
Exposed Strand	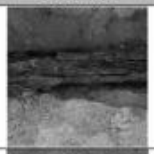	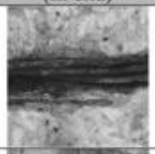		Missing: 3	# samples: 9
				w/ Corrosion: 4	w/ Corrosion: 4
				Pitted: -	Pitted: -
				Heavily Pitted: 4	Heavily Pitted: 2.2
Heavy Efflorescence w/ Rust	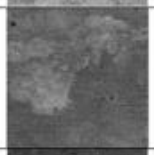		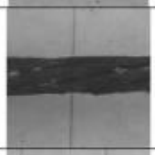	Missing: 0	# samples: 1
				Corrosion: 6	w/ Corrosion: 6
				Pitted: 0	Pitted: 0
				Heavily Pitted: 6	Heavily Pitted: 6
Partial Efflorescence	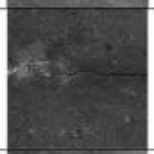	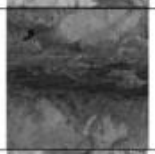	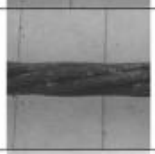	Missing: 0	# samples:1
				Corrosion: 6	w/ Corrosion: 6
				Pitted: 3	Pitted: 3
				Heavily Pitted: 1	Heavily Pitted: 1
Moderate Corrosion Stain	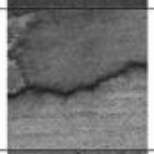	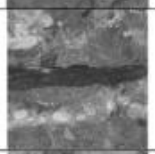	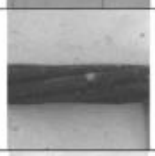	Missing: 0	# samples: 2
				Corrosion: 3	w/ Corrosion: 4.5
				Pitted: 2	Pitted: 1
				Heavily Pitted: 1	Heavily Pitted: 3.5
0.2-mm (0.01-in.) Crack	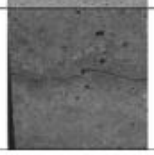	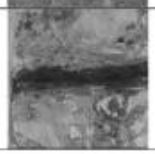	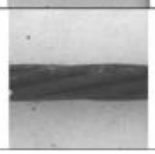	Missing: 0	# samples: 2
				Corrosion: 6	w/ Corrosion: 4.5
				Pitted: 6	Pitted: 1
				Heavily Pitted: 0	Heavily Pitted: 3

Figure 2.3. Rating recommendation by Naito et al. (2010b)[reproduced from Naito et al. (2010b)].

Alfailakawi et al. (2020) proposed a scheme for the evaluation of chloride-induced corrosion damage on prestressing strands based on visual inspection. The proposed approach relied on the results of a series of destructive and non-destructive tests, including, visual inspection, half-cell measurements, chloride titration tests, mechanical tests on prestressing steel, concrete compressive tests, and a series of four-point bending tests on several corroded prestressed bridge girders with I-shaped and Box-shaped section. The algorithm was a modified version of previous studies (Naito et al., 2010a; Naito et al., 2010b) and considers a 40% reduction in the area of strands closest to the crack, a 20% reduction in the area of strands in the vicinity of cracks, a 90% reduction in the area of strands in the patched region, and a 100% reduction in the area of exposed strands, as shown in **Figure 2.4**. Based on the results, the

proposed algorithm was found to give a good estimate of residual strength for I-section girders. It was also found that the residual strength of box-section girders was reasonably estimated by Naito et al. (2010a) approach.

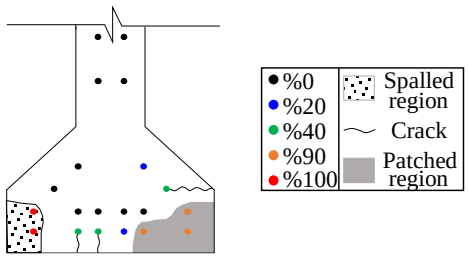

Figure 2.4. Rating recommendations for chloride-induced corrosion damage, proposed by Alfailakawi et al. (2020) [redrawn from Alfailakawi et al. (2020)].

As an additional point, it is worth mentioning that various types of reinforcing materials, such as GFRP or CFRP bars (Aliasghar-Mamaghani and Khaloo, 2019, 2021; Hassanpour et al., 2022), exhibit corrosion resistance properties. However, considering the uncertainties surrounding their mechanical performance in service conditions, prestressing steel strands continue to be the prevailing choice of material in practical applications.

2.2 Mathematical Description of Chloride and Moisture Transport in Sound Concrete

2.2.1 Chloride Transport

Corrosion of prestressing strands embedded in concrete bridges is caused by the intrusion of chloride into the porous network of concrete in coastal bridges or those subjected to the use of deicing salts. The transport of chloride takes place through the porous network of the concrete by means of diffusive and advective transport. The former is driven by the concentration gradient, while the latter is caused by moisture flow which carries chloride ions.

During the early stages of a structure's life, the high alkalinity of concrete leads to the formation of a protective oxide film on the surface area of prestressing strands, which inhibits corrosion. The presence of chloride ions can lead to the destruction of the protective film, leading to the initiation and progression of the corrosion reaction. The content of chloride ions on the surface of prestressing strands or reinforcing bars was shown to give a good estimate of corrosion onset and structure service life (Weyers et al., 1994).

The intrusion of corrosion-inducing chloride ions in concrete bridges is affected by a multitude of physical processes, including chemical diffusion, moisture transport, heat conduction, and coupled moisture, chloride, and heat transport.

A commonly employed approach toward the prediction of chloride in concrete is a closed-form solution of Fick's second law of diffusion (Collepardi et al., 1972; Hansen and Saouma, 1999a), as shown in equation (2.1). Fick's second law is nothing but the application of the conservation of mass principle and the use of Fick's first law of diffusion. The latter is simply chloride flux, i.e., the product of a diffusion coefficient and the concentration gradient.

$$C_x = C_s[1 - erf(\frac{x}{2\sqrt{D_{cl}t}})] \quad (2.1)$$

where C_s is the surface chloride concentration, *erf* is the error function, x is the distance from the exposure surface, D_{cl} is the chloride diffusion coefficient, and t is time.

The simplest assumption is to consider a time-independent value for the chloride diffusion coefficient (Collepardi et al., 1972; Weyers et al., 1994). Several researchers (Conjeaud, 1980; Buenfeld and Newman, 1987; Mangat and Molloy, 1994; Zhang et al., 2021) have recommended using a coefficient that depends on time.

A study by Mangat and Molloy (1994) focused on the long-term prediction of chloride concentration in concrete. Several concrete mixes were considered to investigate the impact of different compositions on chloride diffusion coefficient. On the other hand, the dependency of chloride transport on time was investigated. A mathematical relation based on Fick's second law was proposed, which incorporates the dependency of chloride transport with time. According to the results, the chemical diffusion coefficient was found to be affected by time, described by the following expression.

$$D_{cl} = D_i t^{-m} \quad (2.2)$$

where m is an empirical coefficient governed by the water-to-cement ratio, and D_i is the chloride diffusion coefficient at t = 1 second. Having obtained the dependence of the chloride diffusion coefficient with time, the authors proposed the following expression to describe the long-term intrusion of chloride in concrete.

$$C_x = C_s[1 - erf(\frac{x}{2\sqrt{\frac{D_i}{1-m}t^{(1-m)}}})] \tag{2.3}$$

A number of research studies investigated the influence of physical processes on chloride diffusive transport, through analytical or computational schemes. Saetta et al. (1993) proposed a finite element framework for the transport of chemical species in concrete, which entailed chemical diffusion, moisture transport, cement hydration, and heat transfer. For the sake of simplicity, the implementation of various significant processes was only considered in the chloride diffusion coefficient, given by

$$D_{cl} = D_{iref} \cdot f_1(T) \cdot f_2(t_e) \cdot f_3(h) \tag{2.4}$$

where D_{iref} is the reference chloride diffusion coefficient at temperature $\mathrm{T} = 23℃$, relative humidity $h = 1.0$, and cement hydration degree after 28 days. $f_1(T)$, $f_2(t_e)$, and $f_3(h)$ describes the dependence of chemical diffusion on, heat, hydration degree, and moisture, respectively. According to the results, the pure chloride diffusion gave an inaccurate estimation of chloride content in concrete, and moisture transport was found to play a crucial role in describing chloride transport phenomena. The scheme was found capable of capturing chloride content inside partially saturated concrete, however, the need for further experimental was pointed out.

Tang and Nilsson (1996) introduced an additional dependence on the depth from the exposure surface and proposed the following equation for the chloride diffusion coefficient.

$$D_{cl}(x,t) = \frac{D_0}{\varepsilon_{por}} \cdot f_1(T) \cdot f_2(t) \cdot f_3(x) \tag{2.5}$$

where D_0 is the diffusion coefficient of aged concrete, ε_{por} is the porosity of concrete, $f_1(T)$, $f_2(t)$, and $f_3(x)$ describe the dependence on heat, age, and exposure depth, respectively. While the authors disregarded the impact of advection in the analysis, the proposed scheme was found capable of capturing the profile of chloride from the exposure surface, verified with chloride titration tests. In addition, the isolated facet of the diffusion phenomenon, described by Fick's law, was found to give an inaccurate estimation of the chloride profile.

Maruya et al. (1998) proposed a mathematical scheme to model chloride intrusion in concrete specimens with various mix compositions. They conducted experimental tests to measure the content of chloride in fully and partially saturated concrete specimens. The authors have also introduced a mathematical relation for specimens under wetting-drying cycles. According to the results, the model was capable of capturing the actual chloride profile of specimens under wetting-drying cycles. In general, the method was found to give a reliable estimate of the total chloride profile in various environments, namely submerged, tidal, or splash zones.

A study by Hansen and Saouma (1999) focused on formulating a finite element framework to predict the depth of chloride penetration in concrete bridge decks. The study relied on time- and temperature-dependent chloride diffusion coefficients, while neglecting the advective transport term. The time-dependent scheme relied on a model introduced by Mangat and Molloy (1994), while the temperature-dependent model uses Arrhenius law. The study also accounted for the impact of solar radiation, surface irradiation, and heat convection by considering different boundary conditions on the deck of the bridge specimen. According to the results, the isolated facet of the problem, i.e., time- or temperature-dependent formulations was

found incapable of describing the content of chloride in concrete, while a combination of the two gave a reliable estimate.

Some researchers (Mangat and Molloy, 1994; Tang and Nilsson, 1996) considered the content of total chloride in the diffusion phenomenon, corresponding to the sum of two contributions, namely free and bound chloride. The former is mobile in the porous network of the concrete, while the latter is physically or chemically bound to the pore walls and is generally immobile. Chemically bound chloride is generated upon the formation of chloro-aluminate hydrates, such as Friedel's salt ($Ca_6Al_2O_6 . CaCl_2 . 10H_2O$) and is in the solid phase, while physically bound chloride is adsorbed to the pore walls. Bound chloride can move under specific conditions, such as carbonation and reduction in pH (potential of hydrogen) of the concrete medium. The understanding of total chloride content is very important as the propensity of steel corrosion is affected by the total chloride concentration.

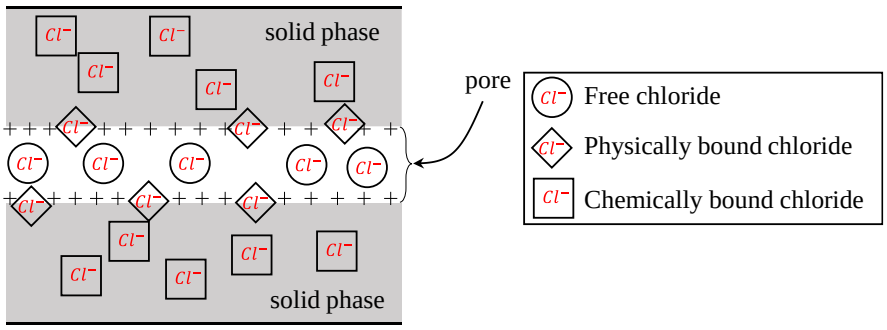

Figure 2.5. Classification of chloride ions in concrete [redrawn from Maruya et al. (1998) and Maekawa (2008)].

Shafei et al. (2012) proposed a finite element framework to obtain the chloride content and corrosion incidence of reinforced concrete structures. The diffusion process was expressed on the basis of Fick's second law, with free chloride content as the field variable. They proposed a chloride diffusion coefficient which was a function of various physical processes:

$$D_{cl} = D_0 \cdot f_1(T) \cdot f_2(h) \cdot f_3(\Re) \cdot f_4(t_e) \cdot f_5(C_f) \quad (2.6)$$

where, $f_1(T)$, $f_2(h)$, $f_3(\Re)$, $f_4(t_e)$, and $f_5(C_f)$ describe the dependence of chloride diffusion on heat, moisture, carbonation, age, and free chloride, respectively. While the proposed framework was deemed capable of capturing various significant phenomena, the need for experimental data from real-life bridges for model calibration and validation was pointed out.

A study by Maekawa et al. (2003) focused on the multi-scale modeling of transport phenomena in structural concrete. Various physical processes including, coupled heat, moisture, chloride, carbon, and oxygen transport were taken into account. Contrary to most of the contributions in the literature that accounted for the impact of advection only on chloride diffusion coefficient, the authors introduced the impact of advection transport directly in the governing differential equation of chloride transport, which is indeed a crucial step for fully coupled analysis. According to the results, the holistic approach was capable of capturing various physical phenomena, verified with experimental results, and the advection-diffusion transport was found to play a significant role in the transport of chloride ions.

Several researchers have focused on the transport of moisture in concrete structures (Bažant and Najjar, 1972; Nilsson, 2002; Maekawa et al., 2003; Baroghel-Bouny, 2007; Rahimi-Aghdam et al., 2019). This is of prime importance as moisture flow transport chloride ions and significantly affects the diffusion of chloride in the porous network of concrete.

2.2.2 Moisture Transport

A mathematical approach for the diffusion of moisture in unsaturated concrete was proposed by Bažant and Najjar (1972) . The field variable is termed relative humidity, instead of evaporable water content. This is because the self-desiccation term in the former was smaller

than that in the latter. Also, the selection of relative humidity was found to give an easy tool in practice, as the boundary conditions are usually expressed in terms of relative humidity. The transport of moisture was expressed by a nonlinear moisture diffusion coefficient, given by

$$C(h) = c_1\left[\alpha_0 + \frac{(1-\alpha_0)}{1+[(1-h)/(1-h_c)]^n}\right] \tag{2.7}$$

where α_0, h_c, n are model parameters, and c_1 is the moisture diffusion coefficient in a fully saturated condition. The proposed law has an S-shaped behavior and is sensitive to model parameters, as shown in **Figure 2.6**.

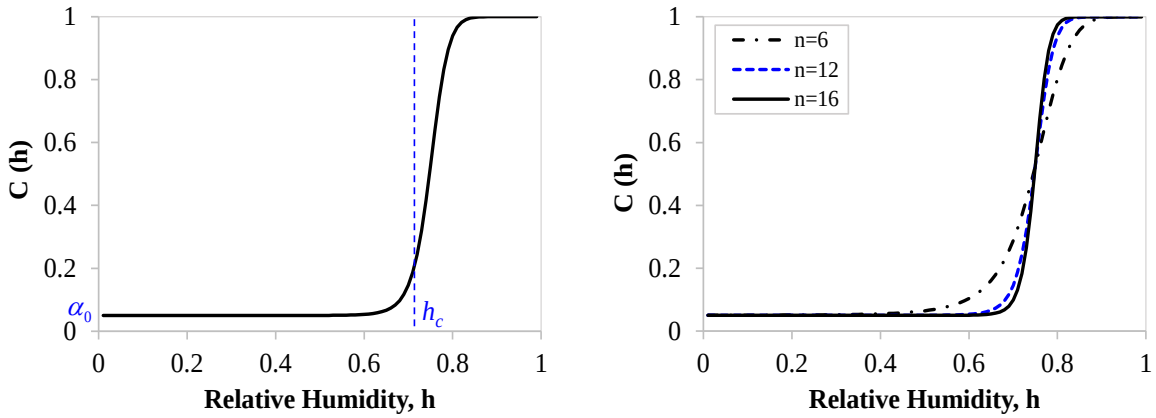

(a) Model parameters in moisture diffusion coefficient

(b) Sensitivity of parameter *n* in moisture diffusion coefficient

Figure 2.6. Moisture diffusion coefficient model, proposed by Bažant and Najjar (1972) (illustrating for c_1=1).

According to the results, Bažant and Najjar (1972) found the transport of moisture strictly nonlinear, with a strong dependence on relative humidity content. The proposed approach was found to give a reliable estimate of moisture content in concrete specimens, verified with experimental data. They also recommended a range of values for model parameters, that are, $h_c \approx 0.75$, α_0, n between 0.05 and 0.10, and 6 and 16, respectively.

The transport mechanism of moisture can be expressed in terms of pore pressure instead of relative humidity by the Kelvin equation (Bažant and Jirásek, 2018)

$$p_l = \frac{RT\rho_l}{M_w}\ln(h) \tag{2.8}$$

where P_l is the pore pressure, M_w is the molar mass of water, and ρ_l is the liquid water density. Maekawa et al. (2003) proposed a transport mechanism for the diffusion of moisture on the basis of pore pressure by considering different phases of moisture, including liquid and gas states. According to the results, the model was found to give a reliable estimate of moisture content in concrete specimens, verified by experimental tests on the advection-diffusion phenomenon.

2.3 Mathematical Description of Chloride-induced Corrosion Damage in Concrete

The presence of even hairline cracks in the vicinity of prestressing strands can be indicative of severe corrosion damage (Naito et al. 2010a). Corrosion-induced cracking is associated with the volumetric expansion of corrosion products, which exert swelling pressure on the surrounding concrete, leading to the development of tensile stresses, cracking, and even complete loss of concrete.

A study by Maekawa et al. (2003) focused on the rate of corrosion reaction in reinforcing steel bars by proposing an approach based on thermodynamic electrochemistry. The electrode potentials of two half-cells were obtained based on the Nernst equation, which for the anodic reaction was given by:

$$E_{Fe} = E_{Fe}^{\Theta} + \frac{RT}{z_{Fe}F} \ln h_{Fe^{2+}} \tag{2.9}$$

where E_{Fe} is the standard iron cell potential, E_{Fe}^{Θ} is the standard iron cell potential at 25℃, R is the universal gas constant, z_{Fe} is the number of charges in iron ion, and $h_{Fe^{2+}}$ is the concentration of the iron ion. The potential of cathodic reaction was obtained from the following equation:

$$E_{O_2} = E_{O_2}^{\Theta} + \frac{RT}{z_{O_2}F} \ln(P_{O_2} / P^{\Theta}) \tag{2.10}$$

where $E_{O_2}^{\Theta}$ is the standard oxygen cell potential at 25℃, z_{O_2} is the number of charge in oxygen, P^{Θ} is the atmospheric pressure, and P_{O_2} is the partial pressure of oxygen. In the next step, the authors considered local conservation of electric charge and proposed the following equation for anodic half-cell:

$$\eta_a = \frac{2.303RT}{0.5z_{Fe}F}\log(i_a / i_0{}^a) \tag{2.11}$$

where i_a is the electric current density at the anodic site, and $i_0{}^a$ the electric current density in equilibrium at anode. The overvoltage for the cathodic half-cell is given by

$$\eta_c = -\frac{2.303RT}{0.5z_{O_2}F}\log(i_c / i_0{}^c) \tag{2.12}$$

where i_c is the electric current density at cathodic site, and $i_0{}^c$ the electric current density in equilibrium at cathode.

Several researchers have proposed analytical approaches to model corrosion of reinforcing steel in concrete structures (Bažant, 1979; Molina et al., 1993; Youping and Richard, 1998; Hansen and Saouma, 1999b). A study by Bažant (1979) focused on the fundamental of the problem and proposed an analytical scheme for modeling corrosion of reinforcing steel in concrete structures. The scheme relied on multitude of processes, some of which were diffusion of moisture and oxygen, chloride transport, and electrochemical oxidation-reduction reaction through anodic and cathodic half cells. While the authors neatly reflected all the processes by mathematical formulations, the need for experimental verification and method improvement was pointed out.

Molina et al. (1993) proposed a framework for time to first cracking of cover concrete caused by corrosion. The model accounts for the volumetric expansion of corrosion products and reduction in elastic modulus. The authors also proposed a mathematical relation to describe the depth of the corrosion attack based on current density, expressed by:

$$\Delta x = 0.032 \cdot I \cdot \Delta t \tag{2.13}$$

where, Δx is the penetration depth, μm, I is the current density, $\mu A/cm^2$, and Δt is the time increment, *day*. The analysis accounted for the occurrence and propagation of cracking by a smeared-fixed crack modeling approach. While the analytical approach could not give a reliable estimate of crack opening displacement, it could successfully characterize some of the experimentally observed behavior. The most controversial part of the analysis scheme was the volumetric expansion of corrosion products, and the need for robust numerical schemes in conjunction with experimental data on the parametric analysis of influential model parameters were pointed out.

A study by Youping and Richard (1998) focused on modeling the time-to-corrosion cracking of reinforced concrete structures subjected to chloride ions. The proposed model accounted for the rate of rust production, which was a function of rebar diameter, and corrosion current density. According to the results, the model could reliably estimate the occurrence of corrosion cracking on the surface of specimens, verified with experimental test results.

Several researchers have experimentally observed the occurrence of corrosion-induced cracking on the surface of reinforced concrete specimens (Al-Sulaimani et al., 1990; Cabrera, 1996; Vidal et al., 2004). The extent of corrosion in reinforcing steel bars was found to be inversely proportional to concrete cover depth (Cabrera, 1996). While the ratio of cover depth to rebar diameter, c/φ_0, was found to have a pressing effect on the initiation of cracking, it did not affect the propagation of cracks (Vidal et al., 2004).

Zhao et al. (2012) performed experimental tests to investigate the cracking pattern and rust distribution in artificially corroded reinforced concrete prisms. The specimens were subjected to saltwater spray under wetting-drying cycles for two years. The authors introduced a procedure for crack initiation, and rust diffusion, which relies on three different rust

configurations, and rusts were found to move in the cracks only in the last stage. As denoted in **Figure 2.7**, Rust1 appears in steel-concrete in black color, termed Fe_3O_4. Rust2 appears at the occurrence of surface cracking in dark-brown color, termed β-FeO(OH). Rust3 occurs after surface cracking in reddish-brown color, termed Fe_2O_3.

According to the results, the width of the cracks on the surface of the concrete was found linearly proportional to the corrosion of reinforcing steel bars. The width of the critical surface crack for predicting reinforcing steel corrosion on the surface of the concrete was defined as 0.07 mm. An interesting conclusion of the research pertains to the mobility of corrosion products (rust). The penetration of rust into the corrosion-induced crack was observed after the occurrence of cracking on the surface of the specimens, however, corrosion products were found immobile before surface cracking.

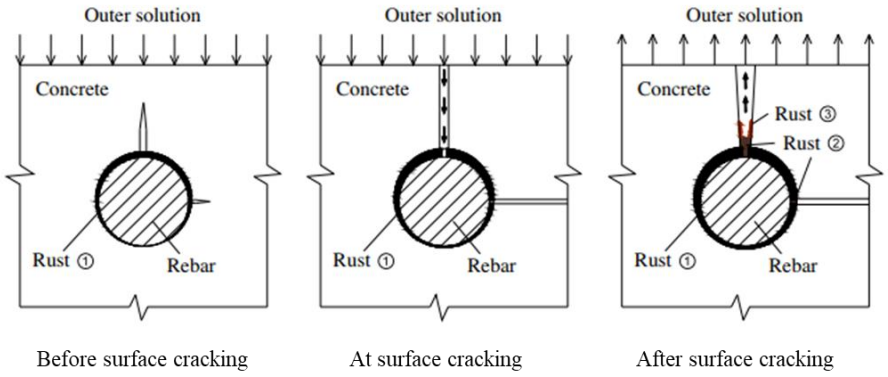

Figure 2.7. Crack initiation, progression, and rust intrusion in concrete due to chloride-induced corrosion damage[figure from Zhao et al. (2012)].

A study by Otieno et al. (2016) focused on chloride-induced corrosion damage for concrete structures in marine environments and proposed a mathematical relationship for the rate of corrosion. The scheme accounted for concrete quality, crack width, and cover depth. The authors have recommended a simplified expression for the rate of corrosion, given by:

$$i_{corr} = (0.64e^{0.06(D_{90\times10^{10}})})(c / w_{cr})^{-0.21e^{0.02(D_{90\times10^{10}})}} \quad (2.14)$$

where D_{90} is the chloride diffusion coefficient at 90 days, c is the cover depth, and w_{cr} is the width of the crack. While the mathematical relation does not incorporate several influential parameters that might influence the physics of the problem, such as heat, and electrochemical process, it was shown to provide an easy tool and a reliable estimate of corrosion rate.

The occurrence of cracking in concrete caused by volumetric expansion of corrosion products affects several intrinsic characteristics of concrete in transport phenomena. Several studies performed experimental tests to determine the impact of crack opening displacement on chloride diffusion coefficient (Win et al., 2004; Kato et al., 2005; Ismail et al., 2008; Akhavan and Rajabipour, 2013; Lu et al., 2017). A study by Win et al. (2004) concluded that the diffusion of chloride ions in cracked concrete is significantly affected by cracking. The transport mechanism was also found to be a function of water to cement ratio. Kato et al. (2005) found the diffusion coefficient a function of the crack width and proposed a simplified relationship to describe the diffusion of chloride in cracked concrete. According to the results, the model was found capable of capturing the actual chloride profile.

Ismail et al. (2008) conducted experimental tests on several concrete specimens to investigate the influence of cracking on chemical diffusion after up to two years. The results show that for a crack opening displacement smaller than $30\,\mu m$, diffusion of chloride was irrespective of cracking. Therefore, the authors reported $30\,\mu m$ as the crack opening displacement threshold.

A computational study by (Ishida et al., 2009) focused on a phenomenological approach to describe the impact of cracking on chloride transport in fully saturated concrete. The authors

proposed the following chloride flux vector for the transport of chloride in sound and cracked concrete, which incorporates some features like constrictivity, and tortuosity.

$$J_{cl} = -\left(\frac{\varphi S_l}{\Omega_s} \delta_s D_{cl} + \xi \frac{\varphi_{cr} S_{cr}}{\Omega_{cr}} \delta_{cr} D_{cl} \right) \vec{\nabla} C_{cl} \tag{2.15}$$

where Ω_s and Ω_{cr} are the tortuosity of sound and cracked concrete, S_l and S_{cr} are the saturation degree of sound and cracked concrete, δ_s is the constrictivity of sound concrete, ξ is model parameter, $\varphi_{cr} = w_{cr} / l_e$, and

$$\delta_{cr} = 0.99 \tanh\left[1.4 \times 10^4 w_{cr} \left(\log\left(w_{cr} \right) + 5.5 \right) \right] + 0.01 \tag{2.16}$$

The constrictivity parameter, δ_{cr} , reduces the transport of chloride for a small crack width. According to the results, the model gave a reliable estimate of the chloride profile in cracked concrete, which was verified with experimental tests. While the phenomenological approach gave a good estimate of experimental response, the author pointed out future validation for the application of the method in real-life structures.

A study by Akhavan and Rajabipour (2013) focused on the influential parameters characterizing the transport of chloride in cracked concrete. The study relied on chloride migration tests on pre-cracked concrete samples with a crack width ranging from 20 to 100 μm . According to the results, the diffusion coefficient was found linearly proportional to the crack volume fraction. In that respect, the proposed linear model gave a reliable estimate of chloride content in cracked concrete. A follow-up study by Lu et al. (2017) indicated that the frequency and spacing of cracks also impact the diffusion of chloride in cracked concrete.

Park et al. (2012a) investigated the impact of cracking on chloride ingress in cracked concrete. They performed several chloride migration and saltwater spray tests on pre-cracked

concrete specimens. Subsequently, the authors proposed a numerical framework by introducing a Representative Element Volume (REV) approach for the transport of chloride in cracked concrete. The scheme accounted for several influential parameters in chloride diffusion coefficient in REV, given by

$$D_{eq} = \frac{\Omega_{cr} D_{cr}}{R_a S_l \varphi} + D_{cl} \tag{2.17}$$

where Ω_{cr} is the tortuosity of the crack, S_l is the degree of saturation, φ is the porosity, and $R_a = A_0 / A_{cr}$ is the ratio of element to crack area, and

$$D_{cr} = D_{cl}(1 + 347.85 w_{cr} - 1642.5 w_{cr}^{\ 2} + 4189.27 w_{cr}^{\ 3}) \tag{2.18}$$

The first term on the right-hand side of equation (2.17) denotes the dependence of the equivalent diffusion coefficient on the cracking. Results have shown that the proposed scheme could give a reliable estimate of chloride profile in cracked concrete, verified with experimental tests. In addition, the diffusion mechanism was found to be significantly affected by crack width.

Cracking in cementitious materials also affects the pace of moisture transport, which may increase by several orders of magnitude. A study by Bazant et al. (1987) is one of the first documents in the literature that investigated the impact of cracking on the permeability of concrete structures. They performed experimental tests on several concrete specimens and proposed a mathematical formulation to describe moisture transport in cracked concrete structures. They proposed a mathematical relation shown in equation (2.19) for the permeability coefficient which incorporates the geometry of the crack in the calculation, in particular, it considers the spacing and width of the cracks as influential model parameters.

$$K_{cr} = K_0 (1 + \frac{k_1}{\beta_p} \frac{(\alpha_p \delta_{cr})^3}{s}) \tag{2.19}$$

where K_0 is the moisture diffusion coefficient in sound concrete, δ_{cr} is the major crack width, k_1 is a coefficient specifying crack passage with neck, and α_p, and β_p are fraction of pore size and length, respectively, as shown in **Figure 2.8**.

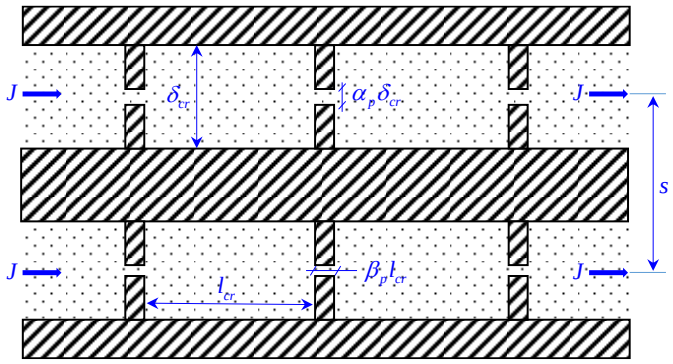

Figure 2.8. Idealized definition of crack model parameters influencing moisture transport in cracked concrete, proposed Bazant et al. (1987) [redrawn from Bazant et al. (1987)].

The authors further simplified their approach and proposed a coefficient for crack geometry [i.e., the last term on the right-hand side of equation (2.19)], which reads as follows:

$$K_{cr} = K_0(1 + k_c \frac{\delta_{cr}^{\ 3}}{s}) \tag{2.20}$$

where $k_c = k_1(\alpha_p^{\ 3}/\beta_p)$, approximated as $k_c = 10^5\,\text{mm}^{-2}$. According to the results, the moisture permeability coefficient in cracked concrete was proportional to the crack width cubed and inversely proportional to crack spacing. According to the results of the experimental tests, the proposed scheme was found to give a reliable estimate of moisture transport in cracked concrete.

A study by Akhavan and Rajabipour (2012) focused on the impact of crack geometry on the permeability of moisture in cracked concrete. The authors proposed mathematical relationships to describe moisture transport in cracked concrete by incorporating various model parameters into account, such as crack width, crack tortuosity, and crack roughness. The

tortuosity of the crack was defined as the ratio of the actual crack path, with respect to the shortest path possible (X_{max} in **Figure 2.9**), and surface roughness denotes the wavy shapes of the crack mouth. The tortuosity of cracks was estimated by

$$\tau_{cr} = \frac{X_{\max}^{\ 2}}{l_e} \tag{2.21}$$

with X_{max} and l_e being the shortest crack path and crack length, respectively, as shown in **Figure 2.9**.

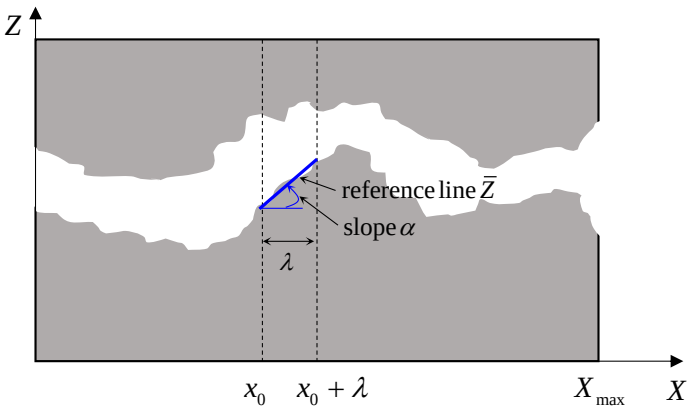

Figure 2.9. Model parameters characterizing the tortuosity and surface roughness of cracks, proposed by Akhavan and Rajabipour (2012) [redrawn from Akhavan and Rajabipour (2012)].

The roughness of the crack was obtained in two steps, the first of which in local coordinate:

$$R_{a,l} = \frac{1}{\lambda}\sum[|\bar{Z}(x) - Z(x)| \cdot \cos(\alpha)] \tag{2.22}$$

with model parameters shown in **Figure 2.9**. Subsequently, surface roughness was averaged over the length of the crack by

$$R_{a,g} = \frac{1}{X_{\max} - \lambda}\sum_{i=1}^{X_{\max}-\lambda}(R_{a,l})_i \tag{2.23}$$

Considering the impact of crack geometries on moisture permeability, the following relationship was proposed:

$$K_{cr} = \frac{\tau_{cr} w_{cr}^{\ 2}}{12(1+8.8R_r^{\ 1.5})} \tag{2.24}$$

where, $R_r = R_{a,g} / 2w_{cr}$ denotes the surface roughness of cracks. According to the results, the proposed moisture permeability coefficient gave a good estimate of moisture transport in cracked concrete. The analytical response was found sensitive to model parameters, and the best response was obtained from the best fitting with the experimental data for $\tau_{cr} = 0.21$, and $R_{a,g} = 8.9\mu m$.

Park et al. (2012b) performed experimental tests and developed a numerical scheme in cracked RVE to investigate the impact of cracking on the transport of moisture in concrete specimens. The proposed approach accounted for crack geometry and properties of moisture material, given by

$$q_{eq} = -\frac{\Omega_{cr}}{8\eta A_0 S_l \varphi}\left(\frac{\varphi}{\Omega_{cr}}\int_0^{r_c} r^2 dV + \frac{w_{cr}^{\ 4}}{3n^4}\right)\frac{dP}{dx} \tag{2.25}$$

where $\Omega_{cr} = \pi^2 / 4$, η is the fluid viscosity, $n = 3.704\times10^{-4}$, P is the vapor pressure, r_c is the critical pore radius, and r is the pore radius. As shown in the last term on the right-hand side of equation (2.25), permeation in cracked concrete was correlated to the fourth power of crack opening displacement. Tests have shown that permeability in cracked concrete significantly increases for a crack width of more than 0.2 mm, in particular, for a crack opening displacement of 0.4 mm, the transport of moisture was found to be more than 1000 times that of the sound concrete. In the end, the proposed scheme was found to give a good estimate of permeability in cracked concrete.

The impact of cracking on permeability has been investigated by several researchers through a model which correlates the moisture permeability coefficient to the second power of crack opening displacement (Rastiello et al., 2014; Shin et al., 2017; Mengel et al., 2020), while other researchers have found a cubic relation between crack opening displacement and permeability coefficient (Fahy et al., 2017; Görtz et al., 2021). A numerical study by Görtz et al. (2021) investigated the impact of cracking on moisture transport in concrete. The proposed scheme incorporated the impact of cracking on the moisture permeability coefficient in a fully saturated condition and moisture capacity. The former was described by

$$K_{cr} = \zeta_f \frac{g w_{cr}^{\ 2}}{12 \nu_k} \frac{w_{cr}}{l_e} \tag{2.26}$$

where g is the gravitational acceleration, ν_k is the kinematic viscosity, and ζ_f is a model parameter.

While the isolated facet of the transport phenomena, i.e., moisture and chemical transport in cracked concrete are significantly affected by crack opening displacement, the coupling effect between the chloride and moisture transport, with the simultaneous existence of mechanical damage is of significant importance. Given the complexity of experimental tests under wetting-drying cycles and numerical difficulties, there have been few research studies in this area (Win et al., 2004; Kato et al., 2005; Lu et al., 2017).

2.4 Uncertainty Quantification

The quantification of uncertainty for various model parameters in the analysis of chloride-induced corrosion damage in prestressed bridge girders provides insights into the underlying factors contributing to the variation in corrosion damage observed across different bridge segments. As an initial step, a literature review is deemed necessary for a better understanding of the range of key model parameters causing chloride-induced corrosion damage. While the range of the model parameters is provided in this section, the deciding factors for selecting impactful parameters will be postponed to subsequent sections.

A comprehensive study by Weyers et al. (1994) focused on the service life estimate of several bridge girders across the united states. More than 2700 concrete samples were taken from 321 bridges subjected to the use of deicing salts for chloride concentration tests. The authors provided valuable experimental data on chloride titration tests and proposed a simplified tool based on Fick's first law to describe the intrusion of chloride in concrete structures. According to the test results, the mean range of surface chloride was found to be between 1.07 kg/m^3 (for the state of Arkansas) and 8.68 kg/m^3 (for the state of New York), with a coefficient of variation of 0.72, and 0.58, respectively.

McGee (1999) performed a series of chloride titration tests on several Tasmanian bridges and proposed a service life modeling approach for bridges exposed to saltwater spray based on the experimental tests on 1158 bridges. The author proposed a range of surface chloride for concrete bridges, characterized by their distance from the coastline. According to the results, the mean range of chloride was between 0.98 kg/m^3 for bridges within 2.84 km from the coastline and 9.31 kg/m^3 for bridges in the coastal zone with a coefficient of variation of 0.653 and 0.487, respectively.

The concentration of chloride for concrete bridges exposed to saltwater spray was also investigated by Val (2007), who found a surface chloride of 7 kg/m^3 for data collected from the atmospheric zone of the Mediterranean coast.

The chloride diffusion coefficient is another influential parameter in the quantification of uncertainty of chloride-induced corrosion damage in concrete bridges. There is a multitude of parameters affecting diffusivity, the most important of which is concrete composition and time. The uncertainty of diffusivity can be found from a range of chloride diffusion coefficients reported in the literature, for instance:

$$D_{cl} = D_{ref}\left(\frac{t_{ref}}{t_{age}}\right)^{\alpha_{age}} \tag{2.27}$$

where t_{ref} is the time corresponds to the reference chloride diffusion coefficient D_{ref}, t_{age} is specimen age, and α_{age} is an age factor characterizing the temporal evolution of diffusion coefficient.

Several researchers have studied the temporal evolution of chloride in concrete specimens. Mangat and Molloy (1994) conducted experimental tests on several concrete prisms and performed model validation with a simplified formulation based on Fick's first law. They suggested various exponents for the temporal evolution of chloride, α_{age}, ranging from 0.40 to 0.86, and proposed the following equation:

$$\alpha_{age} = 2.5(\frac{w}{c}) - 0.6 \tag{2.28}$$

where w/*c* is the water-to-cement ratio.

A study by Maage et al. (1996) concluded a range for the age factor between 0.32 to 0.96. Benz and Thomas (2001) found the age factor varying from 0.20 to 0.44 and proposed an empirical relationship, given by

$$\alpha_{age} = 0.2 + 0.4\left[\frac{\%(FA)}{50} + \frac{\%(SG)}{70}\right] \tag{2.29}$$

where FA and SG stand for fly ash and slag cementitious material.

A study by Lu et al. (2015) focused on the advection diffusion of chloride ions in concrete specimens. A simplified transport model was developed to investigate the content of chloride under wetting-drying cycles and the impact of the age factor. According to the results, the author found a range for the age factor between 0.46 and 0.72.

Shafei et al. (2012) considered an age factor of 0.04, while the fib model code (Schießl et al., 2006) recommended a lower and upper bound of 0.0 and 1.0, with a mean value of 0.30 and a standard deviation of 0.12.

The moisture diffusion coefficient is another influential parameter in the quantification of uncertainty of chloride-induced corrosion damage in concrete bridges. The variability of moisture diffusivity is affected by various parameters, the most important of which is the concrete compositions. A study by Bažant and Najjar (1972) focused on moisture transport in concrete specimens in various settings. According to the fitting with the experimental data, the diffusion coefficient in fully saturated conditions without a temperature gradient was found to vary between $1.667 \cdot 10^{-10}\, m^2 / s$ and $4.421 \cdot 10^{-10}\, m^2 / s$, while the upper bound was found to be $2.234 \cdot 10^{-9}\, m^2 / s$ under a temperature gradient.

Fib model code for structural concrete (FIB, 2013) recommended a mathematical model for the moisture diffusion coefficient in concrete structures under a fully saturated condition, which is proportional to the compressive strength of concrete, given by

$$C_1 = \frac{C_{ref}}{f_c' - 8} \tag{2.30}$$

where, $C_{ref} = 10^{-8} m^2 / s$ is the reference moisture diffusion coefficient and, f_c' is the concrete compressive strength. Given the lower and upper bound of 20 and 50 MPa for compressive strength of concrete, moisture diffusivity takes the value of $8.333 \cdot 10^{-10} m^2 / s$ and $2.381 \cdot 10^{-10} m^2 / s$, respectively.

Rahimi-Aghdam et al. (2019) established a mathematical treatment for the transport of moisture in concrete, which was a follow-up study on Bažant and Najjar (1972) model. The authors recommended a moisture diffusion coefficient given by

$$C_1 = 60[1 + 12(w/c - 0.17)^2]\alpha / \alpha_0 \tag{2.31}$$

where α / α_0 denotes the hydration degree. Given a specific hydration degree, the moisture diffusivity coefficient for water-to-cement ratios of 0.30 and 0.65 varies 3.13 times. A study by Bažant and Jirásek (2018) found that for a concrete specimen with good quality, the moisture diffusion coefficient in a fully saturated condition varies twice, between $1.157^{-10} m^2 / s$ and $2.315 \cdot 10^{-10} m^2 / s$.

Critical chloride content that corresponds to the chloride threshold depassivating the protective film formed on the surrounding area of prestressing steel is an influential model parameter in the uncertainty quantification of chloride-induced corrosion damage of bridge girders. A wide range of values based on the exposure environment and concrete compositions has been reported in the literature.

Stratfull et al. (1975) performed chloride titration tests on twenty-two bridge girders in the state of California in order to identify the critical chloride content characterizing corrosion incidence of prestressing strands. Based on the results, the authors recommended a critical chloride threshold of 0.59 kg/m^3 for the initiation of active corrosion in concrete bridges. On the other hand, the chloride content of 2.97 kg/m^3 on the surface of prestressing steel in one of the specimens was not found to lead to active corrosion, corroborating the uncertain state of the problem.

A study by Vassie (1984) focused on the durability of concrete bridges. According to the results shown in **Table 2.1**, the probability of corrosion is related to the content of chloride ions in concrete bridges. While it was believed that a critical chloride threshold of 0.35% (of cement mass) corresponds to the incidence of corrosion, some specimens had shown signs of corrosion for smaller chloride values.

Table 2.1. Threshold of the chloride characterizing the performance of bridges, reproduced from Vassie (1984).

Chloride range (% of cement mass)	0.20%	0.20-0.35%	0.35-0.50%	0.50-1.00%	1.00-1.50%	1.50%
Number of cases investigated	99	86	43	105	59	54
Number of corroded specimens	2	19	10	34	38	41
Percentage of corroded specimens	2%	22%	23%	32%	64%	76%

Hussain et al. (1996) performed a series of experimental tests to investigate the threshold of chloride initiating corrosion of reinforcing steel embedded in mortar specimens. According to the results, the threshold for free chloride was found irrespective of tricalcium aluminate (C_3A) content, while the threshold based on the total chloride was influenced by C_3A. In particular, the threshold of total chloride varied between 0.48 and 0.59, 0.73 and 0.85, 1.01 and 1.20 (% of cement mass), for cement with 2.43, 7.59, and 14 % of C_3A, respectively.

A study by Henriksen and Stoltzner (1993) focused on the propensity of chloride-induced corrosion damage in various Danish bridge columns. Based on the chloride titration test results, a wide range of variability was found in the relation between chloride content and corrosion incidence. In particular, the minimum threshold for corrosion initiation was found 0.05 % [of concrete mass (or 0.30 % of cement mass assuming a 1:6 concrete to cement ratio)], while some specimens with a critical threshold of 0.10% [of concrete mass (or 0.60% of cement mass] were found free from corrosion damage. **Table 2.2** summarizes the critical chloride content threshold initiating the incidence of corrosion.

Table 2.2. Threshold of the chloride characterizing chloride-induced corrosion damage in reinforced concrete specimens, reproduced from Henriksen and Stoltzner (1993).

Chloride content at steel level (% of concrete mass)	≤ 0.04	0.05	0.06	0.07	0.08	0.10
Percentage of corroded cases	0%	40%	100%	33%	67%	92%

A number of studies have focused on the critical chloride content in reinforced concrete specimens. Maekawa (2008) and Hussain and Ishida (2011) recommended a critical chloride content of 0.40% (of cement mass) for the incidence of corrosion. A study by Shafei et al. (2012) focused on corrosion in bridges suggested a chloride threshold of 1.0% (of cement mass) for corrosion initiation. Fib model code considered a range for critical chloride content with lower and upper bounds of 0.2 and 2.0 % (of cement mass) and a mean value of 0.60% (of cement mass) with a standard deviation of 0.15%.

Several studies have dedicated their focus to the probabilistic approach in determining the corrosion initiation time of reinforcing steel in concrete. A study by Kong et al. (2002) focused on investigating the reliability of chloride penetration in fully saturated concrete as a mean to determine the corrosion initiation time. The analyses incorporated several model

parameters to account for the variability in factors influencing the onset of corrosion. The chloride distribution was obtained using a deterministic approach and then combined with a Monte Carlo simulation to study the temporal evolution of chloride influenced by two influential random variables. The study revealed that the distribution of water/cement ratio had a profound impact on the distribution of chloride. The Monte Carlo method demonstrated good capability in evaluating the propagation of uncertainty in the chloride distribution. Additionally, the method provided the probability of corrosion initiation through a cumulative distribution function.

A study by Val and Trapper (2008), focused on providing a probabilistic overview of corrosion initiation by considering various physical processes. The analyses involved the consideration of various model parameters. Due to the aleatory nature of the problem and limited experimental data, the authors opted for normal distributions for surface and critical chloride, while assigning a log-normal distribution to the moisture and chloride diffusion coefficient. The study found that the variation in ambient relative humidity had a significant impact on chloride transport, which in turn characterized the time to first corrosion initiation. Notably, incorporating a two-dimensional account of exposure was found to substantially reduce the corrosion initiation time.

Bastidas-Arteaga et al. (2011) employed a probabilistic framework to determine the concentration of corrosion-inducing chloride ions in concrete. The study focused specifically on unsaturated concrete and considered several physical processes. The evaluation of corrosion probability was carried out by comparing the content of chloride with the critical chloride.

Consistent with previous works, the distribution of critical chloride was assumed to constitute a normal distribution, while the distributions of moisture and chloride diffusion coefficient were considered log-normal. The primary probabilistic tool utilized in the research was Monte Carlo simulation. Considering a case with one-dimensional exposure condition, the probability of corrosion was found to be higher than 50% after around 25 years. On the other hand, for a case with two-dimensional exposure conditions, the corresponding duration was approximately 20 years.

Chapter 3
Analytical Evaluation of Corrosion-Induced Strength Degradation in Prestressed Bridge Girders

This chapter presents a nonlinear finite element analysis approach to determine the impact of corrosion-induced damage on the load-carrying capacity of prestressed concrete bridge girders. The analyses rely on two types of models, namely, beam models and nonlinear truss models. The latter are deemed necessary to obtain reliable estimates of the shear capacity, as beam models are not well-tailored for capturing shear failures. A procedure to account for the reduction in area and deformability of corroded strands, based on visually observed corrosion damage, is proposed and implemented. The models are calibrated and validated with the results of experimental tests on prestressed girders which exhibited varying levels of corrosion-induced damage. This chapter is published in the Journal of Structural Engineering, volume 148, issue 11, 2022.

Despite the significant amount of previous research focused on the impact of corrosion on the performance of bridge girders, there is still a need for analytical models which will enable the systematic parametric investigation of corrosion-damaged girders. The availability of validated simulation tools will allow the development of design-oriented procedures for evaluating the flexural and shear capacity of designed girders. This chapter employs computational simulation to elucidate the influence of corrosion damage on the load-carrying

capacity of prestressed bridge girders. Nonlinear beam models and truss models were used to analytically estimate the flexural and shear strength of prestressed girders with and without corrosion in the prestressing strands. The models are supplemented by an algorithm to account for visually observed corrosion on the mechanical resistance of the strands and concrete. The models are validated using the results of experimental tests on girders taken from two bridges in Virginia, which exhibited varying levels of corrosion damage. Additional analyses are conducted to quantitatively determine the strength degradation due to corrosion and assess the accuracy of simplified expressions for obtaining the ultimate capacity of damaged girders.

3.1 Description of Experimentally Tested Girders

The present study is focused on prestressed girders which had been removed from two bridges in Virginia. The cross-sectional geometry of the two types of girders is presented in **Figure 3.1**, while the layout of their shear reinforcement is presented in Figure 3.2 (Aliasghar-Mamaghani et al., 2022).

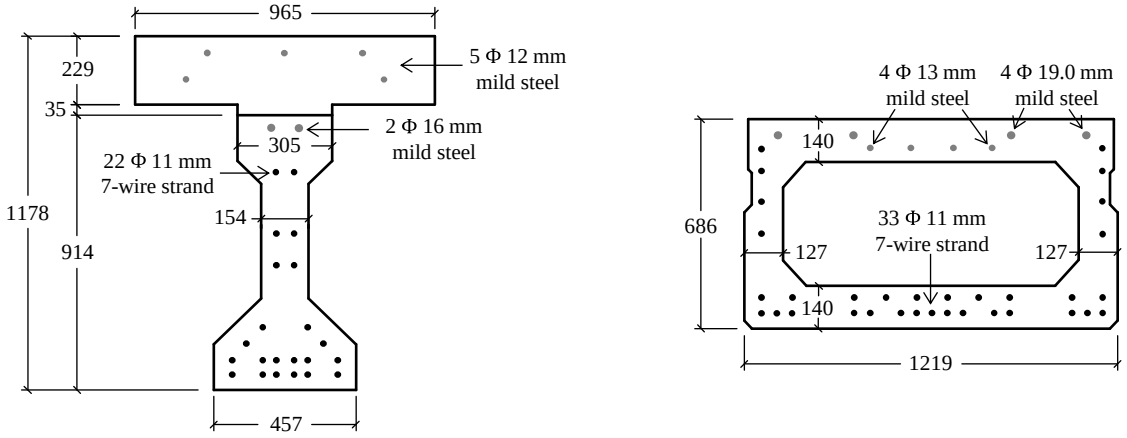

(a) I-section girder (b) Box-section girder

Figure 3.1. Cross-sectional geometry for the two types of girders tested (dimensions in mm)

The girders were experimentally tested at the Thomas M. Murray Structures Laboratory of the Virginia Polytechnic Institute and State University (Alfailakawi et al. 2020; Al Rufaydah 2021). All girders included Grade 270, stress-relieved, 7-wire strands with a nominal diameter of 11 mm (7/16 in.). Four of the girders had an I-section and were removed from the Lesner Bridge located in Virginia Beach after 49 years of service. These girders had a span of 15.16 m (49 ft 9 in.), an AASHTO Type II section with 22 strands**,** a concrete top slab which had a thickness of 178 mm (7 in.) and included mild reinforcement, and a 51 mm (2 in.) concrete overlay, as shown in **Figure 3.1**(a). Each girder was cut from the bridge, and the slab of the as-tested girders had an effective width of 965 mm (3 ft 2 in.). The girders were also reinforced with No. 4 stirrups, with a diameter of 13mm, for shear. The spacing of the stirrups varied along the length of the girder, as shown in Figure 3.2(a).

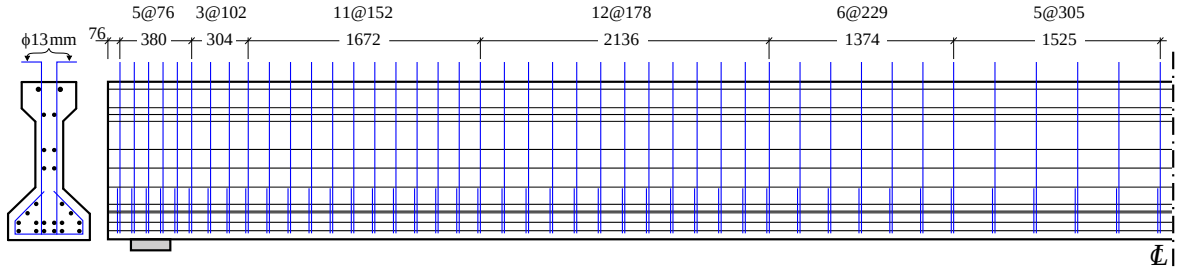

(a) I-section girder

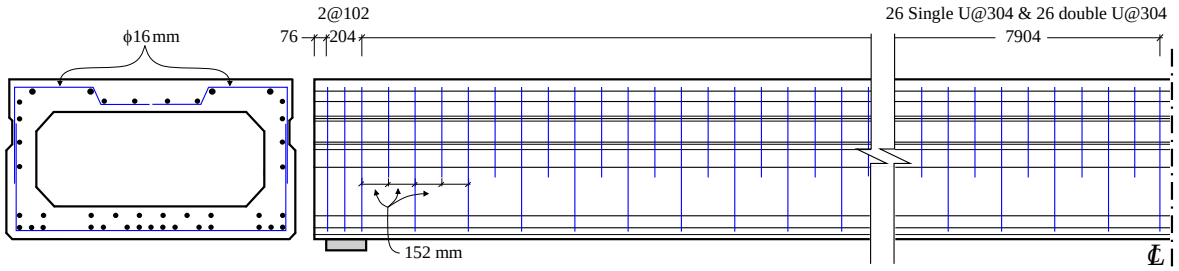

(b) Box-section girder

Figure 3.2. Shear reinforcement arrangement (dimensions in mm)

The remaining four girders had a box-section and were taken from the Aden Road Bridge located near Quantico, Virginia, after 34 years of service. They had a span of 16.76 m (55 ft), a sectional width of 1219 mm (4 ft), a sectional depth of 686 mm (2 ft 3 in.), and a total of 33 strands [**Figure 3.1**(b)]. They were reinforced with single and double U-shaped, No. 5 stirrups, with a diameter of 16 mm and at a spacing of 152 mm, as shown in Figure 3.2(b).

Prior to testing, the girder specimens were inspected for corrosion, and the location and extent of damage were recorded. The corrosion was due to chloride ingress, attributed to sea salt aerosols for the Lesner bridge and use of deicing salts for the Aden Road bridge. The observed damage had the form of cracks parallel to the axis of the girder or loss of concrete cover and exposure of strands, as shown in Figure 3.3a and Figure 3.3b, respectively.

(a) Cracks parallel to girder axis

(b) Section loss

Figure 3.3. Examples of visually observed corrosion damage for tested girders

The first I-section girder was in a relatively undamaged condition (given its age), the second and third I-girder had the damage presented in Figure 3.4a and Figure 3.4b, respectively, in the midspan regions, and the fourth girder had little visible damage.

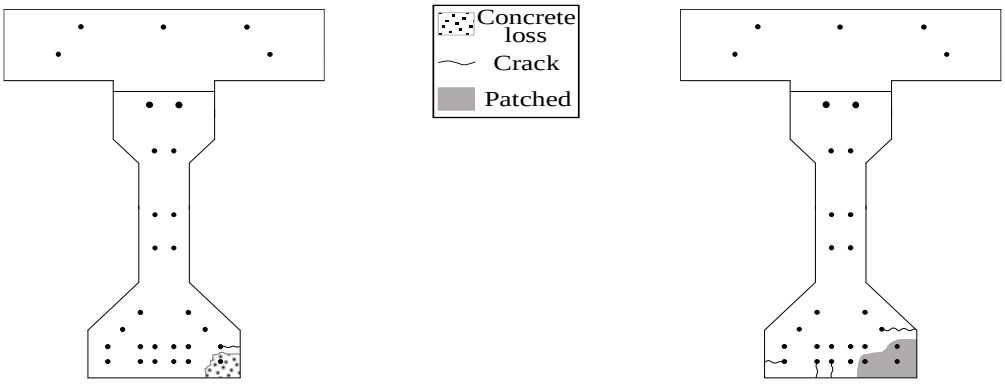

(a) Specimen 2 (b) Specimen 3

Figure 3.4. Typical observed damage for girders with an I-section

The midspan regions of the first three box-section girders exhibited the corrosion damage shown in Figure 3.5. The fourth and final box-section girder specimen had the most severe corrosion damage, which also varied along the length of the specimen, as presented in Figure 3.6.

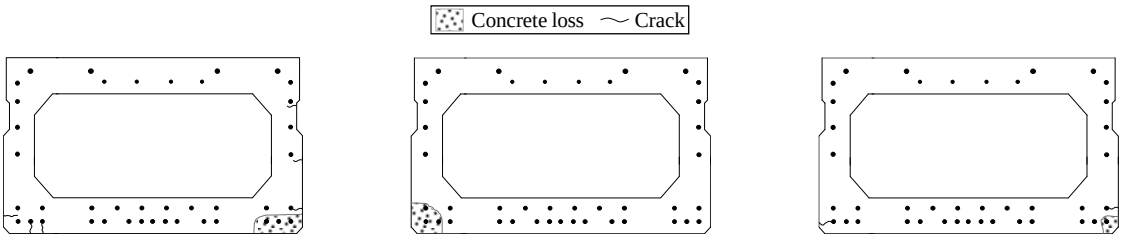

(a) Specimen 1 (b) Specimen 2 (c) Specimen 3

Figure 3.5. Typical observed damage for girders with a box-section

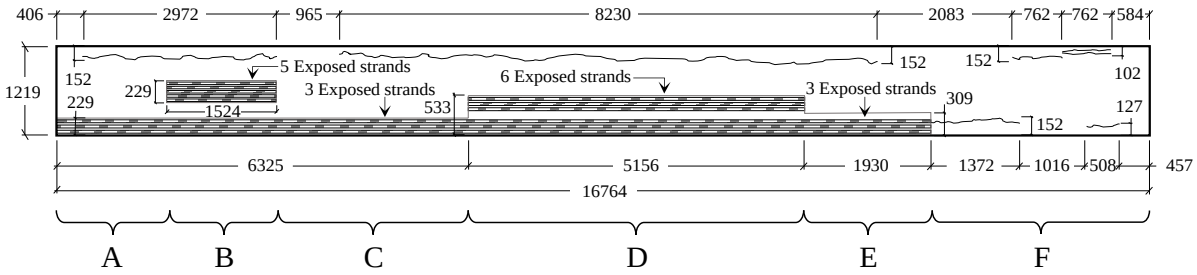

(a) Observed damage along the length (view from bottom; dimensions in mm)

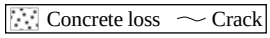

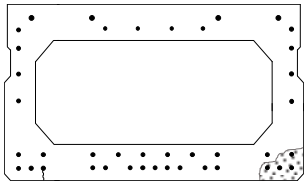

(b) Cross-section in region A

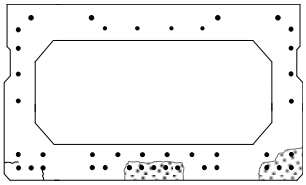

(c) Cross-section in region B

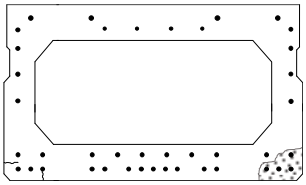

(d) Cross-section in region C

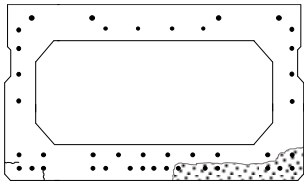

(e) Cross-section in

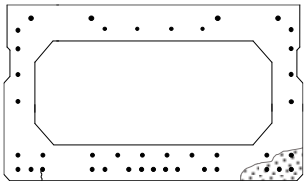

(f) Cross-section in

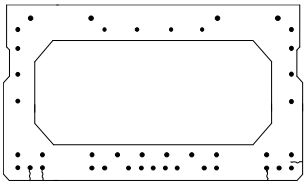

(g) Cross-section in

Figure 3.6. Observed damage for box-section girder 4

A detailed schematic presentation of the damage recorded for the various specimens prior to testing is provided in **Figure 3.7** to **Figure 3.12**. The girders were experimentally tested as simply supported beams, subjected to monotonically increasing vertical downward forces until failure. Six of the girders (three of each type) were tested under a four-point bending setup, with two vertical forces applied at distances of 1.2 m (4 ft) from midspan. The shear-span-to-total-span ratio for the flexure-dominated I- and box-section girders was 0.40 and 0.41, respectively, which corresponded to shear span-to-depth ratios of 5.2 for the I-section girder and 10.0 for the box-section girder. The remaining specimens, which were meant to provide the shear strength of the girders, were subjected to a single vertical load, applied at a distance of

1.8 m (6 ft) and 1.2 m (4 ft) from one of the two supports for the I- and box-section girders, which corresponded to shear span-to-depth ratios of 1.6 and 1.8, respectively. The span length in the shear tests for the I-section girder was 9.91 m (32 ft 6 in.), while the corresponding value for the box-section girder was 16.26 m (53 ft 4 in.). The placement of a single load at a very short distance from the support meant that the girder region between the applied load and the nearest support would be subjected to a very high shear force before the development of significant bending moments, thus ensuring that shear failure would occur before flexural failure.

(a) Front elevation view

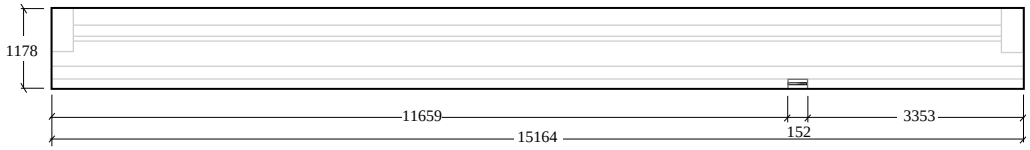

(b) Back elevation view

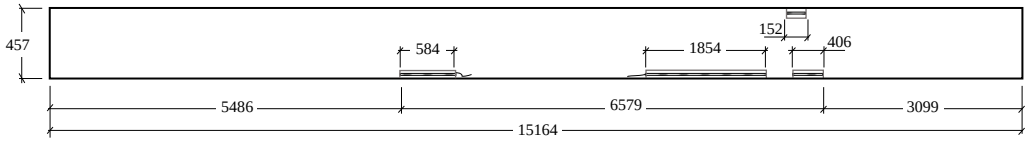

(c) Bottom view

Figure 3.7. Observed damage along the length of I-section specimen 2 (dimensions in mm)

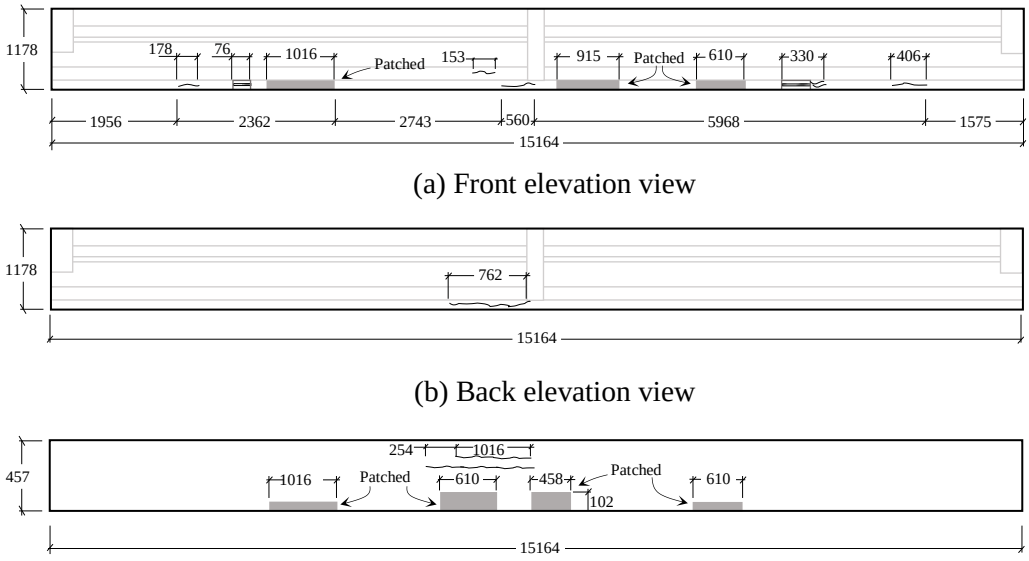

Figure 3.8. Observed damage along the length of I-section specimen 3 (dimensions in mm)

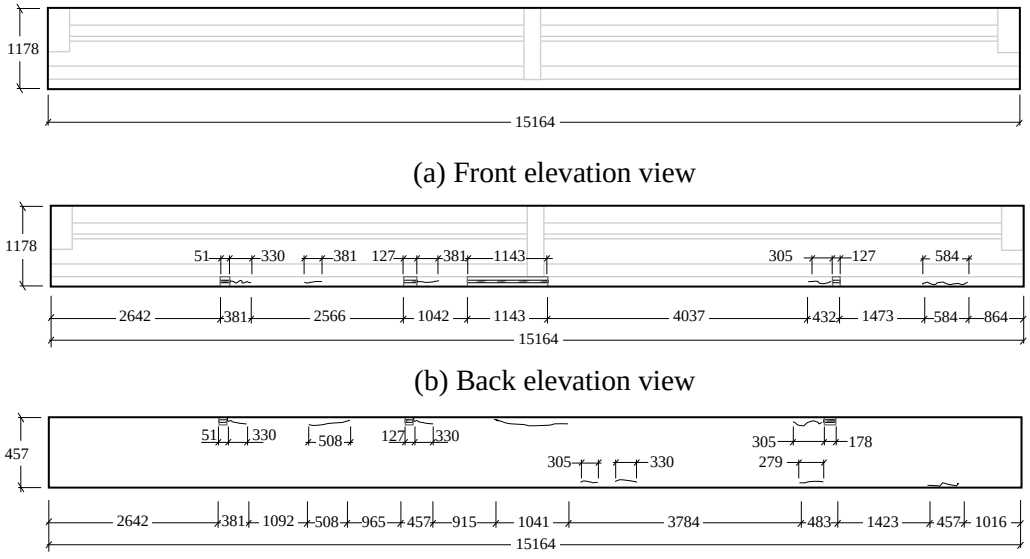

Figure 3.9. Observed damage along the length of I-section specimen 4 (dimensions in mm)

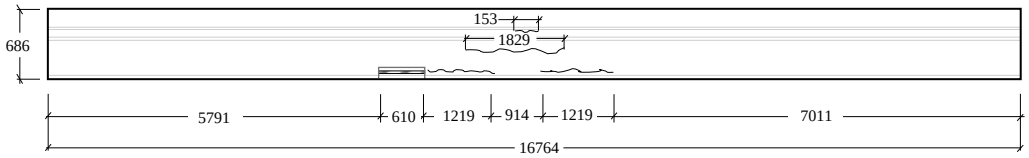

(a) Front elevation view

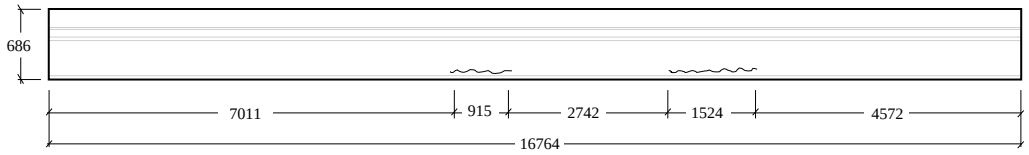

(b) Back elevation view

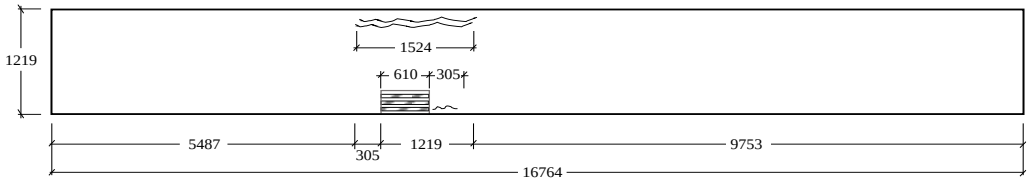

(c) Bottom view

Figure 3.10. Observed damage along the length of box-section specimen 1 (dimensions in mm)

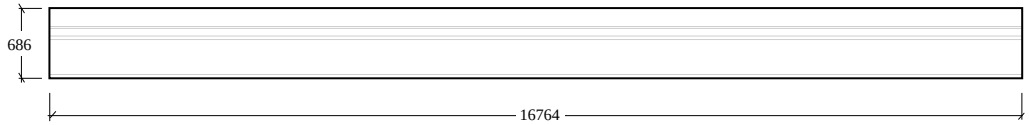

(a) Front elevation view

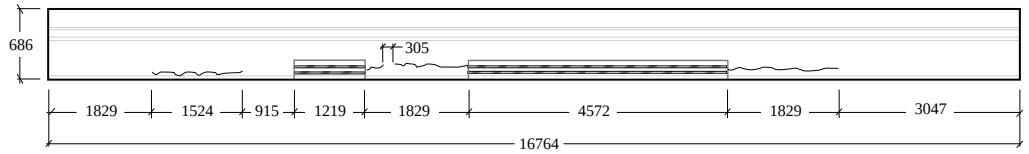

(b) Back elevation view

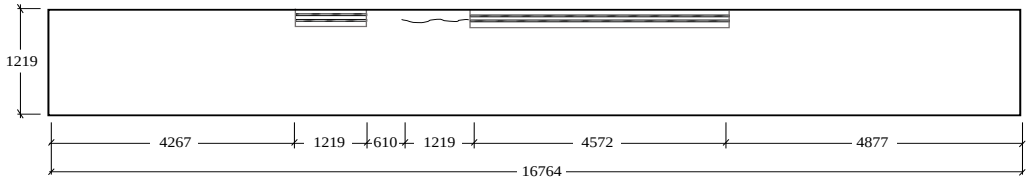

(c) Bottom view

Figure 3.11. Observed damage along the length of box-section specimen 2 (dimensions in mm)

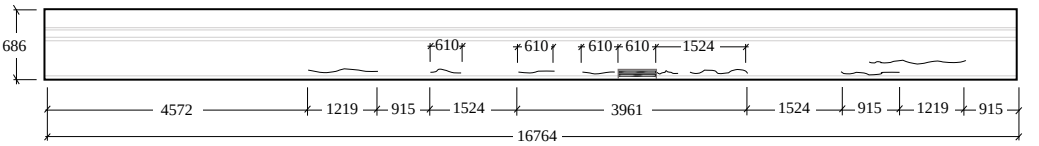

(a) Front elevation view

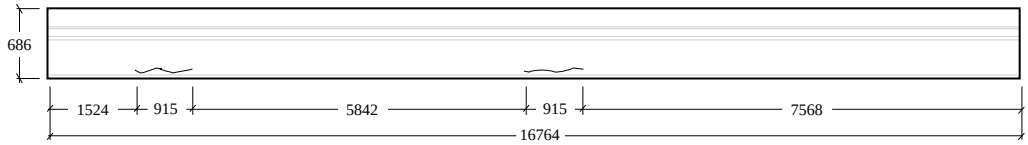

(b) Back elevation view

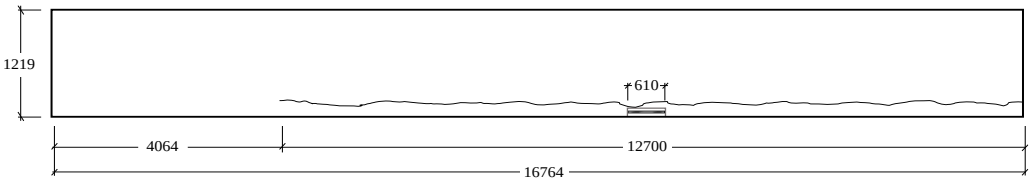

(c) Bottom view

Figure 3.12. Observed damage along the length of box-section specimen 3 (dimensions in mm)

3.2 Analysis Methodology

The analytical simulations of the corrosion-damaged girders employed two modeling approaches, namely, beam models and nonlinear truss models. Both methods, together with the corresponding material laws, have been implemented in the research-oriented program *FE-MultiPhys* (Koutromanos and Farhadi, 2018), which was used for the analyses presented herein.

The first model type relies on discretizing a beam (line) member into multiple 2-node beam finite elements **[**Figure 3.13(a)**]**, whose kinematics are governed by the Euler-Bernoulli theory (e.g., Koutromanos 2018). The finite element approximation uses linear polynomial interpolation functions for the axial displacement and cubic Hermitian polynomial interpolation functions for the transverse displacement (Koutromanos 2018). The calculation of the resistance of each element relies on a fiber sectional model **[**Figure 3.13(b)**]**, wherein the beam cross-section is subdivided into smaller regions, called fibers. Each fiber is assumed to have a constant

axial strain value obtained from the reference axial strain and curvature of the section. Separate fibers are used for the individual prestressing strands and reinforcing bars in the beam section. The stress of each fiber is obtained using a uniaxial stress-strain law. The axial force and bending moment of the cross-section are calculated as sums of the corresponding contributions of the individual fibers. Beam models have been shown to provide an accurate and numerically efficient solution for simulating the nonlinear response and ultimate resistance of flexure-dominated beams (Dall'Asta and Dezi, 1998; Ariyawardena and Ghali, 2002; Dall'Asta et al., 2007).

(a) 2-node element (b) Fiber cross-sectional law

Figure 3.13. Beam elements used in analysis

Nonlinear truss models were also created to simulate the response of girders that failed in shear, given the fact that shear failures (strength degradation associated with large, inclined cracks) cannot be accurately captured by beam-based models. Truss models (Panagiotou et al., 2012) rely on the representation of a concrete member as an assemblage of horizontal, vertical, and inclined truss (line) elements, as shown in Figure 3.14(a). The inclined elements are meant to describe the compression field that develops in cracked members. Truss models have been extensively used with success for simulations of reinforced concrete (RC) wall (Panagiotou et al., 2012; Deng et al., 2021) and column (Moharrami et al., 2015) components undergoing shear failures. The only potential difficulty of nonlinear truss models is the need to manually define

the truss representation of an RC component, which may be cumbersome for practicing engineers. To address this potential issue, the analysis approach used herein, originally presented in Deng et al. (2021), is implemented in such a fashion that each truss standard panel – consisting of four nodes in a rectangular arrangement connected through two horizontal, two vertical, and two diagonal truss elements – is programmed as a rectangular, four-node macro-element, as schematically summarized in Figure 3.14(b). The truss panel is represented as a rectangular element, facilitating the model definition and the post-processing of the results. However, the actual computations for the set of four nodes comprising the panel (i.e., the calculation of internal nodal force vector and tangent stiffness matrix for the specific nodes) use an underlying truss panel assemblage. The area of each element is established as the product of the in-plane effective width, b_{eff}, times the out-of-plane thickness of the concrete beam. The effective width values used for the various elements are schematically presented in Figure 3.14 (c).

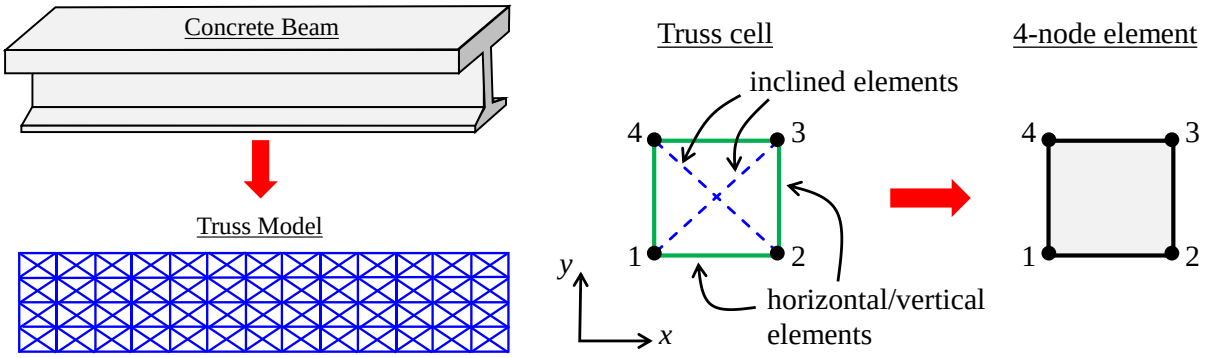

(a) Modeling Procedure

(b) Implementation as a rectangular macro-element [reproduced from Deng et al. (2021)with permission]

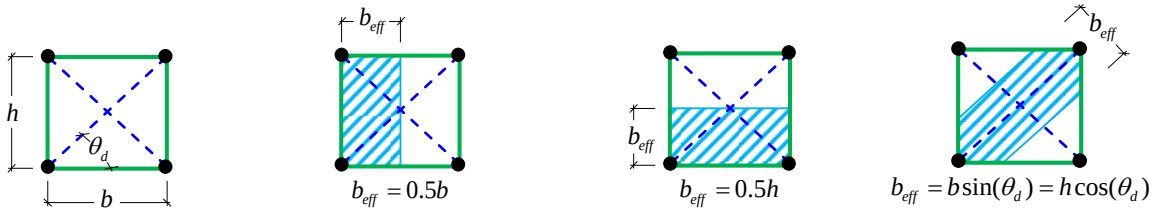

(c) Effective width of truss cell components (vertical, horizontal, and diagonal)

Figure 3.14. Nonlinear Truss Model

3.3 Material Models

3.3.1 Concrete Model

The material stress-strain law used for the concrete is schematically summarized in Figure 3.15(a), and was originally formulated by Lu and Panagiotou (2014). The specific law can account for the nonlinear stress-strain relation before reaching the peak compressive strength, f_c' and for the occurrence of softening associated with compressive crushing. The response in tension is assumed to be linearly elastic, until the stress reaches the tensile strength, f_t, after which the model includes softening to account for tensile strength degradation associated with crack propagation.

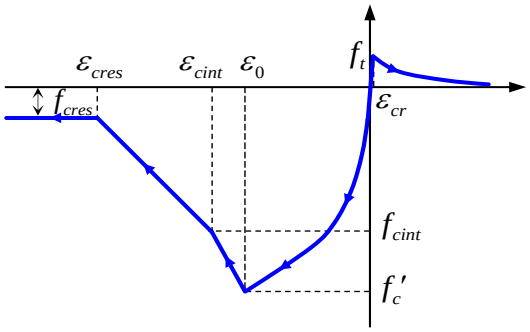

(a) Stress-strain curve

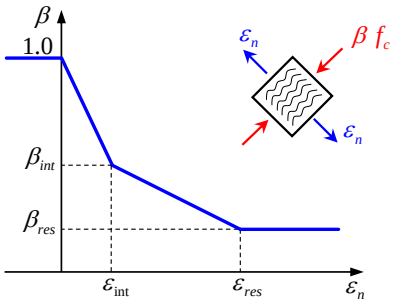

(b) Factor for transverse tension in inclined truss elements

Figure 3.15. Concrete material model

As mentioned in the previous section, the nonlinear truss models used in the analysis include inclined (diagonal) elements meant to describe the compression field forming in the webs of the beam girders. The effect of transverse tensile strains on the compressive resistance of these inclined elements is accounted for, in accordance with the Modified Compression Field Theory (Vecchio and Collins, 1986). Specifically, if an inclined truss element carries a compressive stress, then this stress is multiplied by a reduction coefficient β, which is a function of the tensile strain ε_n in the direction perpendicular to the truss element as schematically shown in Figure 3.15(b).

The material law for concrete involves softening, which introduces spurious mesh-size effects in a finite element analysis, as explained in, e.g., Bazant and Planas (1997). A regularization, i.e. adjustment of the softening portions of the concrete stress-strain law, is conducted to address this issue. The present study adopts the regularization approach by Lu and Panagiotou (2014), which stipulates that the calibrated stress-strain laws of the concrete material correspond to a square panel with a given size, L_{ref}, equal to 600 mm. If the actual

element size is different than L_{ref}, then the softening portions of the stress-strain law will require adjustment, as explained in Lu and Panagiotou (2014).

3.3.2 Steel Model

The stress-strain behavior of the reinforcing and prestressing steel is described through the model by Kim and Koutromanos (2016). As shown in Figure 3.16(a), the specific material model can describe the salient features of the stress-strain curve for reinforcing bars, such as the yield plateau and nonlinear stress-strain relation in the strain-hardening regime. The model can also account for material rupture, by stipulating that the material at a given location loses the capability to carry stresses if an ever-increasing parameter D attains a user-defined threshold value D_{cr}. As described in more detail in Kim and Koutromanos (2016), D is related to the inelastic work accumulated under tensile stresses. The evolution of D is controlled by the following rate expression.

$$\dot{D} = \begin{cases} \left(\frac{f}{f_y} \right)^{2t} \dot{\varepsilon}_p \ , \ if \ f \ > 0 \\ 0 \ \ otherwise \end{cases} \tag{1}$$

where f is the steel stress, f_y is the yield stress, t is a material constant, and $\dot{\varepsilon}_p$ is the rate of the plastic strain.

With proper calibration, the material law is also capable of reproducing the experimentally determined stress-strain curve of prestressing strand specimens removed from the girders, as shown in Figure 3.16(b). As deduced from the same figure, several tested strand specimens ruptured before the development of any inelastic deformations. These specimens corresponded to strands which had visible corrosion damage.

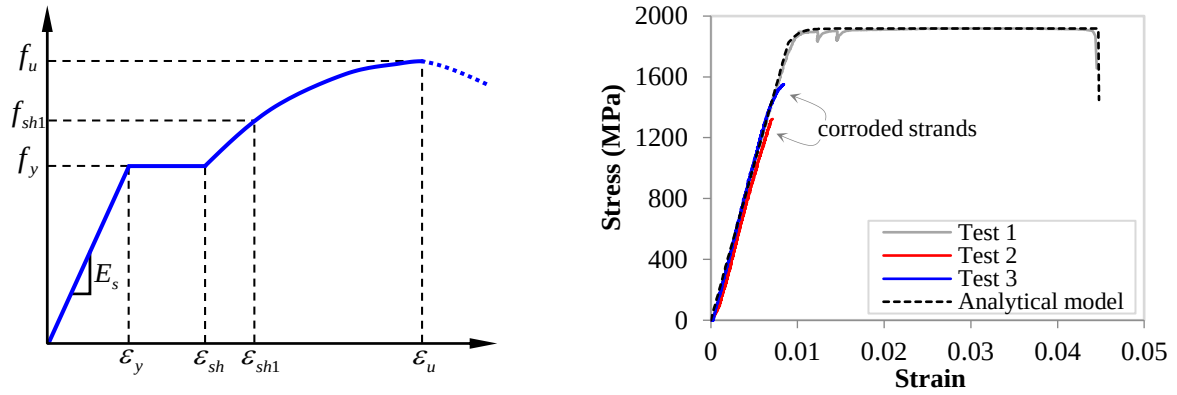

(a) Stress-strain curve for reinforcing steel (b) Example calibration for prestressing strands

Figure 3.16. Material model for prestressing and reinforcing steel

3.4 Accounting for Corrosion Damage

The analytical models are properly adjusted to reflect the visually observed, corrosion-induced damage in the bridge girders simulated. Two types of adjustment are conducted, namely, a reduction in the cross-sectional area of strands and a reduction in the deformability of the strand material. As mentioned earlier, the visually observed damage in the girders can be classified in one of two categories, namely, cracks which are aligned with the axis of the girder, or concrete section loss. The two types of damage for a cross-section, and the affected strands, are schematically presented in Figure 3.17a. As shown in the figure, a corrosion-related crack is assumed to affect the area of two sets of strands. Specifically, the area of the strands directly next to a crack is reduced by 40%, and the area of the adjacent strands (i.e., the strands in the vicinity of, but not directly next to a crack) is reduced by 20%. A strand is assumed to be directly next to a crack if its minimum distance from the crack is less than 4 cm, while it is assumed to be an adjacent strand if the same distance is between 4 cm and 8 cm. An adjustment is also conducted for regions with concrete spalling and exposure of the strands, also shown in Figure 3.17a.

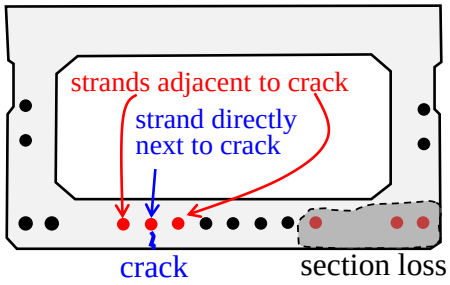

(a) Schematic explanation

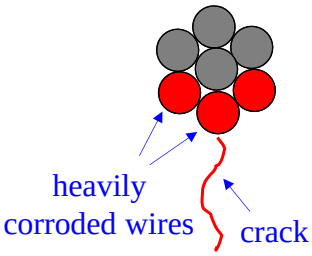

(b) Wires in strand directly next to crack

Figure 3.17. Description of procedure to account for corrosion damage in analytical models

Some of the girders considered in this study had been previously repaired by patching the regions where concrete loss and strand exposure had occurred. Investigation of these repairs demonstrated that strands within the patched region had little remaining cross-sectional area. Therefore, a reduction of 90% is applied to the area of the strands in such patched regions. Finally, it is worth mentioning that testing of the third box-girder specimen revealed that a significant amount of water had accumulated in the hollow region of the box section. This water flowed out of the girder after the occurrence of significant flexural cracking in the experimental test. The presence of this water (and the strand corrosion that it may have entailed) is accounted for in the model of that girder by a 15% reduction to the area of all strands in the affected region, i.e., the bottom flange of the section. As will be shown later, this reduction is important for obtaining accurate estimates of the flexural capacity.

The deformability of several strands removed from the girders was found to have been reduced due to corrosion. To account for this effect, a modified calibration was adopted for heavily corroded wires. These are assumed to be the wires of all strands located in patched regions, and three out of the seven wires in the strands directly next to a crack. The stipulation that only three out of the seven wires will be heavily corroded for the latter type of strands is

based on previous recommendations in the literature (Jeon et al., 2019; Jeon et al., 2020) and the schematic considerations presented in Figure 3.17b, based on which three of the seven wires would be directly exposed to the atmosphere for a strand next to a crack. The heavily corroded wires are assumed to rupture at a tensile strain of 1%, which would correspond to rupture prior to yielding for the stress-strain curves presented in Figure 3.16b. It is worth mentioning that the value of 1% adopted herein for damaged wires is consistent with recommendations established in previous studies in the literature (Zhang et al., 2019; Jeon et al., 2020; Franceschini et al., 2022).

Concrete section loss associated with the corrosion-induced damage is also accounted for in the analyses, by reducing the area of the fibers in the sections of the beam elements and by reducing the area of the elements in the truss models of the shear-dominated girders. The properties of concrete in patched regions were assumed to be identical to those of the undamaged concrete. The impact of corrosion damage on the bond-slip behavior of the strands is neglected in the analyses.

3.5 Analysis Results

This section presents the results from the analyses of the eight girders which were experimentally tested. Each analysis began by first applying an initial (self-induced) strain in the strand material to obtain the effective prestressing of the strands (estimated from hand calculations). The values assigned to the various parameters of the concrete material model are summarized in **Table 3.1**. The compressive strength value for the girder and concrete deck was obtained from tests on cylindrical samples taken from each specimen. Given the compressive strength, the modulus of elasticity was estimated using the equation proposed in the ACI 318

Code (ACI, 2019). The concrete tensile strength f_t was calibrated so that the cracking load value for each analysis matches the corresponding experimental value.

Table 3.1. Properties of concrete for girder specimens and summary of material model parameters in the affected regions

Specimen	Location	f_c' (MPa)	E_c (MPa)	f_{cint} (MPa)	f_{cres} (MPa)	ε_0	ε_{cint}	ε_{cres}	f_t (MPa)	ε_{cr} $\times 10^{-5}$
IG1	Deck	49.6	33347	42.2	5.0	0.0025	0.0028	0.004	2.3	6.97
	Girder	40.0	29930	34.0	4.0	0.0023	0.0027	0.004	2.0	6.68
IG2	Deck	24.1	23250	20.5	2.4	0.0018	0.0028	0.005	1.6	6.97
	Girder	38.6	29410	32.8	3.9	0.0022	0.0027	0.005	2.8	9.38
IG3	Deck	19.7	21017	16.8	2.0	0.0016	0.0025	0.003	1.5	6.97
	Girder	42.1	30694	35.7	4.2	0.0023	0.0028	0.005	4.0	13.14
IG4	Deck	29.4	25651	25.0	2.9	0.0019	0.0028	0.005	2.4	9.36
	Girder	37.0	28772	31.4	3.7	0.0022	0.0030	0.005	2.4	8.34
BG1	Girder	50.3	33578	42.8	5.0	0.0025	0.0030	0.004	2.2	6.57
BG2	Girder	49.6	33347	42.2	5.0	0.0025	0.0030	0.004	2.1	6.20
BG3	Girder	45.7	32000	38.9	4.6	0.0024	0.0028	0.004	2.4	7.54
BG4	Girder	41.9	30644	35.6	4.2	0.0023	0.0030	0.004	2.4	7.90

The steel constitutive model in the analysis of each specimen was calibrated using data from uniaxial tension tests on strand samples taken from the girders. The rupture strain for the strands was set equal to 4.5%, in accordance with pertinent material tests. The calibrated values used for the parameters of the steel material model are provided in Table 3.2.

Table 3.2. Model parameters for reinforcing steel and prestressing wires

Model	E_s (MPa)	f_y (MPa)	f_{sh1} (MPa)	f_u (MPa)	ε_{sh}	ε_{sh1}	ε_u	D_{cr}	Rupture Strain
Strand Wires	206843	1834	1903	1920	0.0088	0.0110	0.045	0.040	4.50%
Corroded Wires	206843	1834	1903	1920	0.0088	0.0110	0.045	0.001	1.00%
Mild Steel Bars	199948	334	448	519	0.0100	0.0490	0.160	0.350	16.00%
Stirrups	199948	414	607	634	0.0100	0.0490	0.100	0.200	10.00%

The results of the analyses involving flexural failure are discussed first, followed by those for the two girders which incurred shear failure. The analysis for each damaged girder was repeated a second time, assuming the absence of any corrosion damage, to analytically determine the impact of corrosion on the capacity. To enable an evaluation of simplified, design-oriented procedures, the ultimate capacity of each girder with corrosion damage was estimated using the equations provided in AASHTO code (AASHTO, 2020)**,** for flexure and shear, respectively, which are detailed through equation (3.1) to (3.5).

The flexural resistance of girders is calculated by the following expression, based on the AASHTO LRFD Specifications (AASHTO, 2020).

$$M_n = A_{ps} f_{ps}[d_p - (a/2)] + A_s f_s[d_s - (a/2)] - A_s' f_s'[d_s' - (a/2)] + \alpha_1 f_c'(b - b_w)h_f[(a/2) - (h_f/2)] \quad (3.1)$$

where A_{ps} is the area of prestressing steel; f_{ps} is the average prestressing steel stress; d_p and d_s are the distance from the extreme compression fiber to the centroid of prestressing strands and mild steel, respectively; A_s and f_s are the area and stress of the mild steel; A_s' and f_s' are the area and stress of the mild compression steel; d_s' is the distance from the extreme compression fiber to the centroid of compression steel; α_1 and β_1 are compressive stress block factors; $a = \beta_1 c$; c is the distance from extreme compression fiber to neutral axis; b is the width of the member's compression face; h_f is the compression flange depth.

The shear capacity is obtained from the following equation (AASHTO, 2020).

$$V_n = V_c + V_s + V_p \quad (3.2)$$

where V_p is the prestressing force component in the direction of the shear force, and V_c and V_s are the contributions of concrete and steel to the shear resistance. The value of V_c (in kip) is obtained from the following equation.

$$V_c = 0.0316\beta\lambda\sqrt{f_c'}\,b_v\,d_v \tag{3.3}$$

where f_c' is the compressive strength in ksi; β is a factor expressing the effect of shear and tensile stress transfer across diagonal cracks in concrete; λ is the concrete density factor; b_v is the effctive width of the web; d_v is the effective shear depth.

The value of V_s is given by:

$$V_s = A_v f_y d_v[\cot(\theta) + \cot(\alpha)]\sin(\alpha)/s \tag{3.4}$$

where A_v is the area of shear reinforcement; s is the stirrup spacing in the longitudinal direction; α is the angle between the shear reinforcement bars and the beam axis; and θ is the angle of the inclined compressive stress field. The value of θ (in degrees) can be obtained from the following equation (AASHTO, 2020).

$$\theta = 29 + 3500\varepsilon_s \tag{3.5}$$

where ε_s is the tensile strain at the centroid of tension reinforcement in the longitudinal direction.

3.6 Results for Flexure-dominated Girders

The analytically obtained load-displacement curves for the three flexure-dominated girders with an I-section are presented in Figure 3.18. The analysis for the undamaged first specimen accurately reproduced the experimentally recorded load-displacement curve, as shown in Figure 3.18(a). Strength degradation was caused by compressive crushing at the top of the deck, which was also the case in the experimental test. The relative error in the analytically obtained ultimate capacity was equal to 3.2%. It is worth mentioning that the experimental testing of the specimen encountered issues associated with the load setup, which necessitated the unloading of the girder before failure, and its subsequent reloading to the failure load. This unloading and reloading process is evident in the experimental curve of Figure 3.18(a). As deduced from the same figure, the AASHTO strength formula gives a quite accurate estimate of the ultimate capacity.

The analytical load-displacement curves for specimens 2 and 3 are compared to their experimental counterparts in Figure 3.18b and Figure 3.18c, respectively. These specimens had minor and extensive corrosion damage, respectively. The analyses provide excellent estimates of the experimentally recorded force-deformation response. It is worth mentioning that the small drops in strength obtained at various levels of displacement for specimen 3 are attributed to the rupture of individual strand wires. Figure 3.18b and Figure 3.18c also provide the load-displacement curves obtained for an analysis of undamaged girders having the same cross-sectional and material properties as the two specimens. As deduced from these figures, the corrosion damage had very minor impact on the behavior of Specimen 2, while it significantly impacted the response of Specimen 3, which experienced rupture of multiple strands. Specimen 2 failed due to compressive crushing at the top of the deck slab, which was also the case for the

analysis of the undamaged girders. The estimated relative reduction in ultimate capacity due to corrosion damage is 6.3% for specimen 2 and 44.3% for specimen 3. The simplified strength estimation method based on the AASHTO code was found to be very accurate for Specimen 3, while it underestimated the capacity of Specimen 2 by 13.1%.

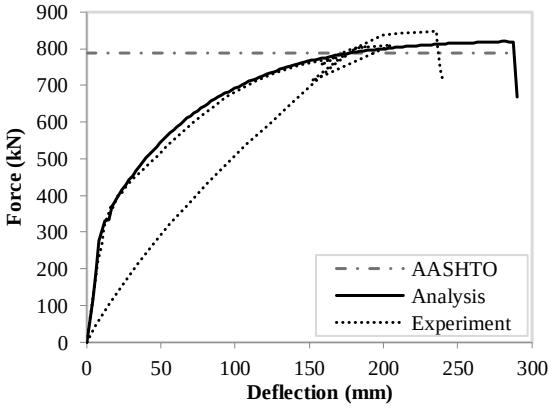

(a) Specimen 1

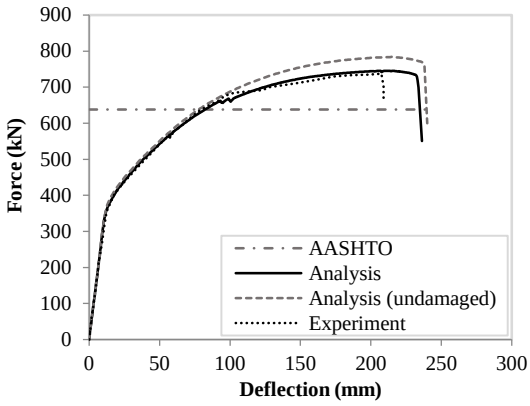

(b) Specimen 2

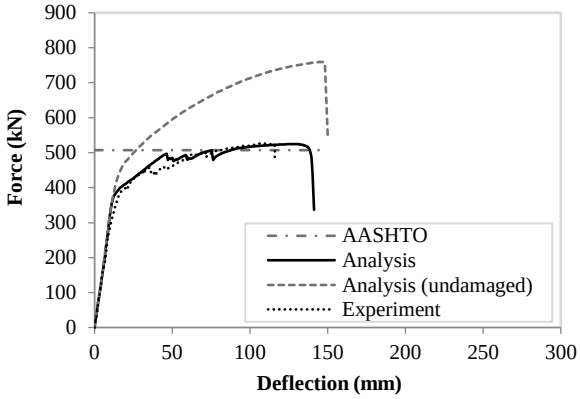

(c) Specimen 3

Figure 3.18. Analysis results for flexure-dominated specimens with an I-section

Figure 3.19 presents the analytically obtained load-displacement curves for the three box-section girders exhibiting a flexural failure mode, together with the corresponding experimental observations. The level of corrosion damage, determined from visual inspection, was moderate in the first two specimens and extensive in the third specimen. The computational models for the first two specimens gave very accurate reproductions of the load-displacement

curves, as deduced from Figure 3.19a and Figure 3.19b. The load-displacement response of Specimen 3 was not recorded during the experimental test, due to a malfunction in the data acquisition system. The only piece of information that was available after the test was the peak capacity, which has been accurately reproduced by the computational simulation with a relative error of 2.8%, as deduced from Figure 3.19(c). The simplified, AASHTO-based methodology gave accurate estimates of the peak capacity for the first two specimens, while it overestimated the capacity of the third specimen by 15.5%.

It is worth noting that corrosion does not affect the deformability of the three specimens in the same way. Specifically, while corrosion is found to have reduced the deformability of specimen 1, it has entailed a very small decrease in the deformability of specimen 2 and has significantly increased the deformability of specimen 3. These results can be explained on the basis of the particular failure modes for each case. The undamaged versions for all three specimens fail due to concrete crushing at the top of the section in the constant-moment region. Corrosion damage leads to a reduction in the area (and, to some extent, deformability) of strands that participate in the tensile force at the bottom of the section developing the ultimate moment capacity. The corrosion damage for specimens 1 and 3 has sufficient extent to cause flexural failure due to strand rupture at the bottom of the section in the constant-moment region. The fact that strand rupture governs the behavior of specimen 3 leads to an increase in the ultimate deflection of that particular girder. Strand rupture for specimen 1 is much more pronounced, with individual, heavily corroded wires rupturing at early stages of the analysis. For this reason, the ultimate deflection, at which the load-carrying capacity is degraded due to extensive rupture of the strands, is lower than that of the undamaged version of the specimen. The corrosion

damage in the strands of specimen 2 slightly decreases the deformability of the section, which still fails due to compressive crushing of the concrete.

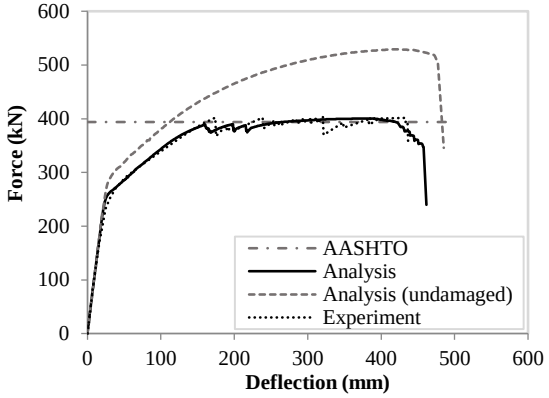

(a) Specimen 1

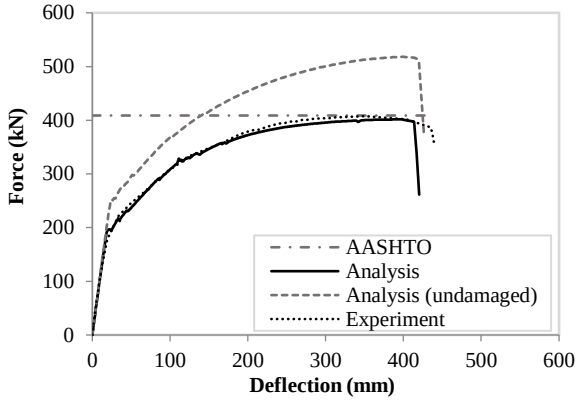

(b) Specimen 2

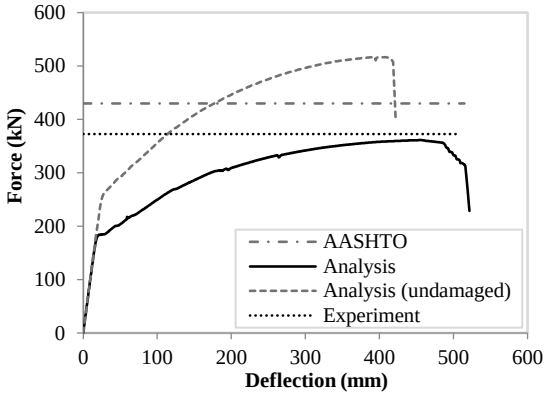

(c) Specimen 3

Figure 3.19. Analysis results for flexure-dominated specimens with a box-section

3.7 Analysis for Shear-dominated Girders

The two shear-dominated girder specimens were analyzed using nonlinear truss models. The inclination angle θ_d was set equal to 34.6 degrees for both specimens, which was the average inclination angle of the shear cracks that formed in these specimens. The value of parameter β_{int} in Figure 3.15b was set equal to 0.50 and 0.30 for I-section and box-section

specimen, respectively. The parameters β_{res}, ε_{int} and ε_{res} in the same figure were assigned identical values for the two specimens, equal to 0.10, 0.01 and 0.025, respectively.

In both cases, failure occurred in the form of a large inclined crack, and the subsequent sudden strength degradation was associated with compressive web crushing. The truss models are capable of satisfactorily capturing the failure mechanism, as deduced from Figure 3.20 for the specimen with the I-section and Figure 3.21 for the specimen with the box-section. The analytically obtained load-displacement curves for the girders with an I-section and a box-section are compared to their experimental counterparts in Figure 3.22a and Figure 3.22b, respectively. The I-section girder did not have significant corrosion damage in the affected region (i.e., within the shear span length), while the box-girder specimen had the significant damage presented in Figure 3.6. The analysis gave near-perfect matches of the ultimate strength of each girder, with a relative error of approximately 1.0% for both cases. The truss modeling approach led to overestimation of the initial stiffness, especially for the case of the specimen with an I-section. A hand calculation was conducted for the stiffness of each specimen, considering the actual cross-sectional dimensions and load setup and assuming linearly elastic material behavior. A straight line with a slope equal to the stiffness obtained with the hand calculation is provided in Figure 3.22a and Figure 3.22b. It is interesting to note that the experimentally obtained initial stiffness for the specimen with an I-section was much lower than the value obtained with the hand calculation. The latter value was practically equal to the initial stiffness of the analysis with the truss model. While it was not possible to determine the source of the discrepancy between the analysis and the experiment for the specific case, it is important to emphasize that such discrepancy is not attributed to corrosion damage, as there were no significant pre-existing cracks in the affected regions which would justify a potential

reduction in the initial stiffness. The bond-slip deformations were also monitored for the specific specimen (Al Rufaydah, 2021) and they were negligible throughout the test, so they too cannot have been a factor for the obtained error in the initial stiffness.

(a) Damage at end of test

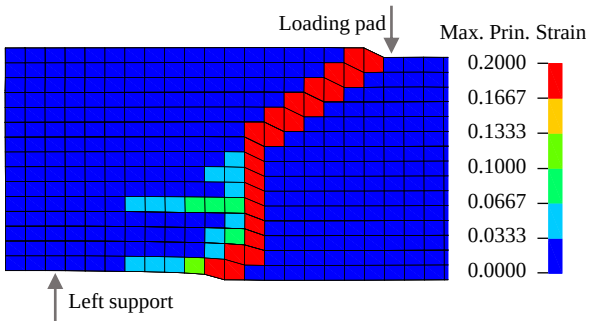

(b) Deformed mesh and principal strain contour at end of analysis

Figure 3.20. Comparison between analytically obtained and experimentally observed damage pattern for the shear-dominated specimen with an I-section

(a) Damage at end of test

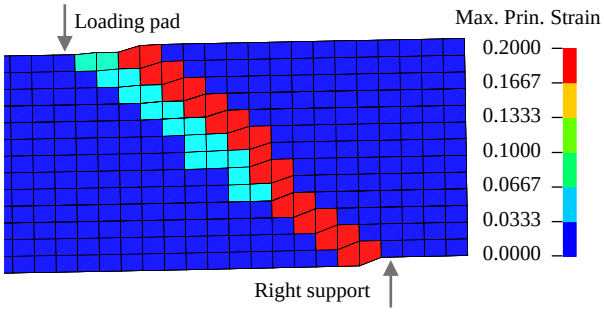

(b) Deformed mesh and principal strain contour at end of analysis

Figure 3.21. Comparison between analytically obtained and experimentally observed damage pattern for the shear-dominated specimen with a box-section.

Given that the specimen with the box-girder section had significant corrosion damage, the impact of this damage to the load-displacement response was determined by means of an

additional analysis of an identical, undamaged girder. The load-displacement curve obtained for the undamaged girder is included in Figure 3.22(b). A comparison of the curves obtained for the analyses of the undamaged and damaged girders indicates that corrosion had minimal impact on the ultimate capacity, which was practically identical for the two cases, but it significantly impacted the deformability of the girder. Specifically, the maximum displacement of the damaged girder was much higher, due to the reduced flexural stiffness corresponding to the damaged regions. The fact that corrosion did not impact the shear capacity was expected, as there was no damage in the stirrups or web concrete, i.e. in the regions which could potentially undermine the shear resistance mechanism. Figures 16a and 16b also provide the ultimate capacity values obtained using the equations in the AASHTO code (2020) with corrosion damage included. These equations underestimated the strength in both cases, with an error of 27.4% for the I-section girder and 25.4% for the box-section girder.

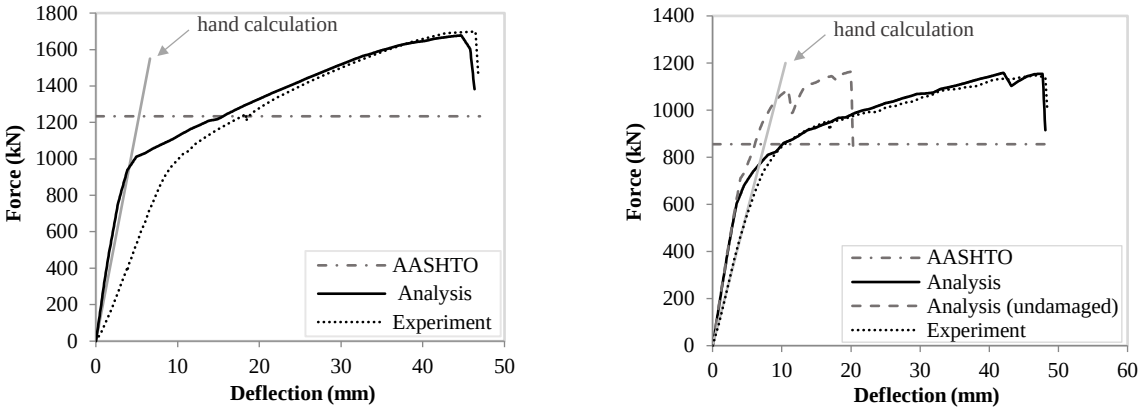

(a) Girder with an I-section (b) Girder with a box-section

Figure 3.22. Analysis results for shear-dominated specimens

3.8 Discussion

The beam-based modeling scheme combined with the procedure to account for corrosion-induced damage was found to give excellent accuracy in terms of predicting the load-displacement response of the six flexure-dominated specimens, for different cross-sectional shapes and varying levels of visually observed corrosion damage. Given the conceptual simplicity and algorithmic efficiency of this scheme, it can be effectively used for systematic parametric studies of corrosion-damaged girders, especially whenever the only information pertaining to the extent of corrosion stems from visual inspection, without more detailed measurements.

The nonlinear truss modeling approach was capable of not only predicting the peak capacity of the two specimens that failed in shear, but also reproducing the failure mode and associated abrupt strength degradation. Given that only one of the two specimens with a shear failure had corrosion damage, and this damage was not related to the stirrups or the compression field developing in the web, the available experimental data did not include a case where corrosion could have affected the shear strength. Further experimental work on girders is necessary for conclusively determining whether excessive shear strength degradation might be a concern. The angle θ_d for the inclined truss elements in the analyses of the shear-dominated girders was determined based on the experimentally observed orientation of the shear cracks. If these models are to be used in predictive simulations of prestressed girders which have not been experimentally tested, then θ_d can be set equal to the inclination angle θ of the compression field in the web of the girder, estimated through the modified compression field theory approach in the AASHTO LRFD Specification (AASHTO, 2020).

An important consideration pertaining to the analysis of box-girders is associated with the possibility of having water trapped in the section of the girder, as observed for the third specimen with a box section. To ensure conservative analytical predictions, a reduction by 15% to all strands at the bottom flange of such girders is recommended. The impact of this reduction is demonstrated in Figure 3.23, which compares the analytically obtained load-displacement curve of the specimen to the corresponding curve obtained without applying the 15% reduction to the strand area. As explained in the previous section, the specific girder incurred a significant reduction to its capacity due to corrosion damage. It can be seen that neglecting the impact of the trapped water (and the associated reduction in strand area proposed herein) would overestimate the capacity, potentially leading to unconservative results.

The capacity values obtained based on the AASHTO formulas also gave very good estimates of the corresponding experimental values, when appropriately accounting for a reduction in strand cross-sectional area based on inspection of the girder condition. Still, some caution may be necessary for the case of box-girders with significant levels of corrosion damage, as the AASHTO-based procedure may lead to unconservative capacity estimates. This was the case for the third specimen having a box-girder section in the present study. The experimental test data and modeling approaches presented in this paper can also be used to evaluate the accuracy of other simplified, design-oriented approaches to determine the capacity of prestressed girders [e.g., (Recupero et al., 2018; ACI, 2019; AASHTO, 2020; Alfailakawi et al., 2020; Al Rufaydah, 2021)].

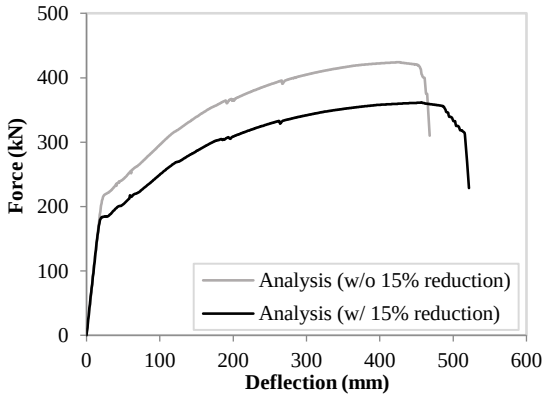

Figure 3.23. Impact of accounting for trapped water in analysis of Specimen 3 with a box-section

As a final remark, it is important to emphasize that the analyses presented in this paper were based on a number of simplifying assumptions, such as neglecting the effect of corrosion-induced bond strength deterioration. While these simplifications did not have a significant impact on the analyses pursued herein, further studies may be necessary to investigate whether and under what circumstances they may lead to significantly unconservative estimates of the capacity. Additionally, the proposed methodology to account for corrosion damage will require future enhancements to enable the accurate simulation of, e.g., girders with corrosion-affected stirrups.

3.9 Conclusions

This study employed computational simulation to quantitatively estimate the impact of corrosion on the capacity of eight experimentally tested prestressed girders having an I- or box-girder section. The analyses used two types of nonlinear models, namely, beam models with a fiber sectional law, and truss models. The latter approach was used for analyses involving shear failure. The models were combined with uniaxial stress-strain laws for the concrete and steel,

and with a procedure to account for the impact of visually observed corrosion damage on the resistance of a girder section.

The analytical models were capable of accurately reproducing the load-displacement response and failure modes for the girders. Additional analyses enabled the determination of the impact of corrosion on the flexural capacity, which was significant for several girders with visible corrosion damage. The use of the flexural strength equations in the AASHTO code generally gave satisfactory estimates of the peak capacity when accounting for corrosion section loss, but it overestimated the strength of one significantly damaged girder with a box section. An important consideration pertaining to box-girders is the possibility of having trapped water in the hollow space of the section, which may exacerbate the degradation of the strands. A conservative approach when evaluating the flexural capacity of such girders is to apply a small reduction to the area of all strands located below the level of the possibly trapped water. Corrosion damage of the longitudinal strands located at the bottom of the section was found to have minimal impact on the shear strength, but it significantly affected the deformability of a girder that failed in shear. The method will require enhancements to enable simulation of girders with corrosion damage not present in the specimens considered herein, e.g., damage in the web stirrups.

Chapter 4
Finite Element Analysis of Chloride Ingress in Prestressed Concrete Bridge Girders Accounting for Service-Life Ambient Conditions

This chapter introduces a computational simulation scheme to describe the intrusion of corrosion-inducing chloride ions in prestressed bridge girders. This phenomenon impacts the durability of bridges in coastal zones or regions where deicing salts are used. The computational study is focused on two girders, decommissioned from separate bridges in Virginia after 34 and 49 years of service. A time-dependent nonlinear finite element scheme accounting for coupled heat, moisture, and chloride transport, is formulated and used in the analyses. The model parameters are calibrated using data from material tests in the literature. Subsequently, two-dimensional analyses are conducted to determine the evolution of chloride in the cross-sections of girders. The simulations are found capable of capturing the actual chloride content at various depths from the surface, measured through titration tests. Further investigations elucidate the impact of advective transport on chloride ingress and the accuracy of simplified, design-oriented equations in the FIB code. This chapter is accepted for publication in the Journal of Structural Engineering.

Despite the significant body of existing research focused on the chloride ingress in concrete specimens, there is still a need for development of computational simulation strategies accounting for multi-dimensional chloride intrusion, and the validation of simulation tools with experimental data from actual bridge girders. The availability of simulation tools predicting the

evolution of chloride content is crucial for the maintenance and – if necessary - timely intervention to prevent extensive corrosion damage. This paper employs computational simulation to determine the extent of total chloride and the onset of corrosion in prestressed bridge girder sections. The finite element modeling approach accounts for various physical processes, namely, heat conduction, moisture movement, and chloride advective and diffusive transport. Contrary to prior studies, which have typically employed various simplifying assumptions and/or were validated with laboratory test specimens, the analysis approach described herein accounts for all important environmental factors which may affect the chloride ingress process, and is validated with measurements taken from actual bridge girders, decommissioned after decades of service.

The boundary conditions are mathematically formulated to account for heat convection, solar radiation, chemical convection, and moisture transfer across the faces of bridge girders, and use values representing the actual climatic data for a given bridge. The analysis scheme is supplemented with a necessary stabilization technique to suppress spatial instability for advective-dominated flow, and a new chloride binding isotherm is introduced for use in concrete made with ordinary Portland cement. The modeling scheme is calibrated with previous experimental tests on concrete cylindrical and prismatic specimens. Subsequently, a series of validation analyses is carried out, using data from chloride titration tests conducted on prestressed girders removed from two bridges in Virginia after 34 and 49 years of service. Further analyses explore the accuracy of the simplified, design-oriented Equation 5.1.143 of the FIB 2010 model code (FIB, 2013), for predicting the temporal evolution of chloride content in concrete bridges.

4.1 Description of the Girders

The present study is focused on two prestressed bridge girder specimens, the chloride content of which was determined through titration tests at the Thomas M. Murray Structures Laboratory of the Virginia Polytechnic Institute and State University (Alfailakawi et al., 2020). The first specimen had an I-section with a top concrete slab and was removed from the Lesner Bridge located in Virginia Beach after 49 years of service. The girder was removed from the bridge by saw-cutting the slab on either side of the I-section girder. The testing was performed two years after the bridge demolition, which corresponded to an age of 51 years. The second specimen is a girder with a box-section, removed from the Aden Road Bridge near Quantico, Virginia. The bridge was demolished after 34 years of service, and the girder was deposited at a different site. The girder had an age of 40 years during testing. The cross-sectional geometry of the two girder specimens is presented in **Figure 4.1**. The I-section girder had a concrete overlay (topping) with a thickness of 51 mm, while the box-section girder had a 38-mm thick asphalt topping, which was removed during the demolition process. Both bridges had a straight longitudinal configuration and their girders included Grade 270, stress-relieved, 7-wire strands with a nominal diameter of 11 mm (7/16 in.).

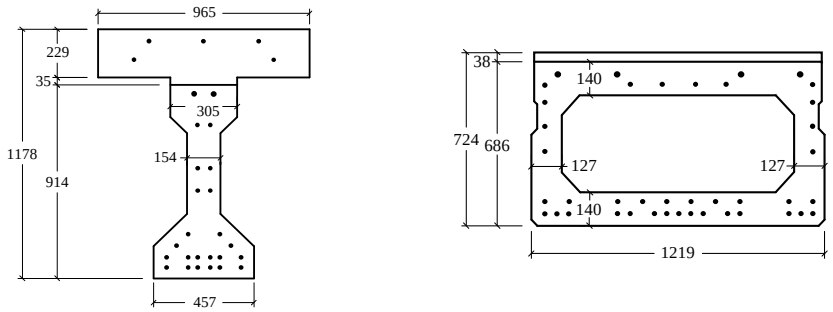

(a) I-section girder (b) Box-section girder

Figure 4.1. Cross-sectional geometry of girders (dimensions in mm)

The two tested girders exhibited significant corrosion damage, which was more pronounced for the strands located near the bottom corners of the sections. For the latter regions, extensive corrosion led to concrete cracking and even complete loss of cover. **Figure 4.2** and **Figure 4.3** present the condition of the girders near the end of service life, the extent of visually observed corrosion-induced damage and the damage maps for the cross-sections of the two girders. Subsequent removal, inspection and mechanical testing of strands removed from the two girders indicated that the bottom-most strands located away from the corners of each section were also corroded, but their damage was slight compared to the strands of the corners.

(a) Condition of the bridge near the end of service life

(b) Severe corrosion of strands near bottom corner and spalling of the concrete

(c) Severe corrosion of wires

(d) Typical estimated damage from visual inspection

Figure 4.2. Corrosion-induced damage in the I-section girder

(a) Condition of the bridge near the end of service life

(b) Severe corrosion of strands near bottom corner and spalling of the concrete

(c) Severe corrosion in bottom corner strands

(d) Typical estimated damage from visual inspection

Figure 4.3. Corrosion-induced damage in the box-section girder

4.2 Mathematical Model for Chloride Ingress

The physical system considered, schematically presented in **Figure 4.4**, involves a bridge girder mathematically described as a domain Ω and exposed to specific ambient conditions. The concrete material comprising the domain is regarded as a porous medium with a constant porosity φ. It is known that the porous network in a concrete medium, characterized by the pore morphology (porosity, shape and spatial arrangement of the pores), varies in space and time (Winslow and Liu, 1990; Kumar and Bhattacharjee, 2003; Aligizaki, 2005; Mehta and Monteiro, 2014), and is affected by the presence of aggregates and their interface with the cement paste. Still, the simplifying assumption for a spatially homogeneous, temporally constant porosity (or pore morphology) adopted in the present study, as well as neglecting the interaction between aggregate and cement paste will be shown to lead to acceptable accuracy for the analyses considered herein.

The mathematical model involves three physical processes, namely, heat transfer, moisture transport and chemical transport of chlorides. The effect of the ambient conditions on the behavior of the system is quantified through the flow of heat, moisture and chlorides across the boundary surface Γ, which depends on the ambient environment. Specifically, the heat flow across the boundary depends on the ambient temperature and solar radiation, while the flow of moisture and chlorides across the boundary is affected by the ambient relative humidity and the surface chloride content, respectively.

The following sections describe the governing differential equations, initial conditions, boundary conditions, and constitutive laws employed for the description of the heat transfer, moisture flow and chloride transport processes. The equations will involve three scalar fields, i.e., temperature T for heat transfer, relative humidity h for moisture flow and free chloride

concentration C_f for chemical transport. These fields will vary in terms of both the spatial coordinates vector, $\underset{\sim}{x}$, and time, t.

While it is known that cracking can significantly affect the moisture (Bazant et al. 1987) and chloride transport (Ishida et al. 2009), as well as the heat transfer process (Ba et al. 2016), the present study employs the simplifying assumption of neglecting the impact of cracking.

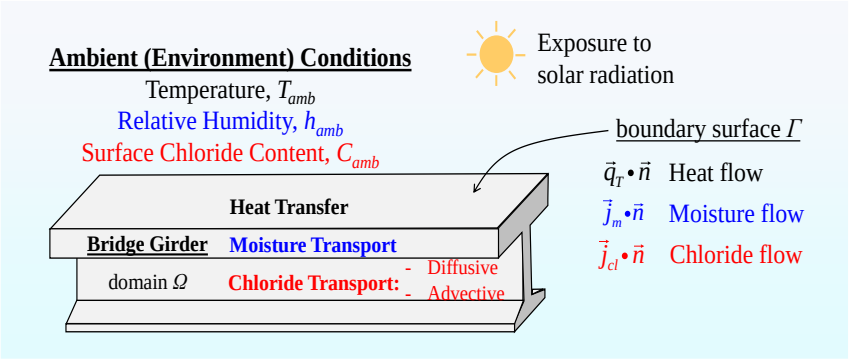

Figure 4.4. Schematic overview of problem setting

4.3 Equations for Heat Transfer

The governing differential equation for heat transfer is obtained by invoking the conservation of energy principle:

$$\frac{\partial T}{\partial t} \cdot \rho \cdot c + \vec{\nabla} \bullet \vec{q}_T = 0 \tag{4.1}$$

where T is the temperature field (K), ρ and c are the density (kg/m^3) and specific heat capacity of the material [J/(kg·K)], and $\vec{q}_T$ is the heat flux vector field (W/m^2). The present study assumes that the heat flux is entirely attributed to conduction, i.e. the presence of temperature differentials in the interior of the domain. This assumption is reflected through invoking Fourier's constitutive law, stipulating that the heat flux is given by the following expression.

$$\vec{q}_T = -k_T \vec{\nabla} T \tag{4.2}$$

where k_T is the thermal conductivity [W/(m·K)] and $\vec{\nabla}T$ is the gradient of the temperature field.

The boundary condition stipulates that the heat flow across the boundary is the sum of two contributions. The first contribution is attributed to the difference between the body surface temperature, *T*, from the ambient temperature, T_{amb}. The second contribution is due to solar radiation. The mathematical expression for the boundary condition attains the following form.

$$\vec{q}_T \bullet \vec{n} = \beta_T (T - T_{amb}) - q_s \tag{4.3}$$

where $\vec{n}$ is the unit normal outward vector, β_T is a constant surface heat transfer coefficient [W/(m^2·K)], and q_s is the added heat per unit surface and per unit time due to solar radiation. The value of q_s is obtained from the following expression (Dilger et al., 1983; Elbadry and Ghali, 1983).

$$q_s = a\, I \tag{4.4}$$

where *a* is a dimensionless surface absorptivity factor and *I* is the solar irradiance (W/m^2). The procedure employed to obtain the value of *I* is discussed in **Appendix A**.

The mathematical description of heat flow is completed by establishing an initial condition for the temperature field, i.e. prescribing the value of the temperature in the domain Ω at time $t = 0$ to equal t given field, T_0. The initial condition is mathematically expressed as:

$$T(\underset{\sim}{x}, t = 0) = T_0(\underset{\sim}{x}) \tag{4.5}$$

4.4 Equations for Moisture Transport

The moisture transport equations are meant to quantitatively describe the flow of evaporable water through the porous structure of the concrete. The governing differential equation is obtained by invoking the conservation of mass principle:

$$\frac{\partial w}{\partial t} + \vec{\nabla} \bullet \vec{j}_m = 0 \tag{4.6}$$

where w is the total moisture content [i.e. moisture mass per unit volume of concrete (kg/m^3)] and $\vec{j}_m$ denotes the moisture mass flux vector [kg/(m^2·s)]. . The moisture content w is the sum of two parts, namely, the evaporable moisture content, w_e, and the chemically bound content. The latter is the so-called interlayer water, which is trapped between the cement C-S-H layers and can significantly vary only under severe conditions, e.g., temperatures higher than 550 ℃ (Bažant and Jirásek, 2018). For this reason, the present study assumes that any change in the moisture content is entirely attributed to the evaporable moisture. The evaporable moisture content can change due to moisture flow or due to self-desiccation (internal drying) of the concrete. A number of studies (Buil, 1979; Baroghel-Bouny et al., 1999; Bažant and Jirásek, 2018) have reported that the effect of self-desiccation is insignificant after an age of 28 days. For this reason, the present paper uses the age of 28 days as the starting point of the moisture transport analysis, and neglects the impact of self-desiccation.

Given that the field variable adopted herein for the mathematical description of moisture transport is the relative humidity h, Equation (4.6) can be transformed into the following form.

$$\frac{1}{k} \cdot \frac{\partial h}{\partial t} + \vec{\nabla} \bullet \vec{j}_m = 0 \tag{4.7}$$

where $k = \partial h / \partial w_e$. A mathematical relation between w_e and h, corresponding to the so-called sorption isotherm, is established to enable the calculation of k. The shape of the isotherm depends on whether adsorption (increase in moisture content) or desorption (decrease in moisture content) is taking place (Coussy, 2011). This implies the presence of hysteretic mechanisms in the relation between moisture content and relative humidity, physically attributed to the so-called ink-bottle effect (Coussy, 2011; Bažant and Jirásek, 2018) The

present study neglects this effect, and assumes a single-valued relation for the sorption isotherm. The isotherm depends on the water/binder ratio, type of cement, and admixture (Baroghel-Bouny, 2007), and a variety of equations have been formulated and used in the literature [e.g., (Langmuir, 1918; Brunauer et al., 1938; Hansen, 1985; Künzel, 1995)]. The isotherm adopted herein relies on the work by Van Genuchten (1980), and establishes the following equation:

$$w_e = w_{e1}\left[(-b\ln h)^{1/(1-m)} + 1\right]^{-m} \tag{4.8}$$

where w_{e1} (kg/m^3) is the maximum possible value of evaporable moisture content and b, m are constant model parameters. It is worth noting at this point that the ratio of w_e over w_{e1} equals the saturation degree S_l of the liquid moisture phase in the water pores.

A phenomenological constitutive law is employed to relate the moisture flux vector, $\vec{j}_m$, and the gradient in the relative humidity:

$$\vec{j}_{\boldsymbol{m}} = -D_m \vec{\nabla} h \tag{4.9}$$

where D_m is an apparent moisture permeability [kg/(m·s)], whose value depends on the water content and the structure of the pore network (Servo and Pihlajavaara, 1969). The value of D_m depends on h in accordance with the model by Bažant and Najjar (1972):

$$D_m = c_1\left[\alpha_0 + \frac{1-\alpha_0}{1+\left[(1-h)/(1-h_c)\right]^r}\right] \tag{4.10}$$

where c_1 [kg/(m·s)] is the permeability at full saturation (i.e., at h = 1) and h_c, r and α_0 are model parameters.

The mathematical description for moisture flow is completed by the boundary and initial conditions. The former is mathematically expressed by the expression:

$$\vec{j}_m \bullet \vec{n} = \eta_e (\ln h - \ln h_{amb}) \tag{4.11}$$

where η_e is a constant moisture emissivity coefficient [kg/(m^2·s)] and h_{amb} is the ambient relative humidity (Bažant and Najjar, 1972). The initial condition for the moisture flow problem stipulates that the relative humidity at time $t = 0$ is equal to a given field, $h_0(\underset{\sim}{x})$:

$$h(\underset{\sim}{x}, t = 0) = h_0(\underset{\sim}{x}) \tag{4.12}$$

4.5 Equations for Chloride Transport

The total chloride content in the concrete is the sum of two contributions, namely, the free chloride content, corresponding to ions which can move through the porous network of the concrete, and the bound chloride content, i.e. ions which are physically or chemically bound to the concrete and cannot move. The following equation must be satisfied:

$$C_t = C_f + C_b \tag{4.13}$$

where C_t is the total chloride concentration (mol/m^3) and C_f, C_b are the concentration values for the free and bound chlorides (mol/m^3), respectively. Given the value of C_f, the corresponding total concentration value C_t can be obtained through the use of an appropriate binding isotherm. The present study proposes an isotherm for specimens made with ordinary Portland cement, which will be discussed in subsequent sections.

The differential equation for chloride transport uses the concentration C_f as the field function and is obtained from the conservation of mass principle for the chloride species.

$$\frac{\partial}{\partial t}\left(\varphi \cdot S_l \cdot C_f\right) + \vec{\nabla} \bullet \vec{j}_{cl} = 0 \tag{4.14}$$

where $\vec{j}_{cl}$ is the chloride ion mass flux in the concrete [mol/(m^2·s)]. The equations for chloride transport account for the movement of the free chloride ions in the concrete pores, which is the

combined effect of two mechanisms (Maekawa et al., 2003; Maekawa, 2008; Ishida et al., 2009). The first mechanism is diffusion, which is driven by gradients in the ion concentration in accordance with Fick's law, and the second mechanism is advective transport driven by the velocity of the moisture flow. On this basis, the chloride flux vector at each location is given from the following equation.

$$\vec{j}_{cl} = -\varphi \cdot S_l \cdot D_{cl} \cdot \vec{\nabla} C_f + \varphi \cdot S_l \cdot \vec{v} \cdot C_f \tag{4.15}$$

where $\vec{v}$ is the moisture flow velocity vector (m/s) and D_{cl} is the chloride diffusion coefficient (m^2/s). The value of D_{cl} depends on the temperature T, in accordance with the following equation which corresponds to Arrhenius law:

$$D_{cl} = D_0 \cdot \exp\left[\frac{Q_d}{R}\left(\frac{1}{T_{ref}} - \frac{1}{T}\right)\right] \tag{4.16}$$

where D_0 is a reference diffusion coefficient (m^2/s), Q_d is the activation energy (J/mol), R is the universal gas constant, equal to 8.3145 J/(mol·K), T_{ref} is a reference temperature equal to 293.15 K (20^oC) and T is the absolute temperature.

The boundary condition for chloride transport stipulates that the chloride mass flow across the boundary is proportional to the difference between the surface free chloride concentration C_f, and the ambient value of chloride concentration, C_{amb}:

$$\vec{j}_{cl} \bullet \vec{n} = \beta_{cl}(C_f - C_{amb}) \tag{4.17}$$

where β_{cl} (m/s) is a phenomenological surface chemical transport coefficient (Saetta et al., 1993). Finally, the initial value of free chloride content throughout the domain, $C_0(\underset{\sim}{x})$, is assumed to be given; thus, the initial condition equation attains the following form.

$$C(\underset{\sim}{x}, t = 0) = C_0(\underset{\sim}{x}) \tag{4.18}$$

4.6 Weak Form and Finite Element Formulation

Before introducing a finite element approximation, the governing equations for the mathematical model considered are transformed into their respective weak, i.e. variational form. This step, which has been described in previous pertinent papers and textbooks [e.g., (Donea and Huerta, 2003; Fish and Belytschko, 2007; Koutromanos, 2018)], is briefly summarized here for completeness. The weak form for heat transfer is obtained by multiplying the differential equation by an arbitrary continuous function *w* and integrating over the domain *Ω*. After a series of mathematical manipulations, described in detail in, e.g. Koutromanos(2018), the following expression is finally obtained.

$$\iiint_{\Omega} w \cdot \frac{\partial T}{\partial t} \cdot \rho \cdot c \; dV + \iiint_{\Omega} k_T \cdot \vec{\nabla} w \bullet \vec{\nabla} T \, dV = -\iint_{\Gamma} w \cdot \left[\beta_T (T - T_{amb}) - q_s \right] dS \tag{4.19}$$

The finite element formulation for heat transfer can now be obtained after discretizing the domain into multiple finite elements, and then stipulating that the temperature and temperature gradient fields are obtained from the following approximations.

$$T \approx [N] \left\{ T^{(e)} \right\} \tag{4.20}$$

$$\nabla T \approx [B] \left\{ T^{(e)} \right\} \tag{4.21}$$

where $\left\{ T^{(e)} \right\}$ is the nodal temperature vector for element '*e*', [*N*] is the polynomial interpolation (shape) function array, and [*B*] is an array containing the derivatives of the interpolation functions with respect to the spatial coordinates, as explained in more detail in Koutromanos (2018).

Using the same type of approximation for the arbitrary function *w* and its gradient in equation (4.19) ultimately leads to the following global, semi-discrete equations for the heat transfer problem.

$$[C_T]\{\dot{T}\} + [K_T]\{T\} = \{F_T\} \tag{4.22}$$

where $\{T\}$ is the nodal temperature vector for the entire finite element mesh, and $\{\dot{T}\} = \partial\{T\}/\partial t$. The arrays $[C_T]$, $[K_T]$ and the vector $\{F_T\}$ can be obtained through an assembly of the corresponding contributions $\left[C_T^{(e)}\right]$, $\left[K_T^{(e)}\right]$ and $\left\{F_T^{(e)}\right\}$ of the individual finite elements. The element contributions can be shown to be obtained from the following expressions (Koutromanos, 2018).

$$\left[C_T^{(e)}\right] = \iiint_{\Omega^{(e)}} [N]^{\mathrm{T}} \rho c [N] dV \tag{4.23}$$

$$\left[K_T^{(e)}\right] = \iiint_{\Omega^{(e)}} [B]^T k_T [B] dV + \iint_{\Gamma^{(e)}} [N]^T \beta_T [N] dS \tag{4.24}$$

$$\left\{F_T^{(e)}\right\} = \iint_{\Gamma^{(e)}} [N]^T \left(\beta_T T_{amb} + q_s\right) dS \tag{4.25}$$

where $\Omega^{(e)}$ and $\Gamma^{(e)}$ denote the part of the domain and boundary, respectively, belonging to element '*e*'.

The same procedure is followed for the moisture transport problem, yielding the weak form:

$$\iiint_{\Omega} w \cdot \frac{1}{k} \cdot \frac{\partial h}{\partial t} dV + \iiint_{\Omega} D_m \cdot \vec{\nabla} w \bullet \vec{\nabla} h \, dV = -\iint_{\Gamma} w \cdot \eta_e (\ln h - \ln h_{amb}) \, dS \tag{4.26}$$

The global semi-discrete equation for the moisture transport is:

$$[C_m]\{\dot{h}\} + [K_m]\{h\} = \{F_m\} \tag{4.27}$$

where $\{h\}$ is the nodal relative humidity vector for the finite element mesh, $\dot{h} = \partial\{h\}/\partial t$, and arrays $[C_m]$, $[K_m]$ and $\{F_m\}$ are obtained from the assembly of the corresponding element contributions $\left[C_m^{(e)}\right]$, $\left[K_m^{(e)}\right]$ and $\left\{F_m^{(e)}\right\}$:

$$\left[C_m^{(e)}\right] = \iiint_{\Omega^{(e)}} [N]^{\mathrm{T}} \frac{1}{k} [N] dV \tag{4.28}$$

$$\left[K_m^{(e)}\right] = \iiint_{\Omega^{(e)}} [B]^{\mathrm{T}} D_m [B] dV \tag{4.29}$$

and

$$\left\{F_m^{(e)}\right\} = -\iint_{\Gamma^{(e)}} [N]^{\mathrm{T}} \eta_e (\ln h - \ln h_{amb})\, dS \tag{4.30}$$

It is worth noting that equations have a nonlinear dependence on the nodal vector $\{h\}$.

The weak form for chloride transport can be developed by similar considerations as for the other problems. In the context of this study, the moisture flow is treated as incompressible, which in turn implies that the divergence of the moisture flow velocity vanishes, i.e. $\vec{\nabla} \bullet \vec{v} = 0$. After a series of mathematical manipulations, the following expression is obtained.

$$\begin{aligned} &\iiint_{\Omega} w \cdot \frac{\partial}{\partial t}(\varphi \cdot S_l \cdot C_f)\, dV + \iiint_{\Omega} \varphi \cdot S_l \cdot D_{cl} \cdot \vec{\nabla} w \bullet \vec{\nabla} C_f \, dV + \iiint_{\Omega} w \cdot \varphi \cdot S_l \cdot \vec{v} \bullet \vec{\nabla} C_f \, dV \\ &\quad = -\iint_{\Gamma} w \cdot [\beta_{cl}(C_f - C_{amb})]\, dS \end{aligned} \tag{4.31}$$

The third term on the left-hand side of Equation (31) is non-symmetric in terms of differentiation of w and C_f. As described in the following section, the non-symmetric term entails the need for the implementation and use of special numerical strategies (Donea and Huerta, 2003; Fish and Belytschko, 2007) to ensure accurate computational simulations.

The semi-discrete, finite element equation for chloride transport is:

$$[C_{cl}]\{\dot{C}_f\}+[K_{cl}]\{C_f\}=\{F_{cl}\} \tag{4.32}$$

where $\{C_f\}$ is the nodal free chloride concentration vector for the entire finite element mesh, $\dot{C}_f=\partial\{C_f\}/\partial t$, and arrays $[C_{cl}]$, $[K_{cl}]$ and $\{F_{cl}\}$ are obtained through the corresponding element contributions $\left[C_{cl}^{(e)}\right]$, $\left[K_{cl}^{(e)}\right]$ and $\left\{F_{cl}^{(e)}\right\}$:

$$\left[C_{cl}^{(e)}\right]=\iiint_{\Omega^{(e)}}[N]^T\,\varphi\,S_l\,[N]\,dV \tag{4.33}$$

$$\left[K_{cl}^{(e)}\right]=\iiint_{\Omega^{(e)}}[B]^T\,\varphi\,S_l\,D_{cl}\,[B]\,dV+\iiint_{\Omega^{(e)}}[N]^T\,\varphi S_l\,\{v\}^T\,[B]\,dV+\iint_{\Gamma^{(e)}}[N]^T\,\beta_{cl}\,[N]\,dS \tag{4.34}$$

and

$$\left\{F_{cl}^{(e)}\right\}=\iint_{\Gamma^{(e)}}[N]^T\,\beta_{cl}C_{amb}\,dS \tag{4.35}$$

4.7 Numerical Solution Scheme

This section describes the numerical analysis scheme, which has been implemented in the finite element program *FE-MultiPhys* (Koutromanos and Farhadi, 2018). The analysis involves the solution of Equations (4.22), (4.27) and (4.32), which can all be cast in the following, generic form:

$$[C]\{\dot{X}(t)\}+[K]\{X(t)\}=\{F(t)\} \tag{4.36}$$

where $\{X\}$ is the nodal value vector (temperature for heat transfer, relative humidity for moisture flow, and free chloride concentration for chloride transport). Equation (4.36) involves continuous functions of time, and it can be numerically solved using any time marching scheme algorithm, to provide the solution vector $\{X\}$ at a set of distinct time instants. The present study adopts an implicit Backward Euler scheme for time-marching. As mentioned above, the

moisture transport equations are nonlinear. This happens because the coefficient arrays [C], [K] and the right-hand-side vector {F} depend on the nodal vector {X}. A Newton-Raphson iterative algorithm is employed to satisfy the nonlinear equations for moisture flow.

Special consideration is necessary for the finite element solution of the chloride transport process, due to the presence of the advective term, i.e. the non-symmetric term of the weak form given by equation (4.32). It is well-established in the literature [e.g., (Donea and Huerta, 2003)] that the use of a standard finite element approximation is problematic for cases where advective transport is more pronounced than diffusive transport, as it may lead to a spatial instability of the numerical solution. The instability is manifested as a noise in the spatial distribution of the approximate field. To address this challenge, the analysis scheme for chloride transport employs a Streamline-Upwind Petrov-Galerkin (SUPG) stabilization approach (Donea and Huerta, 2003). The SUPG technique involves the introduction of an extra stabilizing term to the weak form and the corresponding finite element equations to suppress the propensity for spatial instabilities, as discussed in **Appendix B**.

4.8 Model Calibration and Preliminary Analyses

This section presents the calibration of the model parameters corresponding to heat transfer, moisture flow and chloride transport. Additionally, the results of analyses demonstrating the significance of accounting for the effect of advection on chloride transport in concrete are presented. The calibration relies on data from experimental tests in the literature, which used specimens with concrete properties close to those of the bridge girders, i.e., normal-strength concrete with ordinary Portland cement without additives and a water-to-cement ratio close to 0.5.

4.8.1 Calibration of the Heat Transfer Parameters

The model parameters corresponding to heat transfer are calibrated based on pertinent studies in the literature (Hansen and Saouma, 1999a; Samson and Marchand, 2007; Lee et al., 2009; Yun et al., 2013; Bažant and Jirásek, 2018). The present work adopts the value of $k_T = 2.5\,\mathrm{W/(m\cdot K)}$ for the thermal conductivity, and a heat capacity of $c = 1000\,\mathrm{J/(kg\cdot K)}$ for concrete. The concrete density ρ is set equal to 2400 kg/m^3. The heat transfer coefficient β_T for the boundary is set equal to 20W/(m^2·K), in accordance with recommendations by Elbadry and Ghali (1983).

4.8.2 Calibration of the Moisture Transport Parameters

The moisture model parameters are calibrated using the experimental data reported by Hanson (Hanson, 1968) for a normal-strength concrete specimen which had been cured for 28 days in water, and was subsequently exposed to an environmental relative humidity h = 0.50. The cylindrical specimen was sealed at the top and bottom faces to only allow moisture outflow in the radial direction of the cylinder cross-sectional plane. **Figure 4.5** shows that the analytically obtained evolution of relative humidity at various depths from the surface of the specimen closely matches the corresponding experimental observations. The analysis used the values $c_1 = 1.96\times10^{-8}\,\mathrm{kg/(m\cdot s)}$, $h_c = 0.69$, $r = 6.00$ and $a_0 = 0.01$ for the parameters affecting the apparent diffusion coefficient (Equation 10). The sorption isotherm parameters (Equation 8) were assigned the values w_{e1} = 97.3 kg/m^3, b = 3.10, m = 0.48, which can accurately reproduce the relation between relative humidity and moisture content measured by Baroghel-Bouny (2007) for scenarios involving monotonic drying, i.e. desorption, as shown in **Figure 4.6**a. It is important to note that Baroghel-Bouny (2007) also conducted experimental tests for

monotonic wetting, and a different calibration of the sorption isotherm would be required to match these experimental results. Specifically, as shown in **Figure 4.6**b, the parameters of Equation 8 were assigned the values w_{e1} = 90.2 kg/m^3, b = 17.00, m = 0.34 to match the data for monotonic wetting. The different calibration required for monotonic drying and wetting scenarios is due to the effect of hysteretic mechanisms in the relation between moisture content and relative humidity, i.e. the ink-bottle effect, as mentioned in the section describing the moisture transport equations. The ink-bottle effect has a thermodynamically metastable character (Baroghel-Bouny, 2007). This implies that the extent of hysteresis gradually diminishes with the application of multiple wetting-drying cycles and asymptotically tends to zero (Baroghel-Bouny, 2007). Consequently, the sorption isotherm under multiple wetting/drying cycles tends to become identical to the adsorption isotherm (i.e., the curve shown in **Figure 4.6**b). The remainder of the analyses in the present study involving moisture transport, including the analyses of the bridge girders, are focused on scenarios with very large number of wetting/drying cycles. For this reason, all these analyses use the calibration of the sorption isotherm with parameters corresponding to monotonic wetting.

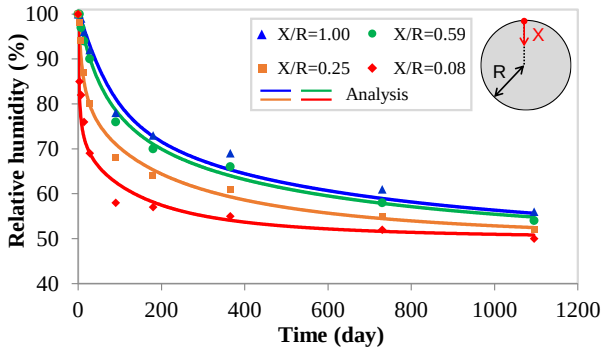

Figure 4.5. Results of calibration analysis for moisture transport using the experimental data in Hanson (1968)

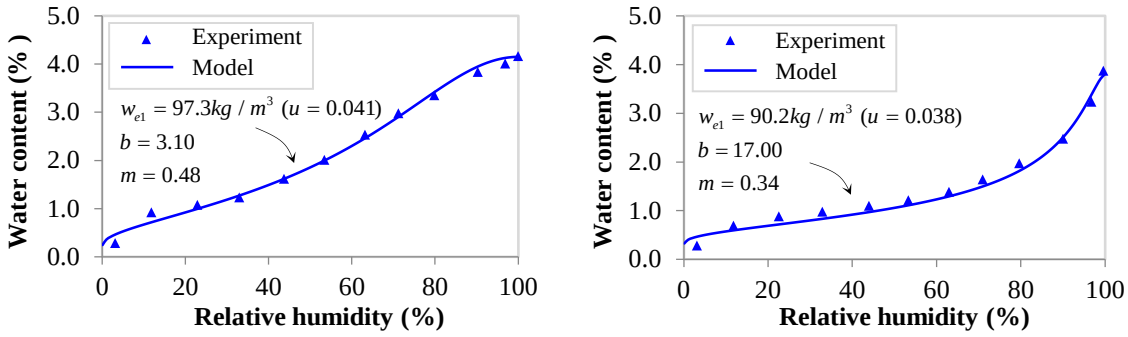

a) Drying (desorption) b) Wetting (adsorption)

Figure 4.6. Calibration of sorption isotherm parameters for experimental tests by Baroghel-Bouny (2007)

4.8.3 Calibration of the Chemical Transport Parameters

The analysis of chloride transport requires the formulation and calibration of a binding isotherm, giving the relation between the free chloride concentration, C_f (obtained from the finite element computation) and the corresponding bound chloride content concentration, C_b. The latter value must be calculated, as the propensity for corrosion of the steel is affected by the total chloride concentration C_t, given by Equation (4.13). Based on pertinent experimental data from the literature (Sergi et al., 1992; Maruya, 1995; Maruya et al., 1998; Samson and Marchand, 2007; Maekawa, 2008; Baroghel-Bouny et al., 2009; Baroghel-Bouny et al., 2014), this paper uses the following mathematical expression for the isotherm.

$$C_{b(m)} = 1.5\left(C_{f(m)}\right)^{0.7} \tag{4.37}$$

where $C_{f(m)}$ and $C_{b(m)}$ are the concentrations of free and bound chlorides, respectively, expressed as percentages of the cement mass.

The binding isotherm and chemical diffusivity parameter D_o for chloride transport have been calibrated with experimental data from (Sergi et al., 1992; Maruya, 1995; Maruya et al., 1998; Maekawa, 2008; Baroghel-Bouny et al., 2009; Baroghel-Bouny et al., 2014; Gang et al.,

2015), shown in **Figure 4.7** and **Figure 4.8** and pertaining to distributions of free and total chloride concentrations with depth in concrete and cement paste specimens. The calibration analyses yield a value $D_0 = 6.0 \times 10^{-12}$ m^2/s for concrete specimens. The calibrated parameters of chloride transport can accurately reproduce the free and total chloride distributions obtained in the various tests, as deduced from **Figure 4.7** and **Figure 4.8**, respectively.

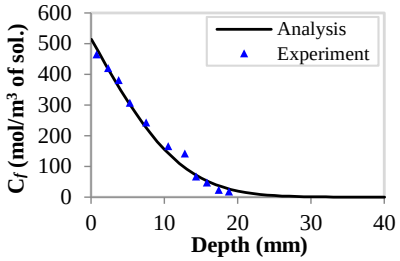

(a) Specimen from (Baroghel-Bouny et al., 2009; Baroghel-Bouny et al., 2014)

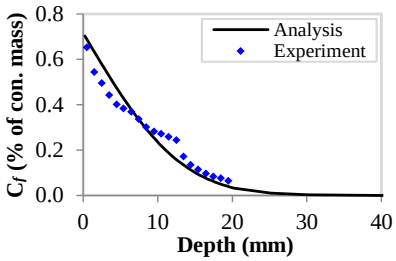

(b) Specimen from (Gang et al., 2015)

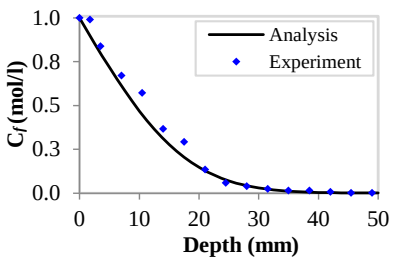

(c) Specimen from (Sergi et al., 1992)

Figure 4.7. Distributions of free chloride with depth obtained from calibration analyses

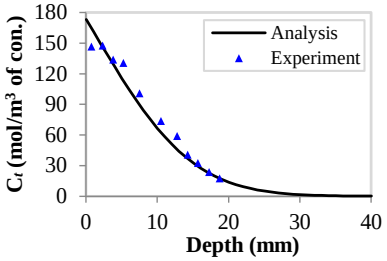

(a) Specimen from (Baroghel-Bouny et al., 2009; Baroghel-Bouny et al., 2014)

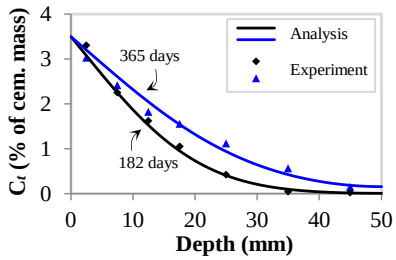

(b) Specimens from (Maruya, 1995; Maekawa, 2008)

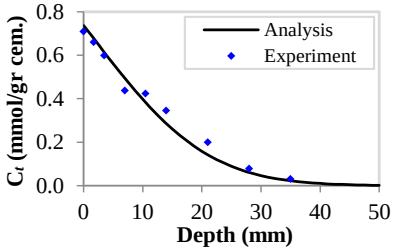

(c) Specimen from (Sergi et al., 1992)

Figure 4.8. Distributions of total chloride with depth obtained from calibration analyses

It is important to mention that the experimental tests in (Sergi et al., 1992; Maruya et al., 1998; Baroghel-Bouny et al., 2009; Baroghel-Bouny et al., 2014; Gang et al., 2015) were conducted for specimens having an age of approximately 90 days. This age is significantly less than the service life of each girder. It is known (Conjeaud, 1980; Buenfeld and Newman, 1987;

Mangat and Molloy, 1994; Martın-Pérez et al., 2001; Shafei et al., 2012; Lu et al., 2015) that the value of the chloride diffusion coefficient may be significantly reduced over time. To account for this effect in the analysis of the girders, the value of D_o obtained from the calibration analyses is multiplied by the reduction factor $(90/t_{age})^{0.47}$, where t_{age} is a representative age value for each bridge, set equal to 10950 days (i.e. 30 years) in the present study. The use of the specific expression for the reduction factor and the adopted value of t_{age} are based on recommendations and findings by previous, pertinent studies (Mangat and Molloy, 1994; Martın-Pérez et al., 2001; Shafei et al., 2012; Lu et al., 2015; Kim et al., 2016).

The parameter Q_d controlling the temperature effect on chloride diffusivity per Equation (16) is calibrated using experimental test data by Samson and Marchand (2007) on cement paste specimens and by Chen and Razaqpur (2021a, 2021b) on cylindrical concrete specimens subjected to various temperature values. Specifically, Q_d is set equal to 22 kJ/(mol·K) and 35 kJ/(mol·K) for cement paste and concrete, respectively. The analytically obtained distributions of chloride content with depth at specific instants of the tests are compared to the corresponding experimental measurements in **Figure 4.9**a and **Figure 4.9**b, for the cement paste and concrete specimens, respectively. Overall, the analyses satisfactorily match the experimental observations. The most significant discrepancy is obtained for the concrete specimen tested at a temperature of -15^{o}C. This observation is aligned with the claim made in previous studies (Samson and Marchand, 2007; Chen and Razaqpur, 2021a) that the validity of Arrhenius law is questionable for temperatures significantly lower than the so-called supercooling temperature of -7^{o}C. Given that the temperature values of interest for the present study are not significantly lower than the supercooling temperature, the presence of such discrepancy is not a concern.

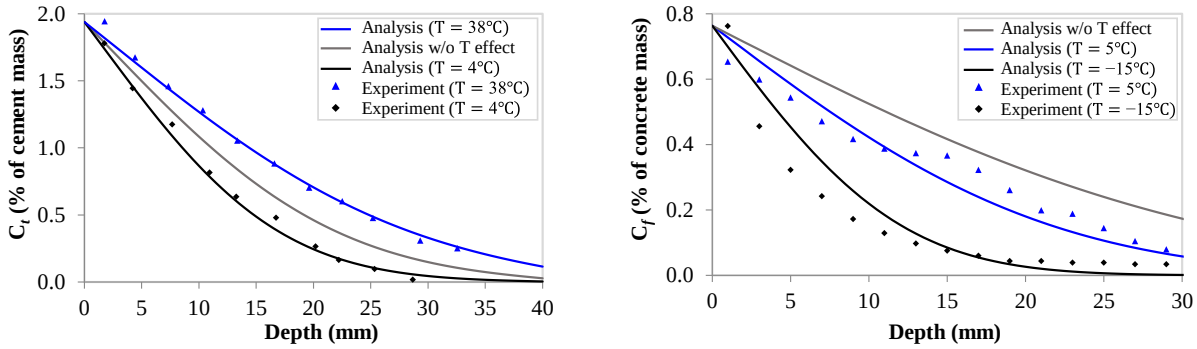

(a) Cement Paste Specimens (b) Concrete Specimens

Figure 4.9. Calibration analyses for impact of temperature on chloride diffusion

4.9 Analyses on Impact of Advection on Chloride Transport

This section demonstrates the significance of the effect of advection on the chloride transport process. To this end, a series of analyses are conducted for experimental tests in the literature involving chloride ingress in concrete prisms under simultaneous application of cyclic wetting and drying. The analyses of this section employed the same calibration for the moisture transport parameters, except for the sorption isotherm. Given that the experiments considered herein involved cyclic wetting-drying (and not monotonic drying, as was the case in the analysis of Section 5.2), the parameters for the isotherm were assigned the values w_{e1} = 90.2 kg/m^3, b = 17.00, m = 0.34. The specific values, which are accurate for monotonic wetting (i.e. adsorption) according to Baroghel-Bouny (2007), were found to give more accurate results for the analyses of this section. The same values are adopted for the isotherm parameters in the analyses of the actual girders (described in the following section), as the specific analyses also involve wetting-drying cycles.

The first analysis is conducted for the experiment of Maruya et al. (1998), focused on concrete prisms made with ordinary Portland cement and subjected to 42 wetting-drying cycles under a constant temperature of 20°C. The drying condition corresponded to an ambient relative

humidity of 60%, and the duration of each cycle was 14 days. The analysis for the specific specimen is conducted twice, i.e. with and without the effect of moisture-induced advective transport. The analysis including the advective transport effect gives time histories of chloride content at various depths which agree with the experimental measurements, as shown in **Figure 4.10**(a). Neglecting the effect of advection leads to significant discrepancy between the analytical results and experimental data, as deduced from **Figure 4.10**(b). Similar observations are reached for the analyses of the tests by Gang et al. (2015) and Lu et al. (2015). The former tests involved a total of 50 wetting-drying cycles under a drying relative humidity of 75% and a temperature of 20°C, and the latter included 15 cycles with a drying relative humidity of 76% and a temperature of 16.3°C. As shown in **Figure 4.11**a and **Figure 4.11**b, which compare the analytical and experimental distributions of chloride content with depth at the end of each test, including the effect of advective transport is necessary for obtaining accurate results.

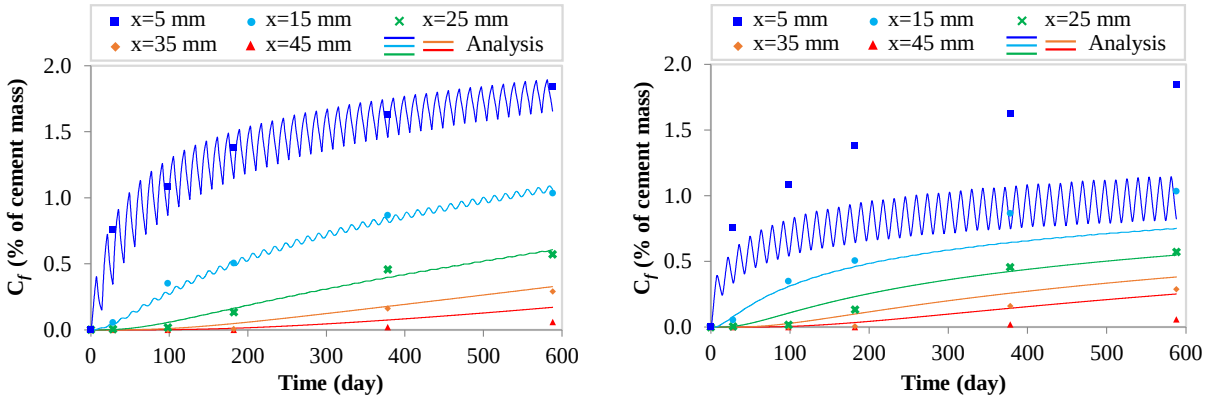

(a) Results for analysis with advective term (b) Results for analysis without advective term

Figure 4.10. Time-evolution of free chloride under different modeling schemes

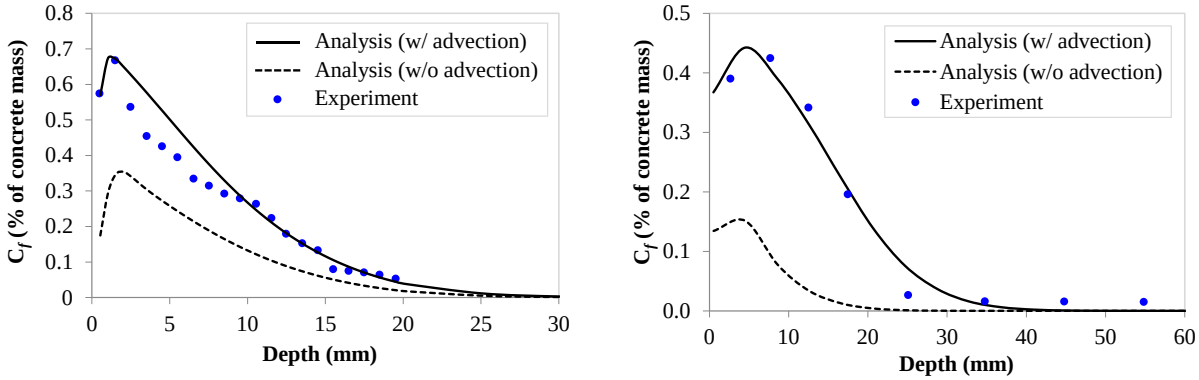

(a) Test by Gang et al. (2015) (b) Test by Lu et al. (2015)

Figure 4.11. Impact of advection on the analytically obtained chloride distribution with depth for experimental test specimens presented in the literature

4.10 Analysis of the Bridge Girders

This section describes the finite element analyses of the two girder specimens using the calibrated modeling scheme. Each analysis employs a two-dimensional mesh of the corresponding girder cross-section. The procedure to establish the ambient conditions in the model of each girder is presented first, followed with a discussion of the analysis results.

4.10.1 Determination of Ambient Conditions

The boundary conditions for the mathematical problems at hand require knowledge of the ambient temperature, T_{amb}, relative humidity, h_{amb}, and chloride content, C_{amb}. The heat flow across the boundary of each girder is also affected by solar radiation, which is assumed to affect the top surface of each girder. The determination of the ambient conditions over the service life of each bridge relied on first estimating representative annual histories of ambient conditions (i.e., each history having a 1-year duration) and then repeating the same histories for each additional year of service life.

The annual variation of ambient temperature and relative humidity were determined based on recorded data for the year 2010, retrieved from meteorological stations in the vicinity of the two bridges. The temperature and relative humidity data for the Lesner bridge are presented in **Figure 4.12**a and **Figure 4.12**b, respectively, while the corresponding data for the Aden Road bridge are shown in **Figure 4.12**c and **Figure 4.12**d. It is worth noting that the shape of the annual evolution of the relative humidity for the two bridges differs from the commonly adopted functional relation in the literature, corresponding to a sinusoidal function [e.g., (Saetta et al., 1993; Shafei et al., 2012)]. The data presented in **Figure 4.12** corresponds to a sampling interval of 1 hour. This same value was used as the solution time-step for the finite element analyses of the two bridges. The calibration of the model parameters associated with solar radiation on the top surface of each girder is presented in **Appendix A**.

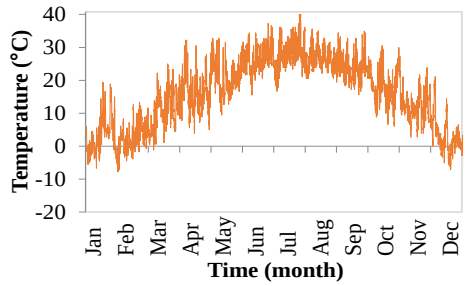

(a) Temperature for I-section girder

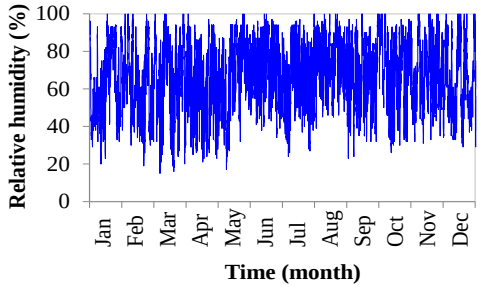

(b) Relative humidity for I-section girder

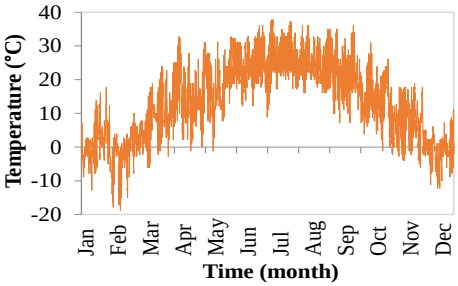

(c) Temperature for box-section girder

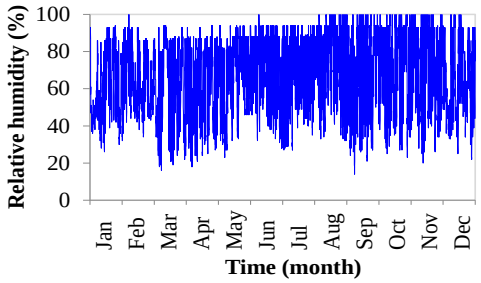

(d) Relative humidity for box-section girder

Figure 4.12. Representative annual variation of temperature and relative humidity used for the analysis of the two girders.

Establishing the ambient chloride value, C_{amb}, is a challenging task. A number of studies in the literature (Weyers et al., 1994; McGee, 1999; Val, 2007) proposed values for the surface chloride content, based on statistical processing of concrete samples collected from actual bridges. The value of C_{amb} depends on the particular location of a bridge. For the Lesner bridge, which was located in a coastal region, the ambient chloride is primarily attributed to sea spray aerosols which carry sea salt particles to the surface of the girder. The analysis uses $C_{amb} = 1.74\,\mathrm{kg/m^3}$, based on the recommendations by McGee (1999) for coastal bridges. The exposure to the ambient chloride content was assumed to apply for all exposed faces of the girder section shown in **Figure 4.1**a, apart from the left and right sides of the slab which were saw-cut during removal of the girder from the bridge. The specific sides were treated as impervious boundaries, i.e. boundaries which do not allow any flow of moisture or chloride, as they were not exposed to the ambient environment during the service life of the bridge. The Aden Road bridge was located away from the coast; for this reason, the chloride ingress was primarily attributed to the use of deicing salts. The value of ambient chloride assumed herein is $C_{amb} = 1.06\,\mathrm{kg/m^3}$, based on the average surface chloride content values reported by Weyers et al. (1994). A field inspection of the bridge during its service life had revealed that grouted shear keys between adjacent box girders had been damaged due to applied loads during the bridge service life. Thus, during application of deicing salts, saltwater would leak through the damaged shear keys, also running along the bottom of the box beam. To indirectly account for this effect, the exposure to the ambient chloride was assumed to apply for all boundary faces of the girder.

As mentioned above, the girders from the Lesner and Aden Road bridges had been in service for 49 and 34 years, respectively, and after this point they were removed from the

bridges and stored for 2 and 6 years, respectively, before the actual chloride content was experimentally measured. To account for this effect in the analyses, the exposure to the ambient chloride content was enforced during the service life of each bridge, and a zero value of C_{amb} was enforced for the part of the analysis corresponding to the storage of each girder away from the bridge. The ambient temperature and relative humidity conditions for the storage stage were assumed to be identical to those of the service life of each bridge.

An additional complication for the analysis of the girder from the Aden Road bridge pertains to the presence of an asphalt overlay at the top surface of the girder during the service life, and the subsequent removal of this layer before the girder was stored away from the bridge. For simplicity, the elements in the asphalt layer have used the same values in the constitutive laws for the various physical processes as those adopted for the concrete. The removal of the asphalt layer is also accounted for in the analysis, through the deletion of the elements in the mesh corresponding to the asphalt layer at an age of 34 years. The top surface of the concrete girder during the storage was assumed to constitute an impervious boundary due to the demolition, for the portion of the analysis corresponding to the storage of the girder before testing.

4.10.2 Analysis Results

The analytically obtained distributions of chloride content with depth from the surface, obtained on the inclined and vertical lateral faces of the girder from Lesner bridge, are compared to the corresponding experimental measurements in **Figure 4.13**a and **Figure 4.13**b, respectively. The specific figures also include the distributions corresponding to the end of the girder service life. It can be seen that the analysis can well reproduce the corresponding experimental measurements. The 2-year storage of the girder after its service life, during which

time there was no exposure to chloride spray on the surface, leads to a significant reduction in the chloride content at very low depths from the surface, as deduced from a comparison of the chloride content curves at the end of service life to the curves obtained on test day. The contour plots of distributions of chloride content over the cross-section at the end of service life and on testing day are provided in **Figure 4.13**c and **Figure 4.13**d, respectively. The specific plots also indicate that the chloride content near the surface was much higher at the end of service life than during testing. An additional important remark pertains to the fact that the chloride content in the vicinity of the bottom corners is higher than the corresponding values away from the bottom corner regions. Similar observations are obtained from the analysis of the girder from Aden Road bridge. **Figure 4.14**a and **Figure 4.14**b provide the chloride distributions with depth from the lateral and top faces of the section, respectively. Once again, the analysis can well reproduce the experimentally measured chloride content distributions.

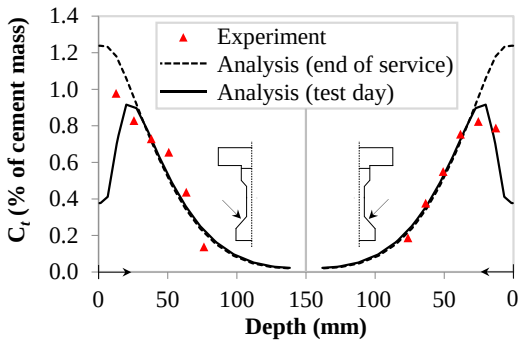

(a) Distribution with depth (inclined face)

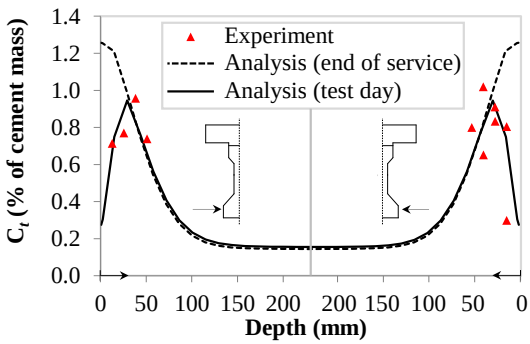

(b) Distribution with depth (vertical face)

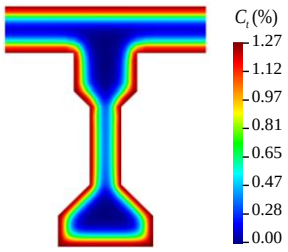

(c) Distribution over cross-section at end of girder service life

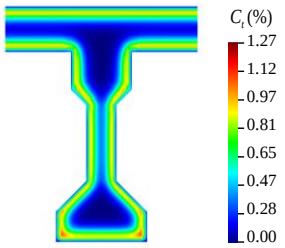

(d) Distribution over cross-section on test day

Figure 4.13. Chloride content obtained for analysis of I-section girder

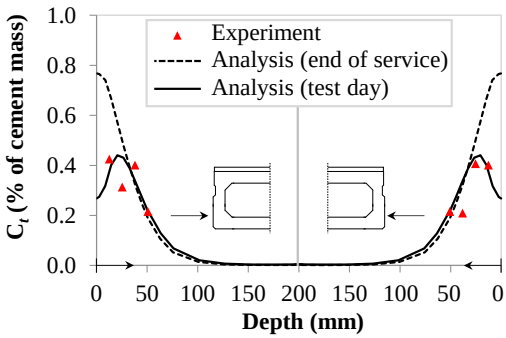

(a) Distribution with depth (vertical face)

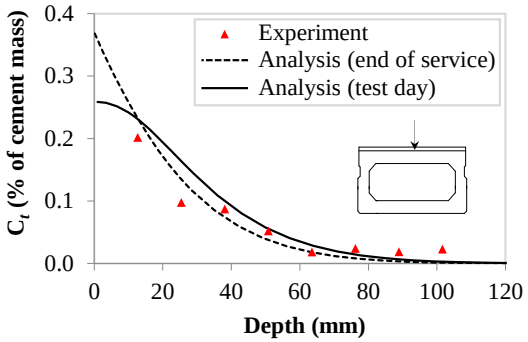

(b) Distribution with depth in concrete (top face)

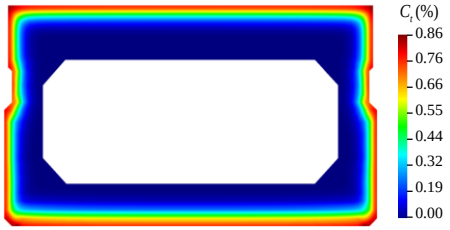

(c) Distribution over cross-section at end of girder service life

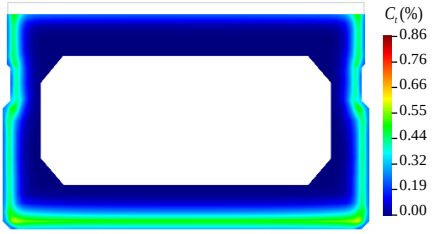

(d) Distribution over cross-section on test day

Figure 4.14. Chloride content obtained for analysis of box-section girder

Another aspect of the simulations that is worthy of consideration pertains to results of the heat transfer analysis. It is well-established that bridge structures are subjected to temperature gradients along the sectional depth, due to the fact that the top face of each girder is exposed to additional heat input due to solar radiation, while the bottom face is in the shade. **Figure 4.15**(a) provides the annual variation of temperature difference between the top and bottom face of the I-section girder. The temperature histories of the top and bottom faces of the girder, recorded over a five-day period during the summer and winter, are provided in **Figure 4.15**(b). The average value for the maximum daily temperature difference during the winter, spring and summer is equal to 5^{o}C, 9^{o}C and 12^{o}C, respectively, which are in close agreement with actual bridge data (Elbadry and Ghali, 1983; Okeil, 2014; Elshoura and Okeil, 2022).

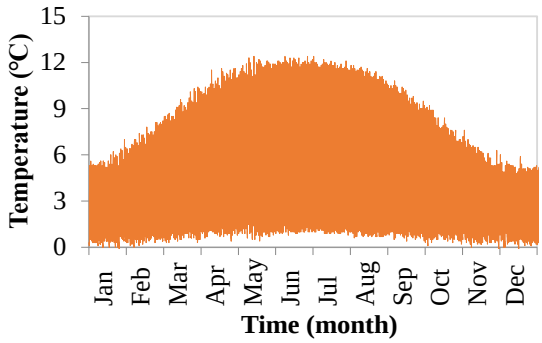

(a) Annual variation

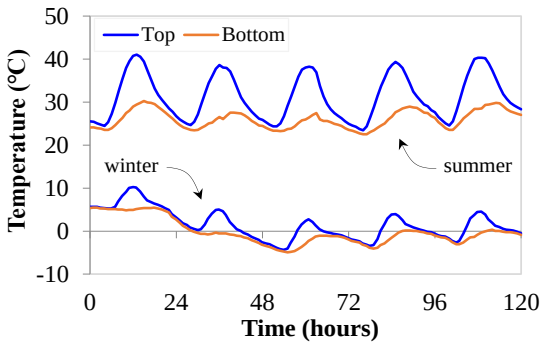

(b) Typical variation for a 5-day interval in the summer and winter

Figure 4.15. Analytically obtained histories of temperature difference between top and bottom faces of the I-section girder.

4.10.3 Estimation of Corrosion Initiation Time and Comparison with Simplified Equations

The analytical results for the two girders can be used to estimate the corrosion initiation time and progress for the outermost prestressing strands in the sections of the two girders. This task requires the comparison of the analytically obtained chloride content at the location of the strands to an estimated critical chloride content, C_{crit}, defined as the value which is expected to lead to breaking down of the passive film around the strands and the initiation of the corrosion electrochemical process. For the Lesner bridge, this study uses a critical chloride content value C_{crit} = 0.6% (normalized with respect to the cement mass), based on recommendations provided in the FIB code (Schießl et al., 2006). The critical chloride content for structures exposed to deicing salts must be assigned a lower value (Vassie, 1984). For this reason, the value of C_{crit} adopted for the Aden Road bridge is equal to 0.3% (normalized with respect to the cement mass), which is the average obtained from a number of references in the literature (Page and Vennesland, 1983; Vassie, 1984; Henriksen and Stoltzner, 1993; Standard, 1997; Oh et al., 2004; Schießl et al., 2006; Kim et al., 2016).

Another point which is worthy of investigation pertains to the accuracy of simplified procedures to determine the evolution of the chloride content during the service life of concrete bridges. To this end, the time evolution of total chloride obtained from the finite element analyses is compared to the corresponding values calculated using the design-oriented equation of the FIB code (Schießl et al., 2006). The specific equation has been obtained by considering the solution of a time-dependent, one-dimensional diffusion problem.

Figure 4.16a and **Figure 4.16**b compare the results obtained with the finite element analyses and the equations of the FIB code, for the girders taken from the Lesner and Aden Road bridge, respectively. The comparison is conducted in terms of the chloride content time histories at the location of the outermost strands for the section of each girder. Two different time histories are provided for the finite element analyses, i.e. one for a strand located in the corner of the section and another one for a strand located away from the corner of the section. For the Lesner bridge, the chloride content at the end of service life for the strands near the corner region was 32% higher than away from the corner. The corresponding value for the Aden Road bridge was 43%. It can also be seen in **Figure 4.16**a and **Figure 4.16**b that the approach of the FIB code systematically underestimates the chloride content obtained by the finite element analysis. The values of chloride concentration obtained by the FIB model at the end of service life for the Lesner and Aden Road bridge are 34% lower and 12% lower, respectively, for the regions away from the sectional corners. The underestimation is much more pronounced near the sectional corners, for which the validity of the assumption for one-dimensional chloride transport (on which the equations of the FIB code rely) breaks down. In these regions, the values obtained by the FIB code approach at the end of service life for the Lesner and Aden Road

bridge are 50% lower and 38% lower, respectively, than the corresponding values obtained from the finite element models.

The plots in **Figure 4.16**a and **Figure 4.16**b also identify the value of critical chloride content, C_{crit}, for each one of the two girders. The finite element analysis results indicate that corrosion would be expected to have taken place during the service life of the two bridges. Additionally, the chloride content at the corners of the section for each girder reaches the C_{crit} value much earlier than away from the section corners, i.e. at an age of 13 years for the Lesner bridge and 12 years for the Aden Road bridge. These results indicate that the extent of corrosion would be expected to be more pronounced near the corners of the section for the two girders, which was indeed the case as deduced from **Figure 4.2**(c) and **Figure 4.3**(c). Assuming that corrosion takes place at a constant rate after the critical chloride content is exceeded in the vicinity of a strand, the Lesner bridge strands near and away from the sectional corners have been subjected to corrosion for a period of 30 and 17 years, respectively. The corresponding corrosion process time estimated for the Aden Road bridge is 17 years for the strands near the corner and 5 years for strands away from the corner. For the specific values of C_{crit} adopted in the simulations of the two girders, the use of the method in the FIB code would not predict any corrosion propensity for the Lesner bridge, while it would predict initiation of corrosion for the Aden Road bridge, but at a much later time than that obtained with the finite element scheme proposed herein.

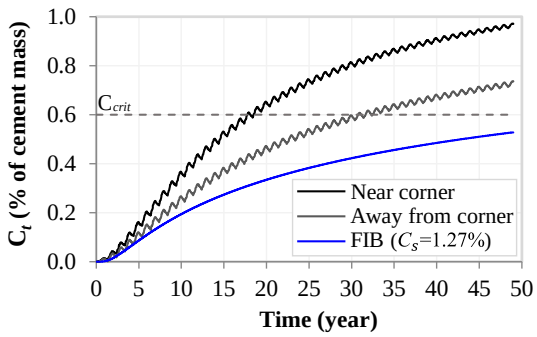

(a) I-section girder (Lesner bridge)

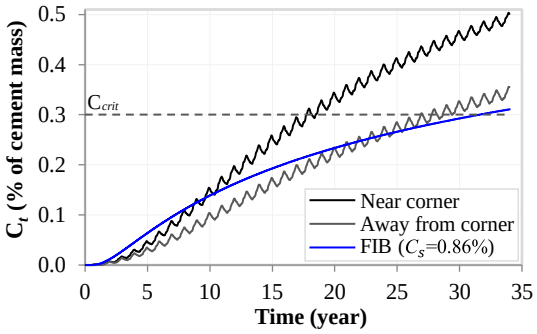

(b) Box-section girder (Aden Road bridge)

Figure 4.16. Comparison of analytically obtained chloride content evolution to estimated critical values corresponding to corrosion initiation and to results obtained with the simplified approach in the FIB code (FIB 2013)

4.11 Discussion

The calibrated modeling approach presented in the previous sections was found capable of capturing the experimentally measured chloride content for the two bridge specimens. As mentioned above, the calibration was focused on laboratory specimens with concrete properties similar to those of the tested bridge girders. The adoption of a number of simplifying assumptions, such as the use of porosity and chloride diffusivity values which do not vary over the course of a simulation and neglecting the effect of hysteresis in the sorption isotherm for cyclic wetting-drying, was not found to significantly impact the predictive capabilities of the finite element models. Still, further studies may be necessary to determine the general validity of the simplifying assumptions and whether a different calibration may be required for bridges with different concrete types.

As mentioned in the previous sections, the finite element equations for chloride transport included SUPG stabilization to prevent the occurrence of spatial instabilities in the solution. The susceptibility of an advection-diffusion finite element computation to spatial instabilities

can be determined on the basis of the Peclet number, P_e, which expresses the relative significance of the advective and diffusive transport terms (Donea and Huerta, 2003; Fish and Belytschko, 2007). Values of P_e greater than 1.0 imply that advection dominates and spatial instabilities are expected to occur unless a stabilization technique is employed. The analyses for the girders gave Peclet numbers which often far exceeded 1.0, thus verifying the need for the incorporation of the SUPG stabilization in the solution of the finite element equations for chloride transport. In fact, the absolute maximum value of P_e obtained in the two analyses equaled 159.7.

Another finding from the finite element analyses pertains to the fact that the chloride content in the vicinity of the sectional corners is much greater than that away from the corners. As mentioned above, this result is aligned with the actual corrosion-induced damage in the girder specimens, which was more pronounced in the corner regions. An implication of this finding is that analysis approaches considering unidirectional chloride transport along the thickness [such as the ones presented in, e.g., (Mangat and Molloy, 1994; Tang and Nilsson, 1996; Hansen and Saouma, 1999a) may not provide reliable estimates of the corrosion initiation time for the strands in the vicinity of the corner.

An interesting question is related to the significance of the advective transport mechanism and to the sensitivity to the analytically obtained chloride content to the fluctuations of the ambient temperature and relative humidity. To elucidate the impact of the aforementioned modeling assumptions, the analysis for the Lesner Bridge girder has been repeated several times. The first repetition neglected the impact of advective transport on the chloride ingress process. The second repetition assumed a constant value for the ambient temperature, T_{amb}, and relative humidity, h_{amb}, equal to 15.9^{o}C and 0.66, respectively. These are the mean annual

values of temperature and relative humidity obtained from the weather station records. The third and final repetition accounted for the fluctuations (with time) to the value of h_{amb}, but assumed a constant value of 15.9°C for T_{amb}. The chloride content histories near the corner of the Lesner Bridge girder section obtained for the various repetitions of the simulation are compared in **Figure 4.17**. One first key remark is that neglecting the effect of advective transport can lead to significant underestimation in the chloride content. The same applies if the analysis uses a constant value for the ambient temperature and relative humidity. This finding corroborates the conclusions of an earlier study by Flint et al. (2014) who had determined that using averaged values (with time) for the ambient climatic conditions can lead to unacceptable errors for coupled heat/mass transport simulations. Finally, it can be seen that the use of a constant value only for the ambient temperature has negligible impact on the results, indicating that the main source of error associated with constant values in ambient conditions is associated with the relative humidity. This is obviously due to the profound effect that relative humidity fluctuations have on the advective transport mechanism. The observations stemming from the results of **Figure 4.17** also apply to the chloride content time histories for a location away from the corner of the cross-section.

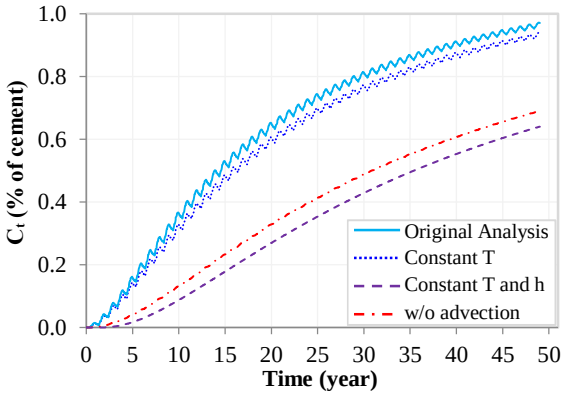

Figure 4.17. Impact of various modeling assumptions on the analytically obtained evolution of chloride content in the corner region of the I-section (Lesner bridge) girder

It is important to reiterate that the analyses presented in the present study neglected the impact of corrosion-induced cracking on the chloride ingress mechanism. While this effect may not be very significant for estimating the corrosion initiation time for a girder exposed to chloride ingress, it must be accounted for in cases aiming to, e.g., quantitatively determine the occurrence and temporal evolution of cracking damage and the reduction in the load-bearing capacity of bridge girders. Another aspect which was not considered in the present study and may warrant future investigations is the potential occurrence of unusual or even extreme weather events and its impact on the evolution of the chloride content. Thus, despite the fact that the analytical scheme presented herein can provide insights into the durability and potential need for intervention to address corrosion-induced damage in prestressed bridges, there is still a need for follow-up research to further enhance the understanding of chloride-induced corrosion.

The use of the design-oriented procedure in the FIB code was found to generally give unconservative results in terms of chloride content and possibility for corrosion. It is important to further investigate the accuracy of the method with measurements taken from actual bridges, to determine whether modifications are required to enhance the accuracy of the specific procedure.

4.12 Conclusions

This study presented a computational simulation framework for describing chloride ingress in prestressed concrete bridge girders. The framework, based on a finite element formulation considering heat transfer, moisture flow and chloride transport, was calibrated with material test data from the literature and validated with data from chloride measurements

conducted on two prestressed girders, which were removed from two bridges in Virginia and exhibited corrosion-induced damage. Further analyses demonstrated the significance of advective chloride transport entailed by the moisture flow, as neglecting the effect of this mechanism was found to lead to significant underestimation of the chloride content. The analyses of the girders were shown to satisfactorily reproduce the experimentally measured distributions of chloride content with depth, while also having the capability to account for the impact of the storage of the girders away from the bridges before the tests. A comparison of the chloride content with the respective critical value estimates, corresponding to corrosion onset, shows that corrosion damage would be expected for both girders, especially for strands in the vicinity of the sectional corners. This finding agrees with the actual corrosion damage that the girders exhibited. The simplified, design-oriented equations of the FIB code were generally found to underestimate the actual chloride content, something that indicates that the specific equations may not lead to conservative results when used to evaluate the possibility for corrosion and the anticipated corrosion initiation time for a bridge girder.

Chapter 5
Coupled Multiphysics Modeling of Chloride-Induced Mechanical Damage in Concrete Bridges

This chapter introduces a simulation scheme to account for corrosion-induced mechanical damage (i.e. cracking) in concrete structures, by incorporating a phenomenological description of the electrochemical oxidation-reduction reaction kinetics, generation of expansive corrosion products, and subsequent development of tensile stresses and damage in the surrounding concrete. The impact of cracking on the mass transport mechanisms of moisture and chlorides is also accounted for. The modeling scheme is validated using data from experimental tests on concrete specimens. Subsequently, the modeling scheme was applied to real-life bridge girders. The simulations are found capable of capturing the time to first surface cracking, spalling of concrete near cross-sectional corner region, verified with experimental test on bridge structures.

5.1 Description of the Girders

The proposed coupled Multiphysics scheme is primarily focused on two concrete bridge girders, decommissioned from bridges in the state of Virginia. The girders were selected for their ability to provide insights into the prevalent bridge construction practices, both within and outside of coastal areas. The first specimen was procured from the Lesner Bridge, located in Virginia Beach, which had been in operation for a duration of 49 years. The extraction process

necessitated saw-cutting the slab on both sides of the girder to separate it from the rest of the bridge structure, which resulted in an I-shaped cross-sectional geometry for the girder specimen. In order to assess the long-term performance of the bridge, a chloride titration test was performed on the girder, two years after the bridge's demolition, which corresponds to an age of 51 years. The other specimen had a box-shaped cross-section and was removed from the Aden Road Bridge near Quantico, Virginia after 34 years of service. Following its removal, the girder was deposited at a separate location and later subjected to testing at 40 years of age. The I-section girder was featured with a 51 mm thick concrete overlay, whereas the box-section girder had a 38 mm asphalt topping that was removed during the deconstruction process.

Both girders exhibited a variety of damage from cracking to the spalling of the concrete, which was particularly pronounced in the cross-sectional corner regions. An overview of the condition of the girders near the end of their service life characterizing the extent of the corrosion damage, is shown in **Figure 5.1** and **Figure 5.3**.

(a) Condition of the bridge near the end of service life

(b) Corrosion damage, bottom view

(c) Corrosion damage, side view

(d) Repaired area, bottom view

Figure 5.1. Corrosion-induced damage in I-section bridge girders at different locations.

(a) Condition of the bridge near the end of service life (b) Corrosion damage, side view (c) corrosion-induced crack, bottom view (d) corrosion-induced crack, side view

Figure 5.2. Corrosion-induced damage in box-section bridge girders at different locations.

5.2 Mathematical Model

The mathematical model corresponds to a bridge girder which constitutes the domain Ω of the physical processes affecting the intrusion of chloride in concrete. The mathematical model comprises five distinct physical processes, including heat transfer, moisture transport, chloride transport, electrochemical oxidation-reduction reactions, and mechanical damage. The boundary conditions across the surface Γ entail radiation form the sun, and the flow of heat, moisture, and chlorine. The following sections detail the governing differential equations that describe the kinetics of various physical processes.

5.2.1 Equations for Heat Transfer

The conservation of energy principle underpins the governing differential equation for heat transfer, which is expressed by the following law:

$$\frac{\partial T}{\partial t} \cdot \rho \cdot c + \nabla \bullet \boldsymbol{q}_T = 0 \tag{5.1}$$

where T, ρ and c denote temperature (K), density (kg/m^3) and specific heat capacity of the material [J/(kg·K)], respectively. Fourier's law provides the basis for deriving the heat flux vector, $\boldsymbol{q}_T$ (W/m^2) given by:

$$\boldsymbol{q_T} = -k_T \nabla T \tag{5.2}$$

where k_T is the thermal conductivity [W/(m·K)] term, and ∇T is the temperature gradient.

The boundary conditions for heat transfer involves heat convection and solar radiation, which are expressed mathematically as follows:

$$\boldsymbol{q_T} \cdot \boldsymbol{n} = \beta_T (T - T_{amb}) - q_s \tag{5.3}$$

where $\boldsymbol{n}$, β_T, denote the unit normal outward vector, and constant surface heat transfer coefficient [W/(m^2·K)]. The added heat per unit surface due to solar radiation is defined by $q_s = a\, I_s$ where a is the surface absorptivity factor and I_s (W/m^2) is the solar irradiance term (Aliasghar-Mamaghani et al., 2023).

5.2.2 Equations for Moisture Transport

The governing differential equation for moisture transport is obtained by enforcing the principle of mass conservation, given by the following equation:

$$\frac{1}{k} \cdot \frac{\partial h}{\partial t} + \nabla \cdot \boldsymbol{j_m} = 0 \tag{5.4}$$

where the moisture capacity term is $k = \partial h / \partial w_e$, h is the field relative humidity, w_e is the evaporable moisture content, and the moisture flux vector is given by $\boldsymbol{j_m} = -D_m \nabla h$, where D_m is the moisture permeability coefficient [kg/(m·s)], and ∇h is the gradient of the relative humidity. The moisture content in concrete is the combination of two components: chemically bound water and evaporable moisture content. The former is trapped within the calcium silicate hydrate (C-S-H) layers and can vary under severe conditions (Bažant and Jirásek, 2018). Therefore, in this study, evaporable water content is solely used to measure moisture variation in the concrete medium.

The correlation between evaporable water content and relative humidity is described by sorption isotherm. The shape of the isotherm depends on whether adsorption (wetting) or desorption (drying) is taking place. This study employs the following equation for sorption isotherm (Van Genuchten, 1980):

$$w_e = w_{e1}\left[(-b\ln h)^{1/(1-m)} + 1\right]^{-m} \tag{5.5}$$

where w_{e1} (kg/m^3) is the maximum evaporable moisture content and b, m are model parameters.

The following law is proposed for the moisture diffusion coefficient which also account for the mechanical damage in the concrete:

$$D_m = \left[1 + k_c \frac{{w_{cr}}^n}{S \cdot l_e}\right] D_{m(s)} \tag{5.6}$$

where w_{cr} is the width of the crack (mm), l_e is the size of the mesh, and n, k_c, S are constant model parameters. The first part of equation (5.6) accounts for the effect of mechanical damage and replicates the transport behavior in cracked specimens, while the subsequent term mimics the transport in sound specimens. The latter is obtained by employing a model proposed by Bažant and Najjar (1972):

$$D_{m(s)} = \left[\alpha_0 + \frac{1-\alpha_0}{1+\left[(1-h)/(1-h_c)\right]^r}\right] c_1 \tag{5.7}$$

where c_1 [kg/(m·s)] is the full saturation permeability, occurring at h = 1, and h_c, r and a_0 are model parameters.

The mathematical model that characterizes the convective transport of moisture across the boundary is expressed by the following equation:

$$\boldsymbol{j_m} \bullet \boldsymbol{n} = \eta_e(\ln h - \ln h_{amb}) \tag{5.8}$$

where η_e represents the constant moisture emissivity coefficient [kg/(m^2·s)] and h_{amb} denotes the ambient relative humidity.

5.2.3 Equations for Chloride Transport

The differential equation governing the transport of chloride is derived by invoking the principle of mass conservation (Maekawa et al., 2003; Maekawa, 2008), mathematically expressed by:

$$\frac{\partial}{\partial t}\left(\varphi \cdot S_l \cdot C_f\right) + \nabla \bullet \boldsymbol{j_{cl}} = 0 \tag{5.9}$$

where C_f is the concentration of free chloride (mol/m^3), and φ and S_l denote the porosity and degree of saturation. The chloride flux vector, $\boldsymbol{j_{cl}}$, is the sum of two contributions, namely diffusion, and advection, which are driven by concentration gradient (∇C_f) and moisture flow velocity ($\boldsymbol{v}$), respectively. The chloride flux is given by the following equation:

$$\boldsymbol{j_{cl}} = -\varphi \cdot S_l \cdot D_{cl} \cdot \nabla C_f + \varphi \cdot S_l \cdot \boldsymbol{v} \cdot C_f \tag{5.10}$$

The following equation is proposed for the chloride diffusion coefficient, which accounts for the mechanical damage in concrete material:

$$D_{cl} = D_0 \cdot \left[\varphi S_l + \frac{\gamma_{cr} w_{cr} S_{cr}}{l_e}\left(1 - e^{-a_{cr}(w_{cr})^{b_{cr}}}\right)\right] \cdot \exp\left[\frac{Q_d}{R}\left(\frac{1}{T_{ref}} - \frac{1}{T}\right)\right] \tag{5.11}$$

where D_0 is the referential chloride diffusion coefficient (m^2/s), Q_d is the activation energy (J/mol), R represents the universal gas constant, equal to 8.3145 J/(mol·K), T_{ref} denotes a reference temperature equal to 293.15 K (20^{o}C), T is the absolute temperature, S_{cr} refers to the crack's saturation degree, and γ_{cr}, a_{cr}, b_{cr}, and n_{cr} are constant model parameters.

The total chloride content (C_t) can be decomposed into two contributions: free chloride, which can move freely in the porous network of concrete, and bound chloride, which is bound to the pore walls. The following mathematical relationship describes the total chloride content:

$$C_t = C_f + C_b \tag{5.12}$$

The mathematical relation describing the bound chloride is described by the following law:

$$C_{b(m)} = 1.5 \left(C_{f(m)} \right)^{0.7} \tag{5.13}$$

where $C_{b(m)}$ and $C_{f(m)}$ are the content of free and bound chloride in percentage of cement mass. The boundary condition accounts for the mass convection across the boundary surface and is described by:

$$\boldsymbol{j_{cl}} \bullet \boldsymbol{n} = \beta_{cl} (C_f - C_{amb}) \tag{5.14}$$

where C_{amb} is the concentration of chloride in the ambient environment and β_{cl} is a surface chloride transport coefficient.

5.2.4 Equations for Stress and Deformation

The governing differential equation for solid mechanics is obtained by invoking the principle of conservation of momentum. By considering a state of static equilibrium, the following equation is derived:

$$\nabla \bullet \boldsymbol{\sigma} + \boldsymbol{b} = 0 \tag{5.15}$$

where $\boldsymbol{b}$ is the body force vector, neglected in this study, and $\boldsymbol{\sigma}$ is the stress tensor. The concrete material model employed in this study uses an elastoplastic formulation for compression-dominated behavior, ensuing the following formulation:

$$\boldsymbol{\sigma} = \boldsymbol{C} : (\boldsymbol{\varepsilon} - \boldsymbol{\varepsilon}^{P}) \tag{5.16}$$

where $\boldsymbol{C}$ denotes the isotropic modulus tensor, the total strain tensor ($\boldsymbol{\varepsilon}$) is given by $\boldsymbol{\varepsilon} = \boldsymbol{\varepsilon}^{e} + \boldsymbol{\varepsilon}^{p}$ and $\boldsymbol{\varepsilon}^{e}$, and $\boldsymbol{\varepsilon}^{p}$ are elastic and plastic part of the strain tensor. The constitutive law in compression is assigned a non-associative flow rule with a yield surface as follows (Moharrami and Koutromanos, 2016):

$$f(\{\hat{\boldsymbol{\sigma}}\}, \kappa) = \frac{1}{1-\alpha}[\alpha \cdot I_1 + r(\theta, e)\sqrt{3J_2}) - c_c(\kappa)] \tag{5.17}$$

where I_1 is the first invariant of the stress tensor, J_2 is the second invariant of the deviatoric stress tensor, $\hat{\boldsymbol{\sigma}}$ is a vector containing principal stresses, and $r(\theta, e)$, κ, $c_c(\kappa)$, and α are model parameters described in detail in (Moharrami and Koutromanos, 2016). The rate of plastic flow is obtained from the following relationship:

$$\dot{\boldsymbol{\varepsilon}}^{P} = \dot{\lambda} \cdot \frac{\partial \psi}{\partial \boldsymbol{\sigma}} \tag{5.18}$$

where $\dot{\lambda}$ is a scalar plastic multiplier, and $\partial\psi / \partial\boldsymbol{\sigma}$ is the plastic flow direction. The plastic potential function corresponds to the following equation (Moharrami and Koutromanos, 2016):

$$\psi = \alpha_p I_1 + \sqrt{2J_2} \tag{5.19}$$

where α_p denotes a dilatancy parameter. The concrete material uses a rotating smeared crack approach for tension-dominated behavior. After the occurrence of cracking, the principal stress ($\hat{\sigma}_i$) in the direction of the principal strain ($\hat{\varepsilon}_i$) is updated and assigned an exponential decay function (Moharrami and Koutromanos, 2016), given by:

$$\hat{\sigma}_i = c_t \cdot [(1 - M_t)\ \exp(-\lambda_t[(\hat{\varepsilon}_i - \hat{\varepsilon}_{ini}) / \ f_t]) + M_t] \tag{5.20}$$

where c_t is tensile strength, $\hat{\varepsilon}_{ini}$ is tensile strain at the beginning of softening, λ_t is a scalar parameter governing the rate of softening, and M_t is the ratio of residual tensile strength with

respect to tensile strength as discussed in detail in Moharrami and Koutromanos (2016). Specific considerations were taken into account to ensure compatibility between elastoplastic and cracking laws, as demonstrated Moharrami and Koutromanos (2016).

5.2.5 Equations for Electrochemical Oxidation-Reduction Reaction

Corrosion is associated with an electrochemical oxidation-reduction (redox) reaction wherein iron in steel is converted to corrosive materials. A redox reaction involved the transport of electrons from one chemical species to the other. This process involves the formation of two electrochemical half-cells, namely anode and cathode. The anode corresponds to the species that loses electrons, i.e. the species that incurs oxidation, while the cathode corresponds to the species that receives electrons (i.e., the species for which reduction occurs). The anodic chemical reaction can be described by the following equation:

$$\mathrm{Fe} \rightarrow \mathrm{Fe}^{2+} + 2\mathrm{e}^{-} \tag{5.21}$$

where iron, Fe, is oxidized into ferrous ion Fe^{2+}. Reduction occurs at the cathode through the adsorption of electrons, which become part of the atoms; specifically, the cathodic reduction reaction is expressed as follows:

$$\mathrm{O_2} + 2\mathrm{H_2O} + 4\mathrm{e}^{-} \rightarrow 4\mathrm{OH}^{-} \tag{5.22}$$

where oxygen, O_2, is reduced to hydroxyl ions, OH^-. The FE^{2+} and OH^- ions then participate in secondary reactions, which result in the formation of iron oxide (rust). The procedure to account for electrochemical oxidation-reduction reaction is described on the bases of thermodynamics electrochemistry. The kinetics of the electrochemical reaction in this research are based on microcell corrosion. In particular, this study assumes corrosion to occur uniformly in the surrounding area of the steel material, without accounting for the potential influence of pitting or localized corrosion, which are associated with macro-cell corrosion mechanisms (Maekawa

et al., 2003; Hussain and Ishida, 2011). The latter holds particular significance for specific structures, such as those exposed to external charges (Wang et al., 2021). Microcell corrosion mechanism involves the formation of anodic and cathodic half-cells in the immediate vicinity of the same metal on a microscopic level (Hussain and Ishida, 2011). The rate of oxidation and reduction reaction is assumed to be controlled by activation polarization. The electrode kinetic behavior of two half-cell reactions [equation (5.21) for oxidation and (5.22) for reduction] are shown in **Figure 5.3**. In a scenario where the surface areas of the anode and cathode are assumed to be equal, it is postulated that all electrons liberated from one cell are subsequently consumed by another cell, thereby ensuring the local conservation of electric charge. Consequently, the rate of reaction in the two half cells is equivalently balanced, resulting in the identification of the intersection point on the polarization curves as the sole point that satisfies this criterion. By projecting this intersection point onto the vertical and horizontal axes, the corrosion potential (E_{corr}) and corrosion current density (i_{corr}) can be ascertained, respectively. The primary objective of the oxidation-reduction reaction is to attain the latter.

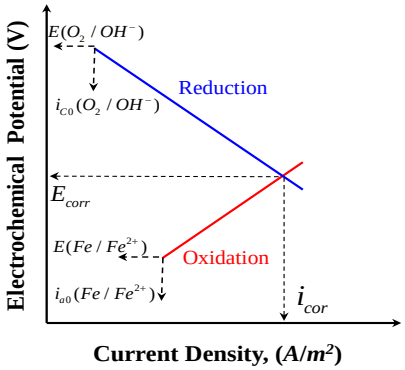

Figure 5.3. Electrode kinetic behavior of oxidation-reduction reaction with activation polarization rate limit

As discussed earlier, the kinetics of the electrochemical reaction is described on the bases of polarization curves. In this regard, the electrode potential at the cathodic branch can be ascertained by

$$E_c = E_{c0} + \beta_c \log(\frac{i_c}{i_{c0(T)}}) \tag{5.23}$$

where E_{c0} denotes the cathodic electrode potential at equilibrium, β_c represents the cathodic Tafel slope, i_c is the electric current density at cathodic site, $i_{c0(T)} = i_{c0}.f_{(T)}$, where i_{c0} is the equilibrium electric current density at cathodic site. The variability of the standard cathodic current density with temperature has been demonstrated (Hussain and Ishida, 2011). As a result, the present study takes this effect into account by adjusting the standard current density in accordance with the Arrhenius law.

$$f_{(T)} = \exp\left[\frac{Q_{d(i)}}{R}\left(\frac{1}{T_{ref}} - \frac{1}{T}\right)\right] \tag{5.24}$$

where $Q_{d(i)}$ is the activation energy term associated with the current density. The standard electrode potential at the cathode is given by the following equation (Hussain and Ishida, 2011; Wang et al., 2021):

$$E_{c0} = E^{\Theta}_{OH^-/O_2} + \frac{RT}{z_{OH^-/O_2}F}\ln(P_{O_2}) - 0.0591pH \tag{5.25}$$

where $E^{\Theta}_{OH^-/O_2}$ is the standard oxygen cell potential at 25 ℃, z_{OH^-/O_2} is the number of electrons transferred in the cathodic half-cell reaction, P_{O_2} is the partial pressure of oxygen, and pH is the potential of Hydrogen.

The electrode potential at anodic branch is defined by the following equation:

$$E_a = E_{a0} + \eta_a \tag{5.26}$$

where E_{a0} is the anodic electrode potential at equilibrium, and η_a is the overvoltage for oxidation half-cell given by (Hussain and Ishida, 2011):

$$\eta_a = \frac{2.303RT}{0.5 z_{Fe/Fe^{2+}} F} \log\left(\frac{i_a}{i_{a0(T)}}\right) \cdot f_p \tag{5.27}$$

where $z_{Fe/Fe^{2+}}$ is the number of electrons transferred in the anodic half-cell reaction, i_a is the electric current density at the anodic site, $i_{a0(T)} = i_{a0} . f_{(T)}$, and i_{a0} the electric current density in equilibrium at the anode, and,

$$f_p = 0.0317 \cdot C_{f(m)}^{-1.04} \tag{5.28}$$

The standard electrode potential at the anode is defined by (Hussain and Ishida, 2011):

$$E_{a0} = E^{\Theta}_{Fe/Fe^{2+}} + \frac{RT}{z_{Fe/Fe^{2+}} F} \ln(C_{Fe^{2+}}) \cdot F_{cl} \tag{5.29}$$

where $E^{\Theta}_{Fe/Fe^{2+}}$ is the standard iron cell potential at $25\,℃$, $C_{Fe^{2+}}$ is the concentration of ferrous ion and,

$$F_{cl} = \frac{1.2 C_{f(m)}}{C_{f(m)} + 1.0} + 0.003 \cdot \ln(1.0 + 10^4 C_{f(m)}) + 1.0 \tag{5.30}$$

Following the establishment of the mathematical framework for the electrochemical oxidation-reduction process, the corrosion current density, i_{cor}, is determined. This quantity is subsequently converted into the corresponding mass loss utilizing Faraday's law, which can be expressed as follows:

$$r_m = \int_0^t \frac{i_{cor}}{z_{Fe/Fe^{2+}} \cdot F} \cdot M \, dt \tag{5.31}$$

where i_{cor} represents the corrosion current density, t denotes the time, and M stands for the molar mass of iron.

5.2.6 Equations for Expansion of Corrosive Product

After determining the mass loss of the strand, the next step is to account for the volumetric expansion of corrosive compounds. The rate of the radius loss ($\dot{r}_{cor}$) can be expressed through the following equation:

$$\dot{r}_{cor} = \frac{-\dot{r}_m}{\rho_s} \tag{5.32}$$

where ρ_s is the density of the steel material (kg/m^3). The mathematical proof for equation (5.32) is provided in **Appendix C.** Subsequently, to feed the expansion law, a rate equation governing the area loss of the steel material needs to be defined:

$$\gamma = 1 - (r_{cor}/r_0)^2 \tag{5.33}$$

here, r_0 and r_{cor} refer to the radius of the original and corroded wire, respectively, as illustrated in **Figure 5.4**.

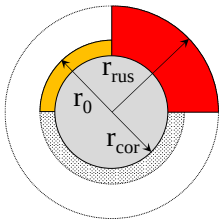

Figure 5.4. Parameters specifying the volumetric expansion of a wire

After some mathematical procedures outlined in **Appendix D**, the radius of the corrosive product is derived through the following equation:

$$r_{rus} = r_0\sqrt{1+\gamma(\alpha_e - 1)} \tag{5.34}$$

where α_e is the volumetric expansion of corrosive product.

The stress induced by the volumetric expansion of corrosive products, $\boldsymbol{\sigma}$, is given by the following expression:

$$\boldsymbol{\sigma} = \boldsymbol{C}_{(E_{eq})} : (\boldsymbol{\varepsilon} - \boldsymbol{\varepsilon}^{aut}) \tag{5.35}$$

where $\boldsymbol{\varepsilon}$ denotes the total strain tensor for the corrosive material, and the plastic part of strain tensor ($\boldsymbol{\varepsilon}^{p}$) is set to zero. $\boldsymbol{\varepsilon}^{aut}$ is the autogenous part of the strain tensor, given by $\boldsymbol{\varepsilon}^{aut} = \boldsymbol{I}\varepsilon_{(\exp)}^{aut}$, where $\boldsymbol{I}$ is the identity tensor and the autogenous true strain is obtained from the following equation:

$$\varepsilon_{(\exp)}^{\ aut} = \int_{r_0}^{r_{rus}} \frac{dr}{r} \tag{5.36}$$

It is important to note that equation (5.36) takes into account the natural strain, and not engineering strain. The tangent modulus tensor for corroded product, $\boldsymbol{C}_{(E_{eq})}$, is dependent on the elasticity modulus given by following equation (Toongoenthong and Maekawa, 2005):

$$E_{eq} = \frac{1 + \gamma(\alpha_e - 1)}{\gamma\alpha_e / E_{rus} + (1 - \gamma)/E_s} \tag{5.37}$$

where E_s is the elastic modulus of steel material, E_{rus} is the elastic modulus of corrosive material.

5.3 Numerical Implementation

The governing differential equations shown in the previous section were transformed into a weak form and then translated into the equivalent finite element formulations for numerical description of all physical processes (Aliasghar-Mamaghani et al., 2023). A necessary stabilization technique is employed in this study to prevent spurious effects of moisture flow in the solution, using the SUPG technique. For scalar field problems, an implicit

backward Euler time-marching scheme and a full Newton-Raphson iterative scheme were used. For solid mechanics, an implicit time-independent solution and an initial stiffness-based Newton-Raphson iterative scheme were employed.

5.4 Model Calibration

This section presents the calibration for a unique set of model parameters of the constitutive law that could describe the experimentally observed behavior and focuses on concrete prisms and cylinders. The calibrations were performed for thermo-hydro-mechanical-chemical processes.

5.4.1 Moisture Transport

The model parameters for moisture transport are calibrated with the experimental data from Hanson (1968), as shown in **Figure 5.5**. The experiment was conducted on normal strength concrete cylinders that had been cured for 28 days. These cylinders were exposed to an environmental relative humidity of h = 0.50 for a duration of three years. The test setup involved sealing the top and bottom faces of the cylinders to create an impervious boundary. This arrangement allowed moisture to flow out only in the radial direction. The model parameters in equation (5.7) corresponding to the moisture permeability coefficient are assigned the following values: $c_1 = 1.96 \times 10^{-8}$ kg/(m.s), $h_c = 0.69$, $r = 6.00$ and $a_0 = 0.01$. The values of w_{e1} = 97.3 kg/m^3, b = 3.10, m = 0.48 are assigned to parameters in equation (5.5) which enable an accurate reproduction of the relationship between relative humidity and moisture content, for scenarios involving monotonic drying, measured by Baroghel-Bouny (2007).

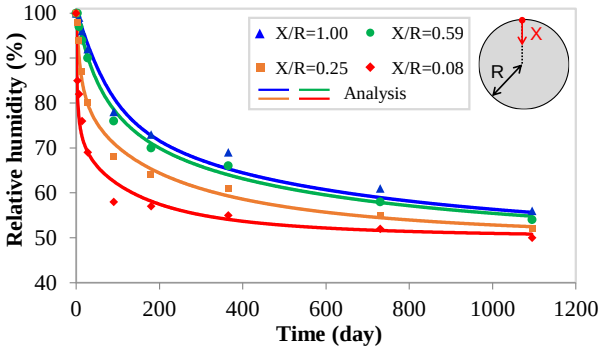

Figure 5.5. Calibration analysis for moisture transport using the experimental data in Hanson (1968)

5.4.2 Chloride Diffusive and Advective Transport in Sound Concrete

The parameter in chloride diffusion model is calibration with a large body of experimental data (Sergi et al., 1992; Maruya, 1995; Maekawa, 2008; Baroghel-Bouny et al., 2009; Baroghel-Bouny et al., 2014), as depicted in **Figure 5.6**. The analyses are assigned a value of $D_0 = 6.0 \cdot 10^{-12}$ m^2/s for concrete specimens and were found capable of capturing the concentration of total chloride, measure through the depth.

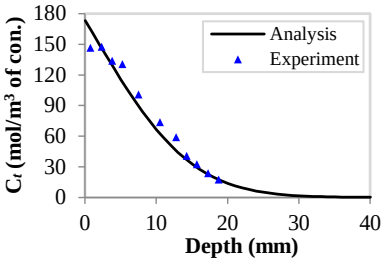

(a) Specimen from (Baroghel-Bouny et al., 2009; Baroghel-Bouny et al., 2014)

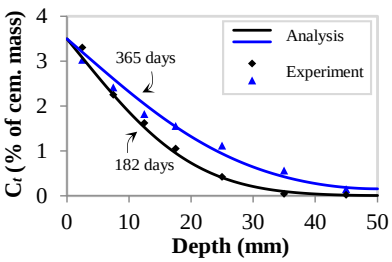

(b) Specimens from (Maruya, 1995; Maekawa, 2008)

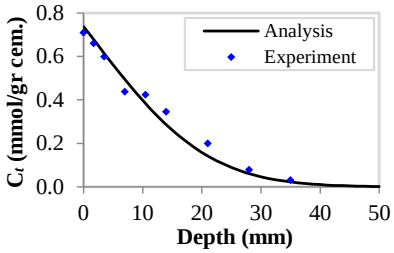

(c) Specimen from (Sergi et al., 1992)

Figure 5.6. Profile of total chloride obtained from calibration analyses.

The calibration analyses for the coupled heat transfer-chloride transport model relied on relevant experimental data (Samson and Marchand, 2007; Chen and Razaqpur, 2021a, 2021b),

which are presented in **Figure 5.7**. The analyses are assigned a thermal conductivity coefficient of $k_T = 2.5\,\mathrm{W/(m\cdot K)}$ and a heat capacity of $c = 1000\,\mathrm{J/(kg\cdot K)}$. The model parameter capturing the coupling effect between heat transfer and chloride transport, i.e., Q_d (activation energy) is assigned a value of 22 kJ/mol and 35 kJ/mol for cement paste and concrete, respectively. As shown in the figure, the analysis results were in good agreement with the experimental observations. However, at temperatures significantly lower than the supercooling temperature of -7°C, the model predictions may deviate due to the questionable applicability of the Arrhenius law, as reported in previous pertinent studies (Samson and Marchand, 2007; Chen and Razaqpur, 2021a). Nonetheless, this issue does not pose a concern for the present study as the temperature range of interest is rarely below the supercooling temperature.

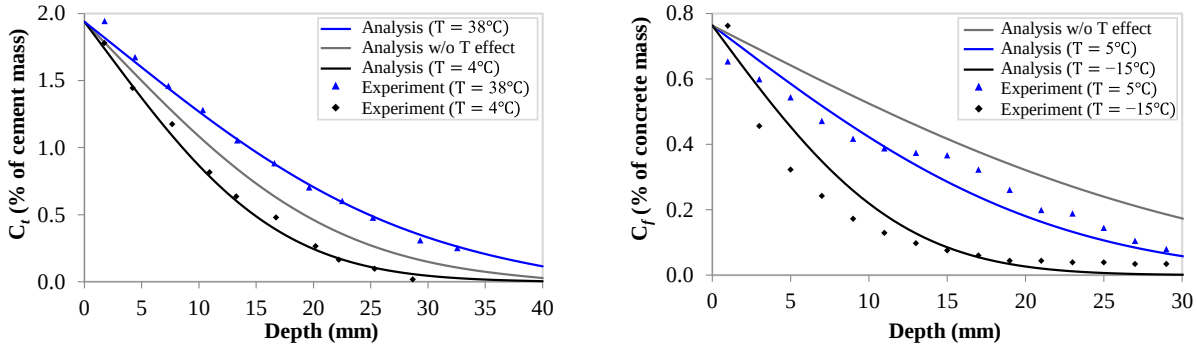

(a) Cement Paste Specimens (b) Concrete Specimens

Figure 5.7. Calibration analyses for coupled heat transfer-chloride transport.

The calibration analyses for coupled moisture-chloride transport, also known as advection diffusion, are shown in **Figure 5.8**. The analyses employ similar calibration for chloride diffusion coefficient discussed above, and similar moisture parameters for constitutive laws of moisture diffusion coefficient. However, the parameters describing the moisture content (sorption isotherm) in equation (5.5), are assigned the following values: w_{e1} = 90.2 kg/m^3, b = 17.00, m = 0.34. These values were specifically chosen to correspond to scenarios involving

monotonic wetting (i.e., imbibition), and have been calibrated using experimental data from Baroghel-Bouny(2007), as shown in (Aliasghar-Mamaghani et al., 2023). It is noteworthy that the elimination of the ink-bottle effect, which is associated with the thermodynamic metastability of adsorption-desorption, provides the rationale for employing monotonic wetting in these analyses.

The analyses and experiments shown in **Figure 5.8** were performed under cyclic wetting-drying conditions. In particular, the experiment conducted by Maruya et al. (1998) focused on concrete specimens and involved a total of 42 wetting-drying cycles. Each cycle lasted for 14 days, and the drying conditions were maintained at a relative humidity of 60%. On the other hand, Lu et al. (2015) conducted tests on concrete specimens involving a total of 15 wetting-drying cycles, with each cycle lasting for 14 days. The drying conditions were maintained at a relative humidity of 76%. The analyses were able to accurately capture the chloride content, highlighting the significance of advective transport within the porous network of concrete structures.

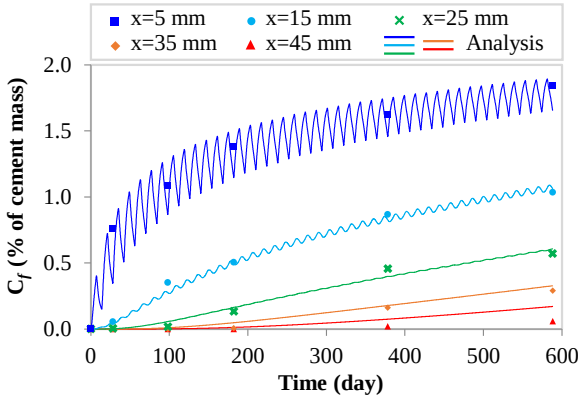

(a) Time-evolution of free chloride; test by Maruya et al. (1998)

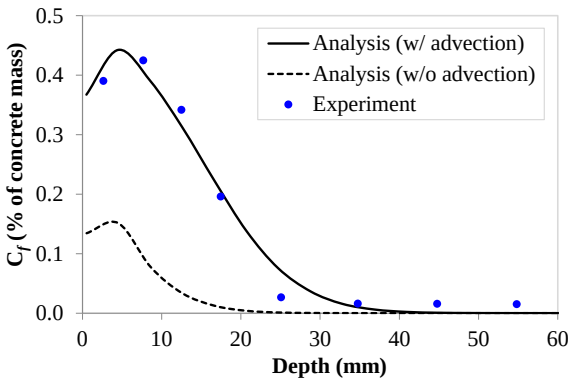

(b) Profile of free chloride distribution; test by Lu et al. (2015)

Figure 5.8. Advective diffusive transport of chloride in concrete specimens.

5.4.3 Chloride Diffusive and Advective Transport in Cracked Concrete

This section aims to describe the coupling effect between mechanical damage in concrete and transport phenomena. It begins by calibrating moisture transport parameters in cracked concrete, followed by the diffusive and advective transport of chloride in cracked specimens.

The calibration for model parameters in equation (5.6), i.e., moisture diffusion coefficient in cracked specimen is performed using the experimental data from Park et al. (2012a). The model is calibrated by assigning values for constant model parameters as: n=3, and $k_c = 1 \cdot 10^5$ mm^{-1} according to the recommendation by Bazant et al. (1987), and S=9.1 mm. The value of l_e is set to 5.0 mm, however it is subject to variation during computation based on the size of the mesh. The model is found capable of capturing moisture diffusion coefficient at different crack with, as shown in **Figure 5.9**.

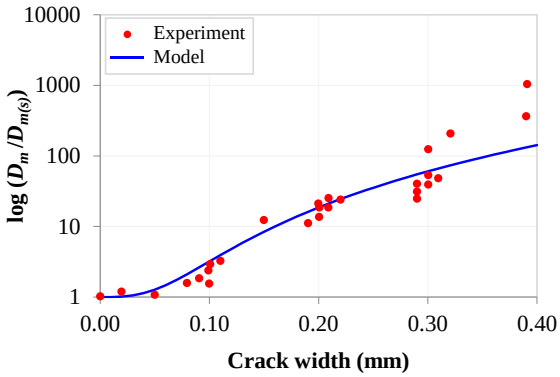

Figure 5.9. Calibration of model parameters for moisture diffusion coefficient in cracked concrete using experimental data from Park et al. (2012a).

The calibration analyses for chloride diffusion in cracked concrete is performed using experimental test data in Kato et al. (2005), which employs specimens with different water/cement ratio, as depicted in **Figure 5.10** and **Figure 5.11**. The model parameters in

equation (5.11) are assigned the following values: γ_{cr} =820.0, a_{cr} =120.0, and n_{cr} =2.0, which were capable of accurately reproducing the experimentally observed behavior.

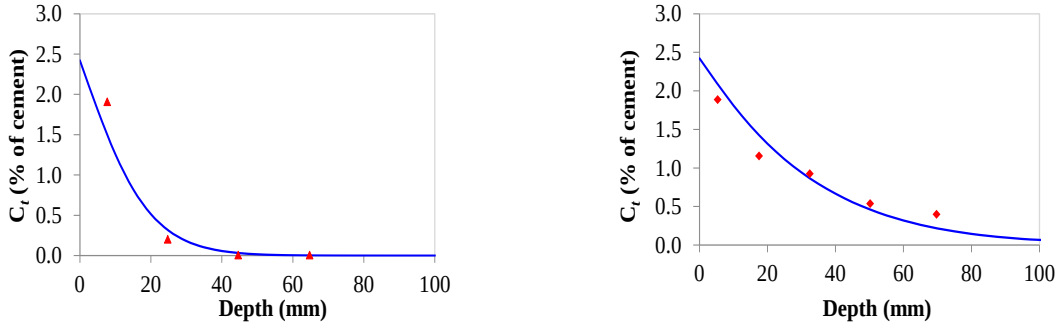

(a) Crack width of 0.060 mm (b) Crack width of 0.200 mm

Figure 5.10. Calibration of chloride diffusion in cracked concrete using experimental data in Kato et al. (2005) for concrete with w/c=0.39.

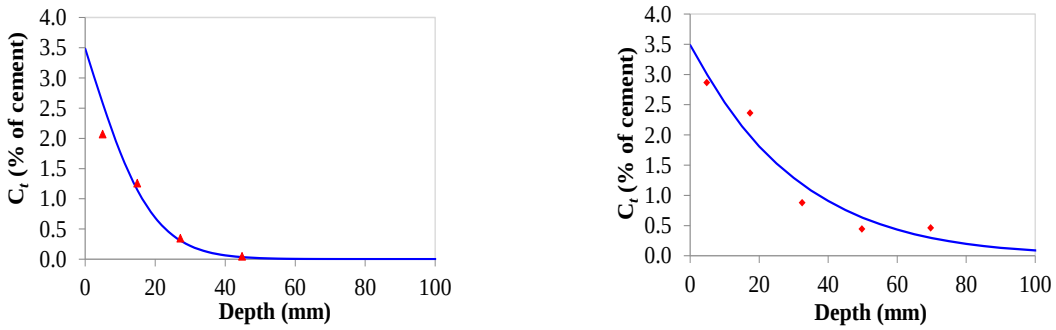

(a) Crack width of 0.055 mm (b) Crack width of 0.200 mm

Figure 5.11. Calibration of chloride diffusion in cracked concrete using experimental data in Kato et al. (2005) for concrete with w/c=0.55.

In real-life, structures are subject to variation in moisture content. Given that, a real-life structure is affected by advection-diffusion and not only diffusion. The parameters affecting the advective diffusive transport of chloride in cracked concrete is identical to the one discussed above for each individual phenomenon (that is moisture and chloride transport in cracked concrete), while here the coupling between the two, are accounted.

The transport modeling scheme in is validated using experimental data in Lu et al. (2017), for specimens under wetting/drying cycles, as depicted in **Figure 5.12**. The scheme was found capable of reproducing experimental data for various crack widths.

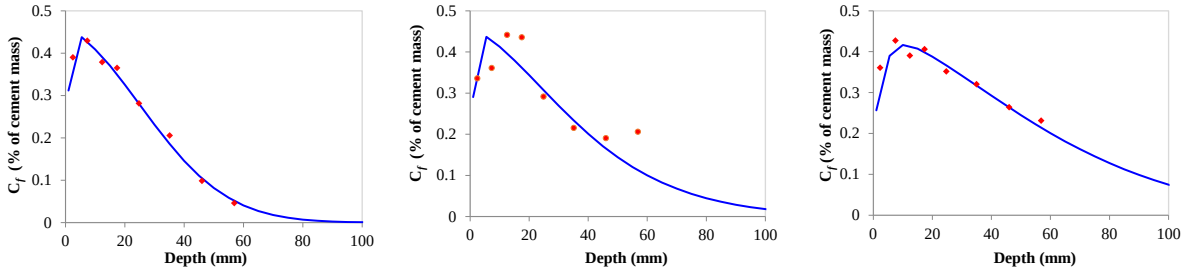

(a) Crack width of 0.048 mm (b) Crack width of 0.135 mm (c) Crack width of 0.205 mm

Figure 5.12. Validation of advective-diffusive transport in cracked concrete using experimental data in Lu et al. (2017).

5.4.4 Electrochemical Oxidation-Reduction Reaction

The calibration of model parameters for electrochemical oxidation reduction kinetic, is shown in **Figure 5.13**. This study assumes free flow of oxygen within the porous network of concrete (Hussain and Ishida, 2011) and assigns a value of 0.142 to the cathodic Tafel slope, β_c. The equilibrium electric current density at cathodic site, i_{c0}, is set equal to 10^{-10}A/m^2. The model parameters corresponding to equations (5.25) and (5.27) are assigned the following values: $z_{OH^-/O_2} = 2.0$, $E^{\Theta}_{OH^-/O_2} = +1.299\text{V}\,(\text{SHE})$, $i_{a0} = 10^{-5}$A/m^2, $z_{Fe/Fe^{2+}} = 2.0$, $E^{\Theta}_{OH^-/O_2} = -0.44\text{V}\,(\text{SHE})$. As shown, the model was found capable of capturing the rate of corrosion with a good rate of accuracy.

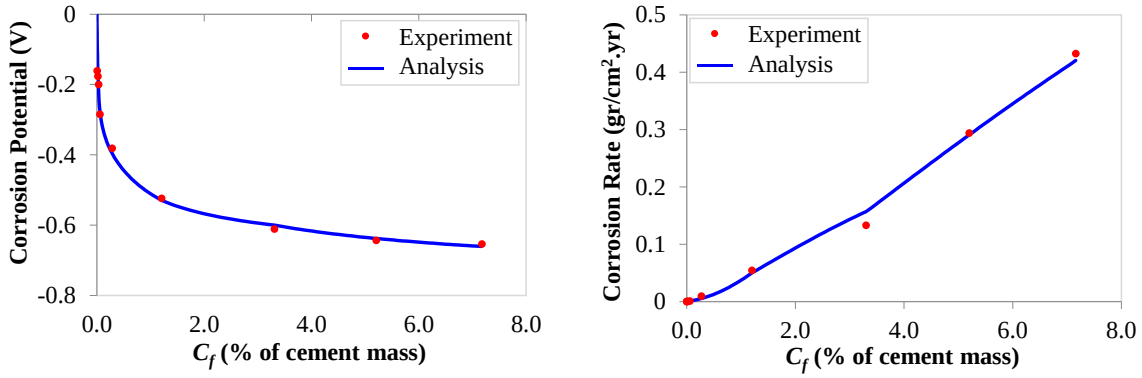

(a) Corrosion potential (b) Corrosion rate

Figure 5.13. Calibration of electrochemical reaction kinetic using experimental data in Hussain and Ishida (2011).

The coupling between heat transfer and electrochemical oxidation-reduction process is established using experimental data from Hussain and Ishida (2011), as shown in **Figure 5.14**. In particular, the only parameter in equation (5.24) characterizing this coupling effect is $Q_{d(i)}$, which is assigned a value of 13kJ/mol, thereby enabling precise replication of the experimental behavior.

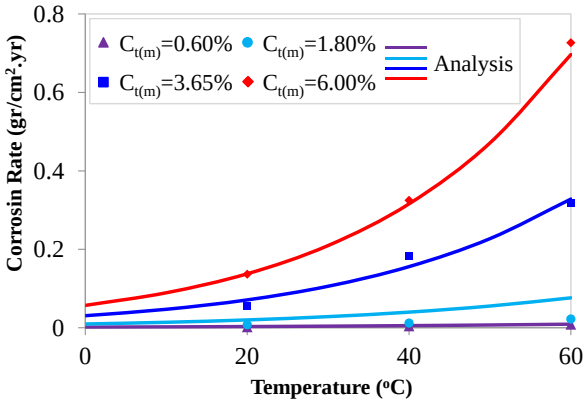

Figure 5.14. Calibration of heat effect on electrochemical reaction kinetic using experimental data in Hussain and Ishida (2011).

5.4.5 Solid Mechanics and Expansion of Corrosive Products

The purpose of the calibration analyses in this section is to determine model parameters that can effectively estimate the cracking pattern resulting from corrosion damage in concrete. The calibration process is initiated by focusing on the cracking pattern in concrete prisms, followed by an analysis to determine the crack width on the surface of the concrete with the level of corrosion damage. This will allow for the establishment of a reasonable connection between the volumetric expansion caused by corrosive products and the maximum crack opening displacement on the surface of the specimen.

The initial calibration analysis employs an experimental test presented in Cabrera (1996), wherein accelerated corrosion testing was conducted to evaluate the cracking pattern in concrete caused by corrosion. The comparison between the analytical response and experimental behavior is illustrated in **Figure 5.15**, which confirms the accuracy of the model in predicting the corrosion-induced cracking pattern in concrete. The volumetric expansion of corrosive agents caused swelling pressure on the surrounding concrete, ultimately resulting in cracking of the concrete.

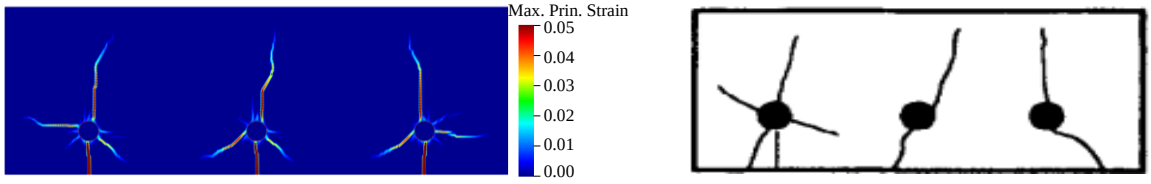

(a) Analysis result (b) Experimentally observed behavior

Figure 5.15. Calibration of the corrosion-induced cracking pattern using experimental data in Cabrera (1996).

The second calibration set in this section involves experimental tests by Molina et al. (1993), which aimed to capture cover cracking caused by corrosion in concrete prisms, as shown in **Figure 5.16**.

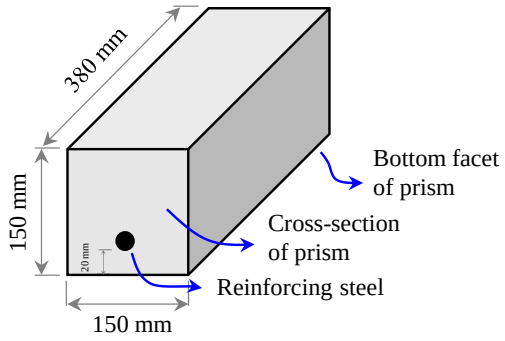

Figure 5.16. Geometric characteristics of the reinforced concrete prism in the study conducted by Molina et al. (1993).

The study focused on accelerated corrosion tests and measured the crack opening displacement at various locations along the length. In addition, the maximum corrosion penetration depth was determined through experimentation. The calibration analysis considers the cross-sectional geometry of the specimen with the objective of establishing a dependable correlation among the volumetric expansion of corrosive materials, the stresses induced in the surrounding concrete, and ultimately the crack opening displacement on the surface of the concrete. This approach intends to provide a robust and accurate understanding of the experimental results. The comparison between experimental data and analysis results is depicted in **Figure 5.17**. The model parameters in equation (5.37) are assigned the following values: E_s=200 GPa, E_{rus} =14 GPa which is close to the values reported in the literature (Toongoenthong and Maekawa, 2005; Wang et al., 2022). In addition, the expansion coefficient is assigned a value of α_e=4.0, which represents the average value for ferrous and ferric

hydroxyl (Youping and Richard, 1998). The tensile strength of the specimen, was assigned a value of 3.55 MPa (Molina et al., 1993), and the fracture energy value of 0.07 N/mm was adopted for concrete in tension. In light of the aforementioned information, the analytically observed behavior, which is illustrated in **Figure 5.17** for the maximum crack opening displacement on the surface of the specimen, was capable of accurately capturing the experimental data.

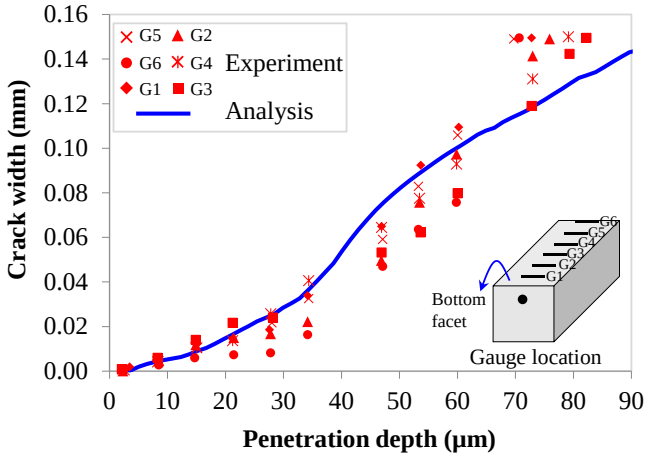

Figure 5.17. Calibration analysis for corrosion-induced cracking using experimental data in Molina et al. (1993).

Figure 5.18 presents a comparison of the cracking pattern caused by corrosive products between the analysis and experiment. The analysis shows a cross-section of the specimen, whereas the experiment displays the bottom view of the specimen. Theoretically, the cracking pattern observed in the bottom view of the specimen should be reproduced on the bottom face of the cross-section in the analysis result. The experiment exhibits branching of the cracks near the longitudinal centerline, which is precisely captured in the analysis, thus confirming the authenticity and validity of the proposed analysis method.

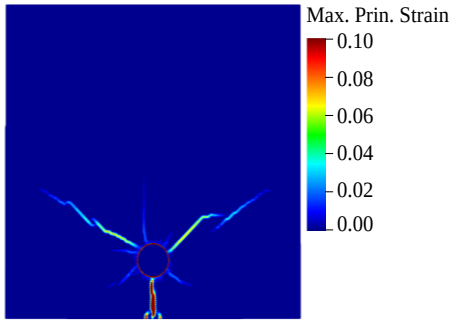

(a) Cross section of the specimen at the end of analysis

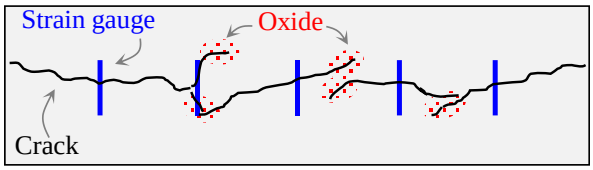

(b) Bottom view of specimen, at the end of the test

Figure 5.18. Calibration of corrosion-induced cracking pattern using experimental observation in Molina et al. (1993).

5.5 Analysis of the Bridge Girders

After establishing our scheme and performing calibration, we employed our coupled multi-physics approach to two distinct bridge girders. The primary objective of this phase was to ensure consistency with our previously established calibration factors and to monitor experimental behavior.

5.5.1 Quantification of Ambient Conditions

The parameters in the mathematical equations for boundary conditions need knowledge of the ambient temperature, T_{amb}, relative humidity, h_{amb}, and chloride, C_{amb}. The process of quantifying the ambient condition of each girder began by obtaining 1-year recorded data (in this case, for the year 2010) from the nearest meteorological station to the bridge locations. These time history values were subsequently replicated for the analysis period.

The ambient chloride, C_{amb}, value is influenced by the particular type of exposure experienced by the specimen, which may include exposure to deicing salt or saltwater spray. For the Lesner bridge, this study employed a value of C_{amb}=1.74 kg/m^3 based on McGee's

(1999) recommendation for coastal bridges. On the other hand, the ambient chloride value for Aden Road bridge was assigned a value of $C_{amb} = 1.06\,\mathrm{kg/m^3}$, in accordance with recommendation by Weyers et al. (1994) for specimens exposed to deicing salts.

As mentioned earlier, the Lesner and Aden Road bridges were in service for 49 and 34 years, respectively, after which they were demolished, and the girders were transported to a separate location where they were no longer exposed to chloride. Specifically, the Lesner and Aden Road bridge girders were stored at different sites for 2 and 6 years, respectively. As a result, the analysis adopts a C_{amb} value of 0 for the time interval of the analysis corresponding to storage.

The analysis takes into account the removal of the asphalt overlay on the top face of the Aden Road bridge girder during the demolition process. The mesh corresponding to the asphalt layer is deleted at the end of the service life. Moreover, for the period of the analysis corresponding to the storage of the girder, the top surface of the concrete girder was deemed to constitute an impervious boundary as a result of the demolition.

5.5.2 Analysis Results

This section presents the results of the two bridge girders, providing key information regarding their service life. **Figure 5.19** illustrates the analysis results for the Lesner bridge girder after ten years. At this specific time, no signs of corrosion damage were observed in the concrete, indicating a low level of corrosion rate in the strands. The figure also includes the entire cross-section of the girder, emphasizing the lack of corrosion-induced damage elsewhere at this age. The absence of corrosion-induced damage suggests that the girder is performing well, and its structural integrity is not compromised.

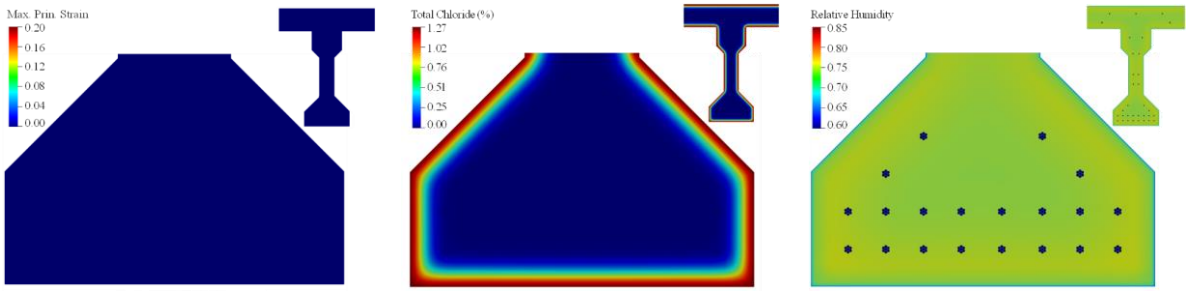

(a) Maximum principal strain (b) Total chloride c) Relative humidity

Figure 5.19. Impact of the corrosion on the Lesner bridge girder at 10 years of age.

The first visible surface crack on the girder was detected at an approximate age of 14.5 years, as shown in **Figure 5.20**(a). The width of the crack at this age was minimal and not discernible to the naked eye. The small crack width did not significantly affect the transport of chloride and moisture, as evident in **Figure 5.20**(b) and **Figure 5.20**(c), where the contour fill for chloride and moisture had consistent concentrations in the vicinity of the crack. The age at which the first surface crack appears is a critical milestone, as it can be considered the time-to-first cracking, after which significant corrosion rate and damage may occur. From a simplified perspective, the point at which corrosion initiation is observed corresponds to the time when the protective film on the surface of the strand is entirely removed.

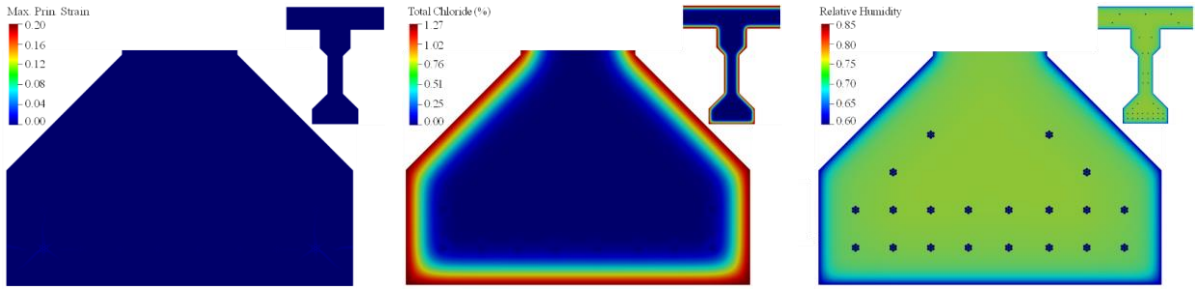

(a) Maximum principal strain (b) Total chloride c) Relative humidity

Figure 5.20. Impact of the corrosion on the Lesner bridge girder at 14.5 years of age.

The results of the analysis at an age of 20 years are presented in **Figure 5.21**, indicating the progression of corrosion and its associated damage. The figure highlights the presence of cracks that have propagated through the concrete, with the tip of the crack reaching the side surfaces. The increased crack width has also led to higher concentrations of chloride and moisture in the immediate vicinity of the cracks, as observed in **Figure 5.21**(b) and **Figure 5.21**(c). This increased concentration of chloride and moisture in the cracks suggests that the corrosion has progressed and started to impact the structural integrity of the girder. Despite the presence of cracks that have reached the side surface, it is noteworthy that at this age, the bottom face of the girder remains undamaged by the effects of corrosion.

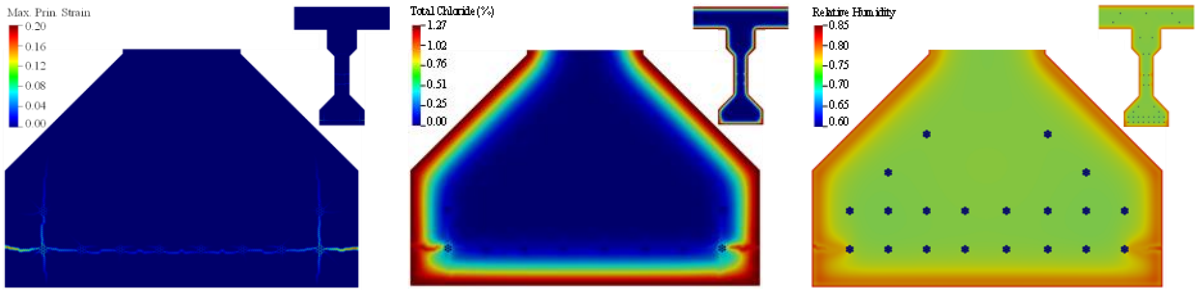

(a) Maximum principal strain (b) Total chloride c) Relative humidity

Figure 5.21. Impact of the corrosion on the Lesner bridge girder at 20 years of age.

A compelling comparison between the simulation results and experimental observation can be established when examining the bridge after 27 years of service. In **Figure 5.22**, the damage map of certain girders and their corresponding simulation counterparts is presented. The experiment illustrates the repaired area implemented at this age. It is crucial to highlight that during this phase, certain preliminary repairs were undertaken on the specimens. Specifically, a meticulous process was employed to remove the deteriorated concrete, which

was manifested as cracks or deterioration in both the side and bottom regions of the girder, within the affected area. This process involved deliberately chipping off the concrete until reaching the level of sound concrete, as visually depicted by a pattern in the figure. After this careful removal, the area was restored using fresh materials. Additionally, it is worth emphasizing that the damage map obtained from the experiment provides observations primarily from the perimeter of the girders. However, the analysis results also demonstrate crack propagation within the interior of the cross-section. The analysis reveals notable cracking in the corner region of the girder's cross-section, subsequently followed by cracking near the bottom region. In particular, the width of the crack in the side is more than 0.5 mm. It is worth noting that, at this stage, the concrete in the corner region exhibits a loose and easily removable nature, aligning with the observations made during the experiment.

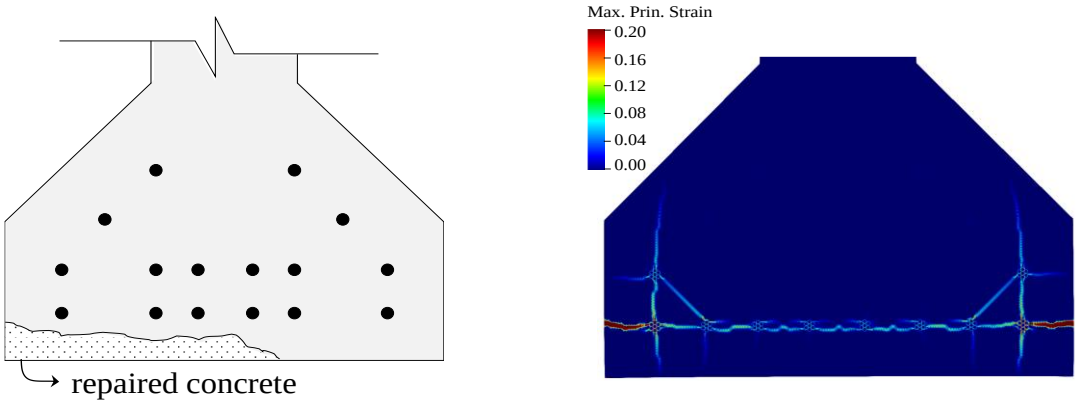

(b) Experimental observation (b) Analysis result

Figure 5.22. Chloride-induced corrosion damage observed in the Lesner Bridge girder after 27 years of service. The repaired area underwent physical chipping to remove the deteriorated concrete.

The next significant milestone occurs when the cracks reach the bottom face of the specimen, which is crucial in estimating the extent of corrosion damage in the corner region. As the width of the cracks continues to widen, the concrete in the cross-sectional corner region gradually loses its tension capacity, eventually leading to spalling in that region. **Figure 5.23**(a)

presents the contour fill for principal strain, illustrating that the tip of the crack on the bottom has only just touched the surface. This is further corroborated in **Figure 5.23**(c), where the moisture content at the bottom surface is higher than that of other regions. The cracks propagating in the side direction have also widened, allowing moisture and chloride to easily intrude into the concrete.

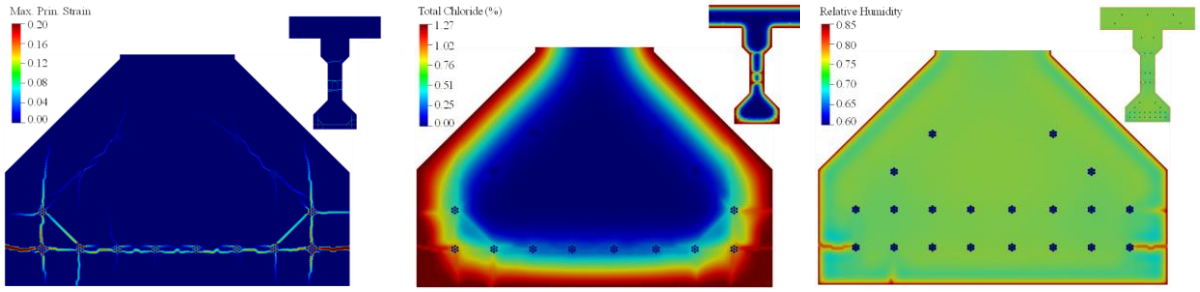

(a) Maximum principal strain (b) Total chloride c) Relative humidity

Figure 5.23. Impact of the corrosion on the Lesner bridge girder at 35 years of age.

Moving forward in the analysis of the girder, the next significant stage is the end of its service life. The analyses shown in **Figure 5.24**, indicate that large crack widths have formed on the bottom corners and sides, which corresponds to spalling. However, it is important to mention that our analysis does not account for element removal due to the limitations of our model. As a result, we cannot observe deterioration or spalling. These results align with the experimental observations depicted in **Figure 5.1**. Specifically, the analysis effectively captures the cracking and deterioration of the concrete on the bottom [**Figure 5.1(b)**] and side faces [**Figure 5.1(c)** and **Figure 5.1(d)**].

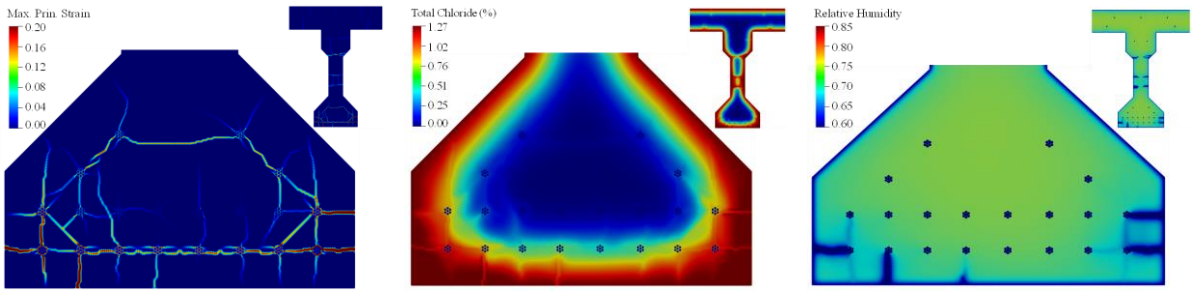

(a) Maximum principal strain (b) Total chloride c) Relative humidity

Figure 5.24. Impact of the corrosion on the Lesner bridge girder at the end of the service life.

The following section discusses the results of the analyses conducted on the Aden Road Bridge girder. **Figure 5.25** depicts the progress of corrosion after ten years. The contour fill for principal strain shows the presence of cracking in the concrete near the shear key region, which can be attributed to the inadequate cover for the strand in that area. The widening of the cracks in this region accelerated the intrusion of chloride, as illustrated in **Figure 5.25**(b) and also the transport of the moisture as shown in the contour fill for relative humidity in **Figure 5.25**(c).

At this age, there were no observed indications of cracking in the lower region of the girder.

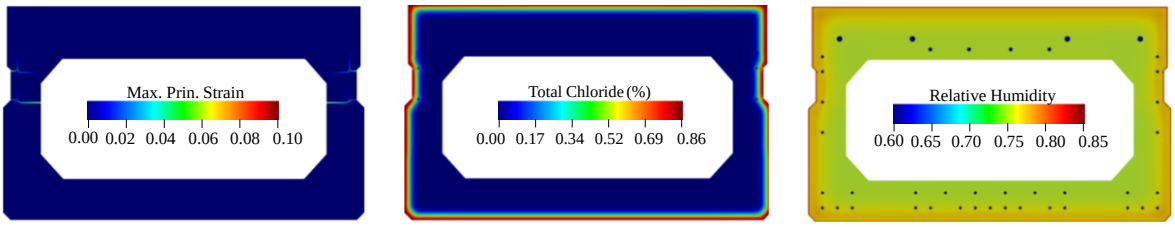

(a) Maximum principal strain (b) Total chloride c) Relative humidity

Figure 5.25. Impact of the corrosion on the Aden Road bridge girder at 10 years of age.

At the age of 16.5 years, the analysis of the girder reached a significant milestone with the emergence of microcracks on its side surface. These cracks were similar in appearance to

those observed on the Lesner Bridge girder, as depicted in **Figure 5.20**. This particular moment marks the time-to-first cracking for the girder under examination.

A critical milestone in the analysis of this girder was reached at 23 years of age, when cracks appeared on the bottom face of the girder. These cracks were observed to have formed in two distinct locations, as illustrated in **Figure 5.26**(a). At this stage, the width of the cracks on the side of the girder had increased, which consequently had a detrimental effect on the intrusion of chloride into the specimen, as depicted in **Figure 5.26**(b). Similarly, the moisture transport was affected, as shown in **Figure 5.26**(c).

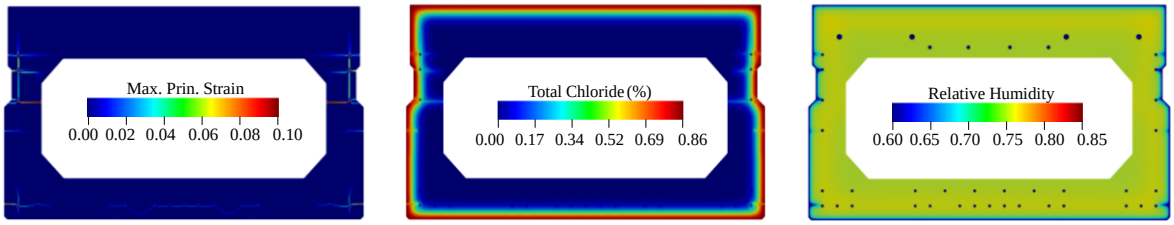

(a) Maximum principal strain (b) Total chloride c) Relative humidity

Figure 5.26. Impact of the corrosion on the Aden Road bridge girder at 23 years of age.

The next significant milestone in the analysis of the girder corresponds to reaching the end of its service life. At this point, the formation of new cracks began, and the width of existing cracks continued to increase. The additional mechanical damage had a significant impact on the intrusion of chloride and moisture in the specimen, as demonstrated in **Figure 5.27**(b) and **Figure 5.27**(c) at the end of service life. The bridge has formed many cracks in the sides and bottom face, which is in close agreement with the experimental observations, shown in **Figure 5.2**. **Figure 5.2**(b) provides a side view of the specimen, revealing corrosion of the strands near the shear key regions, which was accurately captured by the analyses. The formation of chloride-induced corrosion damage on the bottom face [**Figure 5.2**(c)], side face [**Figure**

5.2(d)], and the deterioration of the concrete near the cross-sectional corner region [**Figure 5.2**(a)] are effectively captured by the analysis results.

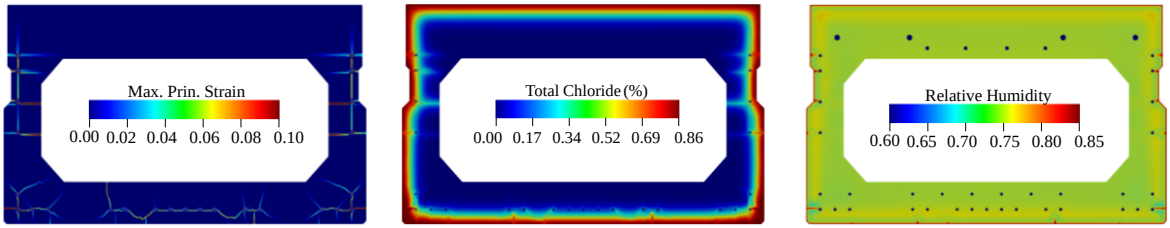

(a) Maximum principal strain (b) Total chloride c) Relative humidity

Figure 5.27. Impact of the corrosion on the Aden Road bridge girder at the end of service life.

5.6 Discussion

The proposed simulation approach has been shown to be highly effective in capturing experimental behavior of concrete specimens, as well as real-life bridge girders.

An important contribution of this research is the comparison of a refined Multiphysics approach with a case that neglects mechanical damage or cracking. The time evolution of chloride for two strands, one in the vicinity and another away from the cross-sectional corner region, for two girders, is illustrated in **Figure 5.28** (Aliasghar-Mamaghani et al., 2023). These analyses were complemented by the results obtained from a closed-form solution discussed in the FIB model code (FIB, 2013). Based on the refined analyses, the time-to-first cracking for strands near and away from the cross-sectional corner region of the Lesner bridge girder is estimated to be 14.5 and 35 years, respectively. In contrast, the coupled analysis without considering electrochemical reactions and mechanical damage showed that the rate of corrosion significantly increased at ages of 18.5 and 31.5 years for strands near and away from the corner region, respectively.

It should be emphasized that corrosion is not a discrete physical phenomenon that is initiated by a switch; rather, it is a process that is always ongoing, with the presence of chloride exacerbating the condition. The two half-cells inducing corrosion are iron and oxygen, which always exist. Therefore, while the term *time-to-corrosion* may not reflect the reality of the situation, the term *time-to-first cracking* is a more accurate representation. The analysis results for the Aden bridge girder indicate a time-to-first cracking of 16.5 and 23.0 years, respectively, when considering chemo-mechanical behavior. In contrast, the analysis results without considering chemo-mechanical behavior predicted a time to significant corrosion reaction rate of 18 and 27 years, respectively.

Additionally, results from the simplified FIB model code are provided, which differ significantly from both the refined model and experimental observations. These findings emphasize the importance of considering chemo-mechanical behavior in accurately predicting the behavior of concrete structures over time. Furthermore, they highlight the limitations of simplified models in capturing the complex behavior of real-world structures.

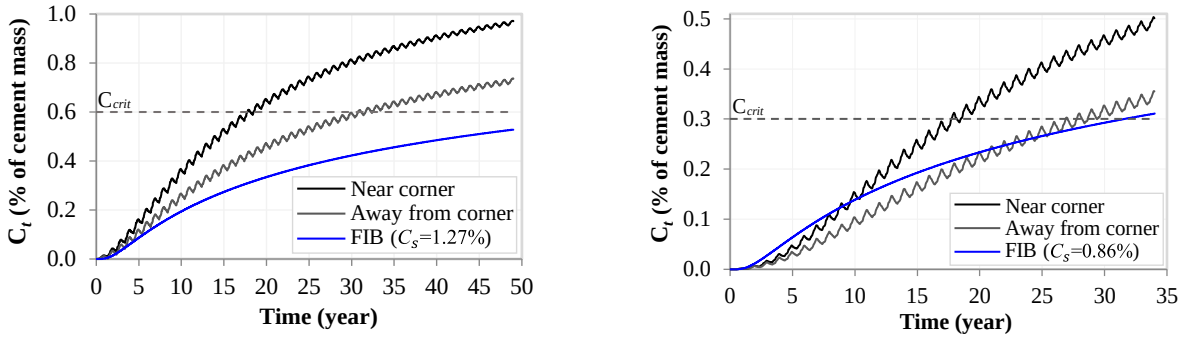

(a) I-section girder (Lesner bridge) (b) Box-section girder (Aden Road bridge)

Figure 5.28. Comparison of analytical model without considering chemo-mechanical behavior with the simplified approach in the FIB code.

The analysis results pertaining to the scenarios where the influence of cracking is disregarded are of paramount importance in comprehending the necessity of coupled analysis

(while accounting for electrochemical reaction). In this regard, a comparative evaluation is conducted on the cross-sectional area loss of prestressing wires between cases with and without cracking. **Figure 5.29** provides a close examination of the analysis results concerning the cross-sectional corner region of the Lesner bridge girder at the end of its service life. The mechanical damage in the concrete caused by the production of expansive corrosive products has significantly impacted the ingress of chloride into the concrete medium, as evident from the contour fills.

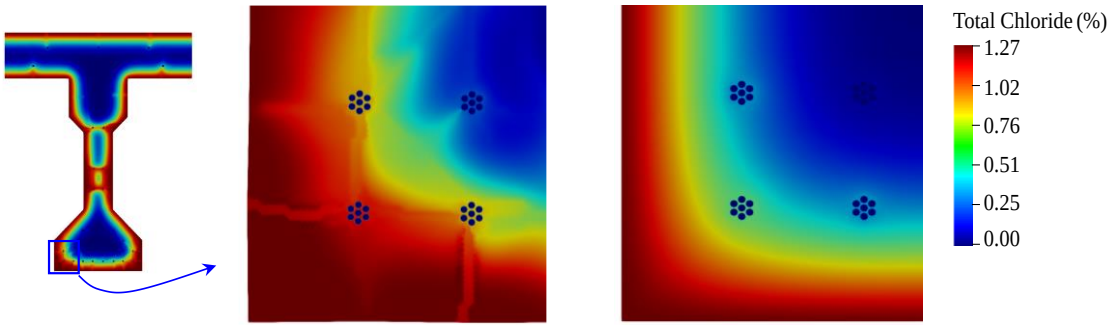

(a) With mechanical damage (b) Without mechanical damage

Figure 5.29. Impact of mechanical damage (cracking) in the chloride ingress in Lesner bridge girder.

A thought-provoking comparison can be made regarding the cross-sectional area loss of prestressing wires. **Figure 5.30** presents a comparison of the normalized area loss of prestressing wire, taking into account the cracking effect in the analysis versus the analysis without considering cracking. Remarkably, the analysis that neglected the cracking effect significantly underestimated the area loss of the steel by more than a factor of two at the end of the service life. This graph effectively highlights the crucial role of mechanical damage in the analysis and emphasizes the necessity of employing a comprehensive thermo-hydro-chemo-mechanical model to obtain a reliable estimate of the service life of bridge girders.

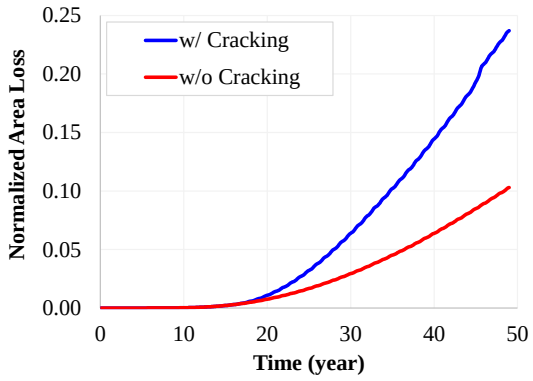

Figure 5.30. Impact of cracking on the cross-sectional area loss of prestressing wires.

5.7 Conclusions

This study presents a novel coupled thermo-hydro-chemo-mechanical modeling approach to accurately describe the intrusion of corrosion-inducing chloride ions into the porous network of concrete and subsequent mechanical damage. The proposed approach includes constitutive laws to capture the coupling between mechanical damage and chloride-moisture transport. The finite element framework focuses on coupled heat transfer, moisture flow, chloride transport, electrochemical oxidation-reduction reaction, and mechanical damage, and it has been calibrated with a large set of experimental data on prismatic and cylindrical concrete specimens. Subsequently, the proposed scheme has been applied to two bridge girders taken from two bridges in Virginia after 49 and 34 years of service. The analyses on concrete specimens demonstrate the importance of coupling between various phenomena, particularly advection-diffusion, coupled with mechanical damage. Furthermore, the analyses of the girders provide a reliable estimate of the experimentally observed behavior of both the chloride-induced corrosion damage in prestressing steel material and the surrounding concrete. The study also compares the proposed coupled Multiphysics approach with a case that does not

consider chemo-mechanical damage, highlighting the importance of cracking in the propagation of damage in strands. In addition, the limitations of the simplified FIB model code in estimating the service life of the girder are shown. These findings emphasize the importance of considering chemo-mechanical behavior and coupling between various phenomena in accurately predicting the behavior of concrete structures over time.

Chapter 6
Uncertainty Quantification for Chloride-Induced Corrosion Damage in Concrete Bridge

This Chapter investigates the impact of uncertainties associated with chloride ingress in prestressed concrete bridge girders. The mathematical description of advective and diffusive chloride transport entails a dependence on quantities associated with the boundary conditions, e.g., the surface chloride quantity, and with the constitution of the concrete material, e.g., the moisture and chloride diffusivity parameters. These parameters are all characterized by aleatory (inherent) uncertainty; accordingly, this uncertainty will propagate into various Quantities of Interest (QoI), namely, the value of chloride content at given locations of the bridge section and at given age values, or the probability of the corrosion at a particular age. The uncertainty quantification study presented herein relies on the so-called stochastic collocation approach, selected for its non-intrusive character, which renders it appropriate for case with high-fidelity computational simulation schemes.

6.1 Analysis methodology

Our first step in this chapter is to develop a finite element approach that can accurately account for the coupled heat-moisture-chloride transport and predict the concentration of chloride at different depths. Once this is established, we will select the most influential model parameters and assign specific values to obtain the desired quantities of interest.

To begin, we will provide a brief summary of the mathematical implementation of our approach. Next, we will elaborate on our scheme for using the stochastic collocation approach,

which can provide an accurate estimate of the Monte Carlo simulation. Due to the complexity of our model, traditional Monte Carlo simulation is not feasible, but we believe the stochastic collocation approach will yield satisfactory results.

6.2 Description of the Girders

This study examines two decommissioned prestressed concrete bridge girders from Virginia, selected as representative examples of common bridge construction in the region. The first specimen, extracted from the Lesner Bridge in Virginia Beach, had served for 49 years before its decommissioning. It featured an I-shaped cross-section, and its extraction process involved carefully saw-cutting the slab on either side of the girder to separate it from the rest of the bridge structure. To evaluate the performance of these bridges, a chloride titration test was conducted on the girder when it reached the age of 51, two years after the bridge's demolition. The second specimen, which had a box-section geometry, was removed from the Aden Road Bridge near Quantico, Virginia after 34 years of service. Following the demolition process at the end of its service life, the girder was relocated to a separate location and tested at 40 years of age.

Figure 6.1 depicts the cross-sectional geometry of the two girders. The I-section girder had a 51 mm thick concrete overlay, whereas the box-section girder had a 38 mm asphalt topping that was removed during the demolition process.

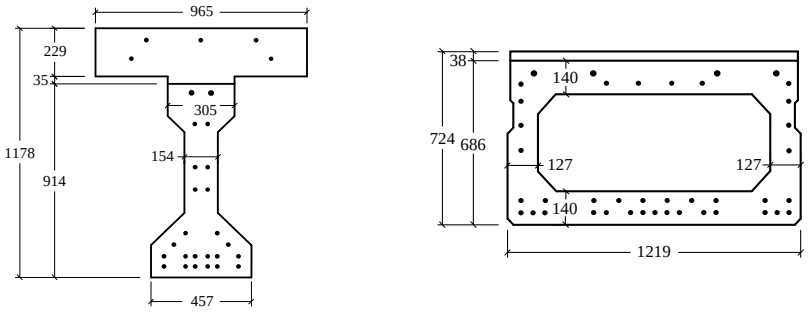

(a) I-section girder (b) Box-section girder

Figure 6.1. Cross-sectional geometry of girders (dimensions in mm)

Both girders exhibited significant corrosion damage, which was particularly pronounced in the strands situated near the lower corners of their sections. This extensive corrosion led to concrete cracking and complete loss of cover in these areas.

Figure 6.2 presents an overview of the girders' condition towards the end of their service life, along with damage maps that illustrate the extent of deterioration across the cross-sections of both girders.

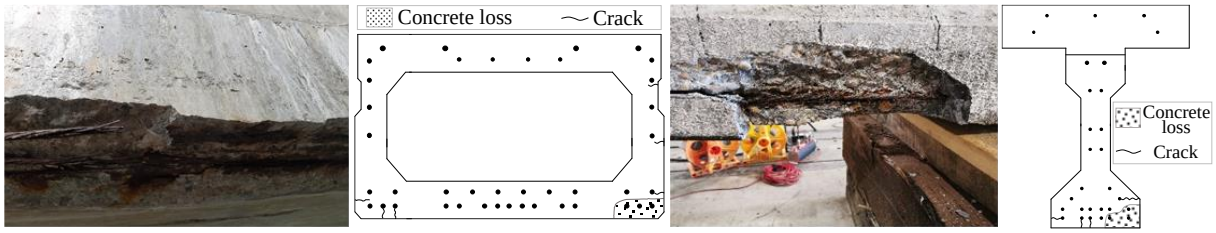

(a) Severe corrosion damage in Box-section girder

(b) Typical estimated damage from visual inspection for Box-section girder

(c) Severe corrosion damage in I-section girder

(d) Typical estimated damage from visual inspection for I-section girder

Figure 6.2. Corrosion-induced corrosion damage in prestressed concrete bridge girders

6.3 Multiphysics Mathematical Model

The mathematical model corresponds to a bridge girder, which constitutes the domain Ω of the physical processes affecting the intrusion of chloride in concrete. The model incorporates three distinct physical processes: heat transfer, moisture transport, and chloride transport through both advection and diffusion mechanisms. The boundary conditions involve the flow of heat, moisture, and chlorine across the surface Γ. The following sections provide a detailed account of the differential equations that govern the kinetics of each physical process.

6.3.1 Equations for Heat Transfer

The conservation of energy principle governs the differential equation for heat transfer, which is expressed by the following law.

$$\frac{\partial T}{\partial t} \cdot \rho \cdot c + \vec{\nabla} \bullet \vec{q}_T = 0 \tag{6.1}$$

where T, ρ and c represent temperature (K), density (kg/m^3) and specific heat capacity of the material [J/(kg·K)], respectively. The heat flux vector, $\vec{q}_T$, represent the amount of heat through a given surface area (W/m^2). This vector field can be obtained from Fourier's law, which describes the relationship between heat flux and temperature gradient in a material:

$$\vec{q}_T = -k_T \vec{\nabla} T \tag{6.2}$$

where k_T represents the thermal conductivity of the material [W/(m·K)] and $\vec{\nabla} T$ denotes the temperature gradient.

The mathematical description of the boundary conditions for heat transfer includes both heat convection and solar radiation, given by:

$$\vec{q}_T \bullet \vec{n} = \beta_T (T - T_{amb}) - q_s \tag{6.3}$$

In this context, $\vec{n}$ represents the unit normal outward vector, β_T is a surface heat transfer coefficient [W/(m^2·K)], and the last term corresponds to the amount of heat added per unit surface area due to solar radiation (Aliasghar-Mamaghani et al., 2023), which is given by $q_s = a\,I$. Here, *a* represents a surface absorptivity factor and *I* is the solar irradiance (W/m^2).

6.3.2 Equations for Moisture Transport

The governing differential equation for moisture transport is derived by applying the principle of conservation of mass, which is mathematically given by:

$$\frac{1}{k}\cdot\frac{\partial h}{\partial t} + \vec{\nabla}\bullet\vec{j}_{\boldsymbol{m}} = 0 \tag{6.4}$$

The first term identifies the moisture capacity, $k = \partial h/\partial w_e$, h represents the field relative humidity, w_e represent the evaporable moisture content, and the moisture flux vector is given by $\vec{j}_{\boldsymbol{m}} = -D_m\vec{\nabla}h$. Here, D_m is the moisture diffusion coefficient [kg/(m·s)] and the $\vec{\nabla}h$ is the gradient of the field function. In concrete, there are two primary types of moisture content: chemically bound water and evaporable moisture content. Chemically bound water is held within the calcium silicate hydrate (C-S-H) layers and can undergo significant fluctuations under extreme conditions, as demonstrated in previous research (Bažant and Jirásek, 2018). As such, in this study, we have exclusively employed evaporable water content as a measure of moisture fluctuations within the porous network of the concrete.

The relationship between evaporable water content and relative humidity can be characterized by the sorption isotherm, which exhibits a distinctive shape depending on whether the process involves absorption (wetting) or desorption (drying). Accordingly, this study utilizes the following equation to describe the sorption isotherm (Van Genuchten, 1980):

$$w_e = w_{e1}\left[(-b\ln h)^{1/(1-m)} + 1\right]^{-m} \tag{6.5}$$

where w_{e1} (kg/m^3) represents the maximum evaporable moisture content and b, m are constant model parameters. The constitutive law describing the moisture diffusion coefficient is in accordance with a model by Bažant and Najjar (1972):

$$D_m = c_1\left[\alpha_0 + \frac{1-\alpha_0}{1+\left[(1-h)/(1-h_c)\right]^r}\right] \tag{6.6}$$

where c_1 [kg/(m·s)] is the permeability at full saturation (i.e., at h = 1) and, h_c, r and a_0 are constant model parameters.

The following formulation corresponds to the mathematical model used to describe moisture convection across the boundary:

$$\vec{j}_m \bullet \vec{n} = \eta_e(\ln h - \ln h_{amb}) \tag{6.7}$$

where η_e is a constant moisture emissivity coefficient [kg/(m^2·s)].

6.3.3 Equations for Chloride Transport

The differential equation that governs chloride transport is derived from the principle of mass conservation and is given by the following equation (Maekawa et al., 2003; Maekawa, 2008):

$$\frac{\partial}{\partial t}\left(\varphi \cdot S_l \cdot C_f\right) + \vec{\nabla} \bullet \vec{j}_{cl} = 0 \tag{6.8}$$

where C_f is the concentration of free chloride (mol/m3), φ represents the porosity and S_l is the saturation degree. The chloride flux vector is the combination of two contributions: diffusion and advection, which are driven by the concentration gradient, $\vec{\nabla} C_f$, and the velocity of moisture flow, $\vec{v}$, respectively. The following law describes the flux term:

$$\vec{j}_{cl} = -\varphi \cdot S_l \cdot D_{cl} \cdot \vec{\nabla} C_f + \varphi \cdot S_l \cdot \vec{v} \cdot C_f \tag{6.9}$$

The chloride diffusion coefficient is influenced by the temperature and is determined from the following equation:

$$D_{cl} = D_0 \cdot \exp\left[\frac{Q_d}{R}\left(\frac{1}{T_{ref}} - \frac{1}{T}\right)\right] \tag{6.10}$$

where D_0 is a reference chloride diffusion coefficient (m^2/s), Q_d is the activation energy (J/mol), R is the universal gas constant, equal to 8.3145 J/(mol·K), T_{ref} is a reference temperature equal to 293.15 K (20°C), and T is the absolute temperature.

The total chloride content (C_t) in concrete is composed of two components: free chloride, which can move freely within the porous network, and bound chloride, which is bound to the pore walls. The total chloride content can be mathematically expressed using the following relationship:

$$C_t = C_f + C_b \tag{6.11}$$

The relationship between bound and free chloride is mathematically described using the following equation (Aliasghar-Mamaghani et al., 2023):

$$C_{b(m)} = 1.5\left(C_{f(m)}\right)^{0.7} \tag{6.12}$$

where $C_{b(m)}$ and $C_{f(m)}$ are the concentration of free and bound chloride in percentage of cement mass. The mass convection across the boundary surface is taken into account through the boundary condition, which can be expressed as:

$$\vec{j}_{cl} \bullet \vec{n} = \beta_{cl}(C_f - C_{amb}) \tag{6.13}$$

where β_{cl} is a surface chloride transport coefficient, and C_{amb} is the concentration of chloride in the ambient environment.

6.4 Quantification of Uncertainty Propagation

As highlighted previously, the objective of the computational is to predict two Quantities of Interest (QoI) in the interior body of the girders. Specifically, these QoIs are the chloride content and probability of corrosion. The latter is associated with the quantity of the chloride that exceeds a threshold value, also known as C_{cr}.

The value of several model parameters affecting the intrusion of the chloride in concrete bridge girders is governed by uncertainty. This uncertainty extends to various boundary quantities, as well as model parameters within the constitutive law of the concrete material. This study adopts the surface chloride content, chloride diffusion coefficient, moisture diffusion coefficient, and critical chloride as key model parameters affecting the uncertainty of chloride-induced corrosion damage. It is thus important to quantitatively evaluate the propagation of uncertainty to the QoI. Among several approaches in the literature (Smith, 2013), the present study rely on Stochastic Spectral Methods (SSM), which establish spectral expansions (also called polynomial chaos expansions) to represent stochastic processes. In order to comprehend the nature of these methods, a stochastic process is defined with the purpose of evaluating a scalar field value, $\Phi(\underset{\sim}{x},t,\{Q\})$, which is also dependent on a set of random-valued parameters, {Q}.

$$\Phi(\underset{\sim}{x},t,\{Q\}) = \sum_{k=1}^{K}(\Phi_k(\underset{\sim}{x},t)\cdot\Psi_k(\{Q\})) \tag{6.14}$$

where $\Psi_k, k = 1,2,3, \ldots, K$, is a set of predefined polynomial functions in the parametric space and $\Phi_k(\underset{\sim}{x},t)$ is the time-dependent field term associated with the k^{th} polynomial. Each $\Phi_k(\underset{\sim}{x},t)$ is calculated through a finite element (piecewise) discretization in space and a step-by-step discretization in time, in accordance with the generalized trapezoidal rule.

The use of spectral expansions gives rise to the Stochastic Galerkin method, which in turn is the basis for the stochastic finite element analysis (Smith, 2013). A practical difficulty of the Stochastic Galerkin method is that the integration in the physical and parametric spaces is coupled. This would lead to a so-called intrusive computational algorithm, in the sense that integration in physical space cannot be decoupled from integration in the parametric space. This would require substantial modification of the finite element scheme, which is deemed undesirable. The present study will rely on the collocation method, which is also a type of SSM and enables the decoupling of the parametric and physical domain integrations during numerical computation. Several decisions were reached before applying the SSM. It is postulated that the distinct model parameters are mutually independent and have a normal distribution. Within the scope of this study, a truncated normal distribution is assigned to each model parameter. The parameters for the truncated normal distribution are established through a review of prior literature (Vassie, 1984; Weyers et al., 1994; McGee, 1999; Maekawa, 2008; FIB, 2013; Bažant and Jirásek, 2018; Aliasghar-Mamaghani et al., 2023). This assumption facilitates the calculation of the joint probability density function of the different model parameters, $\rho Q(q)$.

The range of model parameters for chloride diffusion coefficient, moisture diffusion coefficient, and critical chloride are identical in both girders. In particular, the minimum and maximum values for chloride diffusion coefficient were assigned to a value of 10^{-13} m^2/s and $10^{-11} m^2/s$, respectively (McGee, 1999). The corresponding values for the moisture diffusion coefficients were $5.80 \cdot 10^{-9}$ kg/m.s and $8.33 \cdot 10^{-8}$ kg/m.s, respectively (FIB, 2013; Aliasghar-Mamaghani et al., 2023), as shown in **Figure 6.3**.

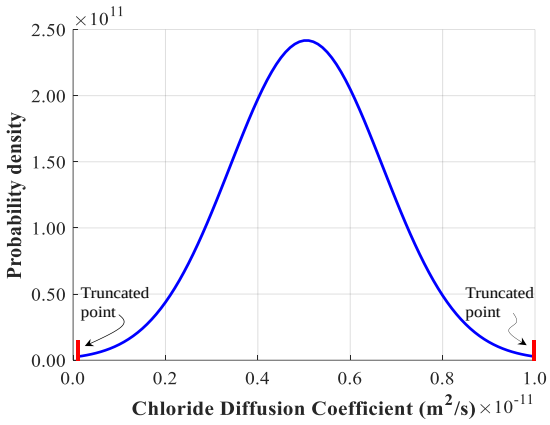

Figure 6.3. Truncated normal distribution for moisture diffusion coefficient.

The minimum value for the critical chloride corresponds to 0.1% (of cement mass) for both specimens, while the maximum value of the critical chloride were assigned 0.55% and 1.3% (of cement mass) for specimens exposed to deicing salts and saltwater spray, respectively. These values led to the selection of the mean value of 0.225% and 0.6% (of cement mass) for specimens exposed to deicing salts and saltwater spray, respectively (Aliasghar-Mamaghani et al., 2023). These values are consistent with the values reported in the literature (Vassie, 1984; Maekawa et al., 2003; FIB, 2013). The source of surface chloride was different for the two girders. As such, the minimum and maximum surface chloride for the Lesner bridge girder, which was exposed to saltwater spray, were assigned values of 0.21 kg/m^3 and 12.83 kg/m^3 (McGee, 1999). However, for the Aden bridge girder, which was exposed to deicing salts, the minimum and maximum surface chloride values were assigned to 0.24 kg/m^3, and 3.364 kg/m^3, respectively (Weyers et al., 1994).

Considering the influential parameters mentioned above, a total of six intervals per parameter were taken into account. This led to a total of 216 analyses for each girder, resulting in 432 analyses in total. The computational time for each analysis varied based on its

complexity. Leveraging the power of 128 CPU cores, the typical duration for each analysis was approximately 12 hours, accumulating to over 660,000 core-hours of runtime.

6.5 Algorithmic Implementation of Spectral Collocation Approach

The Stochastic Collocation (SC) approach provides a non-intrusive solution for solving problems involving two sets of spaces: the physical space and the parametric space. In this approach, a set of collocation points is generated from the parametric space using deterministic or stochastic methods.

The SC method relies on evaluating the governing differential equations at these discrete collocation points to obtain the solution. The discrete projections of the solution involve approximating the solution using integration techniques. By solving the resulting system of equations, which arises from evaluating the differential equations at the collocation points, the solution can be computed for the given set of parameters.

The spectral collocation was implemented as an n-dimensional trapezoidal rule of integration in the parametric space. The collocation points were used as quadrature points in the trapezoidal rule. Given the quantity of interest Y, that can be the concentration of a species at a specific location, at a specific time instant in the computational analysis, and the values of the probability density function, $\rho_{Q,j}$, and the weight coefficient W_j for each point j in the n-dimensional parametric space, the expected value of Y is given by:

$$E[Y] = \sum_{j=0}^{M} [\tilde{\sigma}_j Y_j] \tag{6.15}$$

where $\tilde{\sigma}_j$ is:

$$\tilde{\sigma}_j = \frac{\sigma_j}{\sum \sigma} \tag{6.16}$$

where $\sigma_j = \rho_{Q,j} \cdot W_j$. It is worth mentioning that the purpose of equation (6.16) is to regularize the parameter σ_j and ensure the following condition is met:

$$\sum_{j=1}^{M} \sigma_j = 1.0 \tag{6.17}$$

The probability of corrosion can be attained by incorporating the impact of critical chloride in the analyses. The mathematical description of corrosion probability at a given time can be obtained from the following equation:

$$p\left(\bar{t} \le t_1\right) \approx \sum_{i=1}^{N}\left[p\left(C_{cr} = C_{cr,i}\right)\left(1 - F_{c,t=t1}(C_{cr,i})\right) \cdot W_i \right] = \sum_{i=1}^{N}\left[\rho_i \left(1 - F_{c,t=t1}(C_{cr,i})\right) \cdot W_i \right] \tag{6.18}$$

where N is the number of collocations point for critical chloride, and F_c is the cumulative distribution of chloride.

6.6 Results

The analysis results for the Lesner bridge girder are presented first, followed by the results for the Aden Road bridge girder. **Figure 6.4**(a) shows the time histories of the total chloride, as well as the expected value and the 22nd and 78th percentiles for a strand situated away from the cross-sectional corner region. An important aspect to consider in the analysis of such specimens is the time at which the chloride concentration surpasses the critical value, as this can lead to a significant increase in the corrosion rate. Although this quantity can be obtained from a probabilistic standpoint by incorporating the critical chloride content in the analysis (and the evaluation of corrosion probability), it is of interest to compare the threshold value with the overall time history. Depending on the climatic conditions and with a threshold value of 0.60% (Aliasghar-Mamaghani et al., 2023), the time-to-first occurrence of significant

corrosion rate for some bridges (histories shown in gray) may be less than five years. The expected equivalent value is approximately 16 years, and there may be some bridges that are free from corrosion. The corresponding analysis results for a strand located in the vicinity of the cross-sectional corner are depicted in **Figure 6.4**(b). As expected, the distribution of total chloride for this particular strand is larger than the previous one. By considering a similar concept for the threshold value, the time-to-first occurrence of significant corrosion rate in this particular strand is even shorter.

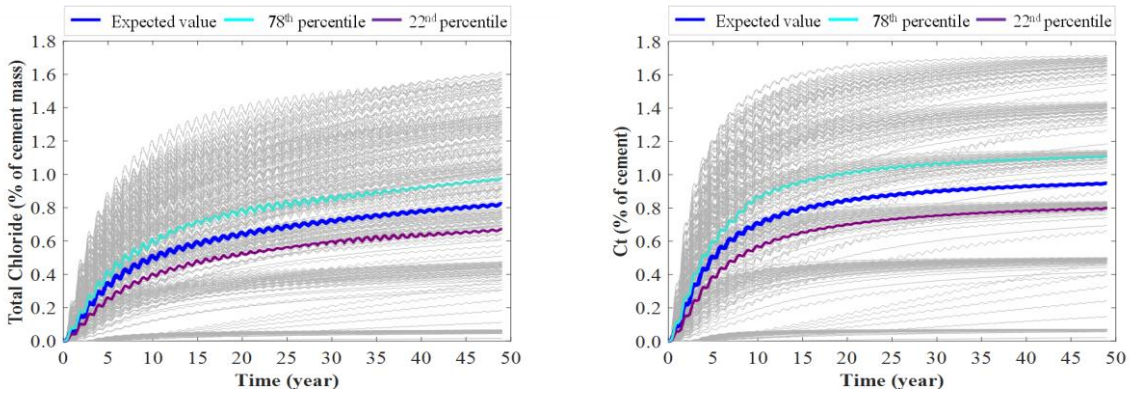

a) Strand away from the cross-sectional corner region

b) Strand in the vicinity of the cross-sectional corner region

Figure 6.4. Stochastic temporal evolution of chloride for two strands at different locations in Lesner bridge girder (I-section girder).

Figure 6.5(a) illustrates the time histories of chloride for a strand located away from the cross-sectional corner region in the Aden Road bridge girder. As the source of the chloride was deicing salt, the concentration in this specimen was relatively low. Assuming a threshold value of 0.22% for this bridge type, the time-to-first occurrence of significant corrosion rate for this strand, similar to the Lesner bridge girder, may vary significantly. **Figure 6.5**(b) displays the time history of the chloride concentration for a strand situated in the vicinity of the cross-

sectional corner region. As expected, the distribution of the time histories and expected value is higher for this specimen due to the strand's location in the corner region.

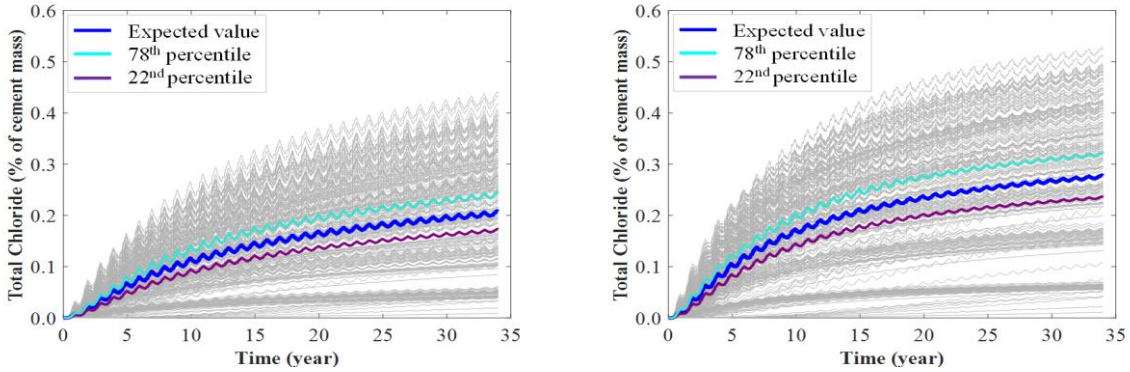

a) Strand away from the cross-sectional corner region

b) Strand in the vicinity of the cross-sectional corner region

Figure 6.5. Stochastic temporal evolution of chloride for two strands at different locations in Aden Road bridge girder (Box-section girder).

The analytical results yield valuable insights into the cumulative distribution of chloride content. **Figure 6.6** (a), demonstrates the cumulative distribution function (CDF) at various time intervals throughout the Lesner bridge girder's service life. Notably, assuming a threshold value of 0.6%, the CDF attains 99% after five years, while the corresponding value after 49 years is 10%. The analysis results for a strand near the cross-sectional corner region reveal lower values, which is related to the specific exposure conditions of that strands in the corner regions.

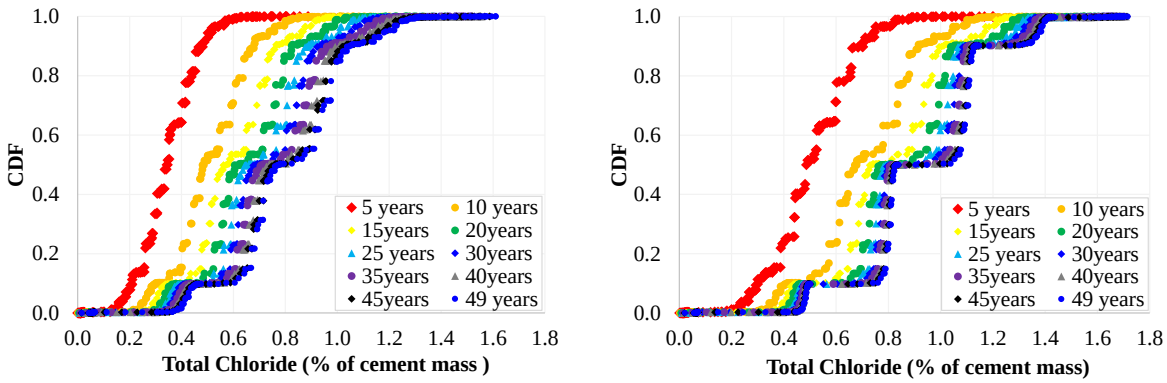

a) Strand away from the cross-sectional corner region

b) Strand in the vicinity of the cross-sectional corner region

Figure 6.6. Cumulative distribution of chloride for strands at different location in Lesner bridge girder (I-section girder)

The cumulative distribution of the total chloride for a strand away from the cross-sectional corner region in the Aden bridge girder is illustrated in **Figure 6.7**(a). It is observed that for a chloride concentration of 0.22%, the CDF reaches unity after five years, with varying values observed at other times. Additionally, the CDF of total chloride content for a strand located away from the cross-sectional corner region is depicted in **Figure 6.7**(b). The CDFs cover a broader spectrum of chloride concentrations, with lower values obtained for a particular total chloride content, which suggests a higher probability for corrosion.

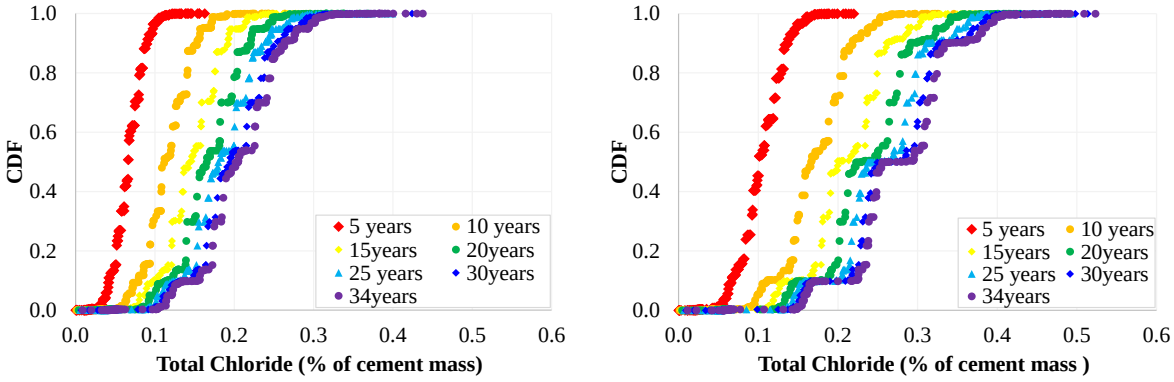

a) Strand away from the cross-sectional corner region

b) Strand in the vicinity of the cross-sectional corner region

Figure 6.7. Cumulative distribution of chloride for strands at different locations in the Aden Road bridge girder (Box-section girder).

A noteworthy inquiry concerns the precision of the stochastic collocation approach and its comparison with the results of Monte Carlo simulation. **Figure 6.8** presents the expected chloride values (or mean, μ) derived from Monte Carlo simulations for strands positioned at different locations within the Lesner bridge girder during its service life. As observed, the stochastic collocation approach yields a reliable estimation that corroborates the accuracy of our methodology versus Monte Carlo simulation. Particularly, the expected chloride values obtained through the Stochastic Collocation approach closely approximate those obtained via Monte Carlo simulation.

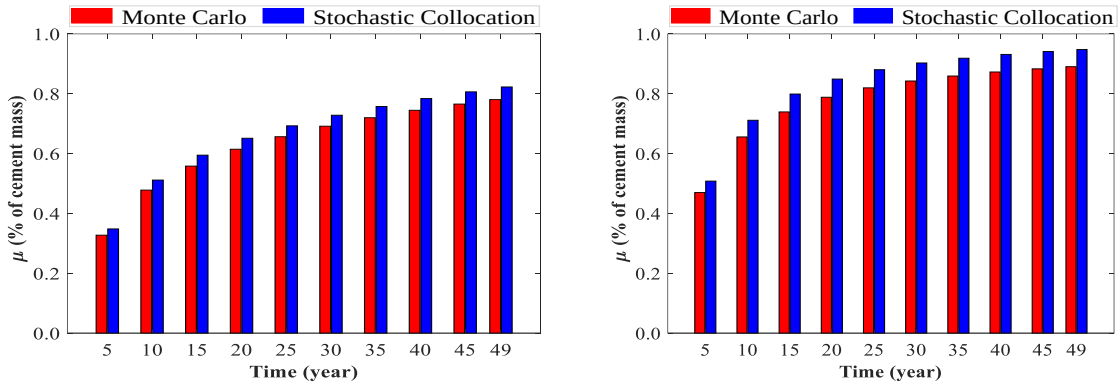

a) Strand away from the cross-sectional corner

b) Strand in the vicinity of the cross-sectional corner

Figure 6.8. Expected chloride content obtained from the Monte Carlo simulation and Stochastic Collocation approach for strands at different locations in Lesner bridge girder (I-section girder).

Within the same context, the expected chloride content for the Aden bridge girder is visually presented in **Figure 6.9**.

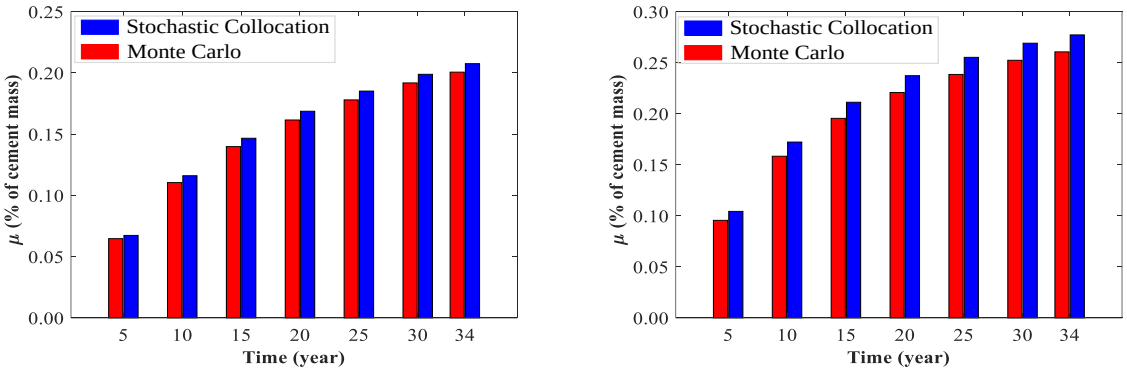

a) Strand away from the cross-sectional corner region

b) Strand in the vicinity of the cross-sectional corner region

Figure 6.9. Expected chloride content obtained from the Monte Carlo simulation and Stochastic Collocation approach for strands at different locations in Aden Road bridge girder (Box-section girder).

The subsequent stride in verifying the effectiveness of the Stochastic Collocation (SC) approach involves comparing the standard deviation (σ) and its correspondence with Monte Carlo (MC) results. In this regard, **Figure 6.10** presents the standard deviation of the expected chloride content for distinct strands within the Lesner bridge girder throughout the bridge's service life. Notably, the outcomes obtained from the SC analysis consistently exhibit a remarkable resemblance to those derived from MC analysis. This proximity between the SC and MC results reinforces the robustness and accuracy of the SC approach.

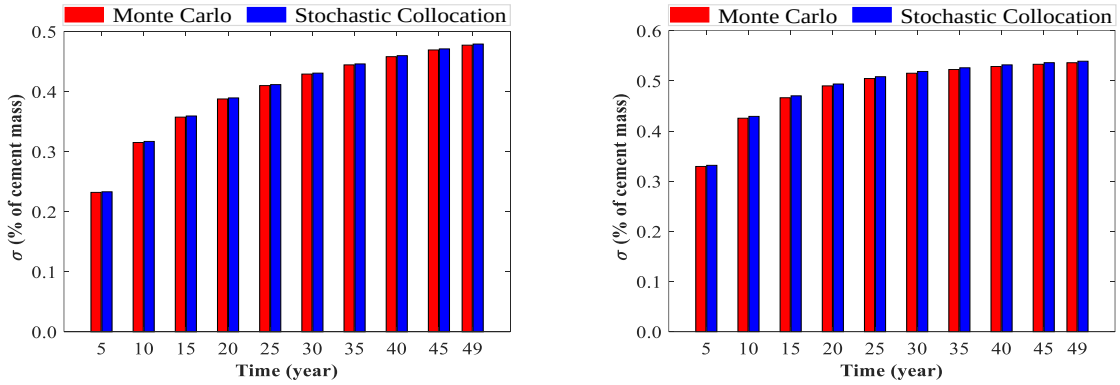

a) Strand away from the cross-sectional corner region

b) Strand in the vicinity of the cross-sectional corner region

Figure 6.10. Standard deviation of chloride content obtained from the Monte Carlo simulation and Stochastic Collocation approach for strands at different locations in Lesner bridge girder (I-section girder).

Proceeding in a similar vein, **Figure 6.11** portrays the standard deviation of strands located at different positions within the Aden bridge girder throughout its service life. Again, a comparison between the SC and MC analyses substantiates the accuracy and effectiveness of the SC method. The SC results exhibit a notable agreement with the corresponding outcomes obtained through MC, affirming the reliability and robustness of the SC approach.

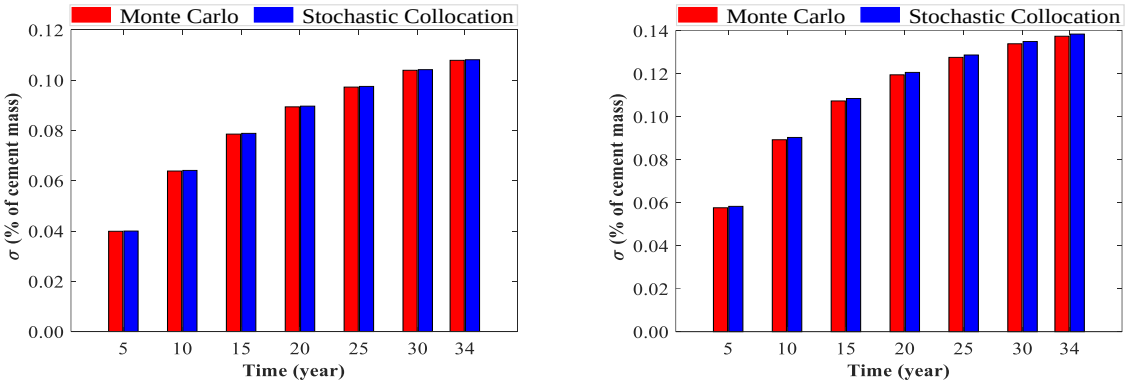

a) Strand away from the cross-sectional corner region

b) Strand in the vicinity of the cross-sectional corner region

Figure 6.11. Standard deviation of chloride content obtained from the Monte Carlo simulation and Stochastic Collocation approach for strands at different locations in Aden bridge girder (Box-section girder).

The probability of corrosion is the ultimate goal of this study. **Figure 6.12** presents the probability of corrosion for strands located in the vicinity and away from the cross-sectional corner region in two different bridge girders. As anticipated, the probability of corrosion for strands in the vicinity of the cross-sectional corner region is higher than for strands located away from this region in both girders. The probability of corrosion for the Lesner bridge girder (shown in **Figure 6.12**a) is in close agreement with the experimental observations presented in **Figure 6.2**d, where signs of corrosion were observed for both strands in the vicinity of and away from the corner region. Along the same lines, the probability of corrosion for the Aden Road bridge girder (shown in **Figure 6.12**b) is consistent with experimental observations shown in **Figure 6.2**b.

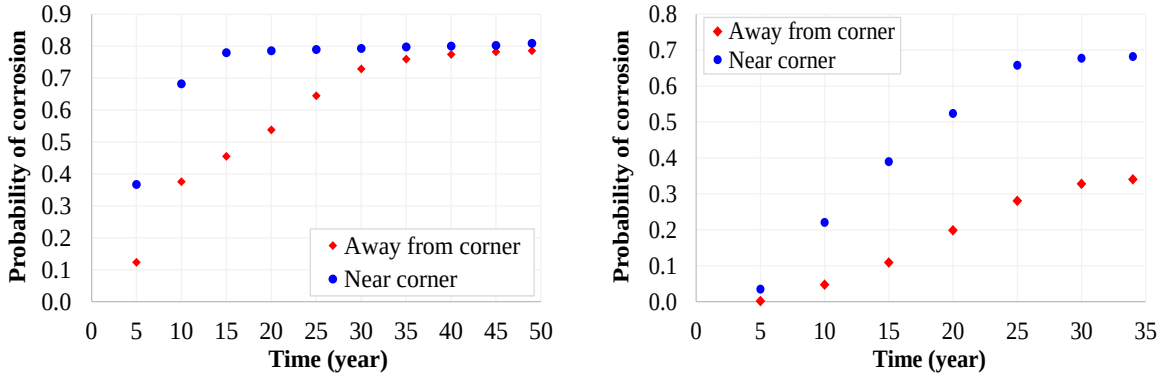

a) Strands in Lesner bridge girder (I-section girder).

b) Strands in Aden Road bridge girder (Box-section girder).

Figure 6.12. Probability of corrosion for strands near and away from the cross-sectional corner region in two different bridge girders.

6.7 Conclusions

This study investigated the impact of uncertainties associated with chloride ingress in prestressed concrete bridge girders. An uncertainty quantification study using a multi-physics scheme is conducted for two quantities of interest, namely the chloride content of strands at different locations, and probability of corrosion. The study focused on two prestressed concrete bridge girders that have been in service for 34 and 49 years. The finite element framework employs a nonlinear Multiphysics scheme that accounts for coupled heat, moisture, and chloride transport, making it a robust and accurate analysis tool. Four influential model parameters, including moisture and chloride diffusion coefficient, surface chloride, and critical chloride, are considered for the analysis, with each parameter divided into six intervals to account for variability. The stochastic collocation approach is used in the analysis to obtain the expected value of chloride for each time interval during the service life of the girders. The analytical model was found successful in capturing the expected value of chloride for strands situated in

both the vicinity and away from the cross-sectional corner region. Additionally, the model provides valuable insights into the cumulative distribution of chloride at specific time intervals, which is a critical parameter in assessing the probability of corrosion. The results from CDF reveal that the probability of corrosion is high for bridges after 20 years of service, with the CDFs for both bridges located in or away from the coastal zone showing a similar level of congestion at that time interval. Overall, the computational framework and analysis provide essential information for bridge engineers to assess the risk of corrosion in bridge girders and develop appropriate maintenance and repair plans.

Chapter 7
Conclusions and Recommendations for Future Research

This chapter provides a summary of the main contributions presented in this dissertation, together with pertinent conclusions reached. The chapter is completed through a series of suggestions for future research, building on the findings of the present study.

7.1 Summary and Conclusions

A computational framework was proposed to provide a quantitative assessment of the impact of corrosion on the capacity of eight prestressed concrete bridge girders that underwent experimental testing. Two types of nonlinear models were utilized in the analysis: beam models with a fiber sectional law and truss models, with the latter approach being used for shear failure analyses. These models were combined with uniaxial stress-strain laws for concrete and steel, as well as a procedure to incorporate the influence of visually observed corrosion damage on the resistance of a girder section.

The analytical models utilized were capable of accurately reproducing the load-displacement response and failure modes for the prestressed concrete bridge girders. Additional analyses facilitated the determination of the significant impact of corrosion on the flexural capacity of several girders that displayed visible corrosion damage. The use of the flexural strength equations in the AASHTO code provided satisfactory estimates of the peak capacity when accounting for corrosion section loss. However, it overestimated the strength of a significantly damaged girder with a box section. A crucial consideration for box-girders is the

potential for trapped water in the hollow space, which may exacerbate strand degradation. A conservative approach for evaluating the flexural capacity of such girders is to apply a small reduction to the area of all strands located below the level of the potentially trapped water. Corrosion damage to the longitudinal strands at the bottom of the section had minimal impact on the shear strength, but it significantly affected the deformability of a girder that failed in shear.

This dissertation also introduced a computational simulation framework to describe chloride ingress in prestressed concrete bridge girders. The framework employed a finite element formulation that considered heat transfer, moisture flow, and chloride transport. Material test data from literature were utilized to calibrate the framework, and data from chloride measurements conducted on two prestressed girders, exhibiting corrosion-induced damage and removed from two bridges in Virginia, were employed for validation purposes. Further analysis demonstrated the significance of advective chloride transport entailed by moisture flow, as neglecting this mechanism resulted in a significant underestimation of the chloride content. The analysis satisfactorily reproduced the experimentally measured chloride content distributions with depth, accounting for the storage of the girders away from the bridges before testing. The comparison of the chloride content with the respective critical value estimates indicated that corrosion damage was expected for both girders, especially for strands in the vicinity of the sectional corners, which is consistent with the actual corrosion damage observed. The simplified, design-oriented equations in the FIB code to determine the evolution of chloride ingress generally underestimated the chloride content, implying that these equations may not provide conservative results when evaluating the likelihood of corrosion and the anticipated corrosion initiation time for a bridge girder.

The third part of this dissertation presents a novel approach for accurately modeling the intrusion of corrosion-inducing chloride ions into concrete and the subsequent mechanical damage. The proposed approach involves Multiphysics descriptions of heat transfer, moisture flow, chloride transport, electrochemical reactions and mechanical damage. It incorporates constitutive laws for concrete that capture the coupling between cracking and chloride-moisture transport. The Multiphysics scheme was calibrated with a large set of experimental data on prismatic and cylindrical specimens, and subsequently applied to two bridge girders taken from Virginia after 49 and 34 years of service.

The analyses on concrete specimens demonstrated the importance of coupling between various phenomena, particularly advection-diffusion coupled with mechanical damage. Furthermore, the analyses of the girders provided reliable estimates of the experimentally observed behavior of both the chloride-induced corrosion damage in prestressing steel material and the surrounding concrete. The study also compared the proposed coupled Multiphysics approach with a case that did not consider chemo-mechanical damage, highlighting the importance of cracking in the propagation of damage. Additionally, the limitations of the simplified FIB model code in estimating the service life of the girder were shown. These findings emphasize the significance of considering chemo-mechanical coupling for accurately predicting the performance and durability of concrete structures.

The last part of this dissertation quantifies the uncertainty governing two significant quantities, namely, the chloride content temporal evolution and the corrosion initiation time for strands located at critical locations of a girder section. The quantification is conducted by means of a stochastic collocation approach, using the modeling scheme described in Chapter 4. Uncertainty was assumed to be the result of propagated aleatory uncertainties governing four

input model parameters, i.e. the moisture and chloride diffusion coefficients, surface chloride, and critical chloride. The uncertainty quantification study reveals a high probability of corrosion occurring after 20 years of service. The results of this study provide critical information for bridge engineers to assess the risk of corrosion in bridge girders and develop appropriate maintenance and repair plans.

7.2 Major Contributions

The present study has provided the following contributions:

- A conceptually simple, computationally efficient and accurate simulation framework for quantitatively assessing the impact of visually observed corrosion damage on the capacity of prestressed concrete bridge girders.
- Evaluation of the accuracy of design-oriented equations, based on the AASHTO specification, for calculating the residual flexural and shear strength of damaged girders.
- A Multiphysics computational scheme to describe chloride ingress in prestressed concrete bridge girders, accounting for actual climatic conditions in the vicinity of a bridge.
- Investigation of the significance of advective chloride transport (affected by moisture movement).
- Evaluation of the capability of the design equations in the FIB code to provide accurate estimates of the chloride content time histories at critical locations of prestressed girder sections.
- Mathematical formulation and computational implementation of a fully coupled, thermo-hydro-chemo-mechanical model, accounting for the occurrence of corrosion-induced cracking and the impact of cracks on the chloride ingress mechanisms.

- Phenomenological laws accounting for the electrochemical corrosion reaction kinetics, the formation of corrosion products and the volumetric expansion associated with these products.
- Quantification of impact of cracking on the chloride content evolution at the locations of prestressing strands.
- Quantification of uncertainty governing decision variables for the maintenance of bridges, such as the corrosion initiation time and the chloride content evolution.

7.3 Recommendations for future research

- The proposed algorithm has demonstrated its effectiveness in estimating the shear and flexural capacity of bridges in a specific region. To further validate its applicability, it is recommended to apply the algorithm to bridges in other regions and assess its performance. Specifically, investigating the impact of corrosion on the ultimate shear strength of bridges would be valuable. Furthermore, the algorithm's ability to accurately predict the shear strength of prestressed concrete girders with significant visual damage in shear reinforcement is of interest and can be explored further. These investigations can provide insights into the algorithm's robustness and its potential for wider application.
- Investigation of performance for bridges located in other states (e.g., Texas, Florida, California), to see impact of different climate conditions on anticipated durability.
- Account for impact of extreme climatic events.
- Account for impact of mechanical damage due to other factors (e.g., traffic, natural hazards such as earthquakes).

- Extend investigation to building structures.
- Account for other potentially important factors which may impact durability, e.g., carbonization, alkali-silica reaction (if applicable).
- Investigate efficient sampling/quadrature approaches to be used in conjunction with stochastic collocation method. These approaches may allow finer discretization in parametric space, while also circumventing the so-called curse of dimensionality (i.e., the huge increase in the number of runs required if we increase the number of intervals and we are considering the variability of many parameters).

Appendix A.
Computation of Solar Irradiance for Solar Radiation

This section provides a comprehensive overview of the solar irradiance, which can be developed in the following form:

$$I = I_n \cos\theta \tag{A. 1}$$

where θ is the incidence angle showing the angle between sun rays and the normal to the surface, and I_n is the solar energy on the earth surface (Kehlbeck, 1975). The value of $\cos\theta$ is obtained from the following equation.

$$\begin{aligned}\cos\theta = {} & \sin\delta \sin\varphi_g \cos\beta - \sin\delta \cos\varphi_g \sin\beta \cos\gamma + \cos\delta \cos\varphi_g \cos\beta \cos\tau \\ & + \cos\delta \sin\varphi_g \sin\beta \cos\gamma \cos\tau + \cos\delta \sin\beta \sin\gamma \sin\tau\end{aligned} \tag{A. 2}$$

where φ_g is the geographic latitude, γ is the surface azimuth angle, i.e., the angle between the projection of the normal to the surface and the local meridian, with zero due south, westward positive, τ is the hour angle, counting from noon and changing $15°$ per hour, with positive and negative signs for the morning and afternoon hours, respectively, β is the surface inclination angle, i.e., the angle between the plane of the surface and the horizontal, and δ is the solar declination, defined as:

$$\delta = 23.45 \sin\left[360\left(284 + D\right)/365\right] \tag{B. 3}$$

where D is the day of the year. The value of I_n is obtained as:

$$I_n = I_{sc}\, K_{tr}\, d_e \tag{A. 4}$$

where the solar constant I_{sc} is the rate of solar energy per unit time at all wavelengths incident received on a surface normal to the sun's rays, outside the earth atmosphere (Iqbal, 2012), K_{tr}

is the transmission factor, accounting for attenuation of solar radiation, and d_e is the mean distance of the earth from the sun, the value of which is estimated herein using the following equation.

$$d_e = 1.000110 + 0.034221\ \cos B + 0.001280\ \sin B + 0.000719\ \cos 2B + 0.000077\ \sin 2B \quad \text{(A. 5)}$$

where,

$$B = 360(D-1)/365 \quad \text{(A. 6)}$$

The transmission factor K_{tr} in Equation (A. 4) can be obtained using the following expression.

$$K_{tr} = 0.9^{\,k_a t_u / \sin(\theta_a + 5^\circ)} \quad \text{(A. 7)}$$

where k_a is the ratio of the atmospheric pressure to that at sea level (assumed here to be equal to 1), t_u is the turbidity factor accounting for the air pollution and clouds, and θ_a is the solar altitude.

The equations accounting for solar radiation require the calibration of two parameters, namely, I_{sc} and t_u. The present study has used I_{sc} = 1353 W/m^2 and t_u = 2, in accordance with recommendations of NASA (NASASP-8005, 1971) and Dilger et al. (1983), respectively.

The heat transfer due to solar radiation is applied in the analyses during the steps corresponding to the presence of daylight, i.e. the part of a day between the sunrise time, t_{sr}, and the sunset time, t_{ss}. For a given day in the year, the two values t_{sr}, t_{ss} are estimated herein using the following equations.

$$t_{sr} = 12 - \left[\cos^{-1}\left(-\tan\delta \tan\varphi_g\right)\right]/15 \quad \text{(A. 8)}$$

$$t_{ss} = 12 + \left[\cos^{-1} \left(-\tan \delta \tan \varphi_g \right) \right] / 15 \quad \text{(A. 9)}$$

The geographic latitude for the location of the Lesner bridge was φ_g = 36.8529˚, while for the Aden Road bridge it was φ_g = 38.6415˚.

Appendix B.
SUPG Stabilization for Finite Element Analysis of Advection-Diffusion Problem

The SUPG technique adds the following term to the weak form for a linear element with zero source term (Donea and Huerta, 2003):

$$\iiint_{\Omega^e} \vec{v} \bullet \vec{\nabla} w \cdot \tau \cdot [\vec{v} \bullet \vec{\nabla} C_f \,]\, dV \tag{B. 1}$$

Accordingly, the coefficient array $\left[K_{cl}^{(e)}\right]$ should be updated by adding the following term:

$$\left[K_{SUPG}\right] = \iiint_{\Omega^e} \left[B\right]^{\mathrm{T}} \{v\}\, \tau \{v\}^{T} \left[B\right] dV \tag{B. 2}$$

where

$$\tau = \frac{\bar{v}}{\|v\|^2} \tag{B. 3}$$

$$\bar{v} = 0.5(\bar{\zeta} \cdot v_{\zeta} \cdot h_{\zeta} + \bar{\eta} \cdot v_{\eta} \cdot h_{\eta}) \tag{B. 4}$$

$$\bar{\zeta} = \coth(P_{e\zeta}) - \frac{1}{P_{e\zeta}} \tag{B. 5}$$

$$P_{e\zeta} = \frac{v_{\zeta} \cdot h_{\zeta}}{2D_{cl}} \tag{B. 6}$$

$$v_{\zeta} = v \cdot e_{\zeta} \tag{B. 7}$$

where h_{ζ} is the element size and e_{ζ} is the unit vector in the direction of parametric axis, ζ , $P_{e\zeta}$ is the Peclet number that quantifies the diffusion or advection dominated flow, along ζ axis. Similar descriptions hold for $\bar{\eta}$ and h_{η} along the η -parametric axis. **Figure B. 1** compares the profile of chloride based upon different approaches. For a relatively small Peclet number, or in diffusion-dominated flow, the analysis could capture the exact solution even without SPUG

stabilization technique. On the other hand, the SPUG stabilization is deemed necessary in advection-dominated flow, as shown **Figure B. 1**(b), where the perturbation induced by the fluid velocity vector is well captured by the SPUG stabilization technique.

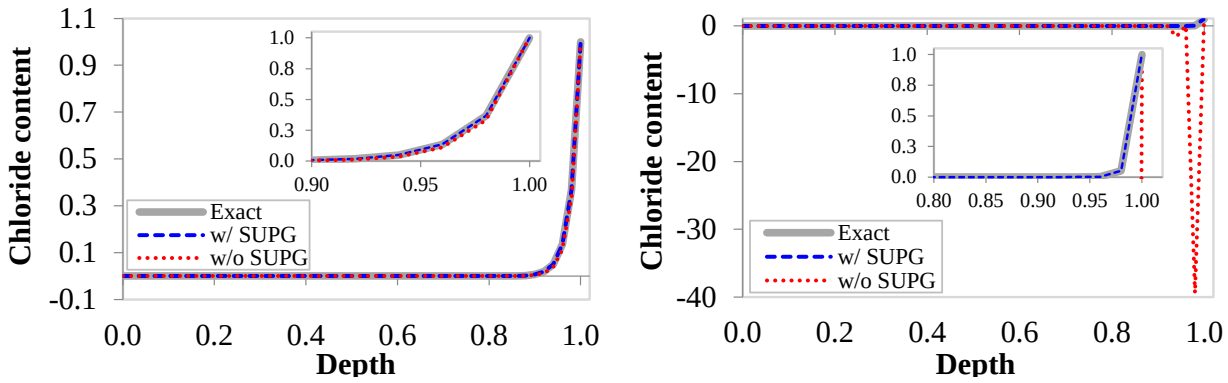

(a) $P_e = 0.5$ (b) $P_e = 1.5$

Figure B. 1. Sensitivity of the analysis to different Peclet number

Appendix C.
Mathematical Proof for Diameter Loss by Corrosion Rate

This section aims to provide mathematical proof for equation (5.32). To facilitate our analysis, we will assume that each wire in a strand has a cylindrical shape, as illustrated in **Figure C. 1**.

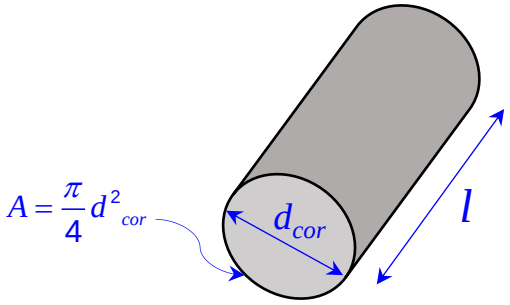

Figure C. 1. Parameters specifying the geometry of a wire

The rate of the mass loss can be defined by the following equation:

$$m_1 = -l \cdot \pi \cdot d_{cor} \cdot \dot{r}_m \cdot dt \tag{C. 1}$$

where l is the length of the wire, d_{cor} is the diameter of the wire, $\dot{r}_m$ is the mass loss per unit surface area per unit time, and dt a small time increment. If we take the cross-sectional geometry of the wire into consideration, we can also express the actual mass loss using the following equation:

$$m_2 = l(A + dA) \cdot \rho_s - l \cdot A \cdot \rho_s \tag{C. 2}$$

where A is the cross-sectional area, and dA denotes the infinitesimal variation in cross-sectional area. By combining equations (C. 1) and (C. 2), we obtain the following expression:

$$\frac{dA}{dt} = -\frac{\pi \cdot d \cdot \dot{r}_m}{\rho_{cor}} \tag{C. 3}$$

Using the chain rule of differentiation, we can write the following expression:

$$\frac{dA}{d(d_{cor})} \cdot \frac{d(d_{cor})}{dt} = -\frac{\pi \cdot d_{cor} \cdot \dot{r}_m}{\rho_s} \tag{C. 4}$$

the first term on the left-hand side, corresponds to:

$$\frac{dA}{d(d_{cor})} = \frac{d}{dt}\left(\frac{\pi}{4} {d_{cor}}^2\right) \Rightarrow \frac{dA}{d(d_{cor})} = \frac{\pi}{2} d_{cor} \tag{C. 5}$$

Given equations (C. 4) and (C. 5), the rate of diameter loss can be expressed by the following expression:

$$\frac{d(d_{cor})}{dt} = -\frac{2\dot{r}_m}{\rho_s} \tag{C. 6}$$

If we consider a specific time instant, we can omit the *dt* term on the left-hand side and the time rate on the right-hand side, which gives:

$$d_{cor} = \frac{-2r_m}{\rho_s} \tag{C. 7}$$

Writing this equation in the rate form gives the following equation, which is identical to equation (5.32):

$$\dot{r}_{cor} = \frac{-\dot{r}_m}{\rho_s} \tag{C. 8}$$

Appendix D.
Mathematical Proof for Increased Volume of Corrosive Material

This section aims to present a mathematical proof for equation (5.34) in a clear and concise manner. To aid in our explanation, we copy **Figure 5.4** herein and name it **Figure D. 1**.

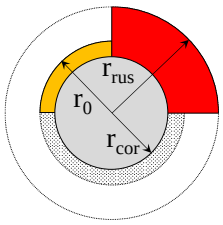

Figure D. 1. Parameters specifying the volumetric expansion of a wire

In this calculation, we will consider a wire of length 1.0 for simplicity. To begin, we need to define the total area (or volume) of the strand after expansion. We can do so by using the following definition:

$$\pi r_{rus}{}^2 = \pi r_{cor}{}^2 + \pi(r_0{}^2 - r_{cor}{}^2)\alpha_e \tag{D. 1}$$

By removing the constant factor on either side of the equation, we can simplify it to the following:

$$r_{rus}{}^2 = \alpha r_0{}^2 + r_{cor}{}^2(1-\alpha_e) \tag{D. 2}$$

The rate of mass loss has been previously defined in equation (5.33). Therefore, we shall proceed to reshape it in the following form:

$$r_{cor}^{\ 2} = r_0^{\ 2}(1 - \gamma) \tag{D. 3}$$

We can derive the following expression by combining equations (D. 2) and (D. 3) together:

$$r_{rus}^{\ 2} = \alpha_e r_0^{\ 2} + r_0^{\ 2}(1-\gamma)(1-\alpha_e) \tag{D. 4}$$

By taking the positive root of r_{rus}, we arrive at the following equation, which is equivalent to equation (5.33):

$$r_{rus} = r_0\sqrt{1 + \gamma(\alpha_e - 1)} \tag{D. 5}$$

Appendix E.
Mathematical Solution for a Scalar Field Problem: Heat Transfer

The first step in analyzing a scalar field problem is to validate the analysis methodology by comparing it with an exact solution. This section provides an overview of the problem, an exact solution, and an example to demonstrate the analysis process. While this section focuses on a linear time-dependent heat conduction problem, the methodology can be applied to other fields as well.

As discussed earlier, we can obtain the governing differential equation for heat transfer by applying the conservation of energy principle. For the purposes of this discussion, we will focus on a one-dimensional, time-dependent model:

$$\frac{\partial T}{\partial t}\cdot\rho\cdot c+\frac{\partial}{\partial x}(-k\frac{\partial T}{\partial x})=0 \tag{E. 1}$$

To increase the simplicity of the notation, let us redefine our symbols as follows:

$$\dot{T}\cdot D_T-T''=0 \tag{E. 2}$$

Here, T is a function of both space and time. To proceed, we will discretize the space-time domain as follows:

$$T(x,t)=F(x)\cdot G(t) \tag{E. 3}$$

Given this definition, it follows that F(x) is a function of space and G(t) is a function of time. Based on this, we can proceed as follows:

$$\dot{T}=\frac{\partial T(x,t)}{\partial t}=F(x)\cdot\dot{G}(t) \tag{E. 4}$$

$$T' = \frac{\partial T(x,t)}{\partial x} = F'(x) \cdot G(t) \tag{E. 5}$$

$$T'' = \frac{\partial^2 T(x,t)}{\partial x^2} = F''(x) \cdot G(t) \tag{E. 6}$$

Given the above, equation (E. 2) can be cast into the following form:

$$\frac{F''(x)}{F(x)} = \frac{\dot{G}(t)}{D_T \cdot G(t)} \tag{E. 7}$$

now, we may posit that equation (E. 7) corresponds to a constant value, which we will denote as $-c^2$. With this assumption in place, we can transform the partial differential equation (PDE) into two separate ordinary differential equations (ODE):

$$F''(x) + c^2 F(x) = 0 \tag{E. 8}$$

$$\dot{G}(t) + c^2 D_T G(t) = 0 \tag{E. 9}$$

Let us consider a one-dimensional bar, with a length of 1m, an initial condition of T_0=20°C, and a zero-boundary conditions, as depicted in **Figure E. 1**:

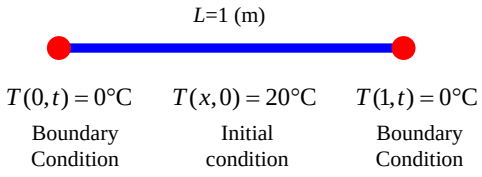

Figure E. 1. One dimensional bar set-up

Considering the boundary conditions, the solution to equation (E. 8), which is a second-order homogeneous ODE, takes the following form:

$$F_n(x) = A_n \sin(\frac{n\pi}{l} x) \tag{E. 10}$$

where c= $n\pi / l$, and n=1,2,3, …. Along the same lines, the solution to equation (E. 9) is given by:

$$G_n(t) = C_n \cdot e^{-c^2 \cdot D_T \cdot t} \tag{E. 11}$$

Now we can find the solution to PDE problem:

$$T(x,t) = F(x) \cdot G(t) \Rightarrow T(x,t) = D_n \cdot \sin(\frac{n\pi}{l} x) \cdot e^{-c^2 \cdot D_T \cdot t} \tag{E. 12}$$

where D_n=$A_n C_n$. Considering Fourier series, we can obtain the coefficient from the following equation:

$$D_n = (\frac{2}{l}) \int_0^L f(x) \sin(\frac{n\pi x}{l}) dx \tag{E. 13}$$

for the case of this study, we can further translate equation (E. 13) in the following form:

$$D_n = \frac{40}{n\pi}[1 - \cos(n\pi)] = \frac{40}{n\pi}[1 - (-1)^n] \tag{E. 14}$$

The solution to the problem is given by the following equation:

$$T(x,t) = \sum_{n=1}^{\infty} D_n \sin(\frac{n\pi}{l} x) e^{-c^2 \cdot D_T \cdot t} \tag{E. 15}$$

With the exact solution now established, we can proceed to compare the results of the analysis with this solution. **Figure E. 2** displays a comparison between the finite element analysis, represented by dotted lines, and the exact solution. It can be observed that the finite element analysis is capable of precisely capturing the transfer of heat in both space and time, with a high degree of accuracy.

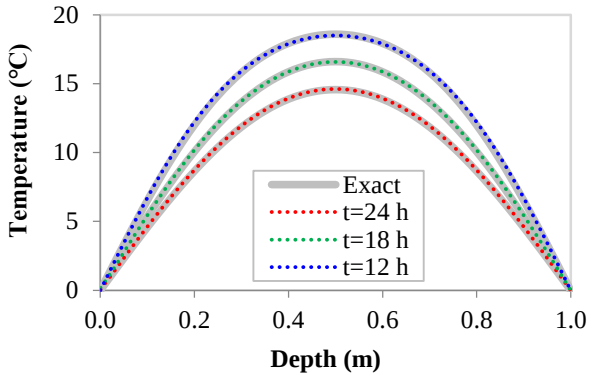

Figure E. 2. Heat transfer in 1D bar using finite element analysis (dotted lines) and exact solution

This section concludes by presenting a comparison between an analytical model for heat conduction and experimental tests conducted on concrete specimens. The experimental data reported by Bai et al. (2020) were used to validate the analytical model. The experiment involved the use of concrete cylinders, which were isolated on the sides and bottom. Depending on the experiment type, the specimens were exposed to different heat sources on the top with temperatures 40°C and 60°C. **Figure E. 3**a provides a comparison between the analytical model and the experimental data for a 12-day exposure period, while **Figure E. 3**b displays the profile at day 10. The analysis accurately reproduces the experimental data with good precision.

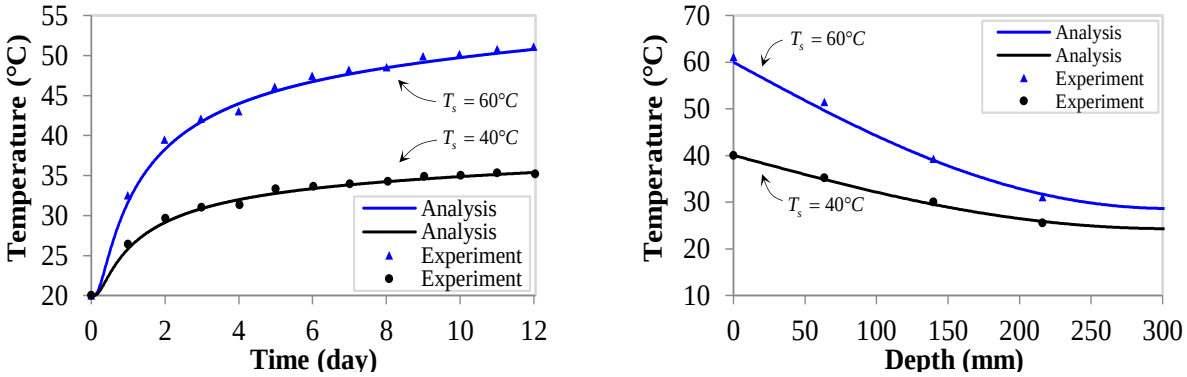

(a) Temperature evolution of temperature at $x = 63.5\,\text{mm}$

(b) Temperature profile after ten days

Figure E. 3. Heat transfer in cylindrical specimen using experimental data reported in Bai et al. (2020)

Appendix F.
Prediction of Chloride in Concrete Structures Using Machine Learning Algorithms

This appendix pursues an alternative approach for predicting the content of chloride in concrete bridge structures. Contrary to the main body of this dissertation, which pursued mathematically rigorous, high-fidelity finite element models, this appendix pursues machine learning (ML) algorithms. Various ML algorithms, including linear regression (LR), least absolute shrinkage and selection (Lasso), multilayer perceptron artificial neural network (MLP-ANN), support vector machine (SVM), Gaussian process regression (GPR), random forest (RF), and voting regressor (VR), are employed to quantify the chloride ion content in reinforced concrete structures. Multiple concrete mixture properties obtained from experimental tests in the literature are considered as input features. The accuracy of each machine learner is evaluated using different metrics, namely the coefficient of determination (R^2), root mean square error (RMSE), mean absolute error (MAE), and mean absolute percentage error (MAPE). The results demonstrate that ML techniques can effectively predict chloride content while investigating the influence of key parameters such as concrete mixtures on the intrusion of chloride in concrete structures.

Research Design and Method

This section presents an overview of the mathematical foundations of various machine learning algorithms.

Machine Learning Algorithms

Linear Regression (LR)

Linear Regression (LR) is a straightforward machine learning technique that establishes a linear relationship between the response variable and the predictor variables. The LR model can be expressed in the following form:

$$y_{out} = \sum_{i=1}^{N} w_i x_i + \varepsilon \tag{F. 1}$$

where y_{out} denotes the output, ε represents the expected error, w_i is the regression coefficient, and x_i is the input. In order to optimize the efficiency of equation (F. 1) and minimize the error between the predicted output (y_{out}) and the actual result (d), Mean Squared Error (MSE) measure is deployed. The mathematical expression for MSE is given as:

$$MSE = \frac{1}{N} \sum_{i=1}^{N} (y_{out} - d)^2 \tag{F. 2}$$

The above equation involves N number of data points in the dataset. To estimate the parameters in the Linear Regression (LR) model, three assumptions are typically made: statistical independence and identical distribution, Gaussian distribution of the errors, and stationarity of the data (Haykin, 2009).

Least Absolute Shrinkage and Selection (Lasso)

Lasso is a regression technique that overcomes some of the limitations associated with ordinary least squares (OLS), such as prediction accuracy and interpretability. It achieves this by setting some coefficients to zero and shrinking the others, effectively combining the strengths of ridge regression and subset selection methods (Tibshirani, 1996). The Lasso model

can be represented in an equivalent Lagrangian form, which is developed as follows (Friedman, 2017):

$$\widehat{\beta}^{Lasso} = \underset{\beta}{\operatorname{argmin}} \left\{ \frac{1}{2} \sum_{i=1}^{N} (y_i - \beta_0 - \sum_{j=1}^{p} x_{ij} \beta_j)^2 + \lambda \sum_{j=1}^{p} \left| \beta_j \right| \right\} \quad \text{(F. 3)}$$

where N and p are the number of samples and features, respectively. Note the last term on the right-hand side is the L_1 lasso penalty, which enforces a constraint that makes the solution nonlinear with respect to the input variable y_i (Friedman, 2017).

Multilayer Perceptron Artificial Neural Network (MLP-ANN)

The MLP-ANN is a subclass of feedforward neural networks that is known for its strong learning capabilities. The ANN model is designed to resemble the behavior of the human brain through a set of organized principles (Jain et al., 1996). The architecture of an MLP includes three major components: an input layer containing input variables, one or more hidden layers to perform processing, and an output layer that contains the outcome. These layers are interconnected by weighted links (Duda and Hart, 1973). In an MLP, each hidden unit computes a net activation through the weighted sum of the inputs to the perceptron. The net activation can be expressed as follows:

$$net_j = \sum_{i=0}^{k} x_i w_{ji} = w_j^t x \quad \text{(F. 4)}$$

where the indices i and j refer to the input and hidden layers, w_{ji} is the synaptic weight associated with the input-to-hidden layer, k is the number of hidden nodes, and x_i is the input signal. Each perceptron in a hidden layer of MLP-ANN uses an activation function to generate an output. There are different forms of activation functions such as threshold, piecewise linear,

Gaussian, hyperbolic tangent, or sigmoid. The most commonly used activation function is the sigmoid function, which has the following form (Duda and Hart, 1973; Jain et al., 1996; Haykin, 2009):

$$f(net_j) = \frac{1}{1 + e^{w_{ji} \cdot net_j}} \tag{F. 5}$$

There are various algorithms available for training MLPs, and among them, the back-propagation (BP) method is the most commonly used. The BP algorithm is a gradient-descent technique that involves two fundamental steps: forward pass and backward pass. The forward pass computes the output and the error associated with that layer, whereas the backward pass updates the synaptic weights based on the output errors (Haykin, 2009).

Support Vector Machine (SVM)

SVM is a binary learning machine method used in ML for both nonlinear regression and pattern-classification problems (Haykin, 2009). The SVM optimizes the regression problem through an optimization scheme with robustness as the primary objective. In this approach, a loss function, also known as an ε-intensive function, is minimized (Haykin, 2009). The first step in SVM training is to increase the dimensionality of the inputs by mapping from low- to high-dimension, which is achieved through the use of a nonlinear kernel function to transition between spaces (Clarke et al., 2005). The second step in training is to find an objective function [$f_{SVM}(x, w)$] with a maximum distance ε from the measured data.

$$f_{SVM}(x, w) = \sum_{i=1}^{n} w_i K_i(x) + b \tag{F. 6}$$

where $K_i(x)$ is the kernel functions which increases the dimension of the input data.

Gaussian Process Regression (GPR)

A Gaussian process is a collection of random variables, any finite number of which have a joint Gaussian distribution (Rasmussen, 2003). The distribution function of a Gaussian process can be expressed as follows:

$$f(x) \sim \mathcal{GP}((m(x), k(x, x')) \tag{F. 7}$$

where $\mathcal{GP}$ is the Gaussian Process and the mean function is

$$m(x) = \mathbb{E}[f(x)] \tag{F. 8}$$

where $\mathbb{E}$ is the expectation function, and the covariance function is given by:

$$k(x, x') = \mathbb{E}[(f(x) - m(x))(f(x') - m(x'))] \tag{F. 9}$$

It is important to note that the covariance function used in GPR is also referred to as the kernel function, as it heavily impacts the outcome of GPR. Additionally, a mean function is often used with a zero value (Rasmussen, 2003; Schulz et al., 2018). Assuming a linear model with Gaussian noise, the target value can be obtained in the following form:

$$y = f(x) + \varepsilon \tag{F. 10}$$

where the independent Gaussian noise is given by:

$$\varepsilon \sim \mathcal{N}(0, \sigma_\varepsilon^2) \tag{F. 11}$$

As previously mentioned, the kernel function is a crucial component in GPR prediction as it determines the similarity between input data points. The choice of kernel function depends

on the expected patterns of data and the desired level of smoothness. In the context of this study, the radial basis function has been selected as the kernel for GPR (Schulz et al., 2018). The radial basis function is expressed as follows:

$$k(x, x') = \exp\left(-\frac{\left\| x - x' \right\|^2}{2l^2} \right) \quad \text{(F. 12)}$$

where the hyperparameter l is the length scale of the kernel.

Random Forest (RF)

Random Forest (RF) is an ensemble learning paradigm used in ML that employs a bagging (Bootstrap Aggregating) sampling technique and random feature selection to construct a set of decision trees with controlled variation (Breiman, 2001; Fawagreh et al., 2014). The decision trees are built using bagging from the training set with replacement. Statistically, there is a 64% chance of having a sample appear at least once in this process, which are called in-bag instances, while the remaining around 34% are called out-of-bag instances (Fawagreh et al., 2014). Each tree in the ensemble acts as a model, fitted to the bootstrapped samples, and the final prediction is obtained by averaging the results. The mathematical relationship for RF regression can be expressed as (Friedman, 2017):

$$\hat{f}_{rf}^{B}(x) = \frac{1}{B} \sum_{i=1}^{B} T(x; \Theta_b) \quad \text{(F. 13)}$$

Here, Θ_b denotes the i-th decision tree in the random forest, and B represents the total number of trees grown in the ensemble.

Voting Regressor (VR)

Voting Regressor (VR) is an ensemble ML technique that constructs the final prediction by averaging the results of individual models (Pedregosa et al., 2011). The term *vote* refers to the equal contribution of each standalone ML technique. However, in situations where the results of some models are more reliable, weighted voting (i.e., weighted average) can be used to assign more weight to those models.

Performance Measurement

This section aims to evaluate and compare the performance of different approaches based on various statistical measures. The metrics considered for this analysis are the coefficient of determination (R^2), root mean square error (RMSE), mean absolute error (MAE) and mean absolute percentage error (MAPE). These metrics can be defined as follows:

$$R^2 = \frac{\sum_{i=1}^{N}(x_i - x_{mean})^2 - \sum_{i=1}^{N}(x_i - \hat{x}_i)^2}{\sum_{i=1}^{N}(x_i - x_{mean})^2} \tag{F. 14}$$

$$RMSE = \left[\frac{1}{N}\sum_{i=1}^{N}\left(x_i - \hat{x}_i\right)^2\right]^{0.5} \tag{F. 15}$$

$$MAE = \frac{1}{N}\sum_{i=1}^{N}\left|(x_i - \hat{x}_i)\right| \tag{F. 16}$$

$$MAPE = \frac{100}{N}\sum_{i=1}^{N}\left|\frac{(x_i - \hat{x}_i)}{x_i}\right| \tag{F. 17}$$

where N is the total number of data, x_i and $\hat{x}_i$ are the real and predicted value of i^{th} data, and x_{mean} is the mean value of the actual output. By analyzing these measures, we can gain insight into the effectiveness of the predictions.

Dataset and Experiments

The research dataset comprises experimental data gathered from multiple sources (Sergi et al., 1992; Maruya et al., 1998; Luping, 2003; Samson and Marchand, 2007; Maekawa, 2008; Baroghel-Bouny et al., 2009; Baroghel-Bouny et al., 2014; Gang et al., 2015; Lu et al., 2015; Alfailakawi et al., 2020; Chen and Razaqpur, 2021a). This study considers various input parameters, with 14 input variables included, namely depth, ordinary Portland cement (OPC), sulfate-resisting Portland cement (SRPC), fly ash (FA), ground granulated blast-furnace slag (GGBS), silica fume (SF), superplasticizer, water, fine aggregate, coarse aggregate, water-to-binder ratio, exposure time, temperature, and surface chloride content.

To facilitate training and testing of the machine learning model, the dataset will be divided into two distinct sets: the training set and the testing set. The ratio of instances in the training and testing sets will be 0.75 and 0.25, respectively. The experiment will follow five major steps, including: (1) splitting the dataset into training and testing sets, (2) normalizing the features by adjusting the mean and standard deviation to 0 and 1, respectively, (3) tuning the hyperparameters using 10-fold cross-validation, (4) testing the model on the remaining data, and (5) evaluating the performance of various machine learning algorithms using different statistical measures.

Results

In this section, the results of 5 standalone machine learning models and 2 ensemble methods is presented.

LR Model

LR is the most basic machine learning algorithm discussed in this section, requiring only a few tuning parameters. **Figure F. 1**a presents a comparison of the LR model's predictions with the training data, while **Figure F. 1**b shows the model's performance when tested on new data. As can be observed, the LR model struggles to accurately predict the chloride content. The model performs better on the test data than on the training data, as evidenced by the higher coefficient of determination obtained for the former.

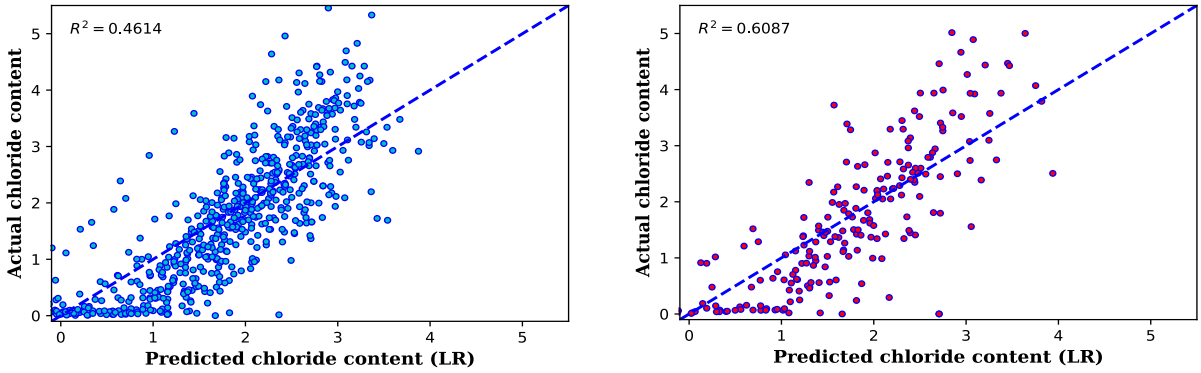

(a) Training set (b) Test set

Figure F. 1. Prediction of chloride content (in % of cement mass) using Linear Regression model

Lasso Regressor

The tunning for Lasso was performed via parameter λ in equation (F. 3) which accounts for the contribution of the L_1 norm. Accordingly, the average score of 10-fold cross-validation for different values of λ is measured and compared. The best performance was obtained for $\lambda = 0.01063$, resulting in a mean cross-validation score of 0.6343. As illustrated in **Figure F. 2**, the Lasso regressor achieved low accuracy on the dataset. Overall, the performance of the Lasso model was poor, similar to the LR model.

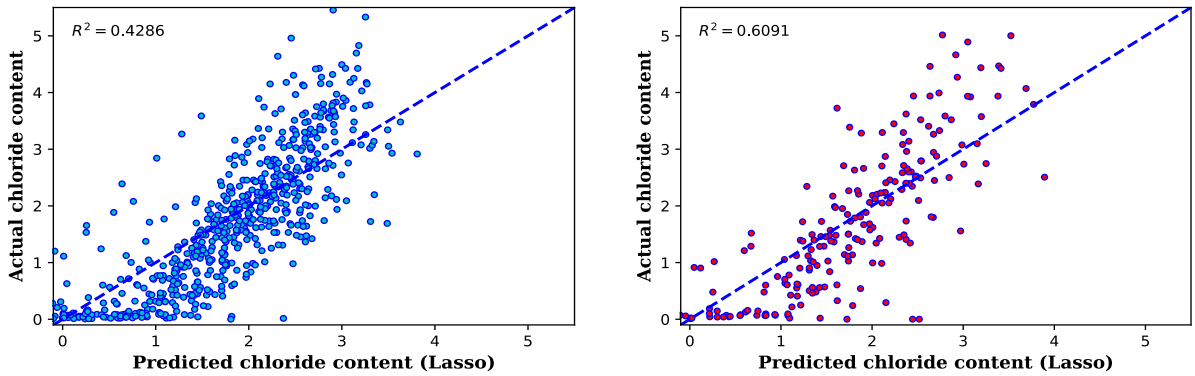

(a) Training set (b) Test set

Figure F. 2. Prediction of chloride content (in % of cement mass) using Lasso model

MLP Regressor

The best performance of the MLP regressor was achieved through tuning multiple hyperparameters using a cross-validation scheme. Table F. 1 presents the performance of the network based on different activation functions, including identity, logistic, hyperbolic tangent, and rectified linear unit. The results show that the hyperbolic tangent function achieved the best performance with an average score of 0.813.

Table F. 1. Score of 10-fold cross-validation for different activation function in MLP

Method	1st	2nd	3rd	4th	5th	6th	7th	8th	9th	10th	avg.
Tanh	0.812	0.788	0.827	0.757	0.776	0.871	0.880	0.840	0.723	0.861	0.813
Relu	0.790	0.763	0.839	0.729	0.770	0.854	0.850	0.817	0.678	0.884	0.798
Logistic	0.697	0.659	0.684	0.735	0.710	0.781	0.754	0.801	0.692	0.812	0.733
Identity	0.659	0.543	0.593	0.669	0.574	0.665	0.646	0.709	0.506	0.694	0.626

The second hyperparameter is the solver, which can be one of three popular forms: a family of quasi-Newton methods (lbfgs), stochastic gradient descent (sgd), and stochastic

gradient-based optimizer (Adam). Table F. 2 summarizes the results of cross-validation for different solver schemes, where the *Adam* solver obtained the best result.

Table F. 2. Score of 10-fold cross-validation for different solver in MLP

Method	1st	2nd	3rd	4th	5th	6th	7th	8th	9th	10th	avg.
Adam	0.795	0.787	0.825	0.738	0.782	0.866	0.868	0.849	0.709	0.865	0.809
sgd	0.770	0.687	0.792	0.712	0.751	0.791	0.778	0.822	0.694	0.808	0.761
lbfgs	0.818	0.889	0.128	0.913	0.553	0.900	0.765	0.919	0.764	0.768	0.742

Learning rate which has contributions to the weight updates is the third hyperparameter that is tuned in this section. Table F. 3 presents a comprehensive analysis of the performance of various learners, and the results indicate that Adaptive rate performs the best, as it achieves the highest cross-validation score.

Table F. 3. Score of 10-fold cross-validation for different learning rate in MLP

Method	1st	2nd	3rd	4th	5th	6th	7th	8th	9th	10th	avg.
Adaptive	0.811	0.776	0.826	0.755	0.800	0.886	0.855	0.840	0.726	0.866	0.814
Invscaling	0.808	0.759	0.821	0.748	0.813	0.875	0.869	0.833	0.719	0.851	0.810
Constant	0.802	0.765	0.827	0.760	0.772	0.854	0.879	0.839	0.711	0.861	0.807

The number of hidden layers and neurons are critical hyperparameters that significantly impact the final prediction of the MLP network. To optimize these hyperparameters, we have designed a set of networks with varying numbers of layers and neurons ranging from 1 to 50. The performance of these networks is evaluated based on the mean value of 10-fold cross-validation score, and the results are summarized in Table F. 4. It is noteworthy that the network with 30 layers and 36 neurons achieves the highest score, outperforming other networks with a different number of layers and neurons.

Table F. 4. Mean cross-validation score for different number of layers and neurons in MLP

No. of layers	30	48	48	45	38	38	36	32	38	31	32
No. of neurons	36	49	39	38	49	45	28	29	37	34	27
Mean score	0.854	0.850	0.850	0.849	0.847	0.847	0.846	0.846	0.846	0.846	0.846

The final hyperparameter that is tuned in this section is the number of epochs, and its value is determined based on the cross-validation score. To optimize this hyperparameter, a range of epochs from 200 to 8000 is considered, and the best performing value is identified. Our analysis indicates that the model performs optimally when trained for 4000 epochs.

Figure F. 3 displays the prediction capability of the MLP model, and it is evident that the it can accurately estimate the chloride content.

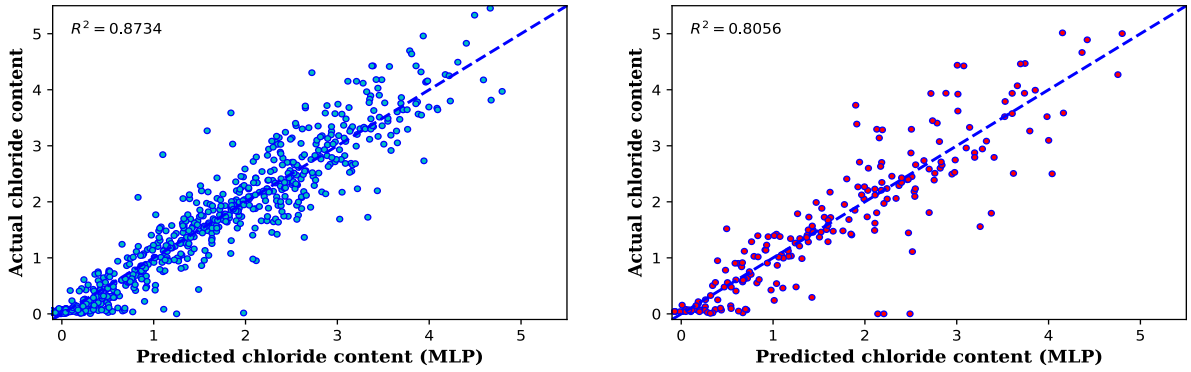

(a) Training set (b) Test set

Figure F. 3. Prediction of chloride content (in % of cement mass) using MLP model

SVM Regressor

The kernel function is a crucial hyperparameter that significantly influences the performance of the SVM model. To optimize this hyperparameter, we evaluated the performance of different kernel functions, including RBF, linear, polynomial, and sigmoid, using cross-validation. The results are summarized in Table F. 5, and it is evident that the RBF kernel function outperforms the other kernel functions, achieving the best performance.

Table F. 5. Mean cross-validation score for different kernel functions in SVM

Kernel	1st	2nd	3rd	4th	5th	6th	7th	8th	9th	10th	avg.
RBF	0.760	0.655	0.805	0.703	0.742	0.815	0.863	0.804	0.611	0.851	0.761
Linear	0.657	0.507	0.538	0.634	0.549	0.631	0.639	0.722	0.528	0.702	0.611
Polynomial	0.632	0.506	0.405	0.663	0.435	0.685	0.564	0.582	0.550	0.638	0.566
Sigmoid	-35.32	-12.18	-10.23	-20.71	-17.87	-12.09	-17.04	-16.22	-14.81	-15.05	-17.15

Figure F. 4 illustrates the performance of the SVM model in predicting the content of chloride, displaying the results for both the training and testing sets. The figure demonstrates that the SVM model can effectively capture the variations in chloride content, indicating the model's robustness and accuracy.

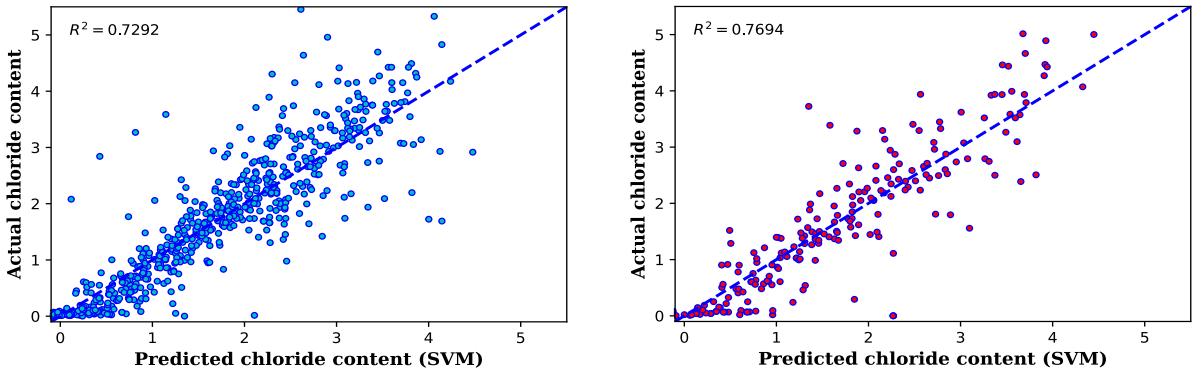

(a) Training set (b) Test set

Figure F. 4. Prediction of chloride content (in % of cement mass) using SVM model

GPR Model

An important hypermeter in the tuning of the GPR model is the variance of the additional Gaussian measurement noise. The 10-fold cross-validation is performed to obtain the best performance score which was 0.85411 for a noise variance of 0.0086. **Figure F. 5** depicts the result of the GPR model. As seen, both training and test sets could accurately predict the content of chloride.

The variance of the additional Gaussian measurement noise is a crucial hyperparameter in the tuning of the GPR model. To determine the best performance score, we conducted a 10-fold cross-validation and obtained a score of 0.85411 for a noise variance of 0.0086. The results of the GPR model are illustrated in **Figure F. 5** , indicating accurate predictions for both the training and test sets in determining the chloride content.

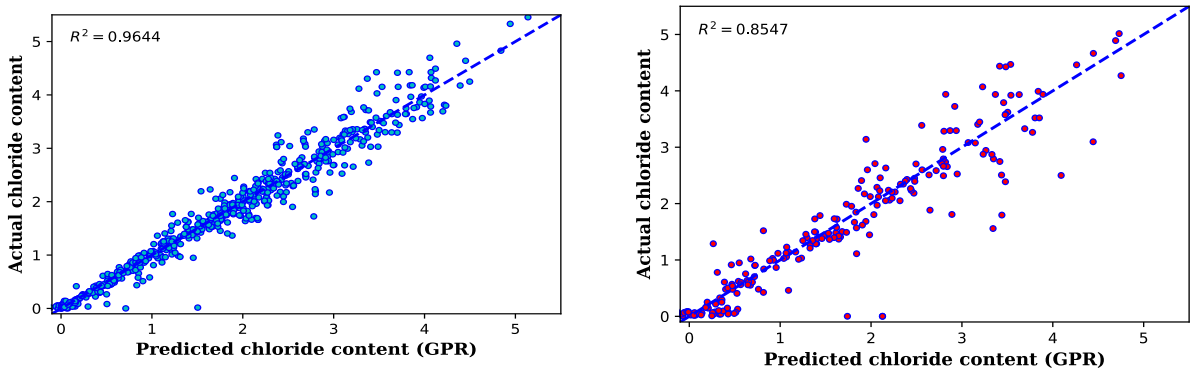

(a) Training set (b) Test set

Figure F. 5. Prediction of chloride content (in % of cement mass) using GPR model

RF Model

The number of trees and the maximum depth of the trees are two critical hyperparameters that significantly impact the performance of the RF model. **Figure F. 6** illustrates the effect of these hyperparameters through the mean of 10-fold cross-validation. As observed, the accuracy of the model approaches an asymptotic value with increasing values of the maximum depth and the number of trees. Therefore, to balance accuracy and computational cost, we selected the number of trees and maximum depth as 150 and 14, respectively.

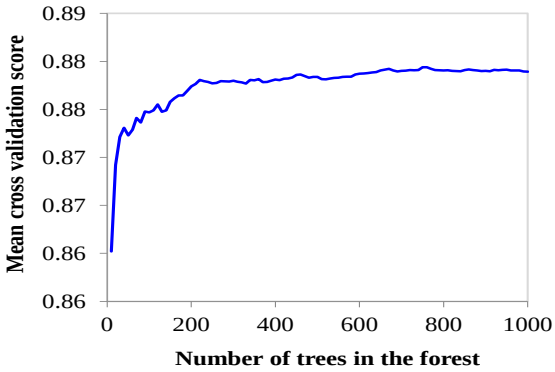

(a) Mean cross validation score for the number of trees in the forest

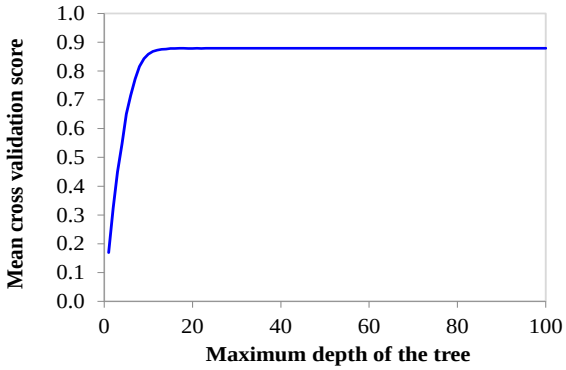

(b) Mean cross validation score for the maximum depth of the tree in the forest

Figure F. 6. Tuning of the hyperparameters in RF model

The number of features is another parameter that significantly affects the accuracy of the model. To find the most efficient and accurate approach, we performed cross-validation scores, as summarized in Table F. 6. The results show that the best performance is achieved with a condition where 12 features were selected.

Table F. 6. Mean cross-validation score for different number of selected features in RF model

No. of features	1	2	3	4	5	6	7	8	9	10	11	12	13	14
Mean score	0.423	0.684	0.818	0.839	0.856	0.860	0.863	0.863	0.882	0.884	0.880	0.884	0.880	0.878

Figure F. 6 presents the precision of the RF model, which indicates the accuracy of the model. Both the training and testing sets have achieved a noteworthy level of accuracy in forecasting the content of chloride ions.

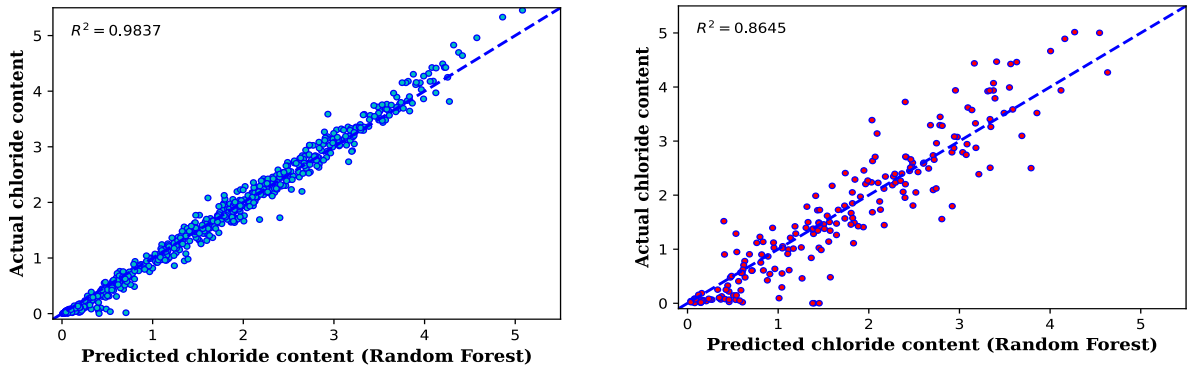

(a) Training set (b) Test set

Figure F. 7. Prediction of chloride content (in % of cement mass) using RF model

VR model

The voting method has been formulated by evaluating various combinations of standalone machine learning models. Based on the performance score of different ML techniques in the preceding sections, a weighted average of MLP, SVM, RF, and GPR was considered. The accuracy of the VR model is demonstrated in **Figure F. 8**. As depicted, both the training and testing sets have exhibited a good degree of accuracy.

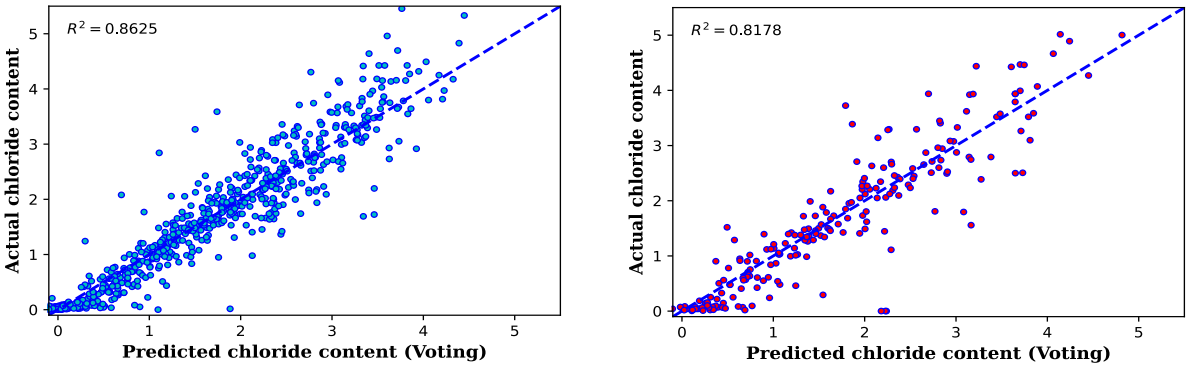

(a) Training set (b) Test set

Figure F. 8. Prediction of chloride content (in % of cement mass) using Voting model

Performance measurement

Table F. 7 presents a summary of the prediction accuracy of various ML techniques utilized in this study. It should be noted that the ideal condition is $R^2 = 1.0$. As evident from the table, RF has demonstrated the highest performance among different techniques with a score of $R^2 = 0.864$. Furthermore, GPR has also performed well on the test set, achieving a good score. Both VR and MLP have also exhibited satisfactory scores.

Table F. 7. Performance measures of different ML models on the test set

Method	R^2	MAE (% of cement)	MAPE (%)	MSE (% of cement)	RMSE (% of cement)
LR	0.609	0.616	35.908	0.708	0.841
Lasso	0.609	0.619	34.058	0.707	0.841
MLP	0.806	0.384	32.711	0.352	0.593
SVM	0.769	0.418	32.624	0.417	0.646
GPR	0.854	0.311	28.409	0.263	0.513
RF	0.864	0.339	20.372	0.245	0.495
VR	0.818	0.364	31.645	0.330	0.574

Sensitivity Analysis

The variation of chloride content concerning various features is a crucial parameter that assists engineers in designing, evaluating the performance, and retrofitting structures. As per the author's knowledge, this is the first instance where sensitivity analysis on the content of chloride has been conducted. **Figure F. 9** provides a comparison of the chloride content with respect to different features. It is important to note that the extraction of the relationship is based on a normal strength concrete mixture, as illustrated in Table F. 8. In this section, the voting method was employed to obtain the relationship between different features. This is because the average of different methods can increase the model's reliability. Moreover, as discussed in the preceding sections, the weighted average of different standalone methods was calibrated in a manner to reduce the noise of each standalone method on the final prediction.

In general, an increase in the depth from the exposure surface results in a decrease in chloride content, as does an increase in the contents of OPC, SRPC, FA, GGBS, SF, Superplasticizer, and coarse aggregate. Conversely, increasing the contents of fine aggregate, w/b ratio, temperature, time, and surface chloride content typically results in an increase in the chloride content.

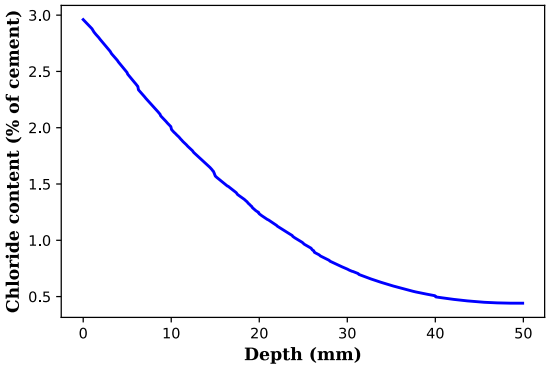

(a) Depth from exposure face

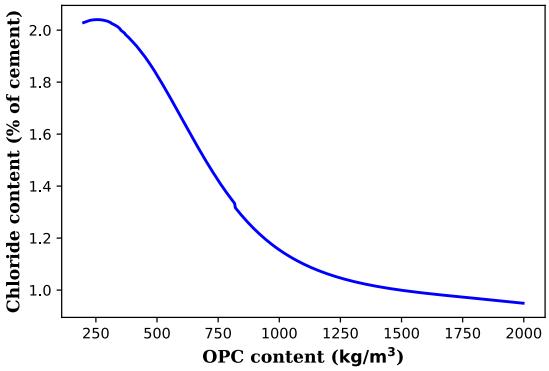

(b) Ordinary Portland Cement

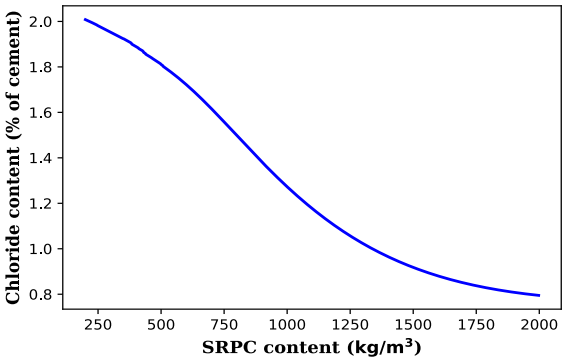

(c) Sulfate-resisting Portland Cement

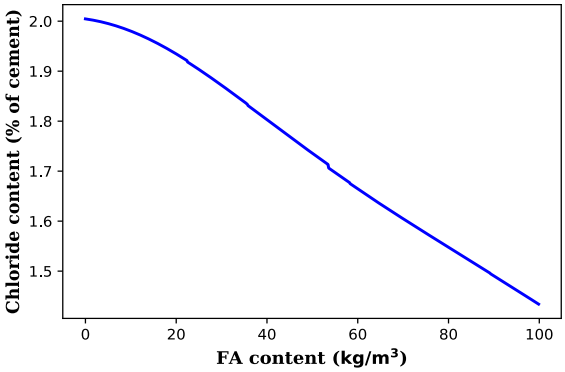

(d) Fly Ash

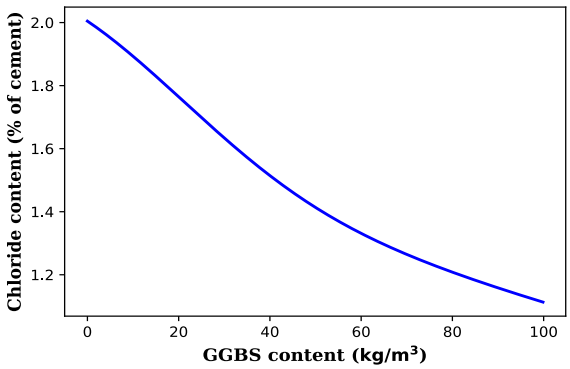

(e) Ground Granulated Blast-furnace Slag

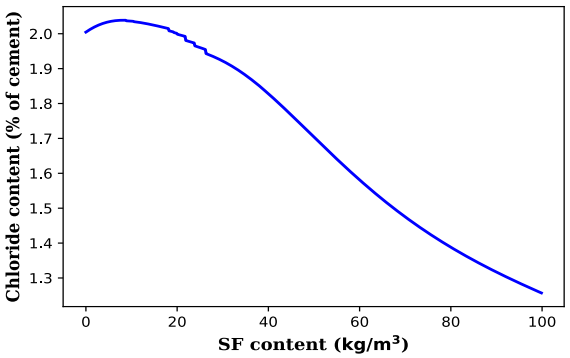

(f) Silica Fume

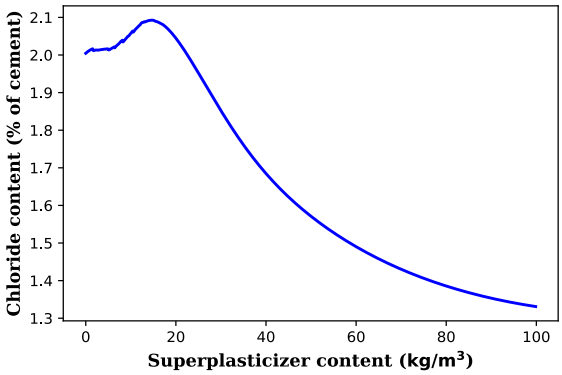

(g) Superplasticizer

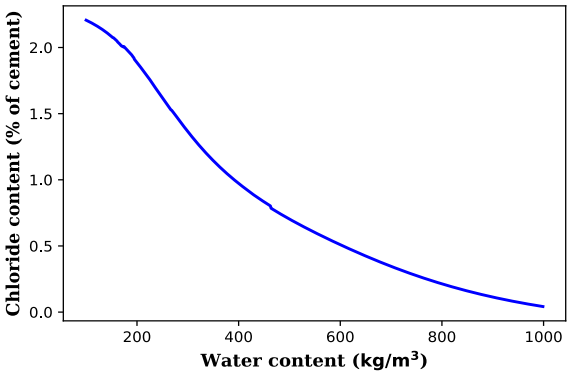

(h) Water

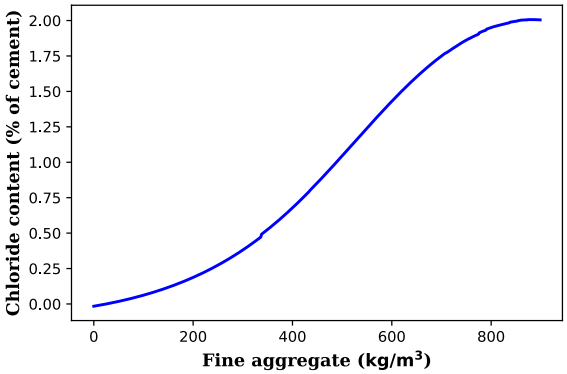

(i) Fine aggregate

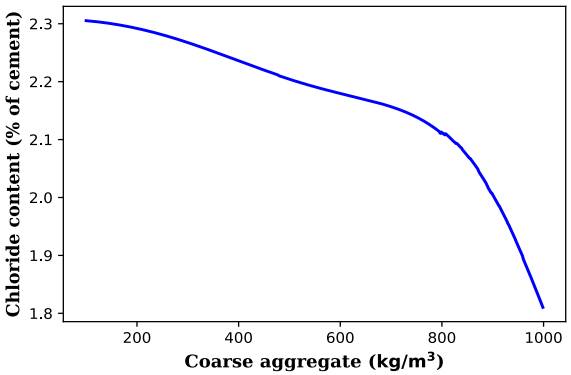

(j) Coarse aggregate

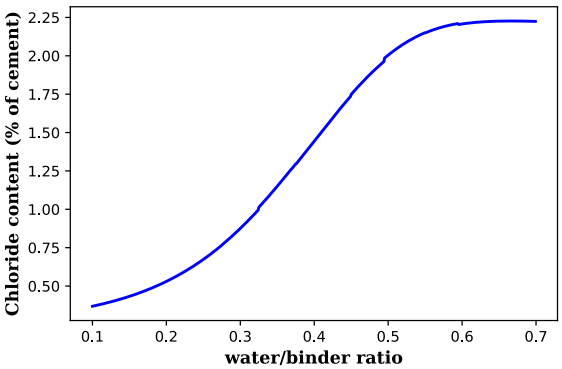

(k) w/b ratio

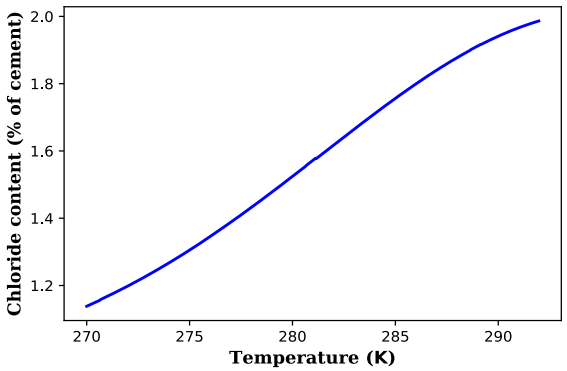

(l) Temperature

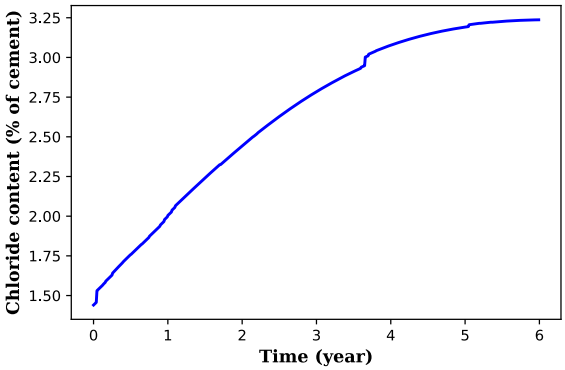

(m) Time of exposure

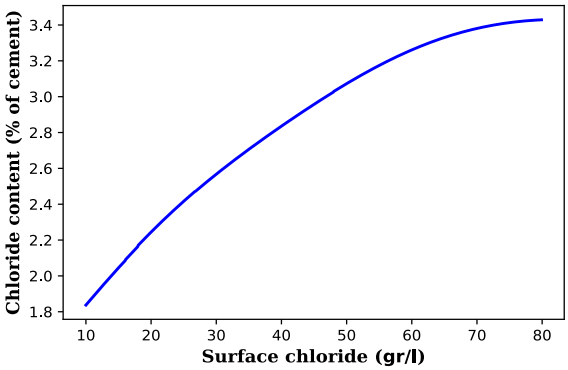

(n) Surface chloride content

Figure F. 9. Impact of different variable on the content of chloride in concrete structures

Table F. 8. Parameters in the sensitivity analysis

Depth (mm)	Cement (kg/m^3)	SRPC (kg/m^3)	FA (kg/m^3)	GGBS (kg/m^3)	SF (kg/m^3)	Superplasticizer (kg/m^3)
10.0	350.0	0.0	0.0	0.0	0.0	0.0
Water (kg/m^3)	Fine agg. (kg/m^3)	Coarse agg. (kg/m^3)	w/b	Time (year)	Temperature (K)	Surface chloride (gr/l)
175.0	900.0	900.0	0.5	1.0	293.15	14.0

Conclusions

The presence of chloride in concrete can have detrimental effects on the serviceability and load-bearing capacity of structures, as it leads to a significant increase in the rate of corrosion. This study explores the application of various machine learning techniques to predict the content of chloride in reinforced concrete structures. Based on the analysis, Random Forest

emerged as the most effective approach, albeit exhibiting a step-wise behavior with some noise due to the model's composition of trees. To mitigate this issue, a voting method was implemented, combining different approaches (MLP, SVM, RF, and GPR) to achieve accurate prediction of chloride content. The primary contribution of this study is not limited to predicting chloride content in reinforced concrete structures but also includes the identification of its relationship with each individual feature. As a result, engineers can better comprehend the correlation of each component in concrete mixtures with chloride, which can be immensely useful in the design, performance evaluation, and retrofitting of concrete structures.

References

AASHTO. (2020). AASHTO LRFD Bridge Design Specifications. 9th Ed., Washington, DC.

ACI. (2019). Building code requirements for structural concrete and commentary ACI 318-19. (Farmington Hills, MI: ACI).

Akhavan, A.,Rajabipour, F. (2012). Quantifying the effects of crack width, tortuosity, and roughness on water permeability of cracked mortars. *Cement and Concrete Research*, *42*(2), 313-320.

Akhavan, A.,Rajabipour, F. (2013). Evaluating ion diffusivity of cracked cement paste using electrical impedance spectroscopy. *Materials and Structures*, *46*(5), 697-708.

Al-Sulaimani, G., Kaleemullah, M., Basunbul, I. (1990). Influence of corrosion and cracking on bond behavior and strength of reinforced concrete members. *Structural Journal*, *87*(2), 220-231.

Al Rufaydah, A. S. (2021). *Shear Strength Assessment of Corrosion-Damaged Prestressed Concrete Girders* Virginia Tech].

Alfailakawi, A., Roberts-Wollmann, C., Hebdon, M., Koutromanos, I. (2020). Experimental and Analytical Evaluation of Residual Capacity of Corrosion-Damaged Prestressed Concrete Bridge Girders. *Virginia. Dept. of Transportation*. https://doi.org/https://rosap.ntl.bts.gov/view/dot/53953

Aliasghar-Mamaghani, M.,Khaloo, A. (2019). Seismic behavior of concrete moment frame reinforced with GFRP bars. *Composites Part B: Engineering*, *163*, 324-338.

Aliasghar-Mamaghani, M.,Khaloo, A. (2021). Effective Flexural Stiffness of Beams Reinforced with FRP Bars in Reinforced Concrete Moment Frames. *Journal of Composites for Construction*, *25*(1), 04020083.

Aliasghar-Mamaghani, M., Koutromanos, I., Roberts-Wollmann, C., Hebdon, M. (2022). Analytical Evaluation of Corrosion-Induced Strength Degradation in Prestressed Bridge Girders. *Journal of Structural Engineering*, *148*(11), 04022188.

Aliasghar-Mamaghani, M., Koutromanos, I., Roberts-Wollmann, C., Hebdon, M. (2023). Finite Element Analysis of Chloride Ingress in Prestressed Concrete Bridge Girders Accounting for Service-Life Ambient Conditions. *Journal of Structural Engineering*. https://doi.org/10.1061/JSENDH/STENG-11686

Aligizaki, K. K. (2005). *Pore structure of cement-based materials: testing, interpretation and requirements*. Crc Press.

Ariyawardena, N.,Ghali, A. (2002). Prestressing with unbonded internal or external tendons: Analysis and computer model. *Journal of Structural Engineering*, *128*(12), 1493-1501.

Bai, Y., Wang, Y., Xi, Y. (2020). Modeling the effect of temperature gradient on moisture and ionic transport in concrete. *Cement and Concrete Composites*, *106*, 103454.

Baroghel-Bouny, V. (2007). Water vapour sorption experiments on hardened cementitious materials: Part I: Essential tool for analysis of hygral behaviour and its relation to pore structure. *Cement and Concrete Research*, *37*(3), 414-437. https://doi.org/https://doi.org/10.1016/j.cemconres.2006.11.019

Baroghel-Bouny, V., Mainguy, M., Lassabatere, T., Coussy, O. (1999). Characterization and identification of equilibrium and transfer moisture properties for ordinary and high-performance cementitious materials. *Cement and Concrete Research*, *29*(8), 1225-1238.

Baroghel-Bouny, V., Nguyen, T., Dangla, P. (2009). Assessment and prediction of RC structure service life by means of durability indicators and physical/chemical models. *Cement and Concrete Composites*, *31*(8), 522-534. https://doi.org/https://doi.org/10.1016/j.cemconcomp.2009.01.009

Baroghel-Bouny, V., Thiéry, M., Wang, X. (2014). Performance-based assessment of durability and prediction of RC structure service life: transport properties as input data for physical models. *Materials and Structures*, *47*(10), 1669-1691. https://doi.org/https://doi.org/10.1617/s11527-013-0144-z

Bastidas-Arteaga, E., Chateauneuf, A., Sánchez-Silva, M., Bressolette, P., Schoefs, F. (2011). A comprehensive probabilistic model of chloride ingress in unsaturated concrete. *Engineering Structures*, *33*(3), 720-730.

Bažant, Z.,Najjar, L. (1972). Nonlinear water diffusion in nonsaturated concrete. *Matériaux et Construction*, *5*(1), 3-20. https://doi.org/https://doi.org/10.1007/BF02479073

Bažant, Z. P. (1979). Physical model for steel corrosion in concrete sea structures—theory. *Journal of the Structural Division*, *105*(6), 1137-1153.

Bažant, Z. P.,Jirásek, M. (2018). *Creep and hygrothermal effects in concrete structures* (Vol. 38). Springer. https://doi.org/https://link.springer.com/book/10.1007/978-94-024-1138-6

Bazant, Z. P.,Planas, J. (1997). *Fracture and size effect in concrete and other quasibrittle materials* (Vol. 16). CRC press.

Bazant, Z. P., Sener, S., Kim, J.-K. (1987). Effect of cracking on drying permeability and diffusivity of concrete. *ACI Materials Journal*, *84*(5), 351-357.

Benz, E.,Thomas, M. (2001). Life-365 Service Life Prediction Model: Computer Program for Predicting the Service Life and Life-Cycle Costs of Reinforced Concrete Exposed to Chlorides. In.

Breiman, L. (2001). Random forests. *Machine learning*, *45*(1), 5-32.

Brunauer, S., Emmett, P. H., Teller, E. (1938). Adsorption of gases in multimolecular layers. *Journal of the American Chemical society*, *60*(2), 309-319. https://doi.org/https://doi.org/10.1021/ja01269a023

Buenfeld, N.,Newman, J. (1987). Examination of three methods for studying ion diffusion in cement pastes, mortars and concrete. *Materials and Structures*, *20*(1), 3-10. https://doi.org/https://doi.org/10.1007/BF02472720

Buil, M. (1979). Contribution à l'étude du retrait de la pâte de ciment durcissante. *RAPP RECH LPC*(92).

Cabrera, J. G. (1996). Deterioration of concrete due to reinforcement steel corrosion. *Cement and Concrete Composites*, *18*(1), 47-59.

Callister, W. D., Rethwisch, D. G., Blicblau, A., Bruggeman, K., Cortie, M., Long, J., Hart, J., Marceau, R., Ryan, M., Parvizi, R. (2021). *Materials science and engineering: an introduction*. wiley.

Chen, B.,Razaqpur, A. G. (2021a). Effect of sub-zero versus sub-freezing temperature on chloride diffusion and binding in concrete. *Construction and building materials*, *287*, 123057. https://doi.org/https://doi.org/10.1016/j.conbuildmat.2021.123057

Chen, B.,Razaqpur, A. G. (2021b). Exposure duration and sub-zero temperature effects on concrete chloride diffusion decay index and binding. *Construction and building materials*, *313*, 125368. https://doi.org/https://doi.org/10.1016/j.conbuildmat.2021.125368

Clarke, S. M., Griebsch, J. H., Simpson, T. W. (2005). Analysis of support vector regression for approximation of complex engineering analyses.

Collepardi, M., Marcialis, A., Turriziani, R. (1972). Penetration of chloride ions into cement pastes and concretes. *Journal of the American Ceramic Society*, *55*(10), 534-535. https://doi.org/https://doi.org/10.1111/j.1151-2916.1972.tb13424.x

Conjeaud, M. (1980). Mechanism of sea water attack on cement mortar. *ACI Symposium Publication*, *65*, 39-62. https://doi.org/DOI:10.14359/6345

Coussy, O. (2011). *Mechanics and physics of porous solids*. John Wiley & Sons.

Dall'Asta, A.,Dezi, L. (1998). Nonlinear behavior of externally prestressed composite beams: Analytical model. *Journal of Structural Engineering*, *124*(5), 588-597.

Dall'Asta, A., Ragni, L., Zona, A. (2007). Simplified method for failure analysis of concrete beams prestressed with external tendons. *Journal of Structural Engineering, 133*(1), 121-131.

Deng, X., Koutromanos, I., Murcia-Delso, J., Panagiotou, M. (2021). Nonlinear truss models for strain-based seismic evaluation of planar RC walls. *Earthquake Engineering & Structural Dynamics, 50*(11), 2939-2960.

Dilger, W. H., Ghali, A., Chan, M., Cheung, M. S., Maes, M. A. (1983). Temperature stresses in composite box girder bridges. *Journal of Structural Engineering, 109*(6), 1460-1478. https://doi.org/https://doi.org/10.1061/(ASCE)0733-9445(1983)109:6(1460)

Dolan, C. W.,Hamilton, H. (2019). Prestressed Concrete. *Building, Design and*.

Donea, J.,Huerta, A. (2003). *Finite element methods for flow problems*. John Wiley & Sons. https://doi.org/DOI:10.1002/0470013826

Duda, R. O.,Hart, P. E. (1973). *Pattern classification and scene analysis* (Vol. 3). Wiley New York.

Elbadry, M. M.,Ghali, A. (1983). Temperature variations in concrete bridges. *Journal of Structural Engineering, 109*(10), 2355-2374. https://doi.org/https://doi.org/10.1061/(ASCE)0733-9445(1983)109:10(2355)

Elshoura, A.,Okeil, A. M. (2022). Study of Statistical Uncertainties for Temperature Gradients in Concrete Bridges. *ASCE-ASME Journal of Risk and Uncertainty in Engineering Systems, Part A: Civil Engineering, 8*(1), 04021083. https://doi.org/https://doi.org/10.1061/AJRUA6.0001209

Fahy, C., Wheeler, S. J., Gallipoli, D., Grassl, P. (2017). Corrosion induced cracking modelled by a coupled transport-structural approach. *Cement and Concrete Research, 94*, 24-35.

Fawagreh, K., Gaber, M. M., Elyan, E. (2014). Random forests: from early developments to recent advancements. *Systems Science & Control Engineering: An Open Access Journal, 2*(1), 602-609.

FIB. (2013). In *fib Model Code for Concrete Structures 2010*. https://doi.org/https://doi.org/10.1002/9783433604090.fmatter

Fish, J.,Belytschko, T. (2007). *A first course in finite elements* (Vol. 1). John Wiley & Sons New York.

Flint, M., Michel, A., Billington, S. L., Geiker, M. R. (2014). Influence of temporal resolution and processing of exposure data on modeling of chloride ingress and reinforcement corrosion in concrete. *Materials and Structures, 47*, 729-748.

Franceschini, L., Vecchi, F., Tondolo, F., Belletti, B., Montero, J. S. (2022). Mechanical behaviour of corroded strands under chloride attack: A new constitutive law. *Construction and building materials*, *316*, 125872.

Friedman, J. H. (2017). *The elements of statistical learning: Data mining, inference, and prediction*. springer open.

Gang, X., Yun-pan, L., Yi-biao, S., Ke, X. (2015). Chloride ion transport mechanism in concrete due to wetting and drying cycles. *Structural Concrete*, *16*(2), 289-296. https://doi.org/https://doi.org/10.1002/suco.201400035

Görtz, J., Wieprecht, S., Terheiden, K. (2021). Coupled model for crack-moisture interaction in brittle porous materials. *International journal of solids and structures*, *224*, 111025.

Hansen, E. J.,Saouma, V. E. (1999a). Numerical simulation of reinforced concrete deterioration—part 1: chloride diffusion. *Materials Journal*, *96*(2), 173-180. https://doi.org/DOI:10.14359/442

Hansen, E. J.,Saouma, V. E. (1999b). Numerical simulation of reinforced concrete deterioration: Part 2-Steel corrosion and concrete cracking. *ACI Materials Journal*, *96*, 331-338.

Hansen, P. (1985). Freiesleben:'Coupled moisture/heat transport in cross-sections of structures'. *Beton og Konstruktionsinstitutet (BKI), Denmark*.

Hanson, J. (1968). Effects of curing and drying enviroments on splitting tensile strength of concrete. Journal Proceedings,

Hansson, C., Poursaee, A., Laurent, A. (2006). Macrocell and microcell corrosion of steel in ordinary Portland cement and high performance concretes. *Cement and Concrete Research*, *36*(11), 2098-2102.

Harajli, M. H., Mabsout, M. E., Al-Hajj, J. A. (2002). Response of externally post-tensioned continuous members. *Structural Journal*, *99*(5), 671-680.

Harries, K. A. (2009). Structural testing of prestressed concrete girders from the Lake View Drive Bridge. *Journal of Bridge Engineering*, *14*(2), 78-92.

Hassanpour, S., Khaloo, A., Aliasghar-Mamaghani, M., Khaloo, H. (2022). Effect of Compressive Glass Fiber-Reinforced Polymer Bars on Flexural Performance of Reinforced Concrete Beams. *ACI Structural Journal*, *119*(6).

Haykin, S. S. (2009). Neural networks and learning machines/Simon Haykin. In: New York: Prentice Hall.

Henriksen, C. F.,Stoltzner, E. (1993). Chloride corrosion in Danish road-bridge columns. *Concrete International*, *15*(8), 55-60.

Higgs, A., Barr, P. J., Halling, M. W. (2015). Comparison of measured and AASHTO LRFD-predicted residual prestress forces, shear and flexural capacities of high-strength prestressed-concrete bridge girders. *Journal of Bridge Engineering*, *20*(1), 05014009.

Hussain, R. R.,Ishida, T. (2011). Enhanced electro-chemical corrosion model for reinforced concrete under severe coupled action of chloride and temperature. *Construction and building materials*, *25*(3), 1305-1315.

Hussain, S. E., Al-Gahtani, A. S., Rasheeduzzafar. (1996). Chloride threshold for corrosion of reinforcement in concrete. *ACI Materials Journal*, *93*(6), 534-538.

Iqbal, M. (2012). *An introduction to solar radiation*. Elsevier.

Ishida, T., Iqbal, P. O. N., Anh, H. T. L. (2009). Modeling of chloride diffusivity coupled with non-linear binding capacity in sound and cracked concrete. *Cement and Concrete Research*, *39*(10), 913-923. https://doi.org/https://doi.org/10.1016/j.cemconres.2009.07.014

Ismail, M., Toumi, A., François, R., Gagné, R. (2008). Effect of crack opening on the local diffusion of chloride in cracked mortar samples. *Cement and Concrete Research*, *38*(8-9), 1106-1111.

Jain, A. K., Mao, J., Mohiuddin, K. M. (1996). Artificial neural networks: A tutorial. *Computer*, *29*(3), 31-44.

Jeon, C.-H., Lee, J.-B., Lon, S., Shim, C.-S. (2019). Equivalent material model of corroded prestressing steel strand. *Journal of Materials Research and Technology*, *8*(2), 2450-2460.

Jeon, C.-H., Nguyen, C. D., Shim, C.-S. (2020). Assessment of mechanical properties of corroded prestressing strands. *Applied Sciences*, *10*(12), 4055.

Ji, Y.-s., Zhao, W., Zhou, M., Ma, H.-r., Zeng, P. (2013). Corrosion current distribution of macrocell and microcell of steel bar in concrete exposed to chloride environments. *Construction and building materials*, *47*, 104-110.

Kato, E., Kato, Y., Uomoto, T. (2005). Development of simulation model of chloride ion transportation in cracked concrete. *Journal of Advanced Concrete Technology*, *3*(1), 85-94.

Kehlbeck, F. (1975). *Einfluss der Sonnenstrahlung bei Brückenbauwerken*. Werner-Verlag.

Kim, J., McCarter, W. J., Suryanto, B., Nanukuttan, S., Basheer, P. M., Chrisp, T. M. (2016). Chloride ingress into marine exposed concrete: A comparison of empirical-and physically-based models. *Cement and Concrete Composites*, *72*, 133-145. https://doi.org/https://doi.org/10.1016/j.cemconcomp.2016.06.002

Kim, S. H.,Koutromanos, I. (2016). Constitutive model for reinforcing steel under cyclic loading. *Journal of Structural Engineering*, *142*(12), 04016133.

Kong, J. S., Ababneh, A. N., Frangopol, D. M., Xi, Y. (2002). Reliability analysis of chloride penetration in saturated concrete. *Probabilistic Engineering Mechanics*, *17*(3), 305-315.

Koutromanos, I. (2018). *Fundamentals of Finite Element Analysis: Linear Finite Element Analysis*. John Wiley & Sons.

Koutromanos, I.,Farhadi, M. (2018). *FE-MultiPhys: A Finite Element Program for Nonlinear Analysis of Continua and Structures*. https://doi.org/DOI:10.13140/RG.2.2.27375.38560

Kumar, R.,Bhattacharjee, B. (2003). Porosity, pore size distribution and in situ strength of concrete. *Cement and Concrete Research*, *33*(1), 155-164. https://doi.org/https://doi.org/10.1016/S0008-8846(02)00942-0

Künzel, H. M. (1995). Simultaneous heat and moisture transport in building components. *One-and two-dimensional calculation using simple parameters. IRB-Verlag Stuttgart*, *65*.

Langmuir, I. (1918). The adsorption of gases on plane surfaces of glass, mica and platinum. *Journal of the American Chemical society*, *40*(9), 1361-1403. https://doi.org/https://doi.org/10.1021/ja02242a004

Lee, Y., Choi, M.-S., Yi, S.-T., Kim, J.-K. (2009). Experimental study on the convective heat transfer coefficient of early-age concrete. *Cement and Concrete Composites*, *31*(1), 60-71. https://doi.org/https://doi.org/10.1016/j.cemconcomp.2008.09.009

Lu, C., Gao, Y., Cui, Z., Liu, R. (2015). Experimental analysis of chloride penetration into concrete subjected to drying–wetting cycles. *Journal of Materials in Civil Engineering*, *27*(12), 04015036. https://doi.org/https://doi.org/10.1061/(ASCE)MT.1943-5533.0001304

Lu, C., Yang, J., Li, H., Liu, R. (2017). Experimental studies on chloride penetration and steel corrosion in cracked concrete beams under drying-wetting cycles. *Journal of Materials in Civil Engineering*, *29*(9), 04017114.

Lu, Y.,Panagiotou, M. (2014). Three-dimensional cyclic beam-truss model for nonplanar reinforced concrete walls. *Journal of Structural Engineering*, *140*(3), 04013071.

Lu, Z.-H., Li, F., Zhao, Y.-G. (2016). An investigation of degradation of mechanical behaviour of prestressing strands subjected to chloride attacking.

Luping, T. (2003). *Chloride ingress in concrete exposed to marine environment-field data up to 10 years exposure*.

Maage, M., Helland, S., Poulsen, E., Vennesland, O., Carl, J. E. (1996). Service life prediction of existing concrete structures exposed to marine environment. *Materials Journal*, *93*(6), 602-608.

Maekawa, K. (2008). *Multi-scale modeling of structural concrete*. Crc Press.

Maekawa, K., Ishida, T., Kishi, T. (2003). Multi-scale modeling of concrete performance integrated material and structural mechanics. *Journal of Advanced Concrete Technology*, *1*(2), 91-126. https://doi.org/https://doi.org/10.3151/jact.1.91

Mangat, P.,Molloy, B. (1994). Prediction of long term chloride concentration in concrete. *Materials and Structures*, *27*(6), 338-346. https://doi.org/https://doi.org/10.1007/BF02473426

Martın-Pérez, B., Pantazopoulou, S. J., Thomas, M. (2001). Numerical solution of mass transport equations in concrete structures. *Computers & Structures*, *79*(13), 1251-1264. https://doi.org/https://doi.org/10.1016/S0045-7949(01)00018-9

Martin, R. D., Kang, T. H. K., Pei, J. S. (2011). Experimental and code analyses for shear design of AASHTO prestressed concrete girders. *Pci Journal*, *56*(1), 54-74. https://doi.org/10.15554/pcij.01012011.54.74

Maruya, T. (1995). *Development of a Method of Analyzing the Movement of Chloride Ions in Concrete* PhD Thesis, The University of Tokyo.].

Maruya, T., Matsuoka, Y., Tangtermsirikul, S. (1998). Modeling of chloride ion movement at the surface layer of hardened concrete. *Doboku Gakkai Ronbunshu*, *1998*(585), 79-95.

McGee, R. (1999). Modelling of durability performance of Tasmanian bridges. *ICASP8 applications of statistics and probability in civil engineering*, *1*, 297-306.

Mehta, P. K.,Monteiro, P. J. (2014). *Concrete: microstructure, properties, and materials*. McGraw-Hill Education.

Mengel, L., Krauss, H.-W., Lowke, D. (2020). Water transport through cracks in plain and reinforced concrete–Influencing factors and open questions. *Construction and building materials*, *254*, 118990.

Moharrami, M.,Koutromanos, I. (2016). Triaxial constitutive model for concrete under cyclic loading. *Journal of Structural Engineering*, *142*(7), 04016039.

Moharrami, M., Koutromanos, I., Panagiotou, M., Girgin, S. C. (2015). Analysis of shear-dominated RC columns using the nonlinear truss analogy. *Earthquake Engineering & Structural Dynamics*, *44*(5), 677-694.

Molina, F., Alonso, C., Andrade, C. (1993). Cover cracking as a function of rebar corrosion: Part 2—Numerical model. *Materials and Structures*, *26*(9), 532-548.

Murray, C. D., Cranor, B. N., Floyd, R. W., Pei, J.-S. (2019). Experimental testing of older AASHTO Type II bridge girders with corrosion damage at the ends. *Pci Journal*, *64*(1), 49-64.

Naaman, A. E. (1982). *Prestressed concrete analysis and design: Fundamentals*. McGraw-Hill New York.

Naito, C., Jones, L., Hodgson, I. (2010a). Inspection methods & techniques to determine non visible corrosion of prestressing strands in concrete bridge components: task 3, forensic evaluation and rating methodology. *Pennsylvania. Dept. of Transportation. Bureau of Planning and Research*.

Naito, C., Sause, R., Hodgson, I., Pessiki, S., Macioce, T. (2010b). Forensic examination of a noncomposite adjacent precast prestressed concrete box beam bridge. *Journal of Bridge Engineering*, *15*(4), 408-418. https://doi.org/https://doi.org/10.1061/(ASCE)BE.1943-5592.0000110

NASASP-8005. (1971). Solar Electromagnetic Radiation. *National Aeronautics and Space Administration*.

Nawy, E. G. (1996). *Prestressed concrete. A fundamental approach*.

Ng, C.-K. (2003). Tendon stress and flexural strength of externally prestressed beams. *Structural Journal*, *100*(5), 644-653.

Nilsson, L.-O. (2002). Long-term moisture transport in high performance concrete. *Materials and Structures*, *35*(10), 641-649.

Oh, B. H., Jang, B. S., Lee, S. C. (2004). Chloride diffusion and corrosion initiation time of reinforced concrete structures. Proceedings of the International Workshop on Microstructure and Durability to Predict Service Life of Concrete Structures Sapporo, Japan,

Okeil, A. M. (2014). Data collection and evaluation of continuity detail for John James Audubon Bridge No. 61390613004101. *Louisiana. Dept. of Transportation and Development*.

Osborn, G. P., Barr, P. J., Petty, D. A., Halling, M. W., Brackus, T. R. (2012). Residual prestress forces and shear capacity of salvaged prestressed concrete bridge girders. *Journal of Bridge Engineering*, *17*(2), 302-309.

Otieno, M., Beushausen, H., Alexander, M. (2016). Chloride-induced corrosion of steel in cracked concrete—Part II: Corrosion rate prediction models. *Cement and Concrete Research*, *79*, 386-394.

Page, C.,Vennesland, Ø. (1983). Pore solution composition and chloride binding capacity of silica-fume cement pastes. *Matériaux et Construction*, *16*(1), 19-25. https://doi.org/https://doi.org/10.1007/BF02474863

Panagiotou, M., Restrepo, J. I., Schoettler, M., Kim, G. (2012). Nonlinear cyclic truss model for reinforced concrete walls. *ACI Structural Journal*, *109*(2), 205-214.

Pape, T. M.,Melchers, R. E. (2011). The effects of corrosion on 45-year-old pre-stressed concrete bridge beams. *Structure and Infrastructure Engineering*, *7*(1-2), 101-108. https://doi.org/https://doi.org/10.1080/15732471003588411

Pape, T. M.,Melchers, R. E. (2013). Performance of 45-year-old corroded prestressed concrete beams. *Proceedings of the Institution of Civil Engineers-Structures and Buildings*, *166*(10), 547-559.

Park, S.-S., Kwon, S.-J., Jung, S. H. (2012a). Analysis technique for chloride penetration in cracked concrete using equivalent diffusion and permeation. *Construction and building materials*, *29*, 183-192.

Park, S.-S., Kwon, S.-J., Jung, S. H., Lee, S.-W. (2012b). Modeling of water permeability in early aged concrete with cracks based on micro pore structure. *Construction and building materials*, *27*(1), 597-604.

Pedregosa, F., Varoquaux, G., Gramfort, A., Michel, V., Thirion, B., Grisel, O., Blondel, M., Prettenhofer, P., Weiss, R., Dubourg, V. (2011). Scikit-learn: Machine learning in Python. *the Journal of machine Learning research*, *12*, 2825-2830.

Pei, J.-S., Martin, R. D., Sandburg, C. J., Kang, T. H.-K. (2008). Rating precast prestressed concrete bridges for shear. *Oklahoma. Dept of Transportation*.

Rahimi-Aghdam, S., Rasoolinejad, M., Bažant, Z. P. (2019). Moisture diffusion in unsaturated self-desiccating concrete with humidity-dependent permeability and nonlinear sorption isotherm. *Journal of Engineering Mechanics*, *145*(5), 04019032.

Rasmussen, C. E. (2003). Gaussian processes in machine learning. Summer school on machine learning,

Rastiello, G., Boulay, C., Dal Pont, S., Tailhan, J.-L., Rossi, P. (2014). Real-time water permeability evolution of a localized crack in concrete under loading. *Cement and Concrete Research*, *56*, 20-28.

Recupero, A., Spinella, N., Tondolo, F. (2018). A model for the analysis of ultimate capacity of RC and PC corroded beams. *Advances in Civil Engineering*, *2018*.

Roberts-Wollmann, C. L., Kreger, M. E., Rogowsky, D. M., Breen, J. E. (2005). Stresses in external tendons at ultimate. *ACI Structural Journal*, *102*(2), 206.

Ross, B. E., Ansley, M., Hamilton, H. (2011). Load testing of 30-year-old AASHTO Type III highway bridge girders. *Pci Journal*, *56*(4).

Saetta, A. V., Scotta, R. V., Vitaliani, R. V. (1993). Analysis of chloride diffusion into partially saturated concrete. *Materials Journal*, *90*(5), 441-451. https://doi.org/DOI:10.14359/3874

Samson, E.,Marchand, J. (2007). Modeling the effect of temperature on ionic transport in cementitious materials. *Cement and Concrete Research*, *37*(3), 455-468. https://doi.org/https://doi.org/10.1016/j.cemconres.2006.11.008

Schießl, P., Bamforth, P., Baroghel-Bouny, V., Corley, G., Faber, M., Forbes, J., Gehlen, C., Helene, P., Helland, S., Ishida, T. (2006). Model code for service life design. fib bulletin 34. In: Februar.

Schulz, E., Speekenbrink, M., Krause, A. (2018). A tutorial on Gaussian process regression: Modelling, exploring, and exploiting functions. *Journal of Mathematical Psychology*, *85*, 1-16.

Sergi, G., Yu, S., Page, C. (1992). Diffusion of chloride and hydroxyl ions in cementitious materials exposed to a saline environment. *Magazine of Concrete Research*, *44*(158), 63-69. https://doi.org/https://doi.org/10.1680/macr.1992.44.158.63

Servo, K.,Pihlajavaara, S. (1969). An approximate solution of a quasi-linear diffusion problem: Tables and nomograms for concentration in slabs in a special case.

Shafei, B., Alipour, A., Shinozuka, M. (2012). Prediction of corrosion initiation in reinforced concrete members subjected to environmental stressors: A finite-element framework. *Cement and Concrete Research*, *42*(2), 365-376. https://doi.org/https://doi.org/10.1016/j.cemconres.2011.11.001

Shenoy, C. V.,Frantz, G. C. (1991). Structural tests of 27-year-old prestressed concrete bridge beams. *Pci Journal*, *36*(5), 80-90.

Shin, K. J., Bae, W., Choi, S.-W., Son, M. W., Lee, K. M. (2017). Parameters influencing water permeability coefficient of cracked concrete specimens. *Construction and building materials*, *151*, 907-915.

Smith, R. C. (2013). *Uncertainty quantification: theory, implementation, and applications* (Vol. 12). Siam.

Standard, B. (1997). Structural Use of Concrete: Code of Practice for Design and Construction, Part 1, BS 8110. In: British Standard Institution, UK.

Stewart, M. G. (2009). Mechanical behaviour of pitting corrosion of flexural and shear reinforcement and its effect on structural reliability of corroding RC beams. *Structural safety*, *31*(1), 19-30.

Stratfull, R., Jurkovich, W., Spellman, D. (1975). *Corrosion testing of bridge decks*. The Laboratory Sacramento, CA, USA.

Tabatabai, H.,Dickson, T. J. (1993). Structural evaluation of a 34-year-old precast post-tensioned concrete girder. *PRECAST/PRESTRESSED CONCRETE INSTITUTE. JOURNAL*, *38*(5), 50-63.

Tang, L.,Nilsson, L.-O. (1996). A numerical method for prediction of chloride penetration into concrete structures. In *The modelling of microstructure and its potential for studying transport properties and durability* (pp. 539-552). Springer. https://doi.org/https://doi.org/10.1007/978-94-015-8646-7_29

Tibshirani, R. (1996). Regression shrinkage and selection via the lasso. *Journal of the Royal Statistical Society: Series B (Methodological)*, *58*(1), 267-288.

Toongoenthong, K.,Maekawa, K. (2005). Simulation of coupled corrosive product formation, migration into crack and propagation in reinforced concrete sections. *Journal of Advanced Concrete Technology*, *3*(2), 253-265.

Val, D. V. (2007). Factors affecting life-cycle cost analysis of RC structures in chloride contaminated environments. *Journal of infrastructure systems*, *13*(2), 135-143. https://doi.org/https://doi.org/10.1061/(ASCE)1076-0342(2007)13:2(135)

Val, D. V.,Melchers, R. E. (1997). Reliability of deteriorating RC slab bridges. *Journal of Structural Engineering*, *123*(12), 1638-1644.

Val, D. V.,Trapper, P. A. (2008). Probabilistic evaluation of initiation time of chloride-induced corrosion. *Reliability Engineering & System Safety*, *93*(3), 364-372.

Van Genuchten, M. T. (1980). A closed-form equation for predicting the hydraulic conductivity of unsaturated soils. *Soil science society of America journal*, *44*(5), 892-898. https://doi.org/https://doi.org/10.2136/sssaj1980.03615995004400050002x

Vassie, P. (1984). REINFORCEMENT CORROSION AND THE DURABILITY OF CONCRETE BRIDGES. *Proceedings of the Institution of Civil Engineers*, *76*(3), 713-723.

Vecchio, F. J.,Collins, M. P. (1986). The modified compression-field theory for reinforced concrete elements subjected to shear. *ACI J.*, *83*(2), 219-231.

Vidal, T., Castel, A., François, R. (2004). Analyzing crack width to predict corrosion in reinforced concrete. *Cement and Concrete Research*, *34*(1), 165-174.

Wang, Y., Zhao, Y., Gong, F., Dong, J., Maekawa, K. (2022). Developing a three-dimensional finite element analysis approach to simulate corrosion-induced concrete cracking in reinforced concrete beams. *Engineering Structures*, *257*, 114072.

Wang, Z., Maekawa, K., Takeda, H., Gong, F. (2021). Numerical simulation and experiment on the coupled effects of macro-cell corrosion and multi-ion equilibrium with pseudo structural concrete. *Cement and Concrete Composites*, *123*, 104181.

Weyers, R. E., Fitch, M. G., Larsen, E. P., Al-Qadi, I. L., Chamberlin, W., Hoffman, P. (1994). Concrete bridge protection and rehabilitation: Chemical and physical techniques. Service life estimates.

Win, P. P., Watanabe, M., Machida, A. (2004). Penetration profile of chloride ion in cracked reinforced concrete. *Cement and Concrete Research*, *34*(7), 1073-1079.

Winslow, D.,Liu, D. (1990). The pore structure of paste in concrete. *Cement and Concrete Research*, *20*(2), 227-235. https://doi.org/https://doi.org/10.1016/0008-8846(90)90075-9

Youping, L.,Richard, E. W. (1998). Modeling the Time-to-Corrosion Cracking in Chloride Contaminated Reinforced Concrete Structures. *ACI Materials Journal*, *95*(6). https://doi.org/DOI:10.14359/410

Yun, T. S., Jeong, Y. J., Han, T.-S., Youm, K.-S. (2013). Evaluation of thermal conductivity for thermally insulated concretes. *Energy and Buildings*, *61*, 125-132. https://doi.org/https://doi.org/10.1016/j.enbuild.2013.01.043

Zhang, G., Tian, Y., Jin, X., Zeng, Q., Jin, N., Yan, D., Tian, Z. (2020). A self-balanced electrochemical model for corrosion of reinforcing steel bar in considering the micro-environments in concrete. *Construction and building materials*, *254*, 119116.

Zhang, W.-p., Li, C.-k., Gu, X.-l., Zeng, Y.-h. (2019). Variability in cross-sectional areas and tensile properties of corroded prestressing wires. *Construction and building materials*, *228*, 116830.

Zhang, Y., Di Luzio, G., Alnaggar, M. (2021). Coupled multi-physics simulation of chloride diffusion in saturated and unsaturated concrete. *Construction and building materials*, *292*, 123394. https://doi.org/https://doi.org/10.1016/j.conbuildmat.2021.123394

Zhao, Y., Yu, J., Hu, B., Jin, W. (2012). Crack shape and rust distribution in corrosion-induced cracking concrete. *Corrosion science*, *55*, 385-393.